UNIVERSITAT DE BARCELONA

Nitrate and Pesticide Removal from Groundwater Using Different Electrochemical Reactors

Roger Oriol López

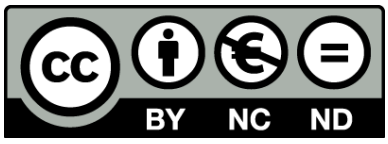

Programa de Doctorat en

Electroquímica. Ciència i Tecnologia

NITRATE AND PESTICIDE REMOVAL FROM GROUNDWATER USING DIFFERENT ELECTROCHEMICAL REACTORS

Memòria presentada per optar al

Grau de Doctor per la Universitat de Barcelona

Roger Oriol López

Director

Dr. Ignacio Sirés Sadornil

Professor Agregat

Tutor Acadèmic

Dr. Enric Brillas Coso

Professor Catedràtic

Barcelona, Juliol de 2023

Facultat de Química

Departament de Ciència de Materials i Química Física

Secció de Química Física

NITRATE AND PESTICIDE REMOVAL FROM GROUNDWATER USING DIFFERENT ELECTROCHEMICAL REACTORS

Roger Oriol López

PhD Thesis

Laboratori d'Electroquímica dels Materials i del Medi Ambient (LEMMA)

Barcelona, Juliol de 2023

Un artista treballa amb el que té

Acknowledgements

I would like to express my sincere gratitude to my supervisor, Prof. Ignacio Sirés Sadornil, as well as to my tutor, Prof. Enric Brillas Coso, for their guidance and trust in me throughout the development of this Thesis. Their professionalism and thoroughness for scientific research have been the main driving force that has inspired me towards the fulfilment of this Thesis. I would like to thank Prof. Pere Lluís Cabot Julià as well for his interest in sharing with me his deep knowledge and experience, and Prof. Elvira Gómez for her helpful advice and carefulness over all these years. In addition, I would like to express my gratitude to other professors from our Physical Chemistry section at the Faculty of Chemistry. Moreover, I would also like to thank in advance the jury members for their acceptance and the valuable suggestions that they will for sure make during my defence.

A warm acknowledgment is also to Prof. José L. Nava Montes de Oca, for accepting my stay at the Universidad de Guanajuato under his guidance. His knowledge encouraged me to broaden my research scope, allowing me to acquire some skills to deal with the fundamentals of computational fluid dynamics and its relevant application to the characterization of electrochemical reactors.

My very sincere thanks also go to all the colleagues at LEMMA group. They have contributed very significantly to my personal and professional growth along these years: Júlia, Oscar, Lele, Anlin, Zhihong, Yanyu, Gengbo, Fengxia, Claudio, Murilo, Diego, Alex, Matheus, Belle, Nathalia, Adalgisa, Carlota, Laye, Camilo, Rafa, Isidoro, Fernanda, Paola, Karen, Maria Pilar…Without their help and support, this Thesis would have been a much harder path.

A special thanks to my family and friends, who have supported me unconditionally all this time, including those periods that were not always easy. Their support has driven me through all the difficulties that appeared from time to time, becoming a cornerstone to successfully finish my PhD Thesis.

Last, I would like to thank the Spanish government (BES-2017-080095) for awarding the public scholarship that has provided financial support for the whole PhD.

Table of contents

List of equations and reactions

(18) $NH_3 + HClO \rightarrow NH_2Cl + H_2O$ 41

(19) $NH_2Cl + HClO \rightarrow NHCl_2 + H_2O$ 41

(20) $NHCl_2 + HClO \rightarrow NCl_3 + H_2O$ 41

(21) $NO_2^- + ClO^- \rightarrow NO_3^- + Cl^-$ 41

(22) $NH_2Cl + NO_2^- + H_2O \rightarrow NO_3^- + NH_4^+ + Cl^-$ 42

(23) $ClO^- + H_2O \rightarrow ClO_2^- + 2H^+ + 2e^-$ 42

(24) $ClO_2^- + H_2O \rightarrow ClO_3^- + 2H^+ + 2e^-$ 42

(25) $ClO_3^- + H_2O \rightarrow ClO_4^- + 2H^+ + 2e^-$ 42

(26) $\%\ \text{Target pollutant removal} = \frac{\Delta C}{C_0} \times 100$ 61

(27) $\%\ \text{TOC removal} = \frac{\Delta \text{TOC}}{\text{TOC}_0} \times 100$ 61

(28) $\%\ \text{MCE} = \frac{n\,F\,V\,\Delta \text{TOC}}{4.32\times10^7\ m\,I\,t} \times 100$ 61

(29) $C_9H_{10}ClN_5O_2 + 31H_2O \rightarrow 9CO_2 + Cl^- + 5NO_3^- + 72H^+ + 66e^-$ 61

(30) $C_9H_{16}ClN_5 + 33H_2O \rightarrow 9CO_2 + Cl^- + 5NO_3^- + 82H^+ + 76e^-$ 61

(31) $\text{FE} = \frac{nF(C_0-C_t)V}{Q_t} = \frac{nF(C_0-C_t)V}{It}$ 62

(32) $\text{EC (Wh g}^{-1}) = \frac{E_{cell}Q_t}{3600(C_0-C_t)MV} = \frac{E_{cell}It}{3600(C_0-C_t)MV}$ 62

(33) $\frac{1}{I_c} = \frac{1}{I_k} + \frac{1}{I_l}$ 62

(34) $\frac{1}{I_c} = \frac{1}{nFAk_hC^*} + \frac{1}{0.62nFAD_t^{2/3}v^{-1/6}\omega^{1/2}C^*}$ 62

(35) $\eta = \frac{R}{R^*} = \frac{k_1 C}{k_1 C^*} = \frac{C}{C^*}$ 63

(36) $k_\mathrm{m} a(C^* - C) = k_\mathrm{h} a C$ 63

(37) $C = \frac{1}{1+\frac{k_\mathrm{h} a}{k_\mathrm{m} a}} C^*$ 63

(38) $R = \eta R^* = \eta k_\mathrm{h} a C^*$ 63

(39) $Da = \frac{k_\mathrm{h} a}{k_\mathrm{m} a}$ 63

(40) $\eta = \frac{1}{1+\frac{k_\mathrm{h} a}{k_\mathrm{m} a}} = \frac{1}{1+Da}$ 63

(41) $R = \frac{k_\mathrm{h} a}{1+Da} C^* = \frac{k_\mathrm{h} a}{1+\frac{k_\mathrm{h} a}{k_\mathrm{m} a}} C^* = \frac{1}{\frac{1}{k_\mathrm{h} a}+\frac{1}{k_\mathrm{m} a}} C^*$ 64

(42) $k_1 = \frac{1}{\frac{1}{k_\mathrm{h} a}+\frac{1}{k_\mathrm{m} a}}$ 64

(43) $Re = \frac{Ud}{v}$ 64

(44) $Sh = \frac{k_\mathrm{m} d}{D}$ 64

(45) $Sc = \frac{v}{D}$ 64

(46) $Sh = \alpha Re^{\beta} Sc^{\gamma}$ 64

(47) $t_{\mathrm{NO_3^-}} = \frac{\lambda_{\mathrm{NO_3^-}} C_{\mathrm{NO_3^-}}}{\sum \lambda_\mathrm{i} C_\mathrm{i}}$ 72

(48) $2H_2O + 2e^- \rightarrow H_2 + 2OH^-$ $E^\mathrm{o} = -0.83$ V vs SHE 72

(49) $H_2O + e^- \rightarrow {}^\bullet H + OH^-$ 73

(50) $2{}^\bullet H \rightarrow H_2$ 73

(51) $H_2O \rightarrow 2H^+ + 1/2O_2 + 2e^-$ $E^o = 1.23$ V vs SHE 73

(52) $\rho(\boldsymbol{u}\cdot\nabla\boldsymbol{u}) = -\nabla P + \nabla\cdot\left((\mu+\mu_{\mathrm{T}})(\nabla\boldsymbol{u}+(\nabla\boldsymbol{u})^{\mathrm{T}})\right)$ 73

(53) $\nabla\cdot\boldsymbol{u} = 0$ 73

(54) $\mu_{\mathrm{T}} = \rho C_{\mu}\frac{k^2}{\varepsilon}$ 74

(55) $\rho(\boldsymbol{u}\cdot\nabla)k = \nabla\cdot\left(\left(\mu+\frac{\mu_{\mathrm{T}}}{\sigma_{\mathrm{k}}}\right)\nabla k\right) + P_{\mathrm{k}} - \rho\varepsilon$ 74

(56) $\rho(\boldsymbol{u}\cdot\nabla)\varepsilon = \nabla\cdot\left(\left(\mu+\frac{\mu_{\mathrm{T}}}{\sigma_{\varepsilon}}\right)\nabla\varepsilon\right) + C_{\varepsilon 1}\frac{\varepsilon}{k}P_{\mathrm{k}} - C_{\varepsilon 2}\rho\frac{\varepsilon^2}{k}$ 74

(57) $u^+ = 5.5 + \frac{1}{\kappa}lny^+$ 74

(58) $\frac{\partial C_{\mathrm{NO_3^-}}}{\partial t} = \nabla\cdot\left(D_{\mathrm{NO_3^-}} + D_{\mathrm{T}}\right)\nabla C_{\mathrm{NO_3^-}} - \boldsymbol{u}\cdot\nabla C_{\mathrm{NO_3^-}}$ 75

(59) $Sc_{\mathrm{T}} = \left\{\frac{1}{2Sc_{\mathrm{T}\infty}} + \frac{0.3\mu_{\mathrm{T}}}{\sqrt{Sc_{\mathrm{T}\infty}}\rho D} - \left(\frac{0.3\mu_{\mathrm{T}}}{\rho D}\right)^2\left[1 - exp\left(-\frac{\rho D}{0.3\mu_{\mathrm{T}}\sqrt{Sc_{\mathrm{T}\infty}}}\right)\right]\right\}^{-1}$ 75

(60) $C^+_{\mathrm{NO_3^-}} = Sc_{\mathrm{T}}\left(\frac{1}{k}ln\,y^+ + 5.5 + P_{\mathrm{c}}\right)$ 76

(61) $C^+_{\mathrm{NO_3^-}} = \frac{\left(C_{\mathrm{NO_3^-,w}} - C_{\mathrm{NO_3^-}}\right)C_{\mu}^{0.25}\kappa^{0.5}}{N_{\mathrm{NO_3^-,w}}}$ 76

(62) $P_{\mathrm{c}} = A\left[\left(\frac{Sc}{Sc_{\mathrm{T}}}\right)^{0.75} - 1\right]$ 76

(63) $\nabla\varphi^2 = 0$ 77

(64) $j = -\sigma\nabla\varphi$ 77

List of acronyms

AOP	Advanced oxidation process
CE	Current efficiency (*see also* FE)
CEC	Contaminant of emerging concern
CFD	Computational fluid dynamics
DE-TBZE	Desethyl-terbuthylazine
DSA®	Dimensionally stable anode
EAOP	Electrochemical advanced oxidation process
EC	Energy consumption
EF	Electro-Fenton
EO	Electro-oxidation
EPR	Electron paramagnetic resonance (*see also* ESR)
ESR	Electron spin resonance (*see also* EPR)
FE	Faradaic efficiency (*see also* CE)
GC-MS	Gas chromatography coupled to mass spectrometry
GO	General objective
GW	Groundwater
HER	Hydrogen evolution reaction
HPLC	High-performance liquid chromatography
IC	Ion chromatography
ICP-OES	Inductively-coupled plasma with optical emission spectrometry
IMC	Imidacloprid
LC	Liquid chromatograph
LSV	Linear sweep voltammetry
MCE	Mineralization current efficiency
NGWA	United States National Groundwater Association
NPOC	Non-purgeable organic carbon

NRR	Nitrate reduction reaction
OCP	Open circuit potential
OER	Oxygen evolution reaction
PFAS	Perfluorinated alkyl substance
POP	Persistent organic pollutant
RCE	Rotating cylinder electrode
RDS	Rate-determining step
ROS	Reactive oxygen species
SDG	Sustainable development goal
SG	Specific goal
SPE	Solid polymer electrolyte
SS	Stainless steel
TAN	Total ammonia nitrogen
TBZE	Terbuthylazine
TC	Total carbon
TN	Total nitrogen
TOC	Total organic carbon
WHO	World Health Organization

List of symbols

a	Volumetric area
Da	Damköhler dimensionless number
E_{cath}	Cathode potential
$^{\bullet}H$	Hydrogen radical or atomic hydrogen
j	Current density
k_h	Heterogeneous charge transfer kinetic constant
k_m	Mass transport coefficient
n	Number of electrons transferred in a given reaction
$^{\bullet}OH$	Hydroxyl radical
pK_a	The negative base-10 logarithm of the acid dissociation constant
Re	Reynolds dimensionless number
Sc	Schmidt dimensionless number
Sh	Sherwood dimensionless number
t	Time
t_R	Retention time
U	Peripheral velocity

Greek symbols

η	Effectiveness factor (also, Electrochemical overpotential)
λ	Wavelength
λ_i	Ionic conductivity
ω	Rotation rate

Abstract

Despite the existence of a large volume of groundwater (GW) contained in intricate interconnected aquifers, the low replenishment rates and large underground extension results in a high vulnerability of the population that depends on this freshwater resource. In order to treat GW to make it suitable for human consumption, it is of paramount importance to identify its main characteristics and the nature and concentration of the pollutants. The strategy to be followed for their removal is tightly related with their chemical structure.

Electrochemical processes for GW treatment have emerged as promising alternatives to the conventional methods. However, GW main characteristics are low conductivity and high hardness, which can be considered main drawbacks that must be conveniently addressed beforehand. A pre-treatment step is thus mandatory, aiming to avoid the precipitation of alkaline-earth hydroxides and carbonates on the cathode surface, since this phenomenon would cause an increase in the electrical resistance and hence, the treatment cost. Two different pre-treatment processes were employed in this work allowing to treat real GW matrices by electrochemical means: one of them was based on sodium-charged zeolites and the other consisted in forcing the precipitation of calcium and magnesium carbonates and hydroxides.

The cell configuration is critical to attain an overall GW decontamination, being necessary to select suitable electrode materials that allow removing the specific pollutants present in the water matrix, as for example nitrate and pesticides investigated in this Thesis. Imidacloprid (IMC) and terbuthylazine (TBZ) degradations have been assessed by direct and indirect electro-oxidation (EO), electrolyzing different water matrices in different cell setups using either DSA® or boron-doped diamond (BDD) anodes. Higher pesticide degradation rates have been achieved in the presence of chloride in the aqueous matrix, at the expense of generating chlorinated oxyanions. When using low current densities, the pesticides have been also removed at a lower rate and the generation of these toxic anions has been minimized. A post-treatment based on a Purolite® A532E resin has been considered to remove such by-products generated along the electrochemical decontamination process.

The electroreduction (ER) of nitrate has been studied employing different steels as electrocatalytic candidates. A higher activity of mild steel as compared to stainless steel has been demonstrated through electrochemical characterization analysis and electrolytic trials. The nitrate reduction reaction (NRR) over a mild steel has been electrochemically characterized using a rotating disk electrode (RDE). Based on a Koutecky-Levich (KL) analysis, it could be determined that the number of electrons involved in the NRR over this material was 8, in agreement with the total conversion to ammonia observed in the electrolytic trials and the heterogeneous charge transfer kinetic constant (k_h) determined at different cathode potentials (E_{cath}). The fundamental role of atomic hydrogen ($^{\bullet}H$) as a reducing agent, generated on the cathode surface from water reduction as an intermediate of the hydrogen evolution, has also been discussed.

The performance of electroreduction and electro-oxidation has been thoroughly evaluated, owing to their operation simplicity and relative low cost, and much emphasis has been put on the integration of both methods in a single electrochemical device for the simultaneous removal of both types of pollutants. Furthermore, aiming to assess the potential scalability of the electrochemical nitrate removal, a rotating cylinder electrode (RCE) reactor has been employed in this Thesis, both under potentiostatic and galvanostatic conditions. The mass transport in the RCE reactor has been characterized for this specific anion in a diffusion-convection system by obtaining the following Sherwood-Reynolds-Schmidt dimensionless correlation: $Sh = 0.7Re^{0.46}Sc^{0.356}$. This lays the foundations for future scale-up of this technology. In addition, this reactor has been modelled in order to predict its behaviour upon use of an electrocatalytic RCE for nitrate removal. Worth highlighting, the developed model has been validated by performing experimental trials, achieving an excellent agreement between the simulations and the experimental trends.

In conclusion, this Thesis presents several novel and original electrochemical strategies to successfully address the treatment of GW as a model complex water matrix for the removal of pesticides and nitrates, even simultaneously. The work has resulted in five scientific publications and a large number of communications in meetings, which adds to other articles published during the PhD Thesis period. A 4-month stay in Mexico has also been carried out to obtain the international mention.

CHAPTER 1

INTRODUCTION

CHAPTER 1. Introduction

1.1. General overview of groundwater

1.1.1. Water scarcity and groundwater pollution

Only 3% of the water in the planet is considered freshwater, being the other 97% saline water present in seas and oceans [1]. Groundwater (GW), which is defined as 'water that is found beneath the surface of the Earth in conditions of 100% saturation' by the US National Groundwater Association (NGWA) [2] constitutes the most important natural freshwater resource and is an essential component of the water cycle. As shown in **Figure 1** [3], it accounts for over 97% of the available freshwater in the globe, excluding ice caps and glaciers, whereas the other 3% belongs to rivers and lakes [4,5]. GW is a crucial resource for human consumption, agriculture and livestock farming and, additionally, it has a pivotal role in very important socio-economic sectors like extraction industries, fishery and mining [6,7]. In 2020, 5.8 billion people (i.e., 74% of the global population) used a safely managed drinking-water service available when needed and free of pollutants [8].

Figure 1. Water reservoirs on Earth [3].

GW has a paramount importance because it is the most prominent element to sustain life, owing to its expected purity being relatively free of contaminants. It allows people to live in arid regions and develop economic activities far away from surface freshwater. This has been considered the traditional source of water supply for rural areas, especially for inhabitants of underdeveloped countries and for all kinds of industries vulnerable to surface water scarcity. In addition, it becomes vital for the water-dependant ecosystems and their biodiversity.

Water resources are divided into renewable and non-renewable. The first ones account for the total volume of GW and surface water that emerges by the natural cycle of water, whereas non-renewable water resources come from deep and hidden aquifers without a relevant replenishment rate on the human time scale [9]. Despite its great importance, GW has been traditionally underrated and poorly understood and, consequently, abused by over pumping.

Often, aquifers have been considered a renewable source of freshwater, as they can be slowly replenished by the thawing of icecaps and by the infiltration of the rainfall over many hundreds or thousands of years. An increasing world population, coupled with global booming of intensive agriculture and farming, as well as growing industrial sector, have resulted in a rising demand of GW supply and, in turn, a rising contamination from these anthropogenic activities. The authorities in charge of the management of the water supply around the world have traditionally allowed the over-exploitation of the accessible freshwater supplies. Nowadays, they are enforced to rely on the extraction of freshwater from aquifers for reliable water supply, aiming at meeting the ever-rising demand at a rate higher than that of the natural replenishment. This eventually transforms deep water into a non-renewable source of water. Furthermore, the climate change contributes to the pressure and reliance on this natural resource. The above considerations contribute to the exacerbation of the dependence on clean freshwater sources, a situation that is forecast to worsen in several regions as a consequence of population growth and progressive desertification [8]. In particular, this is expected to occur in regions that have traditionally suffered from hydric stress [10]. By 2025, it is expected that two-thirds of global population will be under “water stress” (500 – 1000 m^3 $year^{-1}$ per capita), and 1800 million people will inhabit regions with absolute water scarcity (< 500 m^3 $year^{-1}$ per capita) [11].

In 2015, the United Nations General Assembly adopted the Sustainable Development Goals (SDG), a collection of 17 interrelated objectives to promote sustainability by connecting the environmental, social and economic features that are intimately inherent to sustainable development (**Figure 2**). They were conveyed to society through a strategic resolution called "UN's 2030 Agenda", launching a series of specific targets to accomplish the goals by year 2030. Specifically, the 6th SDG is entitled "Clean water and sanitation" and aims at ensuring availability and sustainable management of freshwater and sanitation for the whole population. Through this goal, universal access to safe and affordable drinking water, as well as access to sanitation and standard hygienic conditions is aimed. Moreover, it is necessary to end with the discharge of non-treated defecation effluents, reduce water pollution by minimizing the release of hazardous chemicals and materials. Water scarcity is addressed by increasing freshwater supply and the efficiency of the water use, as well as by protecting and restoring water-based ecosystems, including natural regions. Similarly, the public health international authority (WHO) has leaded new efforts to develop several health-based regulations, acting as advisor of governments to prevent water-related diseases worldwide. These actions have crystallized on the promotion of water sanitation and health by establishing global drinking-water quality guidelines, water safety plans and general drinking-water quality regulations [12].

Figure 2. Sustainable development goals formulated in 2015 by the United Nations General Assembly [13].

GW is usually extracted using pumping wells, since it is located underground in aquifers and saturated sediments and between permeable rocks filling the voids and cracks. These water bodies provide around half of freshwater supply worldwide. Around 40% of that amount is employed in irrigation, whereas about a 30% of the water is supplied for industrial activities, as for example in small-to-medium size factories from agri-food sector [14]. By 2050, feeding a global population of 9 billion people will require an estimate growth of 50% in agricultural production, with a consequent 15% increase in water withdrawals [15]. This type of freshwater not only sustains biodiversity around the globe, but it is also a relevant factor in climate change adaptation, since underground water reservoirs connect a wide extension of land and, across its surface, a large number of rivers and lakes contributes to the replenishment of the underground water masses. This means that GW can actually be exploited far away from the main surface freshwater masses.

The so-called water table is the line where saturated and unsaturated GW layers meet. It is the most susceptible region of the water masses to accumulate a higher concentration of the anthropogenic pollutants, since the leaching and percolation phenomena bring them there when they start to diffuse through the saturated region. In addition, the interconnection of GW with surface water makes it liable to be contaminated by surface pollutants too [16].

The replenishment rates of GW and its origin can be determined by radioisotopes that are naturally present in these water masses. In particular, GW age can be estimated by using the isotopes present in the water molecule (hydrogen, oxygen) and radioisotopes (tritium), dissolved carbon (carbon-14) and noble gases (helium-3, helium-4 and krypton-81). A scientific study of the primary origin of the GW in big aquifers and its replenishment rates is crucial to evaluate their role as reliable long-term water suppliers. The identification of the sources of GW contaminants, as well as the quantification of the transformation and biodegradation pathways in aquifers can be performed by using stable isotopes and radioisotopes. Since remediation of GW pollution is not an easy task, a more simple strategy focuses on determining the origin of the pollutants in order to prevent their discharge from the identified source [17]. The addition or accumulation of unwanted substances to GW with an anthropogenic origin is considered as contamination.

Unfortunately, wishful thinking has long been assumed by the society, with the wrong assumption that waste left on or under the ground simply stays there.

Although the most concerning chemical risks in GW arise from arsenic, fluoride and nitrate contamination [8], dumps and spills also constitute main sources of aquifer pollution. The appearance of contaminants such as pesticides, pharmaceuticals, perfluorinated alkyl substances (PFASs) and microplastics in GW occurs upon their leaching and percolation. The rise in their detected concentrations has worried administrations due to their negative effects on ecosystems and public health. Long-term effects, which include different types of cancer, may result from exposure to certain pollutants. The pollution is then spread far beyond the site of the original source of contamination, thereby becoming extremely difficult, even impossible, to be remediated. The complex accessibility to the big water reservoirs and the huge amount of water contained in these water bodies, which may be contaminated with low concentrations of sometimes highly toxic pollutants of different nature and different origins, are major issues that makes GW decontamination challenging.

Among the many ways to categorize the source of GW pollution, one of them allows distinguishing between point sources, with their subsequent spread of the contaminants, and non-point sources. Accidental spills, landfills, leakage of gasoline or septic tanks are examples of the former category, whereas the pollution originated by the leaching or infiltration of pesticides and fertilizers through the fields are examples of the latter. Among the most significant point sources, municipal landfills and disposal sites for industrial waste stand out, especially when they occur near sand or gravel aquifers. Other point sources like septic tanks are individually less noticeable due to their limited charge of pollutants, although they can become numerous in many countries. Such tanks are designed to distribute the sewage between the container and the surrounding subsoil, being a potentially hazardous when poorly monitored. The pollution of the aquifers can render GW unsuitable for use and, in many cases, the problem is only evidenced once the users of the affected freshwater source have been exposed to the contaminated water. Frequently, since the cost for the remediation of the aquifer is extremely high, the end-users need to find other ways to fulfil the freshwater demand. This usually entails a high cost, especially for the small villages and inaccessible populations in remote regions.

Depending on the region of the planet, the country and its main local activities on which the economy is sustained, the nature of the contamination of GW may differ. Consequently, drinking polluted GW can have health effects according to the specific pollutants present in the contaminated water.

In Spain, the main sources of GW contamination are the use of fertilizers, pesticides and livestock wastes, although depending on the characteristics of the region, problems related to spent motor oil, road salt, underground tanks, and septic systems may arise. Due to the nature of the processes described and the tendency shown during the last years, it can be predicted that over the next few decades, more contaminated aquifers than traditional sources of freshwater for household wells will become polluted, potentially being identified as non-reliable sources of freshwater. Moreover, new pollutants will probably be identified.

A recently contaminated underground aquifer may be unsuitable for human consumption from weeks to decades, while the residence time of the polluting substances introduced in it may be thousands of years depending on their nature. The final effects are even more dramatic than presupposed, since the pollution of such big water reservoirs does not end up with the closure of wells as viable freshwater sources. The migration of the pollutants from spill sites or disposal areas to nearby surface water masses such as rivers or lakes through the hydrologic cycle jeopardizes the quality of the surface water by GW, a collateral problem of major importance. Hence, preventing this kind of contamination is by far the main strategy that should be followed by any government because it is the most practical and less expensive way to deal with the issue.

1.1.2. Relevant groundwater parameters

GW exhibits several physicochemical characteristics that determine its suitability for different uses, being the quality parameters of paramount importance to determine whether it can be used as freshwater or not.

The pH of GW is usually found at near-neutral values, but it can undergo different degrees of acidification or alkalinization that may affect the solubility and mobility of certain pollutants. The temperature tends to be quite stable, but it also depends on factors such as climate, depth and, in some cases, geothermal activity. This parameter has a

strong effect on the solubility of minerals and gases, the mobility of pollutants and the microbial activity and its speciation. Turbidity is related with the number of suspended particles; GW typically has a lower turbidity than surface water bodies due to natural filtration by the saturated rocks and sediments [18].

The dissolved species usually found in GW come from solid and gaseous compounds. On one hand, dissolved solids are mainly the solubilized inorganic substances, such as salts, and represent the mineral content of GW, although low amounts of natural organic are present as well. The mineral content has direct impact on the electrical conductivity, which may serve to have an approximation of the ionic content of the GW. The ionic composition of the water may affect its taste, can negatively impact the treatment processes, and may cause corrosion depending on the actual composition. Some metals may be found in traces and can pose a health risk for human consumption. Water hardness is related directly with the alkaline-earth metals dissolved in the GW; it is a critical problem for industrial use of water, since the deposition of this kind of metals can be the cause of expensive industrial breakdowns. Several essential nutrients for plants, such as nitrate and phosphates, may be found naturally in GW. However, high levels of these species from an anthropogenic origin may cause eutrophication of natural water bodies. On the other hand, the presence of certain dissolved gases can have an effect on the water quality and influence the speciation of microorganisms that can live in it; additionally, this may give information about underground conditions, such as geothermal and local microbial activity. Some examples of the most common dissolved gases are carbon dioxide, oxygen or methane.

The nature of the pollutants that may be found dissolved in a GW body is related with its origin. Some pollutants may have an immediate impact upon human consumption of the GW, whereas others may have a long-term effect. The different chemical structure of the pollutants determines the process that needs to be applied to the water effluent in order to remove them. A low concentration of a certain pollutant may lead to the unexpected inefficacy or high energy consumption of the chosen treatment. The composition and parameters of the GW can have potential impact on the effectiveness of a given treatment to remove specific pollutants, depending on the chemical properties of the pollutant and the specific technology to be employed. A thorough characterization of a given GW matrix is thus mandatory in order to identify the pollutant content and,

afterwards, a specific treatment needs to be designed according to the characteristics, aiming to meet the requirements in terms of pollutant(s) removal.

1.1.3. Occurrence of pollutants in groundwater

There are many different sources of GW contamination (**Figure 3**). Although various pollutants may be the result of natural processes, most of them arise from the dissolution or mixing of anthropogenic pollutants with water streams that refill natural aquifers. Aquifers in agricultural areas are especially prone to contamination from agricultural runoff. Usually, GW pollution stems from the following main sources [19]:

(i) Nitrate contamination in either surface water bodies or GW often has its origin in the agricultural activities, such as the overuse of fertilizers and livestock manure spread on the fields for their management. This kind of pollution can generate eutrophication, which may lead to the overgrowth of algae and other aquatic microorganisms, severely declining water quality and resulting in an ecological imbalance leading to drastic changes in the ecosystems;

(ii) Heavy metal traces or even relevant concentrations of them usually have their origin in mining activities, the uncontrolled industrial discharges, wastewater discharge or even a natural origin through the dissolution of the geochemical components of the area. This kind of metals may harm severely the health of human populations and alter ecosystems;

(iii) Different kinds of organic compounds coming from different economic or social activities may accumulate in aquifers, such as industrial solvents, pesticides, petroleum derivatives, volatile organic compounds, chlorinated chemicals, pharmaceutical products, personal care products, PFASs and others may harm the environment and be dangerous for humans and animals that consume contaminated freshwater. They all have an anthropogenic origin and most of them are categorized as persistent organic pollutants due to their refractory character that makes them resistant to natural degradation (i.e., hydrolysis, photolysis). The fact that they accumulate in low concentrations in GW makes more difficult their detection, while they are protected underground and remain at mil low temperature that confers stability.

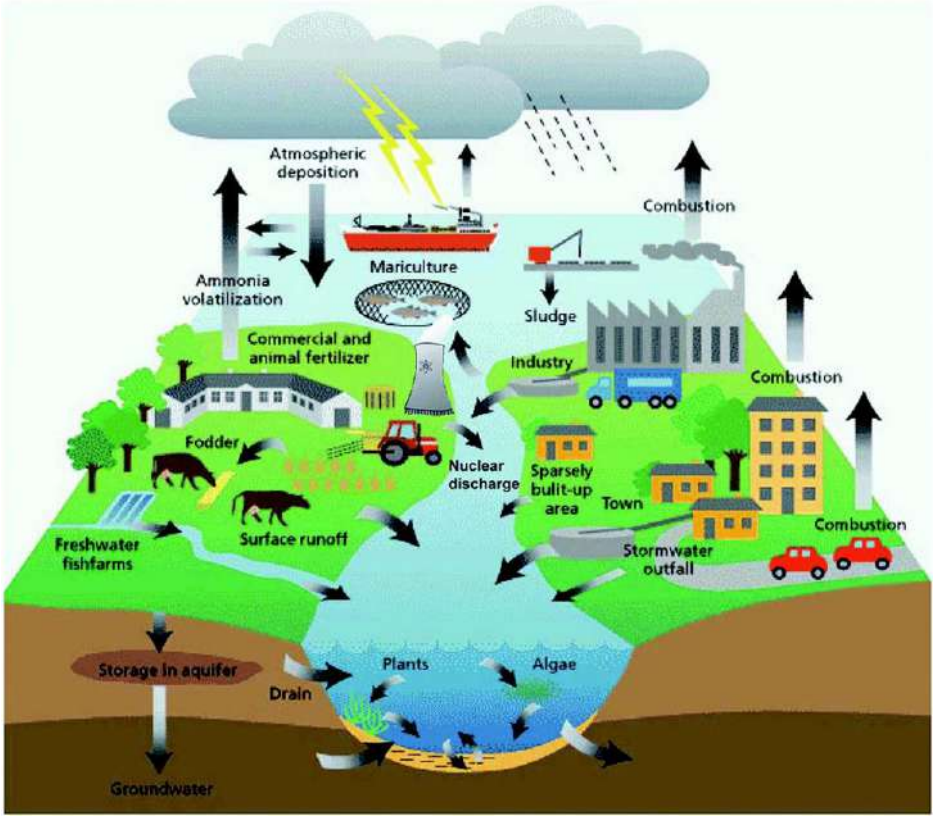

Figure 3. Potential sources of GW contamination [20].

Classification of GW pollution according to its origin

Depending on the origin of the GW pollution, different kinds of contamination can be distinguished. Although there are different criteria to classify the GW pollution, the most general classification differentiates between natural pollution, which occurs spontaneously, and anthropogenic pollution, which is caused by human action. The different types of pollution caused by humans may be split into subcategories [19]: (i) agricultural pollution, which is related with the spread of natural of chemical products for farming; (ii) economical pollution, that mainly includes industrial pollution; and (iii) social pollution, which accounts for the pollution derived from the passive effect of landfills slowly leaching pollutants to GW and the urban pollution, generated through the discharge of polluted streams with different kinds of contaminants mixed in the municipal waste.

Natural contamination may occur as result of different circumstances: from the leaching of salts from the soil minerals into the water masses, causing pollution by iron,

arsenic, manganese, fluoride or sulphide [21]; from the dissolution of methane or other gases from geothermal systems [22]; and from the intrusion of seawater into GW, a common problem in coastal areas that affects water quality [16]. These contaminations may occur from as a point source or as a result of a cumulative effect of different circumstances at the same time, becoming a non-point source.

Agricultural contamination may occur from the leaching of pesticides and fertilizers used in order to increase the productivity of crop fields. As the population is growing, new agricultural technologies have been developed to meet the consequent rising demand. The prevailing strategy has been the use of different families of pesticides and chemical fertilizers to increase the production efficiency by supplying the soil with the necessary nutrients to meet the high productivity needs [23]. Moreover, chemical fertilizers are mostly based on major forms of inorganic nitrogen, such as ammonia or nitrate, becoming a great source of long-term GW contamination. Although nitrogen content in GW may have multiple origins, pesticides and fertilizers stand out [24]. Natural fertilizers like livestock depositions and swine wastewater are used in rural areas due to their high nitrogen concentration. Both kinds of fertilizers, chemical and natural, are employed to supply nitrogen in huge amounts as nutrients for the crops, but they usually end up accumulating in the soil, where the inorganic nitrogen is oxidized by the microbes present on the fields. The resulting nitrate has high solubility and hence, it is leached by the irrigation and rainfall water, eventually accumulating underground in aquifers. For this reason, shallow water tables are especially susceptible to nitrate pollution [25]. Husbandry is an indirect way for GW contamination. The soil around becomes polluted by microorganisms and veterinary drugs. Huge number of wastes with high concentrations of N-containing compounds and metals contribute to the degradation of water quality.

Industrial pollution refers to the environmental and health impact derived from all the economic activities that directly contribute to the contamination of land and water bodies, wither by the direct or indirect discharge of factory process wastes related to their specific activity. Different kinds of industry may lead to completely different types of pollution, depending on the specific chemicals they manage. Mining, for example, pollutes the nearby water bodies with the discharge of contaminated effluents leading to high heavy metals concentrations and acidification, owing to the large number of acids

employed in the process. The chemical industries have enormous impact referred to the discharge of organic compounds or solvents, wastes with high amounts of by-products, as well as high concentrations of different salts, which may alter the environment although being categorized as non-toxic. Several countries have regulations to avoid the direct discharge on the environment. However, the reality is that when the wastes are not properly treated and become accumulated in landfills, eventual leakages occur with dramatic effects.

Urban contamination is related to the intrinsic effect of the massive growth of towns and cities. Different kinds of pollutants are generated from daily life and are spread to the environment by different channels. The pollution of air due to the high density of combustion vehicles, water pollution from wastewater or sewage discharge, and soil pollution due to the landfill leakage and spills are only some examples. Sewage disposal and domestic wastewater discharge produces a terrible environmental impact [26], and the best way to mitigate their impact is through a centralized wastewater treatment system fed by an appropriate sewage network. Although most urban areas around the world have a relatively high sewer lines extension, rural areas are deficient in such facilities due to economic or geographical reasons, thereby becoming an important source of nitrate GW contamination. Moreover, this is the main source of organic pollutants categorized as persistent organic pollutants (POPs), known to possess high resistance to biodegradation, or as contaminants of emerging concern (CECs), whose impact has been discovered only recently due to the need of chronic tests. Some examples of these organic pollutants are antibiotics, personal care products, pharmaceutical products or PFASs.

It is important to mention that several pollutants may have multiple origins, and that the environment and ecosystems may absorb a certain degree of pollution, especially for the less harmful pollutants. However, the human activities and economy models based on continuous consumption lead to an ever-rising generation of wastes and direct and indirect pollution. This eventually surpasses the ability of the ecosystems to get rid of them, thus altering their characteristics and causing natural imbalance, which may lead to awkward situations such as the decrease of animal populations and the pollution of main freshwater sources.

1.1.4. Groundwater in Spain

The Spanish Water Directive defines GW as all subsurface water within the saturation zone, in direct contact with the ground [27]. The fundamental concept for GW management is the so-called GW mass, which stresses the relevance of the content instead of the container (i.e., the aquifer). Spain has 17 hydrographic demarcations, which are land and marine surfaces made up of one or more drainage basins. In these watersheds, all the flowing surface water converges to a single point such as a river, lake or ocean. Each of the hydrographic demarcations accounts for a limited number of GW masses (**Table 1**), resulting in a total of 762 GW masses with a total extension of 360,788 km^2 [28].

Table 1. Hydrographic demarcations in Spain, the number of GW masses in each demarcation, and their total area [28].

Hydrographic demarcations	Number of GW masses (2015-2021)	Water masses area (km^2)
Miño-Sil	6	17,587
Occidental Cantabric	20	13,863
Oriental Cantabric	20	5,733
Duero	64	87,366
Tajo	24	21,852
Guadiana	20	22,479
Guadalquivir	90	33,895
Segura	63	15,230
Júcar	90	40,524
Ebro	105	54,638
Coast of Galicia	18	13,002
Andalucia Mediterranean Watershed	67	10,417
Tinto, Odiel and Piedras	4	1,507
Guadalete and Barbate	14	1,902
Cataluña	37	9,324
Baleares	87	4,749
Canarias	33	6,719
Total	**762**	**360,788**

The hydrological plans of the Spanish hydrographic demarcations are compelled to identify the GW masses put at risk, those not being liable to attain the environmental goals established by the Spanish Hydrological Plan. At present, there are 25 GW masses at risk in Spain, 13 of them due to quantitative risk and 12 due to quantitative and chemical risks (**Table 2**) [29]. The situation is made clear from the map depicted in **Figure 4** [30].

Table 2. GW masses considered at quantitative risk or combined chemical (Chem.) and quantitative (Quant.) risk [29].

Name of the GW mass	Hydrographic demarcation	Type of risk	BOE publication
Aluvial del Azuer	Guadiana	Chem. and Quant.	17/09/2015
Aluvial del Jabalón	Guadiana	Chem. and Quant.	26/09/2015
Mancha Occidental I	Guadiana	Chem. and Quant.	22/12/2014
Sierra de Altomira	Guadiana	Chem. and Quant.	22/12/2014
Rus-Valdelobos	Guadiana	Chem. and Quant.	22/12/2014
Campo de Montiel	Guadiana	Chem. and Quant.	22/12/2014
Lilla-Quintanar	Guadiana	Chem. and Quant.	22/12/2014
Mancha Occidental II	Guadiana	Chem. and Quant.	22/12/2014
Tierra de Barros	Guadiana	Chem. and Quant.	17/09/2015
Campo de Calatrava	Guadiana	Quantitative	27/03/2017
Consuegra-Villacañas	Guadiana	Chem. and Quant.	22/12/2014
Almonte	Guadalquivir	Quantitative	24/08/2020
Marismas	Guadalquivir	Quantitative	24/08/2020
La Rocina	Guadalquivir	Chem. and Quant.	24/08/2020
Conejeros-Albatana	Segura	Quantitative	23/11/2021
Ontur	Segura	Quantitative	23/11/2021
Cingla	Segura	Quantitative	23/11/2021
Sierra Espuña	Segura	Quantitative	23/11/2021
Campo de Cartagena	Segura	Chem. and Quant.	01/08/2020
Villena-Benejama	Júcar	Quantitative	08/10/2020
Jumilla-Villena	Júcar	Quantitative	08/10/2020
Peñarrubia	Júcar	Quantitative	08/10/2020
Serral de Salinas	Júcar	Quantitative	08/10/2020
Sierra del Reclot	Júcar	Quantitative	08/10/2020
Sierra de Crevillente	Júcar	Quantitative	08/10/2020

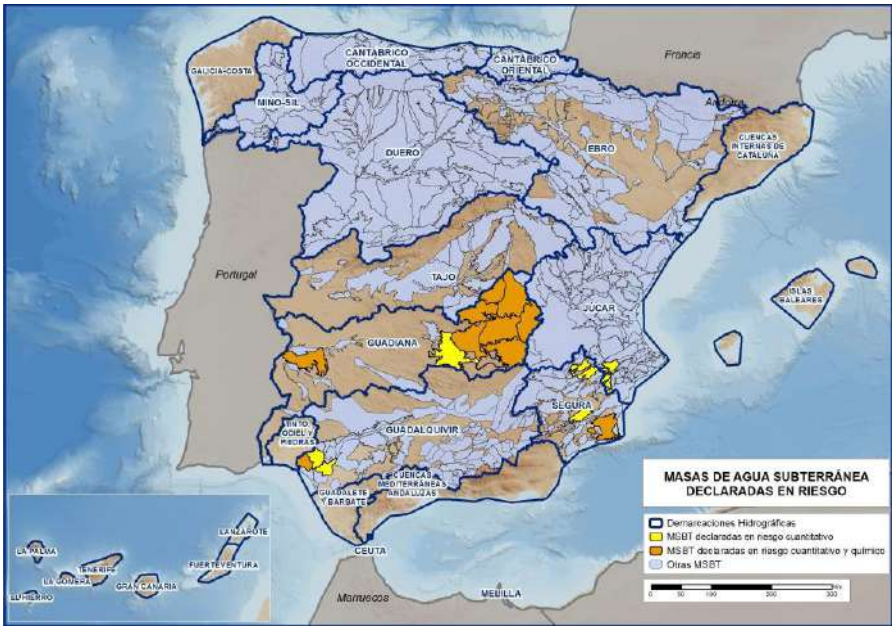

Figure 4. GW masses at risk (quantitative, chemical) in Spain. Hydrographic demarcations are shown [30].

As of October 2022, a study elaborated in collaboration with Greenpeace Spain has reported that 44% of Spanish GW mass is endangered (**Figure 5**). This includes the most critical and ecologically valuable ecosystems like Tablas de Daimiel, Mar Menor and Doñana [30]. The causes for the jeopardizing if aquifers depend upon the specific activities that are carried out in that region. The cause for GW pollution in Spain is nitrate accumulation due to the overuse of fertilizers. Lately, a huge increase has been observed caused by the macrofarms proliferation, with a noticeable concentration of them in specific regions. Regions with high accumulation of pesticides in their GW masses are the second most relevant, whereas saline contamination caused by saline intrusion is the third most common cause.

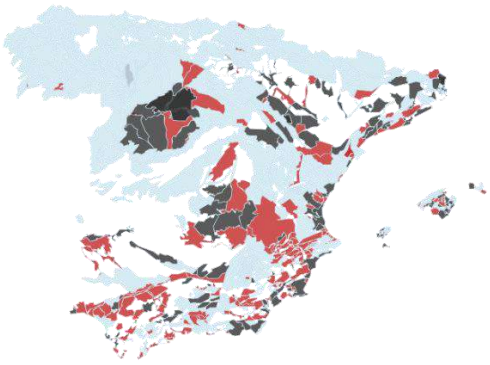

Figure 5. GW masses at risk in Spain: safe (blue), at risk but potentially recoverable by 2027 (red), at risk and improbable to recover before 2027 [30].

1.1.5. Pollutants of interest in this Thesis: Occurrence and treatment

Imidacloprid

Imidacloprid (IMC, $C_9H_{10}ClN_5O_2$, *N*-[1-[(6-chloro-3-pirinidyl)methyl]-4,5-dihydroimidazol-2-yl]nitramide, M = 255.66 g mol^{-1}) (**Figure 6**) is a widely used neuroactive insecticide that belongs to the family of the neonicotinoids. They act on the central nervous system of insects, blocking the transmission through the nerves and resulting in their eventual death. During at least 20 years, IMC has been the most widely used insecticide in the world [31,32] and has been applied to many crops and a large number of fruits and vegetables [33,34]. It has been commercialized under many trade names for many uses, resulting in its consequences for insects, either by contact or through consumption. IMC has been applied with great success by soil injection, spreading over the leaves of the plants by pulverization or nebulization, tree injection, ground application as granular or liquid formulation or as a coating for seeds [35]. IMC has a relatively high solubility in water (0.58 g L^{-1}) [36]. In soil, IMC strongly binds to organic matter, persisting in the field after its application. When it is in aqueous solution and it is irradiated by light, it slowly degrades, giving rise to several by-products [37]. In the dark and under mild conditions, IMC has the potential to persist for prolonged time periods, as is the case of GW contamination. IMC has been found at concentrations up to 0.52 µg L^{-1} in agricultural water and 0.36 µg L^{-1} in urban wastewater [38]. The presence of five nitrogen atoms in its molecule results into the accumulation of stable nitrate in the water masses following a natural degradation process, which worsens its associated problems.

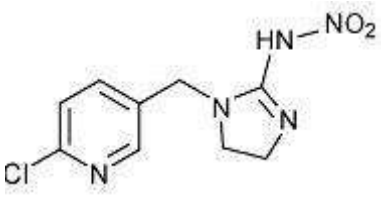

Figure 6. Molecular structure of imidacloprid pesticide.

IMC is also very harmful to birds, causing infertility, and to fishes, since it reduces drastically the insect population although it does have a low direct impact on them [39]. It is especially harmful for ecosystems and the environment because it has a devastating

effect on honeybees, with its subsequent dramatic impact on the reproduction of the plants that depend on bees pollination around the planet [40]. Recent EU regulations have banned IMC, as well as several neonicotinoids, owing to the environmental risks [41,42]. Its tolerance varies from 0.02 mg kg^{-1} in eggs to 3.0 mg kg^{-1} in hops and causes hepatotoxicity, immunotoxicity, nephrotoxicity and oxidative stress effects on animals, being the primary effect of long-term exposure to low concentrations of IMC for mammal's affections on the liver and the thyroid glandule [43].

Several conventional and advanced treatment technologies have been employed to remove IMC from different water matrices, such as ultrapure water, synthetic solutions, real urban wastewater and [38]: photocatalysis [44], photolysis [45,46], ozonation [47], persulfate-based advanced oxidation processes [48], adsorption [49,50], bioretention or bioremediation [51,52], photo-Fenton [53], electro-oxidation (EO) [54–57], electro-Fenton (EF) [58–62] and electrocoagulation [63].

Terbuthylazine

Terbuthylazine (TBZE, $C_9H_{16}ClN_5$, *N-tert*-butyl-6-chloro-*N'*-ethyl-[1,3,5]triazine-2,4-diamine, M = 229.71 g mol^{-1}) is a chlorotriazine similar to atrazine, simazine, propazine and cyanazine (**Figure 7**). It is a selective herbicide used to control broadleaf weeds and grass in certain forests, but it is mainly used to prevent the proliferation of fungi, bacteria and slime-forming algae in non-agricultural environments. TBZE is one of the most used pesticides in Italy, Portugal and Spain [64]. It has been considered a CEC, showing low solubility in water (6.6 mg L^{-1}) and high affinity to soil yields, which confers large persistence in surface water, marine water, and GW, where it has been quantified at concentrations of 0.2 µg L^{-1}, 84 µg L^{-1} and 5 µg L^{-1}, respectively. Worth noting, it has been the second most used pesticide in the USA after glyphosate. TBZE slowly decomposes in water to yield several by-products, including the persistent desethylterbuthylazine (DE-TBZE), which presents more toxicity than its precursor [65].

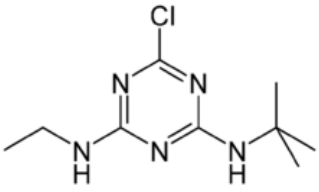

Figure 7. Molecular structure of terbuthylazine pesticide.

The family of triazine pesticides (**Figure 8**) is one of the least toxic to wildlife. In fact, most of them are non-harmful to organisms in punctual and low amounts, but they have a strong impact on ecosystems by unbalancing them, altering their flora and fauna. Long-term exposure to high levels of triazines has caused adverse effects in animals such as tremors, changes in organ weights, damage to the liver and heart, infertility and higher mortality on newborn mammals [66]. TBZE is toxic due to its ability to bioaccumulate, posing long-term risks to mammals. It can cause endocrine disruption [67,68], since it interferes with the female reproductive system [69], with the steroidogenesis and alteration of the genomic integrity [70,71]. It is not clear if TBZE has carcinogenic or mutagenic effects [12]. Some of the triazines are considered moderately toxic to fish and there is no damage reported on bees. Other research has concluded the effect that this family of pesticides has on amphibians by disrupting their metamorphosis timing as well as interfering with information processing, altering the behaviours requires for breeding, feeding and avoiding predators [72]. Recently, most triazines have been banned as herbicides due to relevant accumulations on surface water and GW. The ban on triazine herbicides could have strong effects on maize crops and intensive agricultural activities [73].

Processes for removal of TBZE based on separation technologies have been used so far, involving adsorption on active carbon and carbon nanotubes [74], metal organic frameworks [75], selective polymeric materials [76] and membranes [77]. Transformation or destruction techniques included sunlight/O_3 and sunlight/TiO_2/O_3 [74], UV/B-doped TiO_2/O_3 [78], UV/TiO_2/chitosan [79], and UV/H_2O_2, as well as electrochemical processes such as EO with a boron-doped diamond (BDD) anode [80], bioremediation [81], photodegradation [82] and chemical reduction [83].

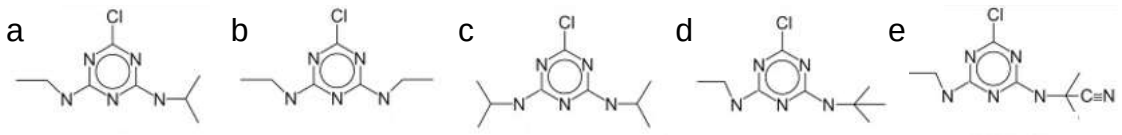

Figure 8. Chemical structures of common s-chloro-triazine pesticides: (a) atrazine, (b) simazine, (c) propazine, (d) terbuthylazine, and (e) cyanazine [84].

Nitrate

Nitrate (NO_3^-, M = 62.00 g mol^{-1}) is an inorganic N-containing anion. It is a common form of nitrogen found in nature because of its high stability. Nitrate has a high solubility, and it is often involved in biogeochemical routes related to the nitrogen cycle. In nature, nitrate can be found naturally in soil and water bodies. Natural sources for nitrogen accumulation include the nitrogen fixation by certain bacteria. However, the prevailing source of nitrate GW contamination are the anthropogenic activities, as for example [85]:

- Agricultural activities: nitrogen-based fertilizers are spread throughout the fields to enhance crop growth, or bacterial metabolism acts on the organic nitrogen present on the lands, in soil and water layers, in the form of livestock manure and urine discharged by farmers;
- Urban wastewater and sewage: discharge of untreated or inadequately treated sewage and urban wastes into water bodies;
- Industrial activities: discharge of industrial or process wastewater effluents containing N-rich compounds;
- Combustion processes: emissions from vehicles, power plants and other combustion sources that release N-containing compounds, such as oxides, into de atmosphere; through rainfall, these can be transformed into nitrate onto the land and water bodies.

Once nitrate is present in the environment, it can undergo several transformations as for example biological. Plants and bacteria can take nitrate from the soil as a nitrogen source nutrient, or it can be converted by microorganisms to other forms of inorganic nitrogen such as nitrogen gas (N_2) through a denitrification process. Moreover, the excess of nitrate accumulation in soil and water bodies can result in health and environmental concerns, since it can leach trough soil and contaminate the main freshwater reservoirs and water sources, as explained above. WHO has set a recommended maximum nitrate concentration in freshwater of 50 mg L^{-1} (10 mg L^{-1} $N\text{-}NO_3^-$) [12]. Although nitrate itself is relatively inert, the associated health risk, especially to the youngest population, arises from its conversion to nitrite, a more harmful inorganic N-containing compound, in the

body during the digestion. More specifically, high nitrate concentration in drinking water can result in [86]:

- Methemoglobinemia, also known as “blue baby syndrome”: babies from 0 to 6 months old are especially vulnerable to this condition because nitrate is converted to nitrite into their bodies, binding to haemoglobin, which reduces its ability to transport oxygen. This results in a bluish colouration of the skin, known as cyanosis, generated by the oxygen deprivation [87,88].
- Gastrointestinal disturbances: the ingestion of high levels of nitrate-polluted water can cause gastrointestinal irregularities, such as abdominal pain, diarrhea and vomiting.
- Carcinogenic potential: an increased risk of certain cancers, such as colorectal, stomach and bladder ones, has been associated with long-term nitrate contaminated water consumption, although further research is needed to ascertain this correlation;
- Endocrine potential disruption: the exposure of organisms to nitrate has been linked to disruption of the thyroid function, disrupting the balance of several hormones, although more specific research is needed to confirm such causality [89–91].

To mitigate these results, it is of paramount importance to ensure safe drinking freshwater supply, especially for the most vulnerable part of the population, by implementing adequate water treatment methods that are able to remove nitrate. Understanding the sources and fate of nitrate is crucial for managing and mitigating its potential impact, especially the environmental and health issues. Monitoring and implementing an optimized use of fertilizers, which are sustainable and follow respectful agricultural practices, and improving wastewater effluents discharge are key factors for ensuring the safety of underground water bodies. Additionally, promoting the awareness of the population through public institutions while improving waste management practices would contribute to the decline of nitrate in water.

Several technologies have been developed over the last years in order to remove nitrate from freshwater, since nitrate pollution started to become a widespread problem. On the one hand, non-electrochemical methods are the most common due to the low

investment requirement for the simplest ones and their facile implementation as a low-scale temporarily solution. The most common non-electrochemical methods for nitrate removal are ion exchange [92,93], biological denitrification [94,95], reverse osmosis [96–98], chemical reduction [99–101], constructed wetlands [102,103], adsorption [104], photoreduction [105] and catalytic reduction [106–110]. On the other hand, electrochemical processes offer effective methods for nitrate removal from freshwater sources, although the electrochemical reactors need to be improved to treat freshwater, whose characteristics differ substantially from the usual effluents to which these methods have been typically employed. The most common electrochemical processes studied for nitrate removal are electrocoagulation [111–114], electrochemical reduction (ER) [115], bioelectrochemical denitrification [116–118], electrochemical capacitive deionization [119–121], electrodialysis [122,123] and Donnan dialysis [124]. Each electrochemical technology has its advantages and limitations in terms of investment (capital and operation expenses), efficiency and energy consumption, and operation complexity. Some electrochemical processes may produce a complex speciation of the by-products, may require additional non-electrochemical steps for the removal of other pollutants and reaction derivatives, or may need the adjustment of the target freshwater quality parameters.

A proper management and system maintenance are essential to ensure the reliability of all the methods, both electrochemical on non-electrochemical, also being important a regular analysis of the output quality standards of the employed system. The selection of the appropriate method depends on factors such as the nitrate concentration, the target removal percentage, the availability of infrastructure or investment capacity and, specially, the specific requirements imposed by the effluent characteristics.

1.2. Non-electrochemical technologies for groundwater treatment

Non-electrochemical processes are widely applied to the treatment of GW effluents, and their effectiveness has been demonstrated by several scholars. However, their efficiency depends on the nature of the target pollutant that needs to be removed. Depending on its chemical structure, some processes may be more suitable than others, being rare that a universal technology may show all the required features. Therefore, in general, a sequence of processes has to be implemented in order to address the

contamination by multiple pollutants, ending up with a freshwater free of toxic species. In this subsection, the main non-electrochemical processes applied to GW treatment for pesticide and nitrate removal are briefly described.

1.2.1. Non-electrochemical technologies for pesticide removal

Several strategies have been developed over the last years for the effective removal of pesticides from GW [125]. They can be classified as chemical or physical methods; alternatively, two groups can be distinguished: destructive, which involve either the oxidation of the molecule, transforming it into harmless by-products, or its reduction to yield de-halogenated products; and non-destructive, in which the pesticide is accumulated in an adsorbent material. Most destructive methods are based on the so-called advanced oxidation processes (AOPs), which are powerful techniques for the destruction and even the mineralization of organic pollutants. They are based on the production of high oxidation power reactive oxygen species (ROS) by different routes. Among them, the well-known hydroxyl radical ($^{\bullet}OH$) stands out due to its high redox oxidation potential. These oxidizing species have low selectivity, being able to oxidize even some very recalcitrant organic compounds, eventually transforming (i.e., mineralizing) them into CO_2 and inorganic ions. These processes can also be used for disinfection. The AOPs offer clear advantages for the removal of non-biodegradable organic compounds, such as the POPs and CECs. The selection of the appropriate AOP to be employed depends on the water effluent characteristics (i.e., water quality), operation parameters and cost considerations. Some of the most employed non-electrochemical processes are introduced below. Some of them might be combined in a single unit or in sequential steps in order to achieve synergies that improve the oxidation process.

Heterogeneous photocatalysis

This heterogeneous process consists in the irradiation of a photoactive material with suitable radiation according to its material bandgap. As a result, electron-hole pairs are produced as charge carriers, which react with water or oxygen to yield oxidizing and reducing radical species. The most widely employed photoactive materials for environmental applications are TiO_2, WO_3 and ZnO_2 [126,127].

Sonolysis

Sonolytic processes are AOPs based on the use of high-intensity ultrasound to generate cavitation bubbles in the water. The collapse of these bubbles generates high temperature and pressure, which can generate high reactive species such as •OH or other radical species that are able to oxidize the organic pollutants [128–131].

Ozonation and UV/O_3

Ozonation process is an AOP (at alkaline pH) that can be applied either by generating the ozone through an electrochemical system or from an O_3 generator. In both cases, this gas is bubbled into a solution and directly oxidizes the organic compounds, breaking them into less harmful compounds. Irradiating ozone with UV promotes the generation of •OH, enhancing the degradation power of the process [132–134].

Fenton and photo-Fenton process

Fenton-based processes are based on the production of •OH in the bulk solution via the well-known Fenton reaction (1), in which H_2O_2 reacts with a dissolved metal species (in general, ferrous iron) at pH ~3. In this case, both reagents are spiked into the solution in order to oxidize the organic compounds, being possible to achieve high mineralization degrees. Other metal ions can be used instead of Fe^{2+} in the so-called Fenton-like processes. If the solution is irradiated with UV light (i.e., photo-Fenton process), the degradation efficiency is higher due to the continuous Fe^{2+} photoregeneration from Fe^{3+} reduction, as has been verified for pesticides in natural water [135,136]. It is even possible to employ a catalyst in a solid form, giving rise to the heterogeneous Fenton processes. This family of processes is one of the most effective for the degradation of organic pollutants [136–138].

$$Fe^{2+} + H_2O_2 + H^+ \rightarrow Fe^{2+} + {}^{\bullet}OH + H_2O \quad (1)$$

Bioremediation

Biological remediation or bioremediation is a technology that consists in the transformation of organic compounds into harmless end products, such as CO_2 and H_2O. It is a low-cost and environmentally respectful technology as compared to other destruction methods, although it requires long treatment times [52,81].

Adsorption

Several adsorbent materials can be used in order to capture the pesticides. Clays are natural materials with low cost and high availability; they are hydrophilic and negatively charged, and can be used for retention of cationic pesticides [139]. Activated carbon is an excellent adsorbent that offers high surface area for trapping pesticides [140–142]. Zeolites, which are crystalline aluminosilicates materials with narrow interconnected pore-size distribution, allow removing pesticides from water at low cost [143]. Polymeric materials seems promising, since they require lower energy for the adsorbent regeneration [76].

Chemical reduction

Different strategies can be used for reducing pesticides, reaching dehalogenated molecules, which dramatically decreases the toxicity. Homogeneous strategies involve the addition of sulphite or thiosulphate [83], whereas heterogeneous ones are based on the zero valent iron (ZVI, Fe^0), as demonstrated for reducing pesticides [144].

Photodegradation

Photodegradation of pesticides is accomplished by direct irradiation of the pesticide solution, or by reaction with chemical species that have been generated upon direct irradiation. When applied directly to soils, the penetration of radiation depends on the wavelength, soil texture and moisture [82].

1.2.2. Non-electrochemical technologies for nitrate removal

Several factors must be considered in order to choose a suitable non-electrochemical process for nitrate removal, such as the pollutant concentration, the complexity to be physically implemented in each specific case, the particular characteristics of the effluent, and the required water quality at the outlet. It is also of paramount importance to consider the efficiency of the process, the cost-effectiveness, and the management of by-products, wastes or polluted streams potentially generated during the treatment. Sometimes, the performance may be enhanced by combining different technologies. The most important non-electrochemical methods for the treatment of nitrate contained are:

Ion exchange

Ionic exchange involves the use of a resin inside a column where the GW effluent flows through. Some resins have more affinity for a specific anionic species, thus promoting its selective adsorption by replacing it with the desorption of another ionic species, typically sulfate or chloride in the case of nitrate exchange. The resin must be regenerated periodically in order to remove the specifically adsorbed pollutant, thereby generating an effluent with high nitrate concentration and, simultaneously, recovering the ability of the resin to adsorb new pollutant [92,93].

Biological denitrification

This process employs specific bacteria to reduce nitrate to N_2 under anaerobic conditions through a complex mechanism that involves the sequential generation of different N-containing species. The process typically occurs in a biofilter or a denitrification bed consisting in an organic material such as a carbon. These bacteria can reduce oxidized forms of nitrogen in response to the oxidation of an electron-donor as part of their respiration, yielding an innocuous gas like N_2 [94,95].

Reverse osmosis

This is a membrane-based water purification filtration process, which employs a semi-permeable barrier to remove nitrate anions from an effluent by applying a pressure gradient across the membrane. As a result, water molecules flow through, whereas the passage of dissolved chemical species as well as contaminants and particles are impeded [96–98].

Chemical reduction

This process is based on the addition of reducing agents that can react with nitrate ions to transform them into less harmful inorganic nitrogen forms. For this, several strategies have been developed, such as homogeneous reaction with ferrous ion [145], and dithionite [146], or heterogeneous processes with zero valent iron [99–101], zero valent aluminium [147], zero valent magnesium [148], and zero valent zinc [149]. It is important to monitor the concentration of the reducing agent by-products accumulated upon its addition, since they can potentially affect the quality of the water effluent.

Photoreduction

These are based on the irradiation of a contaminated solution, producing reactive species that eventually trigger the reduction of nitrate and its by-products [105].

Catalytic nitrate removal

Catalytic treatments have emerged as a promising technology that aims at reducing nitrate and its by-products to N_2 or NH_3. This process is actually close to the electrocatalytic nitrate removal, as both of them rely on the generation of atomic hydrogen as the effective reductant. The catalytic systems generate this radical species from the catalytic reaction between H_2 bubbled in the solution and a platinum group metal. The generated hydrogen radical at the promoter metal surface is then able to react with nitrate. This method allows reducing nitrate effectively and on-demand [106–110].

Wetlands

Constructed wetlands employ plants, microorganisms and a specific substrate to remove contaminants like nitrate from water by flowing the polluted stream through the wetland system. Similar to the biological denitrification, the plants and microorganisms present on the wetlands reduce nitrate to generate other harmless N-containing species, such as N_2 [102,103].

Adsorption

Adsorption is a physical strategy to separate nitrate from the solution without destroying the ion. Several strategies with different materials have been used to remove nitrate from aqueous solutions: polymers [150], clay [151], activated carbon [104], and even industrial wastes [152].

1.3. Electrochemical technologies for groundwater treatment

1.3.1. Challenges for the treatment of groundwater by electrochemical processes

The electrochemical processes can be effective for treating polluted GW, although some challenges and limitations must be highlighted in order to devise a well-conceived setup that allows reaching a high decontamination percentage in an efficient manner. The

strategies may differ for electrochemical reactors operated in batch and continuous modes. Some of the major aspects to be considered are:

- The low conductivity of the GW matrix: the electrochemical processes require an input of electrical energy, which is often not a minor issue; water matrices with poor conductivity are challenging for conventional reactors, since the cost could become prohibitive due the excessive resistivity;
- The plausible fouling of the electrodes: during the electrolytic trials, a noticeable local alkalinization occurs in the cathode vicinity, which results in the precipitation of the earth-alkaline metals (i.e., calcium and magnesium) present in the raw solution. The precipitation of these two elements as hydroxides and carbonates due to the pH increase causes arise in the electrical resistance of the electrochemical system, entailing a higher cell voltage. This is detrimental because of two facts: (i) the greater energy consumption, and (ii) the blockage of cathode sites, which affects its electrocatalytic performance;
- The selectivity for the removal of specific pollutants: the effectiveness of the treatment may differ significantly depending on the chemical structure of the target pollutant. Dissolved metals, organic compounds and certain types of ions may require specific electrocatalytic materials, modifications of the process or the coupling of different technologies (either chemical or electrochemical);
- The electrode stability: either continuous or batch operation modes induce the gradual electrode degradation/corrosion, owing to the local aggressive conditions or the presence of compounds that negatively interact with the electrode surface. Such electrode alteration may require periodic maintenance or replacement;
- The pH imbalance: the electrochemical processes may change the pH of the treated effluent during the electrolysis due to the ongoing reactions. It may be difficult to apply a technology in practice if a given pH value must be maintained throughout the treatment;
- The system complexity: the electrochemical GW treatment may be challenging in terms of system design, process control and operation. The presence of chemical species like natural organic matter (NOM) may affect negatively the process by poisoning the electrode surfaces or by scavenging the oxidant species generated

either at the anode or in the bulk solution. As a consequence, the removal efficiency and the reaction rate may be lower.

Despite these circumstances, the electrochemical technology is becoming successful nowadays to address some of the most challenging problems of society, including water pollution. Different approaches to treat specific pollutants can be developed and, additionally, there is potential for devising pump-and-treat systems. Most of the described challenges can be addressed by carrying out a good design of the electrochemical process, focused on the removal of selected pollutants.

1.3.2. Electrochemical advanced oxidation processes (EAOPs) for pesticides removal

The EAOPs are a subgroup among the AOPs, and they rely on electrochemical reactions to generate (or improve the generation), either directly or indirectly, the highly reactive oxygen species (ROS), especially radicals like $^{\bullet}OH$, to effectively remove organic pollutants from water and wastewater. The combination of AOPs with the electrochemical reactions is known to enhance the overall treatment efficiency. The most relevant EAOPs for the treatment of pesticides are [153]:

Electro-oxidation (EO)

EO is the simplest EAOP, in which organic and inorganic compounds are oxidized, aiming at their gradual removal from water. In this process, the application of direct current leads to the oxidation of pollutants on the anode surface by the so-called anodic oxidation process. Depending on the material employed as anode, $^{\bullet}OH$ adsorbed on the electrode surface by reaction (2) can be generated, enhancing the oxidation capability of the system to degrade and even mineralize organic pollutants. In systems where chloride is present, this anion may be oxidized directly by the anode to active chlorine species, whose speciation depends on pH. This type of species may cause the oxidation through a homogeneous mechanism, thereby upgrading the oxidation system. The active chlorine species have lower oxidation potential than the $^{\bullet}OH$ generated on the anode surface and can potentially yield organochlorine by-products.

$$M + H_2O \rightarrow M(^{\bullet}OH) + H^+ + e^- \quad (2)$$

Photoelectrocatalysis

It is similar to heterogeneous photocatalysis process described in subsection 1.2.1, but in this case the UV or solar light is employed to irradiate the photoactive material that is fixed on a conductive surface, the ensemble being called photoanode. Then, the charge carriers (i.e., holes and electrons) are produced and, in the presence of H_2O and O_2, different radicals like $^{\bullet}OH$ are generated. Photoelectrocatalysis is actually analogous to EO, but the anode is replaced by a photoanode.

H_2O_2 electrogeneration

This electrochemical process consists in the production of H_2O_2, a weak oxidant, via 2 e^- oxygen reduction reduction (ORR) (reaction (3)), either from air using a gas-diffusion cathode or from O_2 dissolved in solution, eventually oxidizing the organic pollutants present in solution.

$$O_2 + 2H^+ + 2e^- \rightarrow H_2O_2 \quad (3)$$

Electro-Fenton process

EF process stands out as one of the most powerful and reliable electrochemical methods for the removal of organic compounds, such as pesticides. It combines the oxidation of the pollutant molecules by $^{\bullet}OH$ generated on the anode surface and in the bulk solution. The latter arise from reaction between cathodically generated H_2O_2 and Fe^{2+} added or present in the solution, according to the abovementioned Fenton reaction (1) at pH ~3. The resulting Fe^{3+} can be reduced back to Fe^{2+} on the cathode surface, which allows regenerating the catalyst to foster a more effective degradation [62].

Photoelectro-Fenton

Photoelectro-Fenton process (PEF) is similar to EF, but an UV lamp is included in the setup to irradiate the solution. This radiation boosts the efficiency of the degradation process because of two main phenomena: (i) the faster Fe^{2+} regeneration that occurs upon photoreduction of Fe^{3+}; and (ii) the photodecarboxylation of complexes formed between Fe^{3+} and carboxylate by-products, such as oxalate and other short-chain aliphatic acids. Solar radiation may be used as the source of photons, giving rise to the so-called solar photoelectro-Fenton (SPEF) process.

Electrochemical ozonation

This is a type of ozonation process described above, with the particularity that O_2 is produced on the anode via reaction (4). The electrochemical ozone generators have been developed in recent years, being possible to employ ultrapure water for co-production of O_3 and H_2.

$$3H_2O \rightarrow O_3 + 6H^+ + 6e^- \quad (4)$$

Electrochemical persulfate activation

Persulfate activation is receiving much attention in the last years. Different routes ca be followed to activate persulfate ion ($S_2O_8^{2-}$) to sulfate radical ($SO_4^{\bullet-}$), including its anodic oxidation and cathodic reduction. The former, which is illustrated in reaction (5), has been investigated in more detail, although the cathodic route has been recently reported as a promising strategy [154]. In aqueous matrices, both hydroxyl and persulfate radicals coexist and can effectively degrade and mineralize the organic pollutants.

$$SO_4^{2-} \rightarrow SO_4^{\bullet-} + e^- \quad (5)$$

The EAOPs offer several advantages for the removal of organic pollutants from water when compared with non-advanced other processes. Their high efficiency and ability to operate at near-ambient conditions make them suitable candidates for upscaling to industrial level. However, as occurs with any water treatment, the EAOPs present certain limitations, such as relatively high energy consumption and some specific requirements related to the effluent characteristics (e.g., conductivity, pH). As mentioned for the AOPs, the EAOPs can be combined with other processes to take advantage of their synergies.

1.3.3. Electrochemical processes for nitrate removal

Lately, several electrochemical technologies have been proposed for nitrate removal from GW. These methods are conceptually different and allow removing dissolved nitrate with the concomitant generation of different species. The most remarkable electrochemical processes are:

Electrocoagulation

Electrocoagulation involves the use of sacrificial electrodes, typically aluminium and iron, to release metal cations into the polluted solution. These ionic species destabilize and coagulate forming large flocs that can adsorb nitrate molecules and suspended particles. The coagulated fraction can then be removed by filtration or sedimentation. Specifically for nitrate removal, electrocoagulation systems lead to better results when aluminium is used; in the case of iron, nitrate becomes adsorbed on the anode surface and blocks the anode sites, thereby impeding its dissolution and resulting in a lower current efficiency. This method removes nitrate from water but generates a solid waste loaded with the adsorbed nitrate [111–114].

Electrochemical reduction or electroreduction

Nitrate electroreduction (ER), also known as electrocatalytic nitrate removal, refers to a heterogeneous electrochemical reduction reaction that occurs upon the application of an electric current through a suitable cathode material. It is one of the simplest electrochemical processes, since it only requires an active material for the reduction of an electroactive species, and the supply of a constant current or potential. The charge transfer step may occur directly to the electroactive species from the cathode surface, or may require the adsorption of the chemical intermediate that acts as reduction mediator; that mediator can reduce nitrate on the cathode or after being transported to the bulk. Depending on the cathode substrate, the electrolyte composition or even the cell configuration, the overall nitrate removal reaction (NRR) may follow a different mechanism or result in a different speciation of the by-products. The cathode potential (E_{cath}) may affect the selectivity (i.e., the speciation) [115]. Most reactions are dependent on pH or temperature. The most common reactions that yield the main nitrate by-products are its full (n = 8-electron) reduction to ammonia by reaction (6), and reaction (7) towards N_2.

$$NO_3^- + 6H_2O + 8e^- \rightarrow NH_3 + 9OH^- \quad (6)$$

$$2NO_3^- + 6H_2O + 10e^- \rightarrow N_{2(g)} + 12OH^- \quad (7)$$

Bioelectrochemical denitrification

Different strategies may be categorized inside the bioelectrochemical denitrification processes, depending on whether the current or electrode potential is imposed from a power supply, or the current is generated spontaneously by setting up a microbial fuel cell [118]. The so-called electro-bioremediation is another microbial electrochemical technology for removing of nitrate, being especially interesting for GW treatment [117]. Biological treatments exhibit several environmental and economic advantages over other technologies, but they require a continuous supply of chemicals as electron donor to be able to reduce nitrate to N_2 [116] through a complex mechanism leading to the global reaction (7). When nitrate is the target pollutant, autotrophic denitrification can be performed with the cathode acting as the electron donor and an inorganic carbon source.

Capacitive deionization

Capacitive deionization or CDI is an emerging water desalination technology that uses low potentials to absorb large amounts of ions inside porous electrodes in order to remove them from a water effluent. The process involves a charging step, in which the ions are stored in the electrode, and a discharge phase, in which the stored ions are released into a concentrated stream, resulting in the overall removal of the polluting ions [119–121].

Electrodialysis

Electrodialysis is a membrane-based electrochemical technology that employs a cation- or anion-exchange membrane (CEM and AEM, respectively) to selectively transport ions, under the action of an electric field, from a freshwater stream to a concentrated permeate [122,123]. This is one of the most robust methods known for water desalination and, by extension, it is very suitable for nitrate separation.

1.4. Nitrate electroreduction

The main reaction pathway for nitrate removal by ER, at relatively low pollutant concentrations and mild conditions such as the ones that are typical from GW, starts by a first step in which the nitrate is adsorbed on the cathode surface, thereby being reduced to adsorbed NO_2^- as shown in reaction (8). This is usually the rate-determining step (RDS) for nitrate. The other electrochemical reactions result in a complex mechanism which takes place faster than the NO_2^- generation step, giving rise to a potential variety of partially reduced inorganic nitrogen species, either in solution or as N-containing volatile compounds. The selectivity of the reaction is influenced by several parameters that are going to be discussed in detail in the specific subsection 1.4.2.

$$NO_3^- + H_2O + 2e^- \rightarrow NO_2^- + 2OH^- \quad (8)$$

$$2NO_2^- + 4H_2O + 6e^- \rightarrow N_{2(g)} + 8OH^- \quad (9)$$

$$NO_2^- + 5H_2O + 6e^- \rightarrow NH_3 + 7OH^- \quad (10)$$

The main by-products are N_2 and NH_3, owing to their thermodynamic stability. The first one, formed via reaction (9), is usually is the most preferred by-product because it is volatile (gaseous product). Its production results from a partial reduction of nitrate and usually requires specific and controlled conditions in order to achieve a good selectivity towards this reaction pathway. The second one, ammonia, stands out as the complete reduction by-product through an 8-electron complex mechanism, reaction (10). As can be seen in reactions (8)-(10), the mass balance of the electrochemical nitrate removal results in the alkalinization of the solution, hence displacing the equilibrium reaction (11) towards the NH_3 molecular form. This promotes its volatilization to the atmosphere, with the consequent decrease of dissolved nitrogen concentration.

$$NH_4^+ \leftrightarrows NH_3 + H^+ \qquad pK_a = 9.25 \quad (11)$$

1.4.1. Challenges to remove nitrate from groundwater by electroreduction

Electrochemical nitrate removal from GW by ER encounters several specific challenges that have to be addressed during the design of the electrochemical treatments. Coming back to the challenges and limitations presented in subsection 1.3.1:

- The low conductivity of the GW matrix: the ER process requires its adsorption on the cathode surface; however, nitrate is a negatively charged ion and hence, it is naturally transported by migration towards the anode. In a system where the number of dissolved ionic species is low or very low, a high transport number is expected for nitrate anion, which negatively affects its mass transport towards the cathode. Conversely, in a system that contains supporting electrolyte at sufficiently high concentration, the negative migration effect can be neglected. Based on this fact, it can be concluded that using as polluted effluent the waste discharge of a nitrate-saturated ion-exchange resin would be an interesting application: the conductivity would increase, resulting in a cheaper treatment thanks to the lower energy consumption, and the transport of nitrate by migration could be disregarded [155];
- The electrode fouling: the precipitation of alkaline-earth metals on the cathode surface affects its electrocatalytic activity and selectivity. This phenomenon is dramatic in terms of loss of efficiency. A softening pre-treatment is thus advisable, with many options investigated in the literature, such as: continuous electrolysis, either through a stainless-steel mesh to force the precipitation of calcium and magnesium [156] or through a thin-layer reactor [157], polarity reversal system to work in continuous mode [158], membrane-based electrochemical precipitation [159], electrocoagulation [160], CDI [161], sodium-loaded ion-exchange system with zeolites or specific exchange resins [162], or simple pH increase forcing the salt precipitation;
- The ER selectivity: a specific material with good activity for electrochemical nitrate removal at relatively low cathode overpotentials should be used, aiming to remove nitrate specifically with a controlled speciation of the by-products;
- The electrode stability: depending on the selected cathode material, cathodic protection would serve to extend the lifespan of the electrode, working in a continuous or batch mode. A deep study could be made in order to understand the corrosion processes that occur in the cathode surface;
- The pH imbalance: nitrate ER, reactions (6) and (7), produces several hydroxide anions per nitrate cation removed and hence, a significant increase of the pH is

expected, depending on the nitrate removal. In order to use the resulting effluent as freshwater, the final pH should be adjusted back to near-neutral;

- The system complexity: depending on the composition of the effluent, secondary reactions affecting the overall process may occur. By-products of the nitrate ER should be removed by including a post-treatment before using he produced water.

Although the ER may not result into freshwater able for human consumption or irrigation directly after electrochemical GW treatment, it may become a relevant step upon integration in a bigger system. The ER characteristics presumably ease the selective nitrate transformation, with a controlled by-product speciation depending on the conditions employed. By combining a pre-concentration step, such as reverse osmosis, as well as other treatments, freshwater ready for human consumption or activities could be obtained, while generated value-added wastes rich in ammonia that can be valorised as a fertilizer (**Figure 9**) [115].

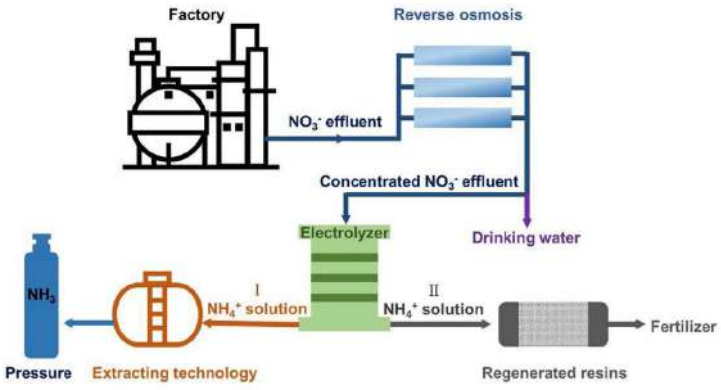

Figure 9. Scheme for the incorporation of nitrate ER to ammonia into an existing technological process for electrochemical nitrate removal [115].

1.4.2. Parameters affecting nitrate electroreduction and process selectivity

The nitrate ER is a complex process (**Figure 10**) [163], in which several electrons can be transferred depending on parameters that dictate the efficiency, the product speciation (selectivity) as well as its overall removal rate. Secondary reactions are feasible, especially the re-oxidation of nitrate by-products when an undivided cell is employed; that phenomenon can regenerate nitrate or produce other N-containing chemical species that remain in solution or escape to the atmosphere as volatiles. The key parameters affecting the nitrate ER are discussed in this subsection.

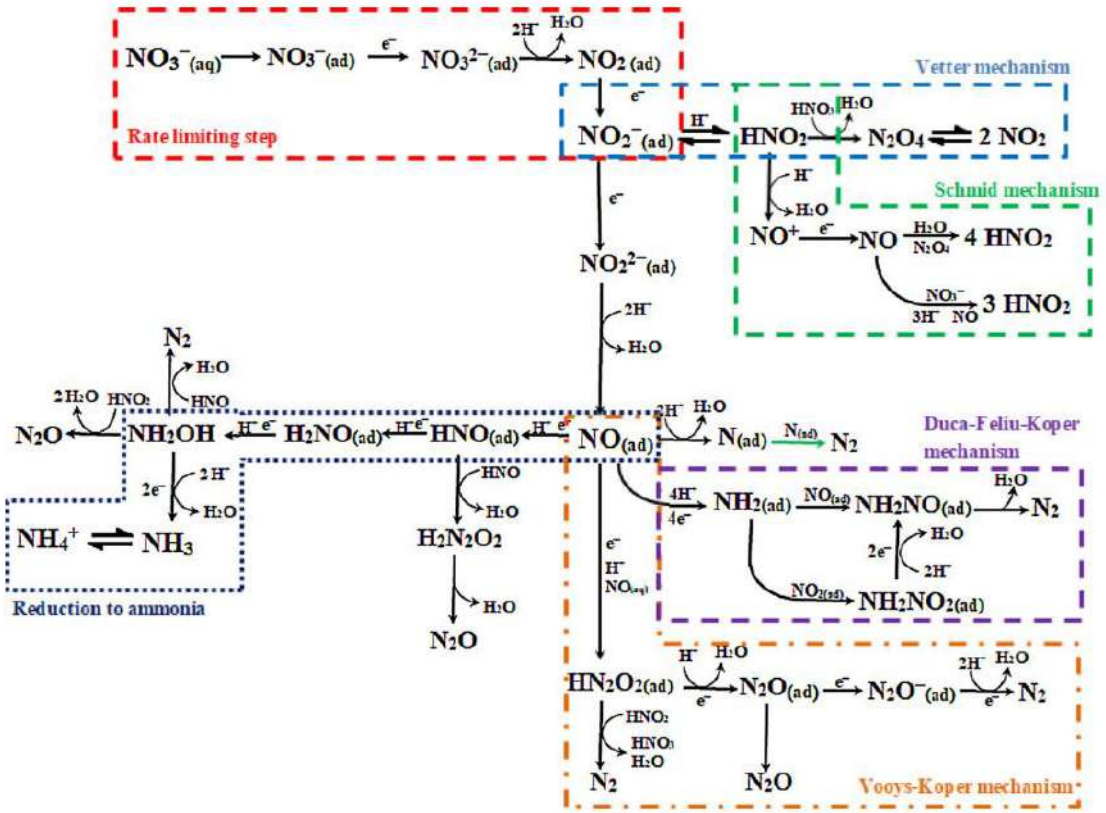

Figure 10. Mechanisms and main processes during electrochemical reduction of nitrate in water. The overall mechanism is divided into different sub-mechanisms to ease the understanding and facilitate the description, as follows: Rate-limiting step, Vetter mechanism, Schmid mechanism, Duca-Feliu-Koper mechanism, Vooys-Koper mechanism and reduction to ammonia [163].

The selection of the cathode material plays a crucial role in the electrocatalytic nitrate removal, since their catalytic behaviour frequently changes for different specific reactions. Some catalytic materials, such as metals from the platinum group, have shown lacklustre results when compared with others like iron- or copper-based materials, owing to the mechanism occurring on their surface when water is used as solvent. Differences in nitrate removal kinetics, speciation of by-products (selectivity), efficiency and energy consumptions have been reported. This has been confirmed using metallic, semiconductor and composite cathode surfaces, such as TiO_2 [164], Co_3O_4/Ti [165], Ti [166], Sn [167], Cu [168], Cu [169,170], Fe [171,172], Cu/Ni composite [173], Sn-modified Pt [174], Sn-modified Pd [175], Pd-Cu [176], nanoparticles (Cu, Pd, Pt and Rh) on reduced graphene oxide [177], Cu/Bi [178], Cu-Sn-Bi [179], Cu-Zn [166], Fe, Cu and Ti [180], BDD [181], Pd-Rh mesh [182], Rh [183], Ag [184], Au [185] and Pt [186], graphite and stainless steel [187]. Some of these studies assessed the effect of the cathode material by comparing

metals (Sn, Bi, Pb, Al, Zn and In), comparing the rate and the distribution of the products [188].

Although the electrochemical nitrate reduction occurs on the cathode, the anode may play some role in the overall process, owing to the possibility of direct oxidation, as exemplified in reaction (12). This reaction is just a simplification in order to show that, if the right conditions are met, the global nitrate removal finally observed may be lower than that really caused by the cathodic reduction reaction. The different N-containing by-products that remain in solution, with different oxidation states, may be prone to re-oxidation at the counter electrode in an undivided electrochemical cell.

$$NH_3 + 3H_2O \rightarrow NO_3^- + 9H^+ + 8e^- \quad (12)$$

Depending on the anode material, the final speciation in an undivided reactor can drastically change [189]. In a divided cell, the faradaic efficiency (FE) increases due to the minimized re-oxidation of by-products. In addition, the nitrate concentration can affect the speciation, by promoting a greater accumulation of partially reduced inorganic nitrogen species in solution at higher nitrate initial concentrations [167].

The concentration and the nature of the supporting electrolyte on the electrochemical reduction are also influential parameters. The cation present in the electrolyte affects the reduction rate by increasing it in the order of $Li^+ < Na^+ < K^+ < Cs^+$. On the other hand, the anion of the supporting electrolyte decreases the reduction rate in the order of $I^- > Br^- > Cl^- > F^-$. The presence of chloride ions in the electrolyte enhances the generation of N_2 as main by-product [190].

The absence or presence of chloride may have a dramatic impact on the nitrate ER [187]. The direct oxidation of chloride generates active chlorine species in solution by reaction (13). These species are weak oxidants that can react with the nitrate by-products, with different outcomes depending on the selectivity of the employed cathode. This will affect the speciation of the by-products in solution by reactions (14) and (15). The speciation of the active chlorine species in solution depends on the pH, which also affects their reactivity with the other species in the medium.

$$2Cl^- \rightarrow Cl_{2(aq)} + 2e^- \quad (13)$$

$$Cl_{2(aq)} + H_2O \rightarrow HClO + H^+ + Cl^- \quad (14)$$

$$HClO \leftrightarrows ClO^- + H^+ \qquad pK_a = 7.53 \tag{15}$$

The result of the homogeneous reaction with active chlorine species, which can oxidize NH_4^+ or NH_3 to N_2 by reaction (16) [191,192], depends on the ratio between the oxidant and NH_3, as well as on the speciation of the former. The speciation of the active chlorine species changes the reactions that occur as well as their kinetics. When there is a low concentration of oxidant, the yield of N_2 increases by reaching the chlorination breaking point [191], which results in the removal of inorganic nitrogen forms (ammonia and chloramines) in solution to favour the innocuous species N_2. In contrast, if the ratio of active chlorine to NH_3 is high, the re-oxidation of this N-containing compound back to nitrate by reaction (17) is promoted, decreasing the overall nitrate removal kinetics with the subsequent loss of current efficiency and rise in energy consumption.

$$2NH_3 + 2ClO^- \rightarrow N_{2(g)} + 2Cl^- + 2H_2O + 2H^+ + 2e^- \tag{16}$$

$$NH_3 + 4ClO^- \rightarrow NO_3^- + H_2O + H^+ + 4Cl^- \tag{17}$$

Depending on the amount of active chlorine species generated and the amount of NH_3 produced through the nitrate ER process, reactions (18)-(20) may also occur. Chloramines thus formed are volatile species that have a relatively low oxidation power but are typically used in water disinfection.

$$NH_3 + HClO \rightarrow NH_2Cl + H_2O \tag{18}$$

$$NH_2Cl + HClO \rightarrow NHCl_2 + H_2O \tag{19}$$

$$NHCl_2 + HClO \rightarrow NCl_3 + H_2O \tag{20}$$

Nitrite generation is the first step along the nitrate ER. Although the set-up, conditions and parameters may favour a final by-product or another, the nitrite generation is the RDS. After its occurrence, the subsequent ER reactions are fast and transform it to the end by-product. In the presence of active chlorine species, nitrite can be re-oxidized either at the electrode surface or in the bulk solution back to nitrate by reactions (21) and (22) [165–172]:

$$NO_2^- + ClO^- \rightarrow NO_3^- + Cl^- \tag{21}$$

$$NH_2Cl + NO_2^- + H_2O \rightarrow NO_3^- + NH_4^+ + Cl^- \quad (22)$$

Different anode materials, such as boron-doped diamond (BDD) [193] or dimensionally stable anodes (DSA®) based on IrO_2 and RuO_2, have been traditionally used in chloride media [171]. The selection of the electrolyte composition and the anode material is of paramount relevance to find synergies for the electrochemical removal of nitrate. Depending on the system, and especially when using a high oxidation power anode like BDD, the active chlorine species may become gradually oxidized by EO to toxic chlorine oxyanions, such as chlorate and perchlorate via reactions (24) and (25) [194], resulting in the accumulation of toxic by-products.

$$ClO^- + H_2O \rightarrow ClO_2^- + 2H^+ + 2e^- \quad (23)$$

$$ClO_2^- + H_2O \rightarrow ClO_3^- + 2H^+ + 2e^- \quad (24)$$

$$ClO_3^- + H_2O \rightarrow ClO_4^- + 2H^+ + 2e^- \quad (25)$$

The electrochemical removal of nitrate by reduction can occur over a wide pH range. This process has been studied from highly acidic to highly alkaline conditions [175–195]. The mechanism for nitrate ER differs from that observed at near-neutral, mild acidic or mild alkaline pH, resulting in a small influence of pH within this range on the overall reaction kinetics (reactions (6) and (7)). However, the speciation of by-products generated may vary upon the successive reductions once reaction (8) has occurred. Depending on the concentration, especially when it is higher than 1 mol L^{-1} at extreme pH values, the mechanism dramatically changes.

1.5. Electrochemical reactors for electrocatalytic nitrate removal

Electrochemical reactors are electrolytic cells in which a current or a potential is set to induce the occurrence of a certain reaction. The electroactive species react on one of the electrode surfaces. At the anode, the electroactive species are oxidized, whereas at the cathode, they become reduced. Simultaneous unexpected reactions can occur as well, which is associated with current leakage resulting in the so-called parasitic reactions. In a three-electrode setup where a reference electrode is connected to the working electrode to control the E_{cath}, the reactions that occur may be discretized through electrochemical characterization in order to know which one prevails at the electrode surface at a specific

applied potential. Working in such system at a specific electrode potential, i.e., potentiostatic mode, is more expensive because of the need for a reference electrode. Moreover, the resulting current is usually lower (bringing about a poor electrochemical kinetics), although it may be advantageous because of the better process control (ending in greater current efficiencies). A two-electrode system is easier for the operation, since the setup consists in a working electrode with an imposed constant current, i.e. galvanostatic mode, and its counter electrode in which the counter-reaction takes place. This latter reactor configuration is usually preferred for upscaling of electrochemical reactors due to its robustness and lower cost. The nitrate ER rate depends on the cell configuration, which has a great effect on the efficiency of the process because the arrangement of the electrodes, the flow pattern and its direction impact the mass transport [196–198]. Different configurations have been employed for electrochemical nitrate removal, either in batch or continuous mode.

The conventional lab-scale undivided electrochemical cell in batch mode, with electrodes arranged as parallel plates, allows studying the fundamentals and running trials aimed at comparing the performance of different materials. This cell configuration shows surprisingly high current efficiencies, probably due to the charge-transfer controlled regime [199]. Other reactors with the optimized lab-scale configuration can subsequently be used in order to evaluate the electrolysis conditions in a system with bigger treatment capacity. The reactor configuration, the shape and dimensions of the electrodes, and the stirring affect the mass transport of the electroactive species. Divided cells are usually composed of two chambers or compartments filled with the same or different solutions separated by an ion-exchange membrane, allowing the passage of certain ions from one half-cell to the other. Using a cationic membrane, the anodic re-oxidation of nitrite accumulated as by-product from reaction (8) is avoided. Divided systems have higher ohmic drops as compared to undivided ones, improving the current efficiency at the expense of a greater final energy consumption. In order to decrease the energy consumption for GW treatment, a system including a membrane as solid polymer electrolyte (SPE) placed between the anode and cathode has been investigated in this Thesis for the removal of both nitrate and pesticides [200]. Due to low conductivity of this kind of natural water matrices, using an SPE cell allows decreasing the cell potential, drastically diminishing the energy consumptions [182].

The rotating cylinder electrode (RCE) reactor is another particular device, which consists in a central cylindrical electrode that rotates promoting the mass transport of the electroactive species toward its surface. This reactor has been mostly used for mass-transport controlled cathodic processes like metal recovery in the electroplating sector [201–203], as well for erosion and corrosion studies since the RCE allows generating a high turbulent flow at low Reynolds (*Re*) dimensionless number values (> 100).

Lab-scale electrochemical reactors are usually operated in batch mode due to its simplicity and, among them, flow setups possess several advantages, such a higher cost-effectiveness, which is the main driver for chemical process scale-up and industrialization, and a higher yield when working under galvanostatic conditions. Batch reactors can be operated in recirculation mode, where the volume at the outlet is mixed with the feeding solution, and the treatment proceeds by flowing the solution several times until the required outcome is achieved. The electrochemical flow reactors may be either flow-through or flow-by, depending on the electrode configuration and their shape. On the other hand, in continuous flow mode (single-pass reactors), the solution to be treated is pumped through the reactor only once at a given flow rate. Nonetheless, this option has been much less explored than the use of batch reactors.

Different reactors to work in batch mode for nitrate removal have been studied or have been suggested as interesting options. For this application, the parallel-plate tank reactor is the most studied one due to its simplicity to work at lab scale [155,196,204,205]. It is usually an open reactor to the atmosphere, either divided or undivided. Some particles may be added in order to generate a bed, which can be made of either electroactive or inert material to improve the contact surface and mass transport [199,206] or just the mass transport [199,207], respectively (**Figure 11**). Several systems equipped with reactive electrode membranes have been studied as well. In this configuration, the nitrate-polluted solution flows through polarized membranes loaded with an electrocatalyst [208,209]. Regarding the thin-layer reactors, they are able to minimize mass transport limitations approaching reaction rates typically obtained in batch reactors [210]. This reactor is made up of electrodes with small interelectrode distance; the mass transport coefficient increases as the inter-electrode distance decreases. The configuration may allow a reference electrode to be set near the working electrode surface.

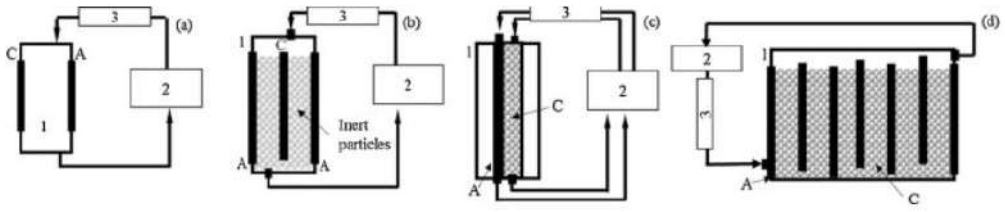

Figure 11. Different flow reactors employed to remove nitrate by ER in batch recirculation mode: (a) parallel-plate electrode cell; (b) inert particles fluidized bed cell; (c) packed bed cathode cell; and (d) vertical moving particle bed cell. (1) Electrochemical cell; (2) electrolyte reservoir; and (3) flow meter. A and C stand for anode and cathode, respectively [163].

1.6. Computational fluid dynamics

Computational fluid dynamics (CFD) has been developed as a branch of fluid mechanics that uses computers to solve algorithms and numerical methods in order to analyse typical fluid mechanics problems, as for example fluid flow or heat flow, aiming at obtaining feasible predictions about the behaviour of a given system under certain controlled conditions. It involves the application of equations, mathematical models and computational algorithms to solve and visualize steady-state or time-dependent behaviour of fluids in scientific and engineering applications. Finding the solution to the governing equations, which describe the conservation of mass, momentum and energy in a system where a fluid flows, is the fundamental purpose of the CFD simulations. These equations are the Navier-Stokes set of equations in a turbulent regime, the continuity equation, and the energy equation. In this Thesis, to solve the turbulent system, the Reynolds-averaged Navier-Stokes (RANS) equations that describe the turbulent flow regime have been used in conjunction with the κ-ε turbulence model, which sets the energy and dissipation energy of the turbulence.

In order to solve the governing equations by CFD, these are discretized into a set of algebraic equations using a numerical method like, i.e., the finite volume method, to find the solution to partial differential equations that describe the fluids behaviour. This method implies the division of the flow domain into a mesh. The integral form of the partial differential equations is used to derive conservation equations for each described finite volume; hence, they can be solved by calculating fluxes across the faces of the volume and obtain a solution at its centre.

Depending on the nature of the system, different solvers can be employed to solve the discretized equations in an iterative way. These solvers provide the values of the velocity, pressure and temperature variables by employing algorithms that solve the discrete equations.

The boundary conditions are a set of equations that describe the behaviour of the fluid flow variables at the surfaces of the computational domain. These conditions can set the specific velocity, pressure or temperature (or other parameters) values in a discrete region of the domain and are key to describe in a realistic way the overall behaviour of the system.

The verification of the CFD simulations requires the convergence of the numerical method. However, their validation has to be done through experimental trials in which the key parameters under study in the developed model are measured. In this Thesis, the ultimate goal of this part of the study is to validate the new mathematical model for nitrate removal with the experimental evidence found using the RCE reactor. An example of results obtained for electrochemical reactor characterization by CFD is shown in **Figure 12**.

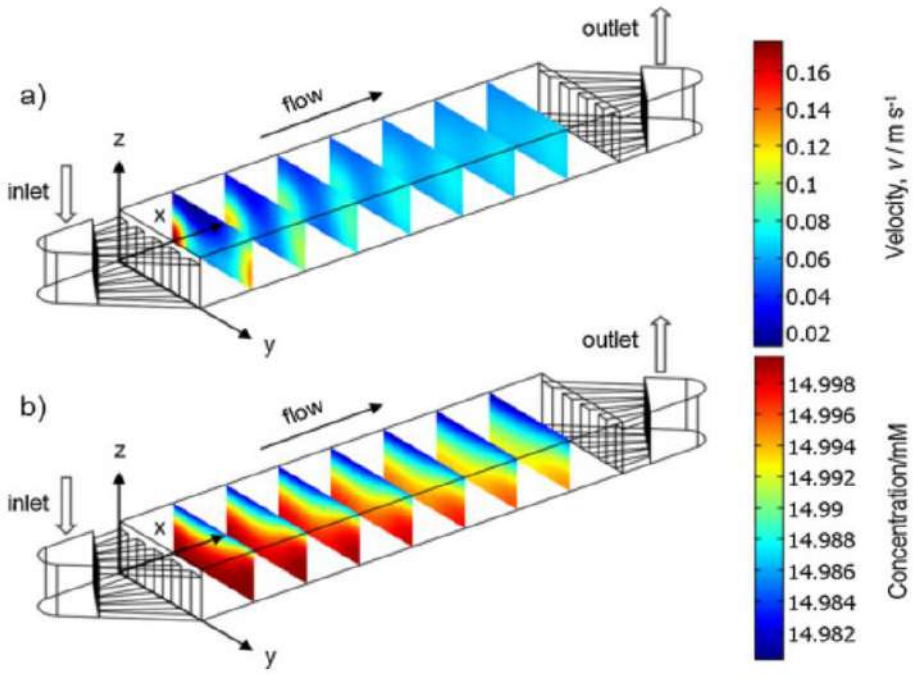

Figure 12. Numerical simulation of mass transport under turbulent flow for ferricyanide ion ER in an FM01-LC reactor under limiting current conditions. (a) Velocity field and (b) ferricyanide ion concentration. COMSOL Multiphysics® software was employed [211].

CHAPTER 2

OBJECTIVES AND STRUCTURE

CHAPTER 2. Objectives and structure

2.1. Objectives

The work carried out in this Thesis aims at fulfilling three general objectives (GO), which have been defined to investigate the electrochemical removal of pesticides and nitrate from actual groundwater:

GO1: Finding smart and practical solutions based on electrochemical approaches to overcome the specific issues associated to the treatment of actual groundwater (e.g., low conductivity);

GO2: Coupling ER and EO for the simultaneous removal of nitrate and pesticides, selected as model organic contaminants present in GW;

GO3: Improving the understanding of electrocatalytic nitrate removal, providing insights for more simple and/or efficient ER;

GO4: Characterizing an RCE reactor for fast electrochemical nitrate removal, and predicting the concentration decays by running CFD simulations based on the development of a suitable mathematical model.

To accomplish these main goals, the following specific goals (SG) have been set:

Regarding GO1: Use of a two-electrode SPE cell to electrolyze low-conductivity GW:

SG1: Investigating the viability of a softening method based on the circular economy concept;

SG2: Studying the degradation and mineralization of IMC as model compound;

SG3: Elucidating the fate of the chlorine and nitrogen heteroatoms that are present in the pesticide molecule;

SG4: Assessing the effect of the water matrix on the process effectiveness.

Regarding GO2: Combination of an active cathode for nitrate removal by ER with different anode materials for pesticide removal in a single cell, aiming at their simultaneous removal in different water matrices including softened GW:

SG5: Comparing the oxidation power of different anode materials for the degradation and mineralization of IMC and TBZE;

SG6: Studying the effect of the electrolyte composition and pH on the electrocatalytic nitrate removal;

SG7: Assessing the influence of simultaneous removal of a pesticide by EO and nitrate by ER in a single-step electrochemical treatment;

SG8: Identifying the speciation of the N- and Cl-containing by-products generated in the different electrolytes under study;

SG9: Assessing the effect of the matrix composition on the removal kinetics of IMC and TBZE in the EO/ER treatment;

SG10: Proposing a degradation pathway for the determination of the main intermediates for IMC and TBZE degradation by EO in different media using different anodes;

SG11: Applying a post-treatment to adress the threat associated to the generation of potentially toxic anions like.

Regarding GO3: Perform the electrochemical characterization of NRR, and devise a system for its potential scale-up:

SG12: Assessing the mechanistic fundamentals of the NRR, thereby establishing a correlation with the distinct behaviour of iron-based steels in terms of nitrate removal performance;

SG13: Investigating the promotion of the mass transport coefficients upon use of rotating electrodes, and the improvement of the nitrate degradation kinetics;

SG14: Characterizing the nitrate mass transport in an RCE reactor, establishing the basis for technology scale-up.

Regarding GO4: Employ a multiphysics software to simulate the nitrate removal by ER in an RCE reactor, and validate the model by running the experimental electrolytic trials:

SG15: Model the nitrate concentration decays attained by ER by solving the hydrodynamics, mass transport and current distribution using CFD simulations;

SG16: Validate the mathematical model with experimental results at different initial nitrate concentration and rotation rates of the RCE.

2.2. Structure

The present work is structured as follows:

- **CHAPTER 1** introduces the occurrence of GW contamination and the main causes that set this phenomenon as one of the most serious dangers for human health and the environment in 21st century. The importance of establishing a global framework to face the main causes that contribute to global discharge of pollutants to freshwater reservoirs is highlighted. The most relevant strategies for addressing this contamination, along with a critical evaluation of the possibilities and main drawbacks of electrochemical and non-electrochemical technologies for this purpose, is described. Finally, several types of electrochemical reactors employed for the implementation of electrochemical technologies for GW treatment are presented, with special focus on those investigated in this Thesis. The simplicity for operation with these systems is remarked.
- **CHAPTER 2** sets the framework of the present Thesis by establishing the global objectives and the specific goals that have been proposed to accomplish them, and describes the structure of this manuscript.
- **CHAPTER 3** presents a description of all the materials, methods and equipment employed to address the experimental and computational tasks that allowed obtaining the results discussed in this dissertation.
- **CHAPTER 4** constitutes the main body of the Thesis work. Selected aspects of the research are highlighted along with the main results. The results can be reviewed more in detail in the five scientific articles related to the Thesis. They describe the study of the electrochemical treatment of actual GW for the removal of pesticides by EO, the simultaneous removal of pesticides and nitrate by performing the EO/ER coupling, and the more fundamental investigation of the NRR that has been further complemented with the characterization of an RCE reactor for nitrate removal by ER, opening the door for the technology scale-up.
- **CHAPTER 5** summarizes the general conclusions drawn in the Thesis and offers some perspectives for future work.

CHAPTER 3

MATERIALS, METHODS, THEORY AND CALCULATIONS

CHAPTER 3. Materials, methods, theory and calculations

3.1. Chemicals

The main properties, environmental concerns, characteristics and applied electrochemical and non-electrochemical processes previously reported in the literature for nitrate and for pesticides degradations investigated in this Thesis have been discussed in detail in subsection 1.1.5.

IMC and TBZE standards were of analytical grade provided by Sigma-Aldrich, whereas nitrate was either supplied by Panreac or Fermont as KNO_3 with purity of 98% or > 99%, respectively. The rest of chemicals were NaOH (98-100%) and H_2SO_4 (95-98%) for pH adjustment were of analytical grade provided by Panreac; Na_2SO_4 (99.9%) and NaCl (99%) used as electrolytes were supplied by BDH Prolabo and Panreac, respectively, In some cases, K_2SO_4 (99.9%) from Panreac was also used. KCl (99%) from Panreac was employed as standard for conductivity measurements, analytical grade sodium nitroprusside dihydrate was purchased from Merck. EDTA (> 99%) was provided by Karal. Phenol (> 99%) was purchased from Sigma-Aldrich and used for ammonia colorimetric determination. Ascorbic acid from Sigma-Aldrich, 1,10-phenantroline monohydrate (99%) from Alfa-Aesar, ammonium acetate (98%) from Panreac and acetic acid (ACS grade, 99.7%) from Panreac were used for soluble iron determination. KH_2PO_4 (99%) and K_2HPO_4 (99%) obtained from Panreac were used as phosphate buffer for HPLC mobile phase and for the determination of active chlorine species alongside *N*,*N*-diethyl-*p*-phenylenediamine (DPD) (> 99%) purchased from Fluka. 5,5-Dimethy-l,1-pyrroline N-oxide (DMPO) used for electron paramagnetic resonance (EPR) analysis was purchased from Sigma-Aldrich.

Phthalic acid (99%) and tris(hydroxymethyl)aminomethane (> 99%) from Alfa-Aesar and Panreac, respectively, were employed as mobile phase reagents for anion quantification in anionic ion chromatography (IC), whereas tartaric acid, boric acid, 2,6-pyridinedicarboxylic acid and 18-crown-6 solution were used as mobile phase reagents for cationic IC.

Analytical grade oxalic-dihydrated, oxamic and cyanuric acids employed as standards for ion-exclusion HPLC were obtained from Sigma-Aldrich, Avocado, and Aldrich, respectively. Acetonitrile of ACS grade was used as mobile phase for reversed-phase HPLC and dichloromethane (CH_2Cl_2) of the same quality was employed for the extraction of organics from aqueous phase to be analysed by GC/MS was purchased from Panreac.

3.2. Water matrices

The electrolytic trials were carried out using different aqueous matrices that can be divided into actual and synthetic water. The latter type was prepared as model solution with either a typical supporting electrolyte concentration or by mimicking the anion content or ionic strength of the actual water, aiming at studying the effect of the electrolyte composition towards the electrochemical removal of pesticides or nitrate. The pesticides were spiked as model organic compounds into the actual GW, whereas the nitrate concentration was always the original one from the polluted GW source.

Raw groundwater

Actual GW effluents were obtained from a water well located in an agricultural land in the surroundings of Barcelona (Spain). Several sets of samples were collected in different days from the same local source, with variations of its main characteristics such as conductivity, TC, TOC and the anion and cation content analysed by IC and ICP-OES, respectively. All samples were stored and preserved in a refrigerator at 4 ºC. The main physicochemical characteristics of the raw GW effluents used as actual water matrices are summarized in **Table 3**. The pH was always near-neutral, ranging from 6.9 to 7.2. Low NOM contents from 1.3 to 2.6 mg L^{-1} were found, whereas inorganic carbon concentrations were between 50 and 65 mg L^{-1}. Regarding the anion content, chloride was always found in a relatively high concentration, but the sulfate content was low. Nitrate concentration was within the range of 101-130 mg L^{-1}, surpassing the limit established by WHO for a high quality freshwater (50 mg L^{-1}) [12]. The concentrations of cations that account for water hardness were found in a ranges of 100-240 mg L^{-1} and 27-55 mg L^{-1}, attributed to calcium and magnesium, respectively.

Prior to the electrolytic trials, the natural water effluents were softened to remove the alkaline-earth divalent cations to avoid the formation of calcium and magnesium carbonates and hydroxides on the cathode surface. This precipitate negatively contributed to the GW electrochemical treatment since it increased the cell voltage, leading to higher energy consumptions and blocking the electrocatalytic activity of the cathode towards the nitrate electroreduction reaction. Two different pre-treatments have been employed to soften the raw water matrices. One is based on Na^+-charged zeolites (NaP1-NA), synthesized by a hydrothermal method from coal combustion fly ashes (CFA), obtained from industrial wastes to encourage the circular economy concept by waste valorisation. For that, 20 g L^{-1} zeolite was dosed, as a softening method to remove hardness from the actual effluent mainly thanks to cation exchange that released Na^+ to the solution. A minor contribution from slight alkalinization from pH of 6.9 to 9.8 must also be noticed. The other softening process consisted in the increase of the pH by adding NaOH up to a pH higher than 12, thus forcing the precipitation of calcium and magnesium carbonates and hydroxides, which resulted in a drastic reduction of their concentration. Afterwards, the softened water matrices were filtered to separate the white precipitate from the softened GW, and a last step consisted in pH adjustment to recover the initial value.

Table 3. Main physicochemical characteristics of the raw GW matrices employed in this Thesis.

Parameter (units)	1st GW	2nd GW	3rd GW
pH	6.9	6.9	7.2
Conductivity (mS cm^{-1})	1.9	1.4	1.7
TC (mg C L^{-1})	67.2	65.2	50.0
TOC (mg C L^{-1})	2.6	2.7	1.3
TN (mg N L^{-1})	24.2	29.2	23.8
NO_3^- (mg L^{-1})	107	130	101
Cl^- (mg L^{-1})	458	366	363
SO_4^{2-} (mg L^{-1})	90	88	78
Ca^{2+} (mg L^{-1}	240	241	100
Mg^{2+} (mg L^{-1})	55	57	27
K^+ (mg L^{-1})	4.5	4	10
Na^+ (mg L^{-1})	80	82	180

A post-treatment consisting in an ion exchange resin was implemented as a final conditioning step in one of the studies to reduce the amount of oxychloride anions

produced during the electrolysis trials by the oxidation of chloride anion by reactions (13)-(15) and (23)-(25). The resulting electrolyzed solution was treated with a Purolite® A532E resin, a polystyrene strong base anion gel in the chloride form that is especially recommended by the provider for perchlorate removal. The final resin-based post-treatment allowed the removal of the chlorate, nitrate and sulfate concentrations alongside the complete removal of 766 mg L^{-1} of perchlorate, concomitantly leading to an increase in the chloride content.

Synthetic GW matrices

In some cases, the simulated aqueous matrices mimicked the main ionic composition of the actual GW effluents without their NOM and hardness (Ca^{2+} and Mg^{2+}) contents. In other cases, the composition was altered to study the effect of a specific species and its concentration on the electrochemical trials such as the presence or absence of chloride towards the removal of either pesticides or nitrate anion. They were prepared with Milli-Q quality water by adding certain amount of salts in order to mimic a composition with similar conductivity and ionic strength values. The solution pH was adjusted in most cases in order to study the effect of its initial value on pesticides and electrochemical nitrate removal.

Electrolyte solutions

The electrolyte solutions were prepared by adding one or more different inorganic salts, such as Na_2SO_4, NaCl and $NaNO_3$ or KNO_3 in Milli-Q quality water.

3.3. Electrochemical systems

Different electrochemical setups were employed to carry out the experiments performed in this Thesis. All the electrolytic experiments were done in batch mode using different solution volumes ranging from 150 to 500 mL in an undivided and open cylindrical cell with a jacket used for recirculation of water kept at 25 ºC. The reproducibility of the trials was ensured by polishing the steel RCE with different-sized sandpaper before each electrolysis with a 20% H_2SO_4 solution. The electrochemical setups are going to be presented for each specific subsection in CHAPTER 4.

A cylindrical glass tank was used to electrolyze 500 mL of Milli-Q, softened GW or synthetic GW solution under vigorous magnetic stirring with a magnetic stirrer at 1100 rpm. A solid polymer electrolyte (SPE) cell, comprising an anode/membrane/cathode sandwich, was immersed in it. The cell was built with expanded metal meshes of 3.5 cm × 7.5 cm of geometric area as electrodes, with a separation of 0.15 mm corresponding to the thickness of the Nafion® N117 ion-exchange cationic membrane previously activated following the instructions of the fabricant. The anode was a Nb mesh with a BDD thin film (3500 ppm of boron/carbon ratio) of 5 µm thickness deposited onto it provided by Condias. The cathode was a Ti/RuO_2 mesh purchased from De Nora Industries. The electrolytic assays were performed at galvanostatic conditions using an EG&G Princeton Applied Research 273A potentiostat-galvanostat, whereas the cell voltage was measured on a Demestres 601BR digital multimeter.

A conventional lab-scale cylindrical cell that contained 150-175 mL of different water matrices was also used to carry out the electrolytic experiments in a two-electrode configuration, operating at 800 rpm using a magnetic follower. The anode was either an IrO_2 electrode purchased from NMT Electrodes (Pinetown, South Africa) or a Si wafer coated with a BDD thin film, purchased from NeoCoat (Le-Chaux-de-Fonds, Switzerland). The cathode was either a mild steel (AISI DC01) or a stainless steel (AISI 304) plate. The electrodes had a geometric area of 10 cm^2 in contact with the solution and were placed in the center of the reactor at a distance of 1.5 mm from each other. Galvanostatic conditions were used to perform the electrolyses using an Amel 2049 potentiostat-galvanostat to provide the constant current density. The cell potential was directly measured by a Demestres 601BR digital multimeter.

Some electrolytic assays were performed with 500 mL of different water matrices at different initial pH in a two-electrode system under stirring with a magnetic follower at 900 rpm. A custom steel mesh (AISI DC01) was used as the cathode, whereas the anode was either an expanded metal Nb mesh coated with a 5 µm BDD thin film (3500 ppm boron/carbon ratio), purchased from Condias, or a RuO_2 provided by De Nora. The electrodes that were immersed into the solution had dimensions of 3.5 cm × 7.5 cm. The electrodes were placed in the center of the tank reactor, separated at a distance of 3 mm. In some cases, two steel cathodes were used, with the anode sandwiched between them keeping a separation of 3 mm with each cathode in order to double up the cathodic

immersed surface. The electrolytic trials were carried out under galvanostatic conditions with an Amel 2051 potentiostat-galvanostat providing a constant current (I) while a Demestres 601BR digital multimeter was used to monitor the cell voltage.

A three-electrode system was used in most electrolytic trials with the RCE reactor to electrolyze 400 mL of synthetic solution consisting in 10 mM $NaNO_3$ + 0.50 M Na_2SO_4 in tri-distilled water at natural pH 6.5. A jacketed glass vessel (13 cm height × 8 cm diameter) equipped with an AISI 1018 carbon steel cylinder employed as cathode (14 cm height × 3.8 cm diameter) in the center of the vessel was surrounded by six commercial IrO_2 anode plates (15 cm height × 2 cm wide). The anodic plates were installed in a 3D printed PLA plastic holder, whereas the cathode was insulated in the bottom with a polypropylene cap. The gap between electrodes was kept at 1.9 cm, and the total anode surface was similar to the cathode exposed area of about 100 cm^2. In order to study the effect of the cathode potential (E_{cath}), potentiostatic electrolyses using a double junction saturated mercury-mercurous sulfate electrode (E^o = +0.64 V vs SHE) as reference electrode, which was placed at a depth of 4 cm inside the solution as close as possible to the RCE, were carried out. A Biologic SP-150 power supply equipped with a Biologic VMP3B-10 booster was used to control E_{cath} at values between -1.6 and -2.2 V. The effect of the rotation rate of the central RCE was assessed by setting its value between 100 and 500 rpm. Galvanostatic trials were performed in a two-electrode set-up to study the effect of the supporting electrolyte concentration on the electrochemical nitrate removal. Several blank experiments were performed to assess the extent of ammonia volatilization due to alkalinization and the flow regime imposed by the RCE.

The two-electrode RCE system was used to validate the mathematical model and the simulations. The system setup was exactly the same as the described above, although in this case an IKA RW 20 variable rotation electric motor was used and the rotation rate of the RCE was set to 300-1000 rpm. A GRELCO GVD310 was used as power supply to provide the galvanostatic current conditions. The cell potential was measured with a Demestres 601BR digital multimeter.

3.4. Analysis of the performance

Removal assessment, mineralization current efficiency and mass balance

The performance of the different electrochemical systems for the removal of pesticides and nitrate was mainly assessed from the determination of the percentages of the removed target pollutants by equation (26) and of TOC from equation (27):

$$\%\, Target\ pollutant\ removal\ = \frac{\Delta C}{C_0} \times 100 \quad (26)$$

$$\%\, TOC\ removal\ = \frac{\Delta TOC}{TOC_0} \times 100 \quad (27)$$

where Δc is the pollutant concentration decay and c_0 is the initial concentration, both in mg L^{-1}. This is analogous for TOC values (in mg C L^{-1}) shown in equation (27). The same equation was applied to calculate the TN removal (in %) by using ΔTN and TN_0, respectively, and changing the units to mg N L^{-1}.

The mineralization current efficiency (MCE) was estimated for a TOC abatement (ΔTOC in mg C L^{-1}) at a given current I (in A) and electrolyses time (t) by equation (28):

$$\%\, MCE\ = \frac{n\ F\ V\ \Delta TOC}{4.32\times10^7\ m\ I\ t} \times 100 \quad (28)$$

where n is the number of electrons consumed per organic pollutant molecule upon complete mineralization, F is the Faraday constant (96485 C mol^{-1}), V is the solution volume (in L), m stands for the number of carbon atoms of the pesticide, and 4.32×10^7 is a conversion factor aiming at units homogenization (3600 s h^{-1} × 12000 mg C mol^{-1}). The theoretical total mineralization reactions for the pesticides by electrochemical incineration are given by reactions (29) for IMC and (30) for TBZE:

$$C_9H_{10}ClN_5O_2 + 31H_2O \rightarrow 9CO_2 + Cl^- + 5NO_3^- + 72H^+ + 66e^- \quad (29)$$

$$C_9H_{16}ClN_5 + 33H_2O \rightarrow 9CO_2 + Cl^- + 5NO_3^- + 82H^+ + 76e^- \quad (30)$$

Faradaic efficiency and energy consumption

The faradaic efficiency (FE) for electrochemical nitrate removal and the energy consumption per g of nitrate (EC) (were calculated by equations (31) and (32), respectively [212]:

$$FE = \frac{nF(C_0 - C_t)V}{Q_t} = \frac{nF(C_0 - C_t)V}{It} \quad (31)$$

$$EC\ (Wh\ g^{-1}) = \frac{E_{cell}Q_t}{3600(C_0 - C_t)MV} = \frac{E_{cell}It}{3600(C_0 - C_t)MV} \quad (32)$$

where n is the global number of electrons transferred according to consecutive accounting for the complete reduction reaction of nitrate to ammonia (n = 8), F is the Faraday constant (96485 C mol^{-1}), C_0 is the initial nitrate concentration and C_t is the nitrate concentration at given time (both in mol L^{-1}), V is the solution volume (in L^{-1}), M is the nitrate molar mass (62 g mol^{-1}) and Q_t is the charge supplied at a given time (in C).

Koutecky-Levich analysis

The Koutecky-Levich (K-L) equation (33) and its derived (34) were applied to analyse the cathodic linear sweep voltammograms (LSV) recorded with an AISI DC01 mild steel custom-made RDE as WE at different rotational speeds (ω) to study nitrate electroreduction. The inverse of the cathodic measured current (I_c^{-1}) was plotted against the inverse of the rotational speed square root ($\omega^{-1/2}$) [212]

$$\frac{1}{I_c} = \frac{1}{I_k} + \frac{1}{I_l} \quad (33)$$

$$\frac{1}{I_c} = \frac{1}{nFAk_h C^*} + \frac{1}{0.62nFAD_t^{2/3}\nu^{-1/6}\omega^{1/2}C^*} \quad (34)$$

where I_k is its pure kinetic term (in the absence of mass transport), I_l is the current limited by diffusion, n is the number of electrons involved in the nitrate electroreduction reaction, A is the electrode area, D_t is the diffusion coefficient of nitrate ion, ν is the kinematic viscosity and C^* is the nitrate bulk concentration. The heterogeneous charge transfer constant (k_h) can then be obtained from the independent term of the linear regression at infinite ω, whereas n can be obtained from its slope.

Effectiveness factor and Damköhler dimensionless number

The effectiveness factor (η) is a parameter that must range between 0 and 1. It gives information about whether the regime is controlled by a charge transfer regime if its value tends to 1 or controlled by a mass transport regime if its value tends to 0. In intermediate situations, the process will be under a non-pure controlled regime, called mixed regime, with combination of mass transport and charge transfer. For a heterogeneous electroreduction process it is described by equation (35) [213]:

$$\eta = \frac{R}{R^*} = \frac{k_1 C}{k_1 C^*} = \frac{C}{C^*} \quad (35)$$

where R is the reaction rate involving the electroactive specie at a certain concentration C, whereas R^* is that of an ideal process considering the bulk concentration C^*. In equation (35), it is assumed that R is described as $dC/dt = -k_1 C$ where k_1 is the global reaction rate. This means that under steady-state conditions, the species arriving by mass transport to the electrocatalytic surface disappears according to a heterogeneous charge transfer rate constant $k_h a$, where a is the volumetric area (here, the ratio between the area A of the RCE and the solution volume V inside the reactor), thereby verifying equations (36)-(38) [51-53]:

$$k_m a(C^* - C) = k_h a C \quad (36)$$

$$C = \frac{1}{1+\frac{k_h a}{k_m a}} C^* \quad (37)$$

$$R = \eta R^* = \eta k_h a C^* \quad (38)$$

where k_m is the mass transport coefficient (m s^{-1}). The dimensionless Damköhler number (Da), which relates the intrinsic charge transfer rate to the convective mass transport, is then defined by equation (39):

$$Da = \frac{k_h a}{k_m a} \quad (39)$$

As a result, the isothermal effectiveness factor η can be expressed in terms of the Damköhler dimensionless number Da from equation (40) [213,214]:

$$\eta = \frac{1}{1+\frac{k_h a}{k_m a}} = \frac{1}{1+Da} \quad (40)$$

Furthermore, *R* can be expressed by equation (41), leading to equation (42), which relates $k_h a$, $k_m a$ and k_1.

$$R = \frac{k_h a}{1+Da} C^* = \frac{k_h a}{1+\frac{k_h a}{k_m a}} C^* = \frac{1}{\frac{1}{k_h a}+\frac{1}{k_m a}} C^* \quad (41)$$

$$k_1 = \frac{1}{\frac{1}{k_h a}+\frac{1}{k_m a}} \quad (42)$$

Sherwood, Reynolds and Schmidt dimensionless numbers and correlation

The Reynolds dimensionless number correlates the inertia forces to the viscous ones, and it is useful to describe the transport properties of a fluid in a given system. For the RCE reactor, its value is calculated by equation (43), and a value over 100 stands for a turbulent flow regime.

$$Re = \frac{Ud}{v} \quad (43)$$

where *U* is the peripheral velocity ($u = \pi \omega d$), *d* stands for the diameter of the RCE and v is the kinematic viscosity.

The Sherwood dimensionless number (*Sh*) correlates convective mass transport with pure diffusion, equation (44), whereas the Schmidt dimensionless number (*Sc*) correlates momentum diffusivity with molecular diffusion, equation (45):

$$Sh = \frac{k_m d}{D} \quad (44)$$

$$Sc = \frac{v}{D} \quad (45)$$

These parameters accomplish equation (46) [215] yielding a useful mass transport correlation under turbulent flow for further scale-up of the process:

$$Sh = \alpha Re^{\beta} Sc^{\gamma} \quad (46)$$

where α is a coefficient related to the reactor dimensions, shape of the electrodes and electrolyte properties, β is associated with the hydrodynamic regime, and γ has a characteristic value of 0.356 for the RCE reactor configuration [215–217]. The mass transport correlations must be experimentally obtained for each particular electrochemical system. However, depending on the roughness of the electrocatalytic

surface or the nature of the electroactive specie the values of the correlation may differ substantially.

3.5. Analytical methods and equipment

All the aliquots were filtered with Whatman 0.45 μm PTFE membrane filters prior to analysis.

3.5.1. Analysis of organic pollutants and by-products

Reversed-phase HPLC

A Waters 600 liquid chromatograph (LC) coupled to a Waters 996 photodiode array detector controlled with Empower® software was used for the determination of pesticide concentration and for the identification and quantification of several by-products by reversed-phase HPLC. Aliquots of 20 μL were injected into the LC upon elution.

The separation of organics for TBZE concentration evaluation over time was carried out with a Spherisorb® S5 ODS2 5 μm (150 mm × 4.6 mm (i.d.)) column at 35 ºC upon elution with a 60:40 (v/v) acetonitrile/water mixture at 1.0 mL min^{-1}. The peak for TBZE appeared at (λ = 222.9 nm and a retention time (t_R) of 7.8 min, with L.O.Q = 0.32 mg L-1 and L.O.D = 0.11 mg L-1. The peak for the main intermediate DE-TBZE at λ = 214.7 nm appeared at t_R = 4.1 min, with L.O.Q = 0.59 mg L^{-1} and L.O.D = 0.19 mg L^{-1}.

The IMC concentration was measured with a Thermo BDS Hypersil C-18 5 μm (250 mm × 4.6 mm (i.d.)) column at 35 ºC, upon elution with a 50:50 (v/v) acetonitrile/0.02 M phosphate buffer (pH 3) mixture at 1.2 mL min^{-1}. The peak for IMC appeared at (λ = 270 nm and t_R =3.2 min, with L.O.Q = 0.298 mg L^{-1} and L.O.D = 0.090 mg L^{-1}.

Ion-exclusion HPLC

The same LC was used to assess evolution of the generated carboxylic acids as final by-products by ion-exclusion HPLC with a Bio-Rad Aminex HPX 87H (300 mm × 7.8 mm (i.d.)) column at 35 ºC. The detector was set at λ = 210 and a 4 mM H_2SO_4

solution was used as mobile phase flowing at 0.6 $mLmin^{-1}$. The acids detected were oxalic (t_R = 7.3 min), oxamic (t_R = 10.3 min) and cyanuric (t_R = 12.6 min).

Gas chromatography

The stable heteroaromatic derivatives from IMC and TBZE degradation were detected by gas chromatography-mass spectrometry (GC-MS) in order to establish the degradation pathways upon electrochemical oxidation. The obtained mass spectra were compared with those reported in the NIST05 database. The organics were extracted at a specific electrolysis time with CH_2Cl_2. Organic volumes were 3×50 mL for 400 mL of the electrolyzed solution with initial concentration of 23.7 mg L^{-1} IMC and 3×15 mL for 50 mL of electrolyzed solution with initial concentration of 5 mg L^{-3} TBZE. Mild current densities were applied to detect the by-products. Upon extraction, the organic phase was dried over anhydrous Na_2SO_4, filtered and its volume evaporated under N_2 stream to be analysed by GC-MS upon re-dissolution with a small volume of about 2 mL of of CH_2Cl_2. To do this analysis, the gas chromatograph was equipped with either a polar Agilent HP-Innowax (30m × 250um × 0.25um (i.d.)) or a non-polar Teknokroma Sapiens X5-MS (30m × 250um × 0.25um (i.d.)) column. The injector worked in a splitless mode with the temperature set at 250 ºC. The temperature of the detector was set at 250 ºC or 320 ºC for the polar and non-polar column, respectively.

3.5.2. Analysis of nitrate and other ionic species

Ion chromatography

Chloride, chlorate, perchlorate, sulfate, nitrite and nitrate concentrations were determined by IC by injecting 20 µL aliquots into a Shimadzu 10Avp LC with a Shimadzu CDD 10 Avp conductivity detector equipped with a Shim-Pack IC-A1 (100 mm × 4.6 mm (i.d.)) anion column at 40 °C. The mobile phase consisted of a 2.4 mM tris(hydroxymethyl)aminomethane + 2.6 mM phthalic acid (pH 4) mixture eluted at 1.5 mL^{-1} min^{-1}. The anionic peaks were displayed at t_r of 2.9 min for chloride, 3.5 min for chlorate, 16.5 min for perchlorate, 7.6 min for sulfate, 3.2 min for nitrite and 4.6 min for nitrate.

A Perkin Elmer ion chromatograph coupled to an Adept Cecil CE4710 conductivity detector set at 25 ºC controlled by Chromera software and equipped with the

same column and mobile phase mentioned above was used in some cases to quantify nitrate concentration during the degradation electrolytic trials. The nitrate retention time was about 5.2 min.

The ammonium content was also monitored with a Shodex IC YK-421, (125 mm × 4.6 mm (i.d.)) cation column at 40 ºC and a mobile phase composed of 5.0 mM tartaric acid, 24.0 mM boric acid, 2.0 mM 2,6-pyridinedicarboxylic acid and 1.5 mM 18-crown-6 solution at a flow rate set at 1.0 mL min^{-1}.

3.5.3. Analysis of Total Organic Carbon (TOC) and Total Nitrogen (TN)

TOC measurements of the initial and electrochemically treated solutions were made on a Shimadzu TOC VCSN analyser upon injection of filtered samples after immediate withdrawal from electrolyzed solutions. An aliquot volume of 50 μL was injected into it with good reproducibility in consecutive three times. The total combustion of the sample in an oven equipped with a catalytic column at 680 ºC gave rise to the total carbon (TC). This corresponded to the sum of inorganic carbon coming from the carbonate speciation present in the aqueous samples at a given pH and organic carbon coming from the NOM in the real water matrices and from the pesticides spiked into the synthetic and the real water matrices. The mineralization of the pesticides and NOM due to EO processes was performed from the non-purgeable organic carbon (NPOC) value, which was measured with a preliminary acidic pH adjustment by the addition of two drops of concentrated sulfuric acid in order to remove all the soluble inorganic carbon by its transformation to CO_2 followed by air bubbling through the taken aliquots.

Total nitrogen (TN) was determined with the same equipment using a coupled TNM-1 module to the TOC system. The most soluble nitrogen present in the solutions was measured by transforming the nitrogen atoms from organic or inorganic N-containing species by catalytic oxidation to a measurable nitrogen gas species in the same catalytic column at 680 ºC. Both measurements were done by an IR quantification in their respective modules.

3.5.4. Colorimetric determinations

Spectrophotometric measurements for several colorimetric methods were done by means of a UV4 Unicam UV/vis spectrophotometer or a PerkinElmer Lambda 35 UV/Vis spectrophotometer.

Determination of ammonia concentration

The ammonia/ammonium concentration was determined by means of the standard phenate colorimetric method (4500-NH_3. F) [218], also called indophenol blue method. In this method, ammonium is transformed into ammonia in alkaline medium to be combined with hypochlorite to form monochloramine (NH_2Cl), which reacts with phenate to form 5-aminophenate. This species is then oxidized in the presence of nitroprusside anion, originating the blue indophenol. our stock reagents solutions of ethylenediaminetetraacetic (EDTA), alkaline phenol, nitroprusside and hypochlorite were prepared. For the measurements, 2 mL of properly diluted sample and 1 mL of phenolic, nitroprusside and hypochlorite solution were added in this specific order and mixed. The final solution showed the characteristic blue colour. The absorbance was then quantified after 60 min at $\lambda = 630$ nm where indophenol solutions showed an maximum absorbance. The main interferences for this method to determine ammonia in GW matrices are the alkaline-earth cations that precipitate as hydroxides and carbonates due to alkalinization. This is avoided by complexing them with EDTA.

Determination of active chlorine species concentration

Active chlorine species were measured by the *N*,*N*-diethyl-*p*-phenylenediamine (DPD) colorimetric method (4500-Cl. G) [218]. In this method, DPD reacts stoichiometrically with a low concentration of active chlorine species at a near-neutral buffered pH to generate the Würster dye, a magenta-coloured compound as shows **Figure 13**. The absorbance can then be quantified to determine the active chlorine concentration of a diluted sample. Moreover, a colourless imine is formed when an excess of active chlorine is in the solution.

Active chlorine species were determined by addition of 0.5 mL of phosphate buffer solution, 10 mL of properly diluted sample and after mixing, 0.5 mL of freshly prepared DPD solution were added to reach a maximum concentration of 4 mg L^{-1} of

active chlorine s. The absorbance of the sample was then measured after 2 min at λ = 515 nm by spectrophotometry. The calibration curve for this method was prepared with $KMnO_4$, being 0.891 g of it equal to 1.000 mg L^{-1} Cl_2.

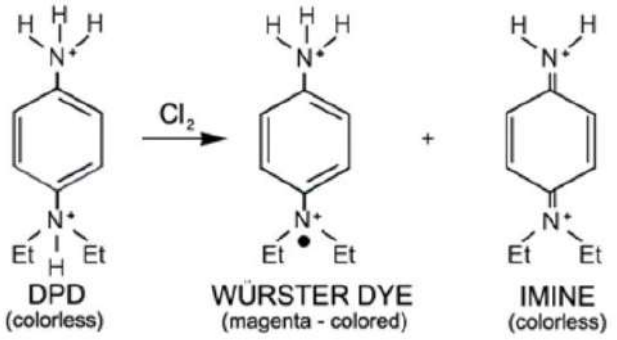

Figure 13. Determination of active chlorine by the DPD method.

Determination of dissolved iron

The determination of solubilized iron was performed using the 1,10-phenantroline method. In this colorimetric method, the ferrous iron (Fe^{2+}) reacts with 1,10-phenantroline in a buffered pH of 4 giving a pink coloured complex (see **Figure 14**).

The Fe^{2+} was measured by mixing 1 mL of properly diluted sample with 1 mL of 0.2% (v/v) 1,10-phenantroline and 1 mL of acetate / acetic acid buffer (pH ~4) , followed by dilution to 10 mL and mixing. The absorbance was then measured at λ = 510 nm. Total iron (Fe^{2+} + Fe^{3+}) concentration was determined with the same method but adding 1-2 spatula of ascorbic acid before the dilution step to reduce Fe^{3+} to Fe^{2+}. The difference between both measurements was the amount of Fe^{3+}.

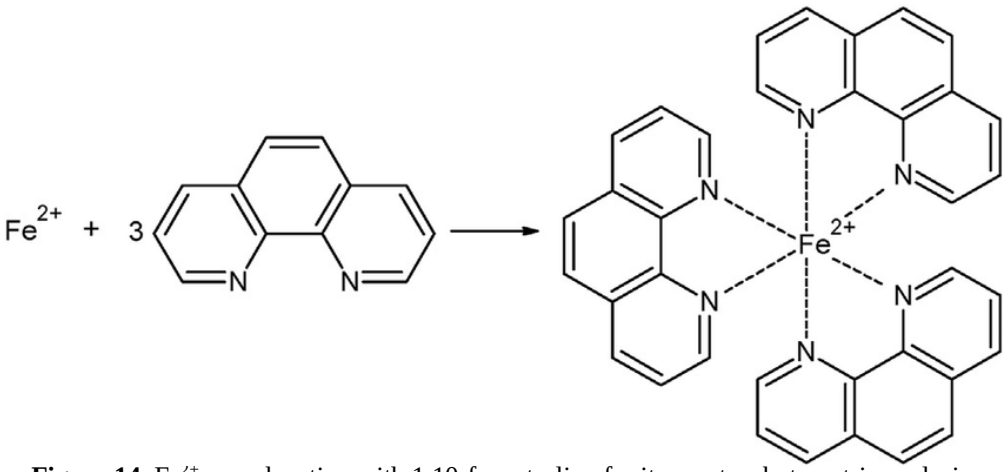

Figure 14. Fe^{2+} complexation with 1,10-fenantroline for its spectrophotometric analysis.

3.5.5. Electrochemical characterization

Linear sweep voltammetries (LSV) were performed with a Biologic SP-150 potentiostat-galvanostat controlled by EC-LAB v11.10 software or an Autolab PGSTAT30 potentiostat-galvanostat controlled by NOVA v2.0 software. Custom-made rotating disk electrodes (RDE) of AISI 1018 steel, AISI 316 stainless steel or DSA® with 4.5 mm diameter were used as working electrode (WE) with a ω set between 0 and 1000 rpm. The counter electrode (CE) was always a graphite bar and the reference electrode (RE) was either a $Hg|Hg_2SO_4|$sat. K_2SO_4 (E^o = +0.64 V vs SHE) or Ag|AgCl|KCl (3 M) (E^o = +0.21 V vs SHE).

An undivided electrochemical cell was used containing 80 or 100 mL of solutions with 0, 2, 5, 10, 20 and 40 mM KNO_3 as electroactive species and 0.50 M Na_2SO_4 as supporting electrolyte. The voltammograms were recorded starting from the open circuit potential (E_{OCP} = -1.050 V vs $Hg|Hg_2SO_4$ or E_{OCP} = -0.620 V vs Ag|AgCl), at a scan rate of 5 mV s^{-1}.

3.5.6. Hydrogen radical detection

The generation of hydrogen radical ($^{\bullet}$H), a strong reducing agent, on the electrocatalytic surface of two different steel materials as cathodes was assessed by electron paramagnetic resonance (EPR) using DMPO as a spin-trapping agent. The *in situ* scavenging of the electrogenerated $^{\bullet}$H over a suitable cathodic surface such as AISI 1018 by DMPO in the form of DMPO-$^{\bullet}$H adduct (see **Figure 15**) was carried out with 15 mL solutions in the presence and absence of 10 mM nitrate after addition of 16.90 µL of 10 mM DMPO.A a single-chamber cell (SCC) with a low oxidant power anode such as a platinum foil under continuous magnetic stirring was used. The samples were collected and placed in Eppendorf tubes and immediately frozen by contact with dry ice. They were further thawed and introduced into a quartz tube to be analysed, always after the same time period from initial sampling and thawing. The EPR spectra were recorded on a Bruker ESP300E spectrometer at room temperature, fixing the resonance frequency of 9.79 GHz, microwave power of 2 mW, modulation amplitude of 1.0 G, sweep width of 100 G (3450-3550), time constant of 40.96, sweep time of 83.97 and receiver gain of 2×10^4.

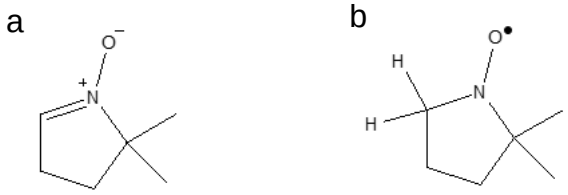

Figure 15. Molecular structure of (a) DMPO and (b) DMPO-•H adduct.

The EPR spectra from the trials with a mild steel AISI1018 steel showed the typical DMPO-•H pattern shown in **Figure 16** composed of 9 peaks with an intensity ratio of 1:1:2:1:2:1:2:1:1. The measured hyperfine coupling constant values were of a_N = 16.52 G for the nitrogen and a_H = 22.58 G for the two equivalent hydrogen nuclei, in agreement with the values determined in the literature for this adduct [219]. There was no signal for the stainless steel AISI316 when employed as cathode.

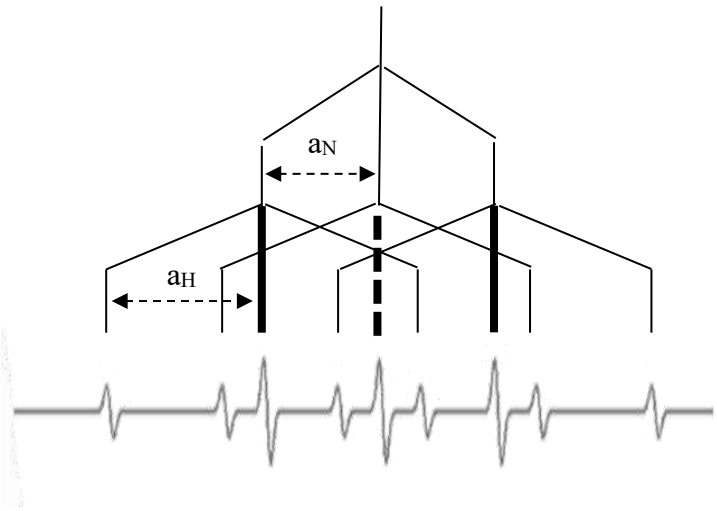

Figure 16. EPR spectrum of DMPO-•H.

3.5.7. Other analyses

The solution pH was measured with a Crison 2200 pH-meter or a HI 3221 pH/ORP/ISE meter from Hannah Instruments. The electrical conductance was measured with a Metrohm 644 conductometer using as conductivity standard previously dried KCl in 0.01 M solution with a tabulated conductivity of 1.42 mS cm^{-1}.

The content of metal ions for GW characterization was obtained by inductively coupled plasma with optical emission spectroscopy (ICP-OES) using a Perkin Elmer Optima 8300 spectrometer.

3.6. Mathematical model for CFD simulations of nitrate electroreduction

The modeling and simulation of nitrate electroreduction in a RCE reactor recreates the hydrodynamics generated by the rotation of the central electrode by solving the Reynold-averaged Navier-Stokes (RANS) equations employing the k-ε turbulent model. This hydrodynamics enhances the nitrate removal by increasing its mass transport towards the electroactive surface where it is reduced by an electrochemical process, being sensitive to electrochemical kinetic parameters such as applied potential, cathode material and composition of the solution. In order to fully describe the system by this model, the mass transport for electrochemical nitrate removal is obtained by solving the diffusion-convection equation where the distribution of the concentration of the RCE surface is related to the current and potential distribution by a wall function. Tertiary current distributions are evaluated by simultaneously solving the mass and potential equations at different current intensities and rotating speeds imposed to the RCE. The model was validated with the experimental trials for the removal of 10 mM nitrate at different currents and rotating speeds applied to the RCE cathode corroborating the simulations. In order to neglect the migration term on the model, a 0.50 M Na_2SO_4 as supporting electrolyte was used, thus lowering the nitrate transport number ($t_{NO_3^-}$) from equation (47), where λ is the ionic conductivity, below 0.01 and simplifying the overall system.

$$t_{NO_3^-} = \frac{\lambda_{NO_3^-} c_{NO_3^-}}{\sum \lambda_i c_i} \quad (47)$$

3.6.1. Electrochemical reactions

This model describes the electrochemical nitrate removal on a suitable cathode surface that shows high activity for this reaction, such as AISI 1018 mild steel. The nitrate reduction reaction (NRR) starts with the adsorption on the cathode surface with a two-electron reduction transforming the electroactive species into nitrite by reaction (8). This reaction is the rate-determining step (RDS) for this cathode material, which shows a high selectivity towards ammonia as final by-product, experimentally shown, resulting in an overall total reduction reaction with 8 electrons involved (reaction (6)). The subsequent reductions after the RDS, involving 6 electrons, take place in cascade towards ammonia.

Additionally, to the NRR, the hydrogen evolution reaction (HER) via reaction (48) takes place:

$$2H_2O + 2e^- \rightarrow H_2 + 2OH^- \qquad E^o = -0.83 \text{ V vs SHE} \qquad (48)$$

The HER reaction may take place not only as a parasitic reaction The initial step of the HER by reaction (49) consists of the generation of atomic hydrogen, also called hydrogen radical ($^\bullet$H), adsorbed on the cathode surface, which can dimerize to H_2 by reaction (50) depending on the electrocatalytic material employed.

$$H_2O + e^- \rightarrow {}^\bullet H + OH^- \qquad (49)$$

$$2{}^\bullet H \rightarrow H_2 \qquad (50)$$

This adsorbed radical has high reducing power and can act as a mediator for the electron transfer of the adsorbed nitrite reduction, generated through the 2-electron RDS and followed towards by ammonia generation through the 6-electron mechanism mentioned above. The overall 8-electron NRR then takes place with the mediation of the $^\bullet$H, whereas the termination reaction between two radicals towards H_2 by reaction (50) is a parasitic reaction.

At the anode, the OER (51) has been considered as the only reaction that takes place since the ammonia re-oxidation at its surface can be neglected because the blank trials showed no nitrate accumulation in presence of ammonia and the LSV did not display any difference in presence and absence of ammonia.

$$H_2O \rightarrow 2H^+ + 1/2O_2 + 2e^- \qquad E^o = 1.23 \text{ V vs SHE} \qquad (51)$$

The electrochemical kinetics of the NRR and HER at the cathode and OER at the anode have been solved from the mass transport equations and current and potential distribution calculations.

3.6.2. Hydrodynamics of the RCE reactor

The rotation of the central RCE in this kind of reactors favours a turbulent regime at low *Re* values ($\geq$ 100) by promoting fluid instability and generation of eddies that enhances the mass transport towards the central electrode. The hydrodynamic simulation of the water volume inside the RCE reactor resulted from the combination of the RANS equations (52) with the continuity equation (53), considering the k-ε turbulence model

[220], which relates the rate of the turbulent kinetic energy (κ) with the dissipation rate of the turbulent energy (ε), and have been widely used in the solution of CFD models dealing with RCE reactors:

$$\rho(\boldsymbol{u}\cdot\nabla\boldsymbol{u}) = -\nabla P + \nabla\cdot\left((\mu+\mu_T)(\nabla\boldsymbol{u}+(\nabla\boldsymbol{u})^T)\right) \quad (52)$$

$$\nabla\cdot\boldsymbol{u} = 0 \quad (53)$$

where $\boldsymbol{u}$ is the averaged velocity vector, P stands for the averaged pressure, μ viscosity and μ_T is the turbulent viscosity defined in equation (54) as [221]:

$$\mu_T = \rho C_\mu \frac{k^2}{\varepsilon} \quad (54)$$

$$\rho(\boldsymbol{u}\cdot\nabla)k = \nabla\cdot\left(\left(\mu+\frac{\mu_T}{\sigma_k}\right)\nabla k\right) + P_k - \rho\varepsilon \quad (55)$$

$$\rho(\boldsymbol{u}\cdot\nabla)\varepsilon = \nabla\cdot\left(\left(\mu+\frac{\mu_T}{\sigma_\varepsilon}\right)\nabla\varepsilon\right) + C_{\varepsilon1}\frac{\varepsilon}{k}P_k - C_{\varepsilon2}\rho\frac{\varepsilon^2}{k} \quad (56)$$

where k is the turbulent kinetic energy and ε is the dissipation rate of turbulent energy. P_k is an energy production term, ρ is the density of the fluid and C_μ, $C_{\varepsilon1}$, $C_{\varepsilon2}$, σ_k, σ_ε are dimensionless constants with values of 0.09, 1.44, 1.92, 1 and 1.3, respectively, given by the model.

The k-ε model describes well the region where the turbulence can be completely developed. However, it cannot properly describe the turbulence occurring on the wall near-region. The velocity of the fluid decreases exponentially when it approaches the viscous zone, the region close to the wall, where the turbulent model begins to disagree imposing the application of wall functions to obtain concordance between simulations and reality. Thanks to these functions, it is possible to know the velocity distribution on the wall immediacies, where the velocity rapidly decreases. The wall function of equation (57) has been previously employed in the modelling of electrochemical reactors with high turbulent hydrodynamics [221,222].

$$u^+ = 5.5 + \frac{1}{\kappa}lny^+ \quad (57)$$

where u^+ is the dimensionless velocity normal to the wall, κ is von Karman constant, and y^+ is the dimensionless distance to the wall ($= \rho u_\tau y/\mu$), where u_τ describes the friction velocity as $u_\tau = C_\mu^{1/4}\sqrt{k}$, and y is the distance from the wall.

In the RCE batch reactor, the motion of the fluid is attributed to the RCE rotation. To solve the Eqs. (52)-(56), the following boundary conditions are chosen:

- At the RCE walls, the rotation of the electrode is taken as a normal stress derived from the tangential velocity vector on the RCE surface, $[(\mu + \mu_T)(\nabla \cdot \boldsymbol{u} + (\nabla \cdot \boldsymbol{u})^T)]\boldsymbol{n} = -\rho \frac{u_\tau}{u^+}\boldsymbol{u}_{tang}$, where:

  $u_\tau = C_\mu^{0.25}\sqrt{\kappa}$, $\boldsymbol{u}_{tang} = \boldsymbol{u} - \frac{\boldsymbol{u}_\omega - (\boldsymbol{u}_\omega \cdot \boldsymbol{n})\boldsymbol{n}}{\|\boldsymbol{u}_\omega - (\boldsymbol{u}_\omega \cdot \boldsymbol{n})\boldsymbol{n}\|}\|\boldsymbol{u}_\omega\|$ and $\boldsymbol{u}_\omega$ is the velocity vector perpendicular to the rotating axis of the RCE as a smooth sliding wall.
- At the fluid open surface, a decreasing shear stress is set to restrain the free movement of the fluid, $[(\mu + \mu_T)(\nabla \cdot \boldsymbol{u} + (\nabla \cdot \boldsymbol{u})^T)]\boldsymbol{n} = 0$, $u \cdot \boldsymbol{n} = 0$, since the RCE reactor has a configuration in which the fluid mass is open to the atmosphere.
- In all the remaining walls, a dimensionless velocity u^+ at a y^+ distance according to the employed wall function by equation (57) has been used.

3.6.3. Mass balance

To neglect the influence of the electric field and the migration term from the Nernst-Planck equation, a high enough concentration of supporting electrolyte to lower the nitrate transport number below 0.01 was used in the experimental trials, simplifying the mass transport to a diffusion-convection mass transport-based system by equation (58). So, under turbulent regime conditions, the nitrate transport towards the RCE electroactive surface where it is consumed, can be assessed by the solution of time-dependent diffusion-convection equation considering a turbulent diffusion coefficient (D_T):

$$\frac{\partial C_{NO_3^-}}{\partial t} = \nabla \cdot \left(D_{NO_3^-} + D_T\right)\nabla C_{NO_3^-} - \boldsymbol{u} \cdot \nabla C_{NO_3^-} \qquad (58)$$

where $C_{NO_3^-}$ is the bulk concentration of nitrate, $\boldsymbol{u}$ is the velocity vector obtained by the solution of Eqs. (52)-(57), and $D_{NO_3^-}$ and D_T refer to the regular diffusion and turbulent

diffusion coefficients, respectively. D_{T} can be calculated with the turbulent Schmidt number ($Sc_{\mathrm{T}} = \mu_{\mathrm{T}}/\rho D_{\mathrm{T}}$).

To obtain the value of $\mathrm{Sc_T}$, the Kays-Crawford model of equation (59) is used:

$$Sc_T = \left\{\frac{1}{2Sc_{T\infty}} + \frac{0.3\mu_T}{\sqrt{Sc_{T\infty}}\rho D} - \left(\frac{0.3\mu_T}{\rho D}\right)^2\left[1 - exp\left(-\frac{\rho D}{0.3\mu_T\sqrt{Sc_{T\infty}}}\right)\right]\right\}^{-1} \quad (59)$$

where $Sc_{\mathrm{T}\infty}$ = 0.85. Equation (59) was included during the simulation of the diffusion-convection equation (58) to obtain D_{T} considering the local values of Sc_{T} and μ_{T}.

The concentration on the electrode surface is not zero and the turbulent phenomena affecting the mass transport near the wall cannot be neglected. The Launder-Spalding model is then used to describe the nitrate concentration at the near-wall region through a dimensionless concentration (C^+) at a certain y^+ by equations (60) and (61) to link the impact of the turbulence of the viscous region with the turbulent zone.

$$C^+_{NO_3^-} = Sc_T\left(\frac{1}{k} ln\, y^+ + 5.5 + P_c\right) \quad (60)$$

$$C^+_{NO_3^-} = \frac{\left(C_{NO_3^-,w} - C_{NO_3^-}\right)C_\mu^{0.25}\kappa^{0.5}}{N_{NO_3^-,w}} \quad (61)$$

where $\mathrm{C^+_{NO_3^-}}$ is the dimensionless nitrate concentration, $\mathrm{C_{NO_3^-,w}}$ is the nitrate concentration in the region near the wall, $\mathrm{N_{NO_3^-,w}}$ is the nitrate flux towards the RCE electroactive surface where it is being reduced, and $\mathrm{P_c}$ is a term described by an empiric relation from equation (62) that describes the mass transfer resistance between the viscous and turbulent regions.

$$P_c = A\left[\left(\frac{Sc}{Sc_T}\right)^{0.75} - 1\right] \quad (62)$$

where A is an empirical constant fitted to adjust the experimental data. The mass transport wall function was employed to describe the rate of nitrate transport towards the RCE.

The corresponding boundary conditions to solve equation (58) are:

- At the RCE walls, the nitrate flux is expressed as $-D_{\mathrm{NO_3^-}}\frac{\partial C_{\mathrm{NO_3^-}}}{\partial \xi} = N_{\mathrm{NO_3^-}} = \frac{j_{\mathrm{NO_3^-},0}\left(\frac{C_{\mathrm{NO_3^-,w}}}{C_{\mathrm{NO_3^-}}}\right)\exp\left(\frac{\eta_{\mathrm{NO_3^-}}}{b_{\mathrm{NO_3^-}}}\right)}{nF}$, where $\mathrm{j_{NO_3^-,0}}$ is the exchange current density for nitrate

reduction, $b_{NO_3^-}$ is the Tafel slope for nitrate reduction, $\eta_{NO_3^-}$ is the nitrate reduction overpotential, n is the number of electrons involved in the electrochemical reduction of nitrate (n = 8) and F stands for Faraday's constant (96485 C mol^{-1}). The electrokinetic value of $j_{NO_3^-,0}$ and the Tafel slope were obtained by LSV using the same nitrate and supporting electrolyte concentrations.

- In all the remaining walls, a zero-flux condition is chosen since the conversion of ammonia as the main by-product to nitrate by re-oxidation at the anodic surface was discarded by specifically designed experimental trials.

The initial condition to solve the time-dependent equation (58) is stated as:

- At t = 0, $C_{NO_3^-} = C_{NO_3^-}(t = 0)$, being the initial nitrate concentration.

3.6.4. Tertiary current distribution

In each electrochemical process, the reactions are conditioned by the current density and electric potential at the electrode coming from the potential or current constant imposition. The distribution of the electric potential in the solution is described by the Laplace equation (63):

$$\nabla\varphi^2 = 0 \tag{63}$$

where φ is the electric potential in the dissolution, while the local current density on the electrode surface can be obtained from the Ohm's law of ionic conductance by equation (64):

$$j = -\sigma\nabla\varphi \tag{64}$$

where j is the current density vector, and σ is the ionic conductivity of the dissolution.

The boundary conditions proposed to solve the potential and current equations are:

- At the RCE, the overall cathodic current density considers the electrochemical nitrate reduction as well as the HER, $-\sigma\frac{\partial\varphi}{\partial\xi} = j_c = j_{NO_3^-,0}\left(\frac{C_{NO_3^-,w}}{C_{NO_3^-}}\right)\exp\left(\frac{\eta_{NO_3^-}}{b_{NO_3^-}}\right) + j_{HER,0}\exp\left(\frac{\eta_{HER}}{b_{HER}}\right)$, where $j_{HER,0}$, b_{HER}, and η_{HER} are the exchange current density, Tafel slope and overpotential attributed to HER, respectively. Both reactions

assume that the nitrate concentration depletes the applied current density to favour the HER.

- At the anode, a Tafel kinetic is assumed for the oxygen promotion as counter-reaction defined as $-\sigma \frac{\partial \varphi}{\partial \xi} = j_a = j_{OER,0} \exp\left(\frac{\eta_{OER}}{b_{OER}}\right)$, where $j_{OER,0}$, b_{OER}, and η_{OER} are the exchange current density, Tafel slope and overpotential attributed to OER, respectively.
- In the remaining insulating walls, a zero-flux condition is set ($-\sigma \frac{\partial \varphi}{\partial \xi} = 0$).

The overpotential is defined as $\eta = \varphi_M - \varphi - \varphi_{OCP}$, where φ_M is the electrode potential and φ_{OCP} stands as the open circuit potential.

The concentration overpotential $\left(\frac{C_{NO_3^-,w}}{C_{NO_3^-}}\right)$ is present at the cathodic boundary conditions related to the RCE in equations (58) and (63) since the mass transport and potential distribution are interdependent. The dependency of φ on the nitrate concentration near the wall in both state equations compels the simultaneous solution of the mass transport and potential and current distribution models. Both parameters are related by a flux condition defined by Faraday Law on the working electrode.

3.6.5. Computational method for CFD simulations

The RCE reactor described above was modelled for the electrochemical nitrate removal at the rotating electrode. The finite element method was used to solve numerically the state equations proposed in this model using the commercial software COMSOL Multiphysics® 6.0 with two Intel® Xeon ™ 2.30 GHz processors, having a 96 GB RAM memory and a 64-bit operating system. The hydrodynamics was solved in stationary state with an iterative GMRES method with a relative tolerance of 10^{-3}. Hydrodynamics simulations lasted around 180 min, whereas the time-dependent model was solved in 120 min for a total simulation time of approximately 300 min.

CHAPTER 4

RESULTS AND DISCUSSION

CHAPTER 4. Results and discussion

This chapter summarizes the most relevant results obtained from the research carried out in this Thesis, in good accordance with the following scientific articles that have been published or submitted:

1. **R. Oriol**, D. Clematis, E. Brillas, J.L. Cortina, M. Panizza, I. Sirés*, Groundwater treatment using a solid polymer electrolyte cell with mesh electrodes.
ChemElectroChem 6 (2019) 1235-1243.
https://www.doi.org/10.1002/celc.201801906

2. **R. Oriol**, M.P. Bernícola, E. Brillas, P.L. Cabot, I. Sirés*, Paired electro-oxidation of insecticide imidacloprid and electrodenitrification in simulated and real water matrices.
Electrochimica Acta 317 (2019) 753-765.
https://www.doi.org/10.1016/j.electacta.2019.05.002

3. **R. Oriol**, E. Brillas, P.L. Cabot, J.L. Cortina, I. Sirés*, Paired electrochemical removal of nitrate and terbuthylazine pesticide from groundwater using mesh electrodes.
Electrochimica Acta 383 (2021) 138354
https://www.doi.org/10.1016/j.electacta.2021.138354

4. **R. Oriol**, J.L. Nava*, E. Brillas, I. Sirés*, Characterization of mass transport regime in a rotating cylinder electrode reactor used for electrochemical denitrification.
Journal of Environmental and Chemical Engineering 10 (2022) 108839.
https://www.doi.org/10.1016/j.jece.2022.108839

5. **R. Oriol**, J.L. Nava, E. Brillas, O. Cornejo*, I. Sirés*, Modeling hydrodynamics, mass transport and current distribution for nitrate removal in a rotating cylinder electrode reactor.
Chemical Engineering Journal
Submitted; Manuscript No. CEJ-D-23-13591.

The main findings and conclusions from each article are detailed below, accompanied with an electronic copy of the manuscripts.

4.1. Groundwater treatment using a solid polymer electrolyte cell with mesh electrodes

This work was focused on the removal of the neonicotinoid pesticide IMC, spiked into different low-conductivity water matrices, by EO with a BDD mesh anode employing an SPE cell equipped with a Nafion® N117 membrane sandwiched between the electrodes. The natural GW was softened before electrolysis using recovered industrial waste. Total removal of the pesticide was achieved with mineralization degrees of 87% within 240 min. Physisorbed hydroxyl radical at the BDD surface and active chlorine species in the bulk were the main oxidants. Comparative studies using a synthetic solution that mimicked GW served to assess the interference of NOM in the GW electrochemical treatment. Trials carried out in ultrapure water showed the conversion of the initial nitrogen and chlorine atoms present in the pesticide molecule into nitrate and chloride ions, being the latter subsequently oxidized to toxic chlorate and perchlorate.

The removal of IMC (see details in subsection 1.1.5), at 1.2 – 59.2 mg L^{-1}, was studied in a 500 mL reactor by EO in the SPE system. The ultimate goal was to validate the possibility of working with a low conductivity water matrix such as GW, showing lower cell voltage values (key parameter to evaluate the viability of electrochemical technologies) than those obtained with the same water matrix through conventional systems. In this case, BDD and DSA® mesh electrodes were used as anode and cathode, respectively, in the form of a sandwich separated by a Nafion membrane that provided sufficient conductivity. First assays were carried out with raw GW contained spiked IMC, at pH 6.9 and 25 ºC. However, the cell voltage rapidly increased over time due the passivation of the cathode by a grey jelly film compromising the reproducibility of the trials. To prevent the fouling of the cathode, the actual GW was decalcified via ion exchange using sodium-loaded NaP1 zeolites. These zeolites, generated by industrial incineration waste recovery and further activated with NaOH, were used for the ion exchange of the divalent cations present in the matrix. The content of these ions was drastically reduced, being replaced by Na^+, as can be observed from the physicochemical characteristics of the GW, before and after the treatment by zeolites (**Table 1** in the related paper). This pre-treatment allowed performing the electrolysis of the actual water matrix eluding the blockage of the cathode surface by calcium and magnesium carbonates and

hydroxides. The kinetics of IMC removal were determined by evaluating its concentration by HPLC, and the degrees of mineralization by measuring the solution TOC.

The degradation rate of the pesticide was studied in different aqueous matrices: ultrapure water, actual GW decalcified with the valorised material described above, and a synthetic aqueous matrix that mimicked the anion content of the actual GW. All of them were adjusted to pH 10 (i.e., the pH resulting from zeolite pre-treatment) to make a reliable comparison between them. **Figure 1a** and **b** show the change of IMC concentration over time and the related pseudo-first-order kinetics when applying 0.5 A for 240 min. Total disappearance was achieved in ultrapure water, simulated water and softened GW at 150, 180 and 240 min, respectively. The faster removal of the pesticide in the ultrapure and simulated matrices can be explained by the absence of NOM, which competes for the physisorbed hydroxyl radical species (reaction (2)) generated at the anode surface, as well as for the active chlorine species present in the bulk (reactions (13-15)). **Figure 2a** and **b** depict the TOC abatement and the corresponding MCE values with the electrolysis time for these experiments. The mineralization rates decreased in the sequence: ultrapure matrix > real matrix > synthetic matrix, resulting in TOC reductions of 87%, 82 and 75%, respectively. In the absence of chloride ions in the matrix, the only oxidant in the ultrapure water matrix electrolysis was the physisorbed hydroxyl radical, whereas in the simulated and decalcified GW this radical was scavenged by the chloride anion. The higher mineralization achieved for the decalcified water matrix can be explained by the concomitant mineralization of the NOM. The experiment carried out in ultrapure water allowed studying the fate of the chlorine and nitrogen atoms of the IMC molecule. As can be seen in **Figure 3**, the nitrogen was mainly converted into nitrate, and the chlorinated oxyanions were progressively oxidized to chlorate and perchlorate anions.

The influence of different applied current values (0.1; 0.25; 0.50; 1.00; 1.50 A) on the IMC degradation and its kinetics is shown in **Figure 4**, and on dissolved TOC and MCE appears in **Figure 5**. By increasing the current from 0.10 to 1.50 A, a gradual increase in the removal rate can be observed, achieving the complete abatement of 23.7 mg L^{-1} of IMC in a progressively shorter time from 240 min to 120 min, respectively. It was quite similar for 1.00 and 1.50 A, which demonstrates that the maximum degradation was already attained under the applied stirring. The values obtained for mineralization were 65%, 69%, 75%, 80% and 86% at 0.1, 0.25, 0.50, 1.00 and 1.50 A, respectively.

The improved pesticide removal when increasing the applied current can be explained by the higher amount of physisorbed hydroxyl radicals produced at the BDD surface. The percentage of TOC abatement was higher as the current increased because a larger amount of by-products was mineralized. Higher MCE values were then calculated with lower pesticide contents, although they decayed over time due to the consumption of initial organic by-products that yielded more refractory ones (**Figure 5b**). The most efficient processes were then achieved at lower current. The concentration of active chlorine electrogenerated by chloride oxidation at the anode was evaluated over time at different applied current as well. It was accumulated at shorter times as the current was increased, as can be seen on **Figure 6**, owing to its transformation into chlorate and perchlorate.

Electrolyses with different concentrations of spiked pesticide (1.2; 4.8; 11.8; 23.7; 59.2 mg L^{-1}) were carried out. **Figure 7a** shows a quicker removal at lower pesticide concentration because of the faster attack of similar oxidant amounts with lower organic matter content. The k_1-values determined as the slopes of **Figure 7b** and the percentage of TOC removed shown in **Figure 7c** increased progressively upon decrease of the pesticide concentration.

Finally, tartaric acid was detected and quantified by HPLC as a stable oxidation by-product, whereas the primary derivatives 6-chloro-nicotinonitrile and 6-chloro-pyridyne-3-carbaldehyde were detected by GC-.MS.

ChemPubSoc Europe

DOI: 10.1002/celc.201801906

CHEMELECTROCHEM Articles

Groundwater Treatment using a Solid Polymer Electrolyte Cell with Mesh Electrodes

Roger Oriol,[a] Davide Clematis,[b] Enric Brillas,[a] José L. Cortina,[c, d] Marco Panizza,*[b] and Ignasi Sirés*[a]

This article reports the high performance of a solid polymer electrolyte cell, equipped with a Nafion® N117 membrane packed between a Nb/boron-doped diamond (Nb/BDD) mesh anode and a Ti/RuO_2 mesh cathode, to degrade the insecticide imidacloprid spiked at 1.2–59.2 mg L^{-1} into low conductivity groundwater by electrochemical oxidation. The natural water matrix was first softened using valorized industrial waste in the form of zeolite as reactive sorbent. Total removal of the insecticide, always obeying pseudo-first-order kinetics, and maximum mineralization degrees of 70%–87% were achieved, with energy consumption of 26.4 ± 1.6 kWh m^{-3}. Active chlorine in the bulk and •OH at the BDD surface were the main oxidants. Comparative studies using simulated water with analogous anions content revealed that the natural organic matter interfered in the groundwater treatment. Trials carried out in ultrapure water showed the primary conversion of the initial N and Cl atoms of imidacloprid to NO_3^- and Cl^- ions, being the latter anion eventually transformed into ClO_3^- and ClO_4^- ions. 6-Chloro-nicotinonitrile, 6-chloro-pyridine-3-carbaldehyde, and tartaric acid were identified as oxidation products.

1. Introduction

Over the last decade, great progress has been made to address the removal of recalcitrant organic pollutants from urban and industrial wastewater thanks to the development of more suitable technologies, in particular the so-called electrochemical advanced oxidation processes (EAOPs).[1–4] These are considered environmentally friendly treatments that are easy to operate and maintain, also being safe, readily scalable and relatively cost-effective, typically involving the use of ambient pressure and temperature. Electrochemical oxidation (EO),[1,5–8] electro-Fenton (EF),[2,9–13] and photoelectro-Fenton (PEF),[2,14–16] are ubiquitous EAOPs for effective wastewater treatment in which organics pollutants are mainly destroyed by the strong oxidant hydroxyl radical (•OH). This radical is generated in situ at the anode surface and/or in the bulk from Fenton's reaction, being assisted by the photocatalytic action of UV radiation in PEF. The simplest method is EO in inert electrolytes (e.g., sulfate, nitrate, perchlorate), since organic molecules are only attacked by the species generated at the anode. In the absence of Cl^- ion, the non-active boron-doped diamond (BDD) thin films are the best anodes for EO. The H_2O oxidation at the BDD surface via Equation (1) produces larger amounts of physisorbed •OH, denoted as BDD(•OH), as compared to other anodes.[1,6,17–19] In contrast, the presence of Cl^- ion in the reaction medium complicates the situation because it can be easily oxidized at the BDD anode, giving rise to competing oxidizing agents like active chlorine species (Cl_2, HClO, and/or ClO^-, depending on pH) from Equations (2)–(4).[20–23] HClO and ClO^- can then evolve to other oxychlorine ions like ClO_2^-, ClO_3^-, and ClO_4^- from Equations (5)–(7), with a conversion degree that depends on the initial Cl^- and organics concentration, the applied current and the flow rate.

$$BDD + H_2O \rightarrow BDD(^{\bullet}OH) + H^+ + e^- \quad (1)$$

$$2Cl^- \rightarrow Cl_{2(aq)} + 2e^- \quad (2)$$

$$Cl_{2(aq)} + H_2O \rightarrow HClO + Cl^- + H^+ \quad (3)$$

$$HClO \leftrightarrows ClO^- + H^+ \qquad pK_a = 7.56 \quad (4)$$

$$HClO + H_2O \rightarrow ClO_2^- + 3H^+ + 2e^- \quad (5)$$

$$ClO_2^- + H_2O \rightarrow ClO_3^- + 2H^+ + 2e^- \quad (6)$$

$$ClO_3^- + H_2O \rightarrow ClO_4^- + 2H^+ + 2e^- \quad (7)$$

The EO treatment is typically applied over a long period of time. The major impact on the energy consumption of this process is exerted by the solution conductivity. High values of this parameter are usually recommended, because it is directly correlated with a lower cell voltage and hence, with a smaller

[a] R. Oriol, Prof. E. Brillas, Prof. I. Sirés
Departament de Química Física
Facultat de Química
Universitat de Barcelona
Martí i Franquès 1–11, 08028 Barcelona, Spain
E-mail: i.sires@ub.edu
[b] D. Clematis, Prof. M. Panizza
Dipartimento di Ingegneria civile, chimica e ambientale
Università degli Studi di Genova
Fiera del Mare, Piazzale Kennedy 1, Pad. D-16129 Genova, Italy
E-mail: marco.panizza@unige.it
[c] Prof. J. L. Cortina
Chemical Engineering Department
Escola d'Enginyeria de Barcelona Est (EEBE)
Universitat Politècnica de Catalunya (UPC)-BarcelonaTECH
Eduard Maristany 10–14, Campus Diagonal-Besòs, 08930 Barcelona, Spain
[d] Prof. J. L. Cortina
Barcelona Research Center for Multiscale Science and Engineering
Campus Diagonal-Besòs, 08930 Barcelona, Spain

Supporting information for this article is available on the WWW under https://doi.org/10.1002/celc.201801906

An invited contribution to a Special Collection dedicated to Trends in Synthetic Diamond for Electrochemical Applications

energy requirement. Unfortunately, natural water, urban wastewater, and many industrial and hospital effluents present very low conductivities, which may prevent the direct application of EO for their decontamination. This is the main reason to explain the scarce expansion of EO as a technology for natural water treatment. The most common approach to overcome this limitation is the addition of supporting electrolyte, typically Na_2SO_4 and/or NaCl. Less explored alternatives have considered the direct application of EO to raw low conductivity aqueous matrices using microfluidic reactors,[24,25] or solid polymer electrolyte (SPE) cells.[26–32] An SPE cell presents a sandwich configuration, i.e., anode/polymer electrolyte/cathode, which ensures an appropriate electron flow when immersed in a low conductivity medium. The cost of the membrane and its potential fouling, have been described as possible drawbacks for this cell.[32] SPE cells have been mainly employed in the electrochemical production of ozone.[26–28] They have also offered good performances for water treatment, although only synthetic solutions prepared with deionized water have been tested so far.[29–32] For example, the successful mineralization of benzyl alcohol using a BDD/Nafion®/BDD cell,[29] and the dyes Safranin T[31] and Crystal Violet[32] using a BDD/Nafion®/RuO_2 cell has been described. However, no previous studies have reported the use of SPE cells to decontaminate natural wastewater.

An important parameter to keep under strict control for the electrochemical decontamination of groundwater is water hardness, since calcium and magnesium ions can induce cathode scaling upon precipitation in the form of hydroxides and carbonates. In order to avoid the electrode passivation, some kind of softening pre-treatment is required.[33] Within the context of circular economy, the valorization of industrial waste to yield added-value products is of major interest nowadays. Reactive powdered sorbents like Na^+- and K^+ -loaded synthetic zeolites can be prepared from coal combustion fly ash.[34] Further, they can be added to the natural water matrix to trap calcium and magnesium cations, prior to subsequent electrochemical treatment.

Imidacloprid ($C_9H_{10}ClN_5O_2$, $M = 255.66\ g\,mol^{-1}$) is a widely used neonicotinoid insecticide in agriculture. It is classified as moderately toxic by the USEPA, with tolerance from $0.02\ m\,kg^{-1}$ in eggs to $3.0\ mg\,kg^{-1}$ in hops. Its ingestion by animals can produce pre-eminently hepatotoxicity, along with immunotoxic, nephrotoxic, and oxidative stress effects.[35] Imidacloprid is highly resistant to degradation and, consequently, it has been detected at concentrations up to $52\ \mu g\,L^{-1}$ in agricultural water[36] and $0.36\ \mu g\,L^{-1}$ in urban wastewater.[37] The destruction of this pollutant was feasible using ultrasounds combined with UV radiation and H_2O_2,[38] as well as EAOPs like EO[39,40] and EF.[41–43] In these electrochemical treatments, large mineralization (>80%) was attained from highly conductive synthetic solutions containing pure water, sulfate and 0.1–10 mM imidacloprid, using anodes of BDD, PbO_2, and mixed metal oxides of Ru, Ir, and Ti (i.e., dimensionally stable anodes, DSA®). However, the use of low conductivity media and natural water has not been described yet.

This work reports the destruction of imidacloprid, spiked into groundwater, by EO using an SPE cell composed of a Nafion® membrane in contact with a Nb/BDD mesh anode and a Ti/RuO_2 mesh cathode. Mesh electrodes were employed to ensure the H^+ passage through the membrane. Comparative experiments were performed with simulated water whose anions content was similar to that of groundwater, in the absence of natural organic matter (NOM). The effect of applied current and pesticide concentration was examined. The action of active chlorine was assessed from a comparative treatment in pure water. The transformation of the N atoms and the fate of Cl^- released or present in the medium were analyzed, and the main oxidation products were identified.

2. Results and Discussion

2.1 Comparative Imidacloprid Treatment in Different Aqueous Matrices

First assays were carried out by electrolyzing 500 mL of $23.7\ mg\,L^{-1}$ imidacloprid (i.e., $10.0\ mg\,C\,L^{-1}$ total organic carbon (TOC)) spiked into the raw groundwater at pH 6.9, using the SPE cell at 0.50 A and 25 °C. However, a gradual increase of cell voltage with time was observed, also resulting in a slower pesticide abatement and a lack of reproducibility upon successive trials. These findings were attributed to the passivation of the cathode, which became coated with a grey jelly film due to the precipitation of hydroxides and carbonates of alkaline earth metal ions (Ca^{2+} and Mg^{2+}) present in the matrix. On the other hand, preliminary assays allowed discarding any adsorption of the insecticide on the electrodes or membrane. To prevent the cathode fouling, the raw groundwater was softened using a Na^+-loaded zeolite, as explained in the Experimental Section. Table 1 collects the physicochemical characteristics of the raw and pre-treated groundwater. Upon softening, an increase of pH up to 9.8, conductivity up to $2.95\ mS\,cm^{-1}$, and Na^+ concentration up to $780\ mg\,L^{-1}$ was found, whereas Ca^{2+} and Mg^{2+} concentrations were drastically

Table 1. Physicochemical characteristics of the groundwater used as real water matrix, before and after softening with zeolite.

Parameter (units)	Raw groundwater	Softened groundwater
pH	6.9 ± 0.1	9.8 ± 0.1
Conductivity ($mS\,cm^{-1}$)	1.87 ± 0.07	2.95 ± 0.12
TC ($mg\,C\,L^{-1}$)	67.2 ± 1.0	143.2 ± 1.6
TOC ($mg\,C\,L^{-1}$)	2.6 ± 0.1	2.8 ± 0.1
NO_3^- ($mg\,L^{-1}$)	107 ± 3	107 ± 3
NO_2^- ($mg\,L^{-1}$)	n.d.[a]	n.d.[a]
Cl^- ($mg\,L^{-1}$)	458 ± 20	473 ± 19
SO_4^{2-} ($mg\,L^{-1}$)	90 ± 4	110 ± 4
Ca^{2+} ($mg\,L^{-1}$)	240 ± 10	12.3 ± 0.5
Mg^{2+} ($mg\,L^{-1}$)	55 ± 2	2.3 ± 0.1
K^+ ($mg\,L^{-1}$)	4.5 ± 0.2	60 ± 3
Na^+ ($mg\,L^{-1}$)	80 ± 2	780 ± 31
NH_4^+ ($mg\,L^{-1}$)	n.d.[a]	n.d.[a]

[a] Not detected.

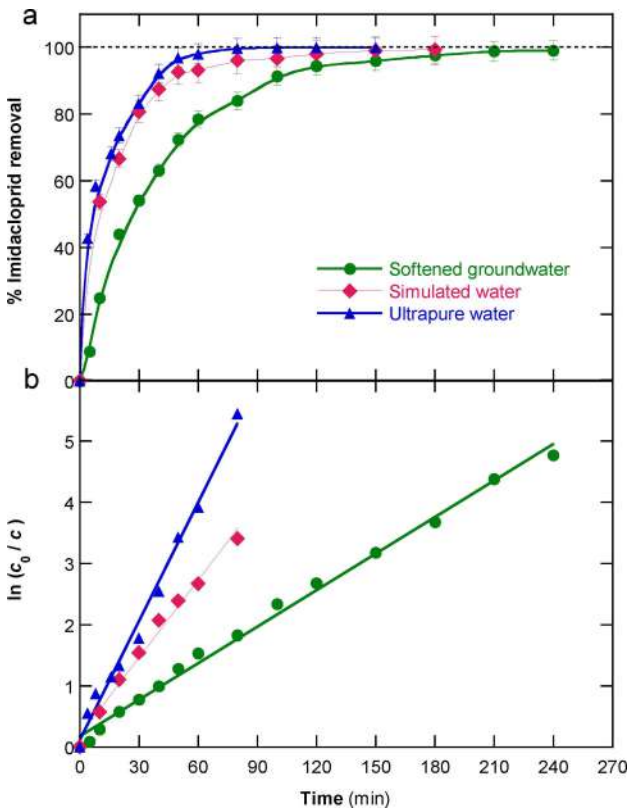

Figure 1. a) Percentage of imidacloprid removal and b) pseudo-first-order kinetic analysis of each decay trend at increasing electrolysis time for the electrochemical oxidation of 500 mL of 23.7 mg L^{-1} of the insecticide in several aqueous matrices at pH 9.8 and 25 °C using an SPE cell with a Nb/BDD mesh anode and a Ti/RuO_2 mesh cathode at 0.50 A.

reduced down to 12.3 and 2.3 mg L^{-1}, respectively. The rise in Na^+ content, with much higher molar conductivity than replaced Ca^{2+} and Mg^{2+}, explains the greater conductivity of the softened groundwater. The content of significant anions such as NO_3^-, Cl^-, and SO_4^{2-} remained practically constant during the pre-treatment. The softened groundwater was employed in all further EO treatments focused on real matrix since a stable current and cell voltage were obtained, without any additional fouling. For comparative degradation studies, two synthetic aqueous matrices of very low conductivity were also employed: a simulated water matrix with anions composition similar to that of the softened groundwater, and an ultrapure water matrix (see Experimental Section). The pH of these two matrices was adjusted to 9.8 to mimic that of the pre-treated groundwater. All the experiments were run at this pH, aiming at simplifying and making less expensive the conditioning process in future applications of this technology.

Figure 1a depicts the change of the percentage of imidacloprid removal with electrolysis time for the EO treatment of solutions containing 23.7 mg L^{-1} insecticide in the three matrices at 0.50 A for 240 min. Total disappearance was achieved after 150 min in ultrapure water, 180 min in simulated water, and 240 min in groundwater. This trend is indicative of a quicker attack of BDD(•OH), originated from Equation (1), as single oxidant over the organic molecule in the former matrix, as compared to its combined attack with active chlorine, formed from Equations (2)–(4), in the two latter matrices. It is also worth mentioning that the scavenging effect of the inorganic carbon, present in such alkaline media, causing some BDD(•OH) consumption that can diminish the oxidation power of the EO process.[23] The faster insecticide removal in the simulated water matrix compared to that obtained in groundwater can be explained by the simultaneous destruction of the NOM contained in the real sample, thus reducing the amount of available oxidants to attack the insecticide.

The excellent linear trend lines found from the pseudo-first-order kinetic analysis of the concentration decays in the above trials are presented in Figure 1b. From their slopes, decreasing apparent rate constants (k_1) of $(6.4\pm0.3)\times10^{-2}$ min^{-1} ($R^2=0.990$) in ultrapure water, $(4.2\pm0.2)\times10^{-2}$ min^{-1} ($R^2=0.986$) in simulated water, and $(2.0\pm0.1)\times10^{-2}$ min^{-1} ($R^2=0.994$) in groundwater were determined. This behavior suggests the reaction of imidacloprid with a constant amount of BDD(•OH) and/or active chlorine in each case.

Figure 2a shows the percentage of TOC removal vs. electrolysis time for the assays of Figure 1. Again, the most powerful EO treatment was achieved in ultrapure water, giving rise to 88% mineralization, whereas the oxidation ability of the SPE cell was inverted for the other two matrices as compared to the insecticide removal. A greater mineralization rate can be observed in Figure 2a for the trial in groundwater (12.8 mg C L^{-1} of initial TOC), attaining 82% mineralization, as compared to that in simulated water (10.0 mg C L^{-1} of initial TOC) where only

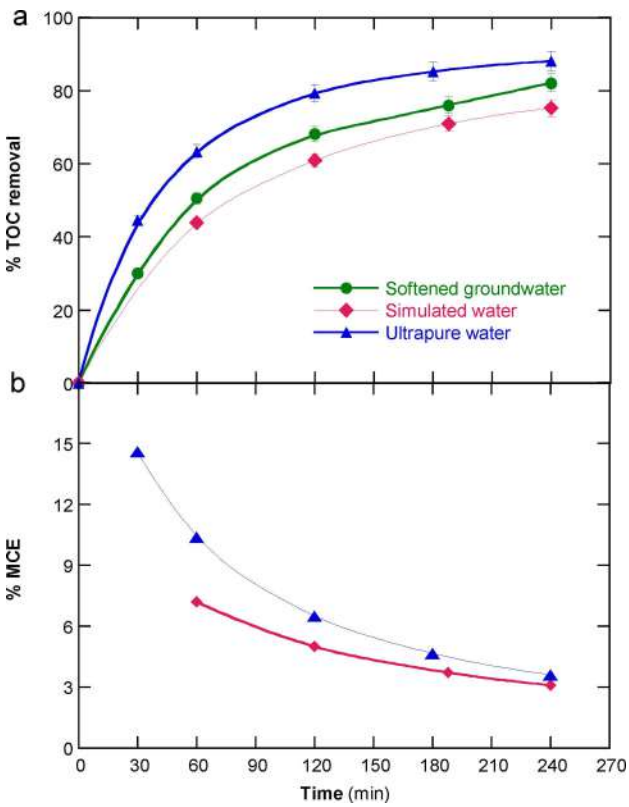

Figure 2. Change of the percentage of a) TOC removal and b) mineralization current efficiency with electrolysis time for the assays of Figure 1.

75% mineralization was reached. This accounts for a larger destruction of a quantity of about 2.8 mg C L^{-1} TOC in groundwater, which means that the NOM content was completely mineralized in the SPE cell (see Table 1) under the action of BDD(•OH) and active chlorine. On the other hand, the superior mineralization of the insecticide in ultrapure water is due to the action of BDD(•OH) as single oxidant, in contrast to the simultaneous attack of active chlorine over the organics in the two chlorinated matrices, yielding chloroderivatives that are more recalcitrant and hence, less prone to transformation into CO_2.[3,4,22,23] It should be noted that the solution pH did not vary when the degradation was studied in groundwater, whereas it decayed from 9.8 to 7.5 in the case of simulated water. In contrast, this pH change was found after 150 min of treatment in ultrapure water, whereupon it continuously dropped down to pH near 5. These results suggest the formation of acidic products, whose effect was much less evident in groundwater probably because of the buffering capacity conferred by the large amount of HCO_3^- and/or CO_3^{2-} (see Table 1).

During the above mineralization assay in ultrapure water, the fate of the N and Cl atoms of imidacloprid was assessed. The results obtained are shown in Figure 3a and b, respectively. Figure 3a highlights that the initial N was pre-eminently mineralized to NO_3^- ion, although its content gradually increased to attain only 27.1% conversion. In contrast, the conversion of N to NO_2^- ion was very low, dropping from 1.1% at 30 min to 0.3% at 240 min because it became oxidized to NO_3^- ion as the solution pH decreased. A small content of NH_4^+ ion was also accumulated, with a maximum final conversion of 3.8%. At the end of the EO treatment with 88% mineralization, a small proportion of 31.0% of initial N was released as nitrogenated ions. This can be explained by the loss of volatile nitrogenated products, probably N_2, N_xO_y, and chloramines, as typically reported for other organics.[4,22,23] Figure 3b highlights that the Cl atom of the insecticide was initially released as Cl^- ion, attaining a maximal of 32.0% at 60 min, whereupon it decreased dramatically down to a final value of 9.7%. This decay was due to its oxidation to active chlorine (Cl_2/HClO/ClO^-) from Equations (2)–(4), but such species were not detected since they were partially oxidized to ClO_3^- and ClO_4^- ions via Equations (5)–(7), reaching final conversions of 7.1% and 20.6%, respectively. Since only a 37.4% of the initial Cl was detected in the form of chloride and oxychlorine ions, one can infer that most of the active chlorine reacted either with organics to form chloro-organics or with NH_4^+ ion to form chloramines.[20–23] However, the amount of lost chlorine was so small (0.06 mM as maximal) that, in practice, in this matrix imidacloprid and its oxidation products were more rapidly oxidized and to much larger extent by BDD(•OH), giving rise to the quickest insecticide and TOC decays as compared to those in the two chlorinated matrices, as shown in Figures 1a and 2a. On the other hand, the final concentration of the above species after the EO treatment in simulated water and groundwater were also quantified. In the case of nitrogenated ions, neither NO_2^- nor NH_4^+ ions were detected, whereas the initial 107 ± 3 mg L^{-1} of NO_3^- ion rose up to 125 ± 5 mg L^{-1}, meaning that its surplus (18 mg L^{-1}) came from the initial N of imidacloprid (6.49 mg L^{-1}). This represents a conversion of 62.6% into this ion, much superior to 27.1% found in ultrapure water, suggesting that the pathway originating NO_3^- is favored in the chlorinated matrices. SI Table S1 confirms the oxidative transformation expected for the Cl contained in both chlorinated matrices (i.e., Cl of the insecticide + Cl^- in the medium). So, in both cases, the Cl^- concentration initially accumulated was dramatically reduced, being transformed into active chlorine that was further oxidized to ClO_3^- ion and, to a smaller proportion, to ClO_4^- ion. Note that the production of ClO_3^- and ClO_4^- ions is likely dependent on the applied current, diminishing as current decreases.[3] Moreover, active chlorine reacts with organics to yield, in many cases, chloroderivatives that release Cl^- ion when they became mineralized.[2–4] A simple mass balance of the data of Table S1 reveals that < 2% of initial Cl was lost from each medium, probably due to the release of volatile chloramines causing that the small NH_4^+ content expected from the initial N of imidacloprid (see Figure 3a) was not detected.

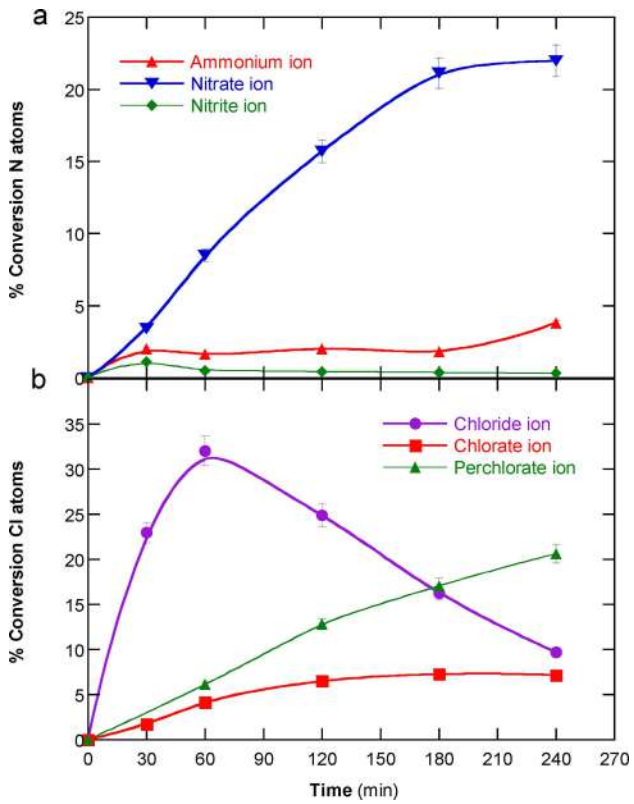

Figure 3. Evolution of a) nitrogenated and b) chloride and oxychlorine ions percentages during the experiment shown in Figure 2 carried out in ultrapure water as aqueous matrix.

From the aforementioned findings, the mineralization reaction of imidacloprid involves the formation of CO_2, Cl^- as primary ion and NO_3^-, as shown in Equation (8), with a number of consumed electrons $n = 66$:

$$C_9H_{10}ClN_5O_2 + 31H_2O \rightarrow 9CO_2 + Cl^- + 5NO_3^- + 72H^+ + 66e^- \quad (8)$$

On this basis, the percentage of mineralization current efficiency (MCE) for a TOC decay (ΔTOC, in mg C L^{-1}) in a given assay at current I (A) and time t (h) was estimated from Equation (9):[2,3]

$$\%\ \mathbf{MCE} = \frac{n\ F\ V\ \Delta\mathbf{TOC}}{4.32 \times 10^7\ m\ I\ t}\ 100 \quad (9)$$

where F is the Faraday constant, V is the solution volume (L), 4.32×10^7 is a factor for units homogenization (s mg C h^{-1} mol^{-1}), and m is the number of carbon atoms of the insecticide.

Figure 2b shows the MCE values calculated for the EO experiments in ultrapure and simulated water, which did not contain NOM, depicted in Figure 2a. According to Equation (9), greater ΔTOC yields higher MCE and, for this reason, the current efficiency was greater for the process using ultrapure water, decaying from 14.6% at 30 min to a final value of 3.6%. The same profile can be observed in the simulated water, where the MCE value dropped from 7.2% at 30 min to 3.1% at 240 min. The progressive decrease of MCE can be ascribed to the loss of organic matter, along with the formation of more refractory products that impede the achievement of total mineralization of the insecticide.[1,2]

2.2 Imidacloprid Treatment in Simulated Water

The influence of the applied current on the oxidation ability of EO to remove imidacloprid in simulated water using the SPE cell was assessed because this parameter determines the amount of generated oxidizing agents as well as the resulting cell voltage, which is of paramount importance in low conductivity media. To do this, 500 mL of 23.7 mg L^{-1} of the insecticide (10.0 mg C L^{-1} of TOC) in this matrix at pH 9.8 and 25 °C were treated at a constant current between 0.10 and 1.50 A for 240 min. Figure 4a illustrates a rapid and continuous removal of imidacloprid in all cases, whose rate is enhanced as the applied current is increased. Total removal was reached at shorter times of 240, 210, 180, and 120 min at 0.10, 0.25, 0.50, and 1.00 A, respectively. Similar degradation rates with disappearance at the same time can be observed at 1.00 and 1.50 A, being slightly quicker than the degradation at 0.50 A. This means that the process attained the maximum degradation power. The enhancement of the insecticide decay at higher current can be associated with the concomitant acceleration of all electrode reactions. Greater amounts of BDD(•OH) from Equation (1) and active chlorine from Equations (2)–(4) are then produced, allowing a faster attack over the target organic pollutant.

The imidacloprid concentration decay in the above trials always obeyed a pseudo-first-order kinetics, as shown in Figure 4b. SI Table S2 shows that the k_1-values obtained from this analysis gradually increased from $(2.4\pm0.1)\times10^{-2}$ min^{-1} at 0.10 A to $(6.5\pm0.2)\times10^{-2}$ min^{-1} at 1.50 A. The analogous k_1-

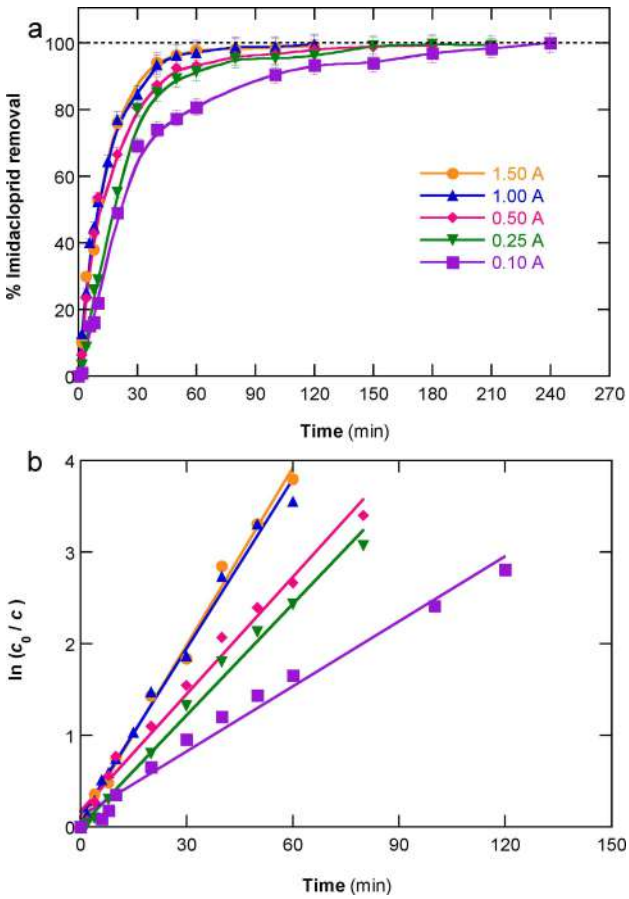

Figure 4. Effect of applied current on the a) percentage of imidacloprid removal and the b) pseudo-first-order kinetic analysis of each decay trend vs. electrolysis time for the electrochemical oxidation of 500 mL of 23.7 mg L^{-1} of the insecticide in simulated water at pH 9.8 and 25 °C using an SPE cell with a Nb/BDD mesh anode and a Ti/RuO_2 mesh cathode.

value determined for the two latter currents confirms the limitation of the degradation ability of the electrolytic setup from 1.00 A, at least for the removal of this pesticide. The pseudo-first-order reaction found at each current can be related to the attack of a constant, but different, quantity of BDD(•OH) and active chlorine over the insecticide molecules, despite the simultaneous destruction of its oxidation products, as will be discussed below.

The variation of the percentage of TOC removal with electrolysis time during the above experiments is depicted in Figure 5a. A progressively larger mineralization as the electrolyses were prolonged can be seen in all cases, showing a higher rate as current was increased. After 240 min of EO treatment, TOC was reduced by 65%, 69%, 75%, 80%, and 86% at 0.10, 0.25, 0.50, 1.00, and 1.50 A, respectively. This tendency is analogous to that described for imidacloprid removal, meaning that the rise in concentration of generated oxidants was able to destroy more rapidly all the organics present in the medium, not just the parent compound. Note that the TOC removal reached at 1.50 A was clearly higher than that at 1.00 A, which differs from the similar degradation profile of the insecticide at both current values. This points to consider that the mineraliza-

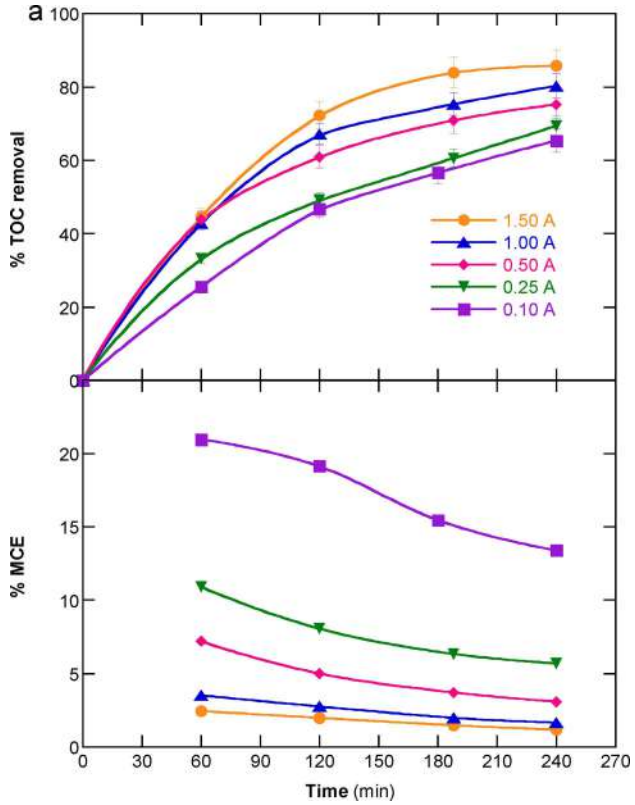

Figure 5. Variation of the percentage of a) TOC removal and b) mineralization current efficiency with electrolysis time for the trials of Figure 4.

tion power of the EO process in the SPE cell was not really limited at such high current. This suggests that the excess of generated oxidants at 1.50 A were actually able to destroy preferentially some oxidation products that were less recalcitrant than the pesticide.

The percentage of MCE calculated from Equation (9) at each time for the trials of Figure 5a is depicted in Figure 5b. In contrast to the greater mineralization achieved at higher current, a progressive decrease of MCE can be observed. This is not surprising because a high increase of *I* in the denominator of Equation (9) involves a much lower MCE. So, the greatest MCE values were determined at 0.10 A, decreasing from 20.9% at 60 min to 13.4% at 240 min as a result of the loss of organic matter and the generation of more recalcitrant products, as pointed out above. This informs about a relative loss of the oxidation power of the EO process, because an increasing amount of oxidizing agents are wasted when current increases and hence, a much lower relative proportion of oxidants is available to attack the organics, decreasing the MCE value. In the case of BDD($^{\bullet}$OH), the main waste reaction is its oxidation to O_2 from Equation (10).[1] Other reactions are the dimerization to yield H_2O_2 from Equation (11), and the reaction between the two latter species to yield the weak oxidant hydroperoxyl radical ($HO_2^{\bullet}$) from Equation (12).[3,22]

$$2BDD(^{\bullet}OH) \rightarrow 2BDD + O_2 + 2H^+ + 2e^- ZS > \quad (10)$$

$$2BDD(^{\bullet}OH) \rightarrow 2BDD + H_2O_2 \quad (11)$$

$$BDD(^{\bullet}OH) + H_2O_2 \rightarrow BDD + HO_2^{\bullet} + H_2O \quad (12)$$

The waste reactions of active chlorine include its consecutive oxidation to ClO_2^-, ClO_3^-, and ClO_4^- ions from Equations (5)–(7), as experimentally confirmed for the simulated water during EO (see Table S1). Figure 6 evidences a greater

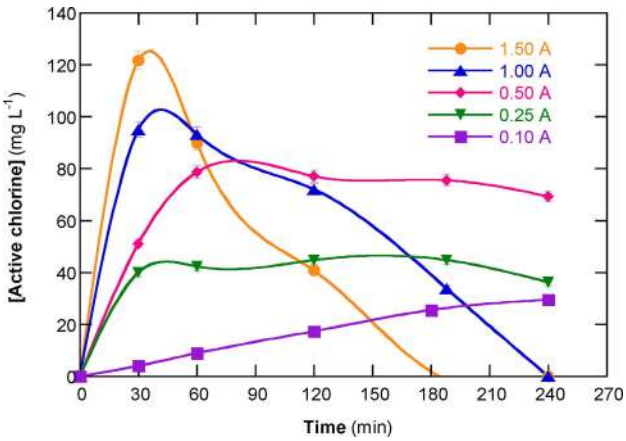

Figure 6. Time course of the concentration of active chlorine generated during the assays of Figure 4 and 5.

initial production of active chlorine as current was increased, attaining maximum concentrations of 29.5, 44.8, 78.6, 94.9, and 121.7 mg L^{-1} after 30–60 min. However, a decay of the accumulated active chlorine concentration can be observed at longer electrolysis time, to larger extent as the current rose, except at 0.10 A. This decrease was slow at 0.25 and 0.50 A, whereas complete disappearance of active chlorine species occurred after 240 min at 1.00 A and 180 min at 1.50 A. These findings are indicative of the initially higher production of active chlorine by the acceleration of Cl^- oxidation from Equation (2) at higher current, which enhanced imidacloprid destruction, but also of its greater destruction from Equations (5)–(7), thus decreasing its relative content and MCE. Therefore, the use of lower current favors the accumulation of a lower quantity of undesirable oxychlorine ions, although at the expense of a slower degradation and lower mineralization ability.

2.3 Detection of Oxidation Products

The oxidation products originated after 30 min of EO treatment of 23.7 mg L^{-1} imidacloprid at 0.50 A were identified by gas chromatography-mass spectrometry (GC-MS). Two stable heteroaromatic intermediates, namely 6-chloro-nicotinonitrile (*m/z* 140 (^{37}Cl)/138 (^{35}Cl)) and its derivative 6-chloro-pyridine-3-carbaldehyde (*m/z* 142 (^{37}Cl)/140 (^{35}Cl)), were identified. The former product is originated from the cleavage of the imidazole ring of the parent molecule, which is subsequently oxidized with transformation of the nitrile group into a carbaldehyde one. These products differ from 6-chloronicotinic acid, 6-

chloronicotinaldehyde, and 6-hydroxynicotinic acid identified by the same technique when imidacloprid was treated in sulfate medium by EO with a Pt or BDD anode and EF with the same anodes and a carbon felt cathode.[42]

Operating with 23.7 mg L^{-1} of the insecticide at 0.50 A, the feasible generation of final short-chain linear aliphatic formed from the cleavage of the pyridine and imidazole moieties of imidacloprid during the EO treatment in simulated water as well as in groundwater, was evaluated by ion-exclusion HPLC.[40] In both media, traces of oxalic and formic acids, which are directly transformed into CO_2,[2–4] were found, suggesting that they are oxidized as they are formed. Only large contents of tartaric acid were detected. SI Figure S1 illustrates that this acid was released rapidly at the beginning of the treatment, attaining 3.2 mg L^{-1} at 40 min in simulated water and 5.1 mg L^{-1} at 20 min in groundwater. At longer time, it decreased progressively to disappear at 120 min in the former matrix and to be reduced down to 0.6 mg L^{-1} at 240 in the latter one. This suggests that the contribution of final carboxylic acids to the residual TOC in both media (see Figure 2a) is insignificant, as expected if the undetected final organics products are even more recalcitrant than those ones.

2.4 Electrochemical Oxidation Treatment in Softened Groundwater

The oxidation ability of EO using the SPE cell was assessed within a large range of insecticide concentrations, from 1.2 to 59.2 mg L^{-1}, spiked into softened groundwater. Lower concentrations were assayed but no accurate results could be obtained. Figure 7a highlights that overall removal of imidacloprid was reached after 210–240 min of electrolysis, regardless of its initial concentration. Note that, in a pure electrolyte, a gradual decrease in rate of pollutant removal is typically observed because of the presence of a larger organic load under the action of similar amounts of generated oxidants. However, this trend is not observed in Figure 7a, since the degradation rate decreased from 1.2 to 4.8 mg L^{-1}, whereupon gradually rose up to 59.2 mg L^{-1}. This is corroborated from the pseudo-first-order kinetic analysis depicted in Figure 7b. A fluctuating k_1-value was determined, varying between $(2.1 \pm 0.1) \times 10^{-2}$ min^{-1} at 1.2 mg L^{-1} and $(2.5 \pm 0.2) \times 10^{-2}$ min^{-1} at 59.2 mg L^{-1}, as can be seen in SI Table S2. This anomalous behavior can be related to the simultaneous oxidation of the NOM contained in the matrix, which consumes part of the generated BDD($^{\bullet}$OH) and active chlorine. Up to 4.8 mg L^{-1}, it seems that the NOM interference is very significant and largely reduces the insecticide removal, whereas at higher content, the attack of the oxidants over imidacloprid became predominant and its destruction was gradually enhanced. These results allow concluding that the EO process is very efficient to remove organics from pre-treated groundwater, despite the negative influence of NOM on the degradation rate, especially at small organic loads.

Figure 7c evidences the NOM interference when evaluating the percentage of TOC decay of the above solutions. Only accurate TOC measurements were possible for pesticide contents $\geq$11.8 mg L^{-1} (7.8 mg C L^{-1} of initial TOC). At this concentration, an exponential profile can be observed in Figure 7c, meaning that imidacloprid mineralization was progressively accelerated as NOM was converted into CO_2, attaining 70% TOC reduction. This effect was less evident at 23.7 and 59.2 mg L^{-1} of insecticide, corresponding to initial TOC of 12.8 and 27.8 mg C L^{-1}, due to the smaller proportion of NOM and thus, TOC was reduced by 82% and 87%, respectively. This confirms again the high oxidation power of the electrolytic system to destroy imidacloprid and its oxidation products. In these trials, the cell voltage (E_{cell}) remained very stable, ca. 6.6 $\pm$ 0.4 V, which corresponded to a low energy consumption (= E_{cell}

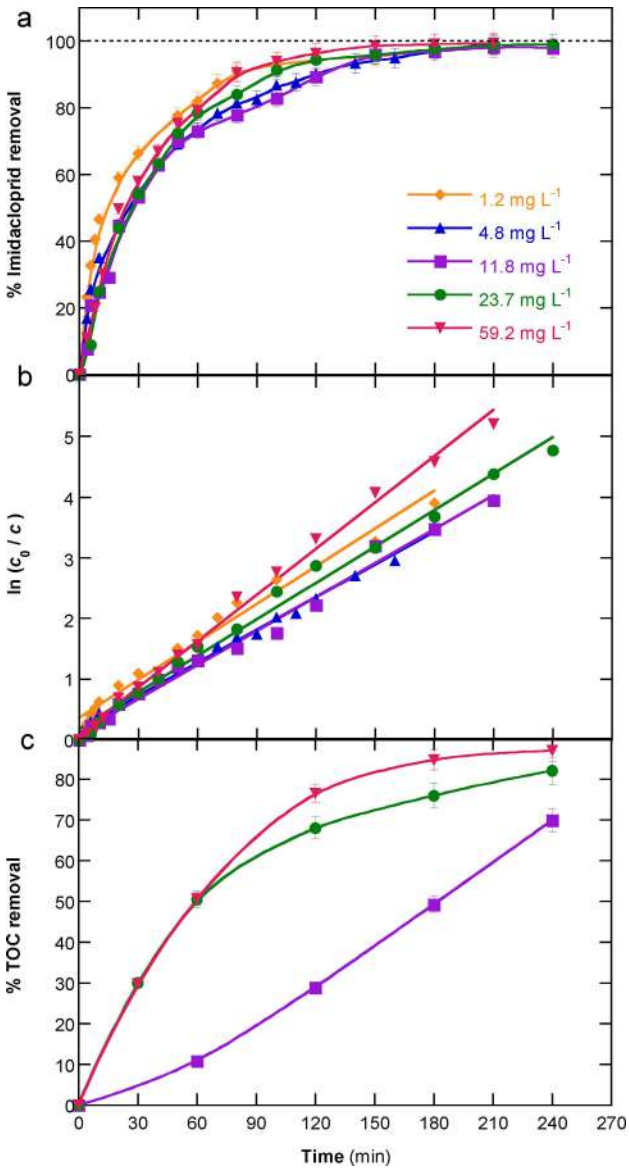

Figure 7. Effect of insecticide concentration on the variation of the a) percentage of imidacloprid removal, b) pseudo-first-order decay kinetics, and c) percentage of TOC removal with time for the electrochemical oxidation of 500 mL of the insecticide spiked into softened wastewater at pH 9.8 and 25 °C using an SPE cell with a Nb/BDD mesh anode and a Ti/RuO_2 mesh cathode at 0.50 A.

I t V^{-1}) of 26.4 ± 1.6 kWh m^{-3}, being very appealing for future scale-up of EO technology with SPE cell.

3. Conclusions

It has been shown that the use of zeolites obtained from valorized industrial waste ensures sufficient groundwater softening, further allowing its effective electrochemical decontamination. Imidacloprid concentrations between 1.2 and 59.2 mg L^{-1}, spiked into pre-treated groundwater at pH 9.8, were degraded at a similar rate until 100% removal was reached by EO using an SPE cell with mesh electrodes at 0.50 A. High mineralization degrees up to 87% were achieved, with energy consumptions as low as 26.4 ± 1.6 kWh m^{-3}. Comparative studies in simulated water revealed a quicker removal of the target pollutant, but with slower mineralization, due to the absence of NOM. Organics were destroyed by BDD(•OH) at the anode surface and active chlorine formed in the bulk. The greater production of both oxidants as the applied current was increased from 0.10 to 1.50 A accounted for by the quicker degradation and mineralization, in concomitance with a progressive decay in MCE. Analogous trials using ultrapure water without any dissolved electrolyte showed a quicker destruction of all organics due to their efficient oxidation by BDD(•OH). It was found that the initial N atoms were mainly as NO_3^- ion, with only minor accumulation of NO_2^- and NH_4^+ ions. The initial Cl was transformed into Cl^- ion, which was further transformed into ClO_3^- and ClO_4^- ions. All the imidacloprid decays obeyed a pseudo-first-order kinetics. 6-Chloro-nicotinonitrile, 6-chloro-pyridine-3-carbaldehyde, and tartaric acid were detected as stable oxidation products. This work demonstrates the feasibility of electrochemical groundwater treatment with BDD anode, although low current should be applied to minimize the formation of undesirable oxychlorine ions.

Experimental Section

Analytical standard imidacloprid (*N*-{1-[(6-Chloro-3-pyridyl)methyl]-4,5-dihydroimidazol-2-yl}nitramide, PESTANAL®) was purchased from Sigma-Aldrich. Analytical grade H_2SO_4 (95–98%) and NaOH (98–100%) were purchased from Panreac. The salts used for the preparation of the simulated water were: Na_2SO_4 (99.9%) from BDH PROLABO®, KNO_3 (98%) from Panreac and NaCl (99%) from Panreac, all of analytical grade. Carboxylic acids and other chemicals were of either analytical or HPLC grade provided by Merck, Fluka, and Probus. Synthetic and analytical solutions were prepared with Milli-Q water (resistivity > 18.2 MΩ cm).

Three different aqueous matrices were employed:

(i) A real groundwater sample, which was obtained from a water well in an agricultural area near Barcelona (Spain). Upon collection, the raw sample was preserved at 4 °C in a refrigerator. Table 1 shows its main characteristics: circumneutral pH, low conductivity, large amount of inorganic carbon (i.e., HCO_3^- and CO_3^{2-}), as well as NO_3^-, Cl^-, and SO_4^{2-} ions, and alkaline earth metal ions (Ca^{2+} and Mg^{2+}). Before the EO treatments in the SPE cells, the groundwater sample was conveniently softened by adding 20 g L^{-1} of a Na^+-zeolite (NaP1-NA), synthesized by a hydrothermal method from coal combustion fly ash (CFA).[44] The properties of this material have been well characterized in earlier work.[45] Softening was completed upon vigorous magnetic stirring at 1100 rpm for 24 h, at room temperature. Decalcified samples were finally obtained after vacuum filtration using 0.22 μm cellulose acetate filters from Frisenette. Analysis of these samples (Table 1) revealed a drastic reduction of the alkaline earth metal ions content, with concomitant accumulation of the alkali metal ions (Na^+ in particular). This enhanced the solution conductivity and, even more significant, caused the alkalization of the groundwater to reach pH 9.8. Solutions with this initial pH were always employed in the EO assays.

(ii) Simulated water mimicking the anions content of the softened groundwater. It was prepared with Milli-Q water and contained 1.70 mM KNO_3, 12.52 mM NaCl, and 0.92 mM Na_2SO_4. The pH was adjusted to 9.8 with 1 M NaOH, yielding a conductivity of about 1.8 mS cm^{-1}.

(iii) Ultrapure (i.e., Milli-Q) water adjusted to pH 9.8 with 1 M NaOH.

An open, cylindrical glass tank, jacketed to circulate thermostated water from a water bath at 25 °C, was used to keep 500 mL of solution under stirring with a magnetic stirrer at 1100 rpm. It became operative when the SPE cell, i.e., the anode/membrane/cathode sandwich, was immersed in it. The cell was composed of mesh electrodes of 3.5 cm (width) × 7.5 cm (height). The thickness was 0.90 and 0.20 mm for Nb/BDD and Ti/RuO_2, respectively, yielding approximate surface areas of 34 and 21 cm^2. Their separation was 0.15 mm, which corresponded to the thickness of the Nafion® N117 ion exchange membrane. The anode was a BDD thin film (3500 ppm of boron/carbon ratio) of 1.5 mm thickness deposited onto a Nb mesh, purchased from Condias. The cathode was a Ti/RuO_2 mesh provided by De Nora Industries. More information about the characteristics of the SPE cell is given in previous work.[31,32] All the electrolytic assays were performed at constant current using an EG&G Princeton Applied Research 273 A potentiostat/galvanostat, whereas the cell voltage was measured on a Demestres 601BR digital multimeter.

The solution pH was monitored with a Crison 2200 pH-meter, whereas a Metrohm 644 conductometer was employed for the conductance measurement. The *N*,*N*-diethyl-*p*-phenylenediamine colorimetric method was utilized to determine the active chlorine content, using a Shimadzu 1800 UV/Vis spectrophotometer set at λ = 515 nm.[46] For all the analyses in matrices containing chloride ion, a small volume of thiosulfate solution was added to the aliquots just after withdrawal from the reactor in order to neutralize the remaining active chlorine, thus stopping the degradation process. All the aliquots were filtered with 0.45 μm PTFE membrane filters from Whatman before further analysis.

The imidacloprid concentration was monitored by reversed-phase high-performance liquid chromatography (HPLC). This analysis was carried out by injecting 20 μL aliquots into a Waters 600 LC fitted with a Thermo BDS Hypersil C-18 5 μm (250 mm × 4.6 mm (i.d.)) column at 35 °C. It was coupled to a Waters 996 photodiode array detector selected at λ = 270 nm and controlled by Millennium-321 software. The mobile phase was a 50:50 (v/v) acetonitrile/0.02 M phosphate buffer mixture, at pH 3, which was eluted at 1.2 mL min^{-1}. The chromatograms displayed a well-defined peak for the pesticide at retention time (t_r) of 3.2 min, with L.O.D. = 0.090 mg L^{-1} and L.O.Q. = 0.298 mg L^{-1}. The same equipment, with a Bio-Rad Aminex HPX 87H (300 mm × 7.8 mm (i.d.)) column at 35 °C, the photodiode array selected at λ = 210 nm, and a 4 mM H_2SO_4 solution at 0.6 mL min^{-1} as mobile phase was employed to detect and quantify the produced carboxylic acids by ion-exclusion HPLC. Tartaric acid exhibited a well-defined peak at t_r = 8.4 min.

The solution TOC was obtained with a Shimadzu VCSN TOC analyzer by adding 50 μL aliquots into it and using the non-purgeable organic carbon (NPOC) method, with L.O.D. = 0.211 mg L^{-1} and L.O.Q. = 0.708 mg L^{-1}, showing ±1% accuracy. NH_4^+, NO_3^-, NO_2^-, Cl^-, SO_4^{2-}, ClO_3^-, and ClO_4^- concentrations were determined as reported elsewhere.[22,47] Alkaline earth metal and alkali metal ions in the raw and softened groundwater were measured by inductively coupled plasma with optical emission spectroscopy (ICP-OES) using a Perkin Elmer Optima 8300 spectrometer.

All the assays were performed at least in duplicate and average values with error bars within a 95% confidence interval are given.

Heteroaromatic products formed after 30 min of EO treatment of 500 mL of a 23.7 mg L^{-1} imidacloprid solution in the simulated matrix at 0.50 A were detected by GC-MS and identified using the NIST05 database. Organics were extracted from the treated solution with CH_2Cl_2 (6×15 mL) and the resulting organic sample was dried with anhydrous Na_2SO_4, filtered, and its volume reduced to about 2 mL under N_2 stream for analysis. The GC-MS procedure used is analogous to that detailed in earlier work.[47]

Acknowledgements

The authors thank the financial support from project CTQ2016-78616-R (AEI/FEDER, EU). R. Oriol acknowledges the FPI grant awarded by MINECO (Spain).

Conflict of Interest

The authors declare no conflict of interest.

Keywords: electrochemical oxidation · groundwater treatment · imidacloprid · solid polymer electrolyte · water softening

[1] M. Panizza, G. Cerisola, *Chem. Rev.* **2009**, *109*, 6541–6569.
[2] E. Brillas, I. Sirés, M. A. Oturan, *Chem. Rev.* **2009**, *109*, 6570–6631.
[3] I. Sirés, E. Brillas, M. A. Oturan, M. A. Rodrigo, M. Panizza, *Environ. Sci. Pollut. Res.* **2014**, *21*, 8336–8367.
[4] C. A. Martínez-Huitle, M. A. Rodrigo, I. Sirés, O. Scialdone, *Chem. Rev.* **2015**, *115*, 13362–13407.
[5] M. S. Çelebi, N. Oturan, H. Zazou, M. Hamdani, M. A. Oturan, *Sep. Purif. Technol.* **2015**, *156*, 996–1002.
[6] M. Panizza, D. Clematis, G. Cerisola, *J. Environ. Chem. Eng.* **2016**, *4*, 2692–2697.
[7] L. Labiadh, A. Barbucci, M. P. Carpanese, A. Gadri, S. Ammar, M. Panizza, *J. Solid State Electrochem.* **2017**, *21*, 2167–2175.
[8] S. Lanzalaco, I. Sirés, A. Galia, M. A. Sabatino, C. Dispenza, O. Scialdone, *J. Appl. Electrochem.* **2018**, *48*, 1343–1352.
[9] M. Panizza, M. A. Oturan, *Electrochim. Acta* **2011**, *56*, 7084–7087.
[10] A. Özcan, Y. Sahin, M. A. Oturan, *Water Res.* **2013**, *47*, 1470–1479.
[11] A. R. F. Pipi, A. R. De Andrade, E. Brillas, I. Sirés, *Sep. Purif. Technol.* **2014**, *132*, 674–683.
[12] H. Olvera-Vargas, N. Oturan, M .A. Oturan, E. Brillas, *Sep. Purif. Technol.* **2015**, *146*, 127–135.
[13] S. Lanzalaco, I. Sirés, M. A. Sabatino, C. Dispenza, O. Scialdone, A. Galia, *Electrochim. Acta* **2017**, *246*, 812–822.
[14] J. R. Steter, E. Brillas, I. Sirés, *Electrochim. Acta* **2016**, *222*, 1464–1474.
[15] D. R. V. Guelfi, F. Gozzi, I. Sirés, E. Brillas, A. Machulek Jr., S. C. de Oliveira, *Environ. Sci. Pollut. Res.* **2017**, *24*, 6083–6095.
[16] A. Thiam, I. Sirés, R. Salazar, E. Brillas, *J. Environ. Manage.* **2018**, *224*, 340–349.
[17] A. Anglada, A. Urtiaga, I. Ortiz, D. Mantzavinos, E. Diamadopoulos, *Water Res.* **2011**, *45*, 828–838.
[18] O. Scialdone, A. Galia, S. Randazzo, *Chem. Eng. J.* **2011**, *174*, 266–274.
[19] G. Coria, I. Sirés, E. Brillas, J. L. Nava, *Chem. Eng. J.* **2016**, *304*, 817–825.
[20] M. Mascia, A. Vacca, A. M. Polcaro, S. Palmas, J. R. Ruiz, A. Da Pozzo, *J. Hazard. Mater.* **2010**, *174*, 314–322.
[21] A. Thiam, E. Brillas, F. Centellas, P. L. Cabot, I. Sirés, *Electrochim. Acta* **2015**, *173*, 523–533.
[22] A. Thiam, I. Sirés, J. A. Garrido, R. M. Rodríguez, E. Brillas, *Sep. Purif. Technol.* **2015**, *140*, 43–52.
[23] C. Ridruejo, C. Salazar, P. L. Cabot, F. Centellas, E. Brillas, I. Sirés, *Chem. Eng. J.* **2017**, *326*, 811–819.
[24] O. Scialdone, E. Corrado, A. Galia, I. Sirés, *Electrochim. Acta.* **2014**, *132*, 15–24.
[25] P. Ma, H. Ma, S. Sabatino, A. Galia, O. Scialdone, *Chem. Eng. J.* **2018**, *336*, 133–140.
[26] K. Onda, T. Ohba, H. Kusunoki, S. Takezawa, D. Sunakawa, T. Araki, *J. Electrochem. Soc.* **2005**, *152*, D177–D183.
[27] Y. Honda, T. A. Ivandini, T. Watanabe, K. Murata, Y. Einaga, *Diamond Relat. Mater.* **2013**, *40*, 7–11.
[28] P. A. Christensen, T. Yonar, K. Zakaria, *Ozone Sci. Eng.* **2013**, *35*, 149–167.
[29] A. Kraft, M. Stadelmann, M. Wünsche, M. Blaschke, *Electrochem. Commun.* **2006**, *8*, 155–158.
[30] K. Zakaria, P. A. Christensen, *Electrochim. Acta* **2014**,*135*, 11–18.
[31] D. Clematis, G. Cerisola, M. Panizza, *Electrochem. Commun.* **2017**, *75*, 21–24.
[32] N. Klidi, D. Clematis, M. P. Carpanese, A. Gadri, S. Ammar, M. Panizza, *Sep. Purif. Technol.* **2019**, *208*, 178–183.
[33] D. Hasson, H. Shemer, R. Semiat, *Desalin. Water Treat.* **2016**, *57*, 23147–23161.
[34] M. Hermassi, C. Valderrama, N. Moreno, O. Font, X. Querol, N. Batis, J. L. Cortina, *J. Chem. Technol. Biotechnol.* **2016**, *91*, 1962–1971.
[35] Komal, *Pharma Innov.* **2018**, *7*(4), 999–1002.
[36] M. A. Daam, A. C. Santos Pereira, E. Silva, L. Caetano, M. J. Cerejeira, *Ecotoxicol. Environ. Saf.* **2013**, *97*, 78–85.
[37] A. M. Sadaria, R. Sutton, K. D. Moran, J. Teerlink, J. V. Jackson, R. U. Halden, *Environ. Toxicol. Chem.* **2017**, *36*, 1473–1482.
[38] A. L. Patil, P. N. Patil, P. R. Gogate, *Ultrason. Sonochem.* **2014**, *21*, 1778–1786.
[39] M. B. Brahim, H. B. Ammar, R. Abdelhedi, Y. Samet, *Korean J. Chem. Eng.* **2016**, *33*, 2602–2609.
[40] L. M. Silva, R. P. A. dos Santos, C. C. O. Morais, C. L. Vasconcelos, C. A. Martinez-Huitle, S. S. L. Castro, *J. Electrochem. Soc.* **2017**, *164*, E489–E495.
[41] H. Zhao, Y. Wang, Y. Wang, T. Cao, G. Zhao, *Appl. Catal. B: Environ.* **2012**, *125*, 120–127.
[42] M. Turabik, N. Oturan, B. Gozmen, M. A. Oturan, *Environ. Sci. Pollut. Res.* **2014**, *21*, 8387–8397.
[43] H. Zhao, L. Qian, Y. Chen, Q. Wang, G. Zhao, *Chem. Eng. J.* **2018**, *332*, 486–498.
[44] X. Querol, N. Moreno, A. Alastuey, R. Juan, J. M. Andrés, A. López-Soler, C. Ayora, A. Medinaceli, A. Valero, *Geol. Acta* **2007**, *5*, 49–57.
[45] M. Hermassi, J. Dosta, C. Valderrama, E. Licon, N. Moreno, X. Querol, N. H. Batis, J. L. Cortina, *Sci. Total Environ.* **2018**, *630*, 781–789.
[46] APWA, AWWA, WEF, Standard Methods for the Examination of Water and Wastewater, 21 st Ed. Method Number 4500-Cl Chlorine (residual)-G. DPD Colorimetric Method, American Public Health Association, Washington D. C., **2005**, pp. 4–67 and 4–68.
[47] C. Ridruejo, F. Centellas, P. L. Cabot, I. Sirés, E. Brillas, *Water Res.* **2018**, *128*, 71–81.

Manuscript received: December 31, 2018
Accepted manuscript online: February 4, 2019

Supporting Information

Groundwater Treatment using a Solid Polymer Electrolyte Cell with Mesh Electrodes

Roger Oriol, Davide Clematis, Enric Brillas, José L. Cortina, Marco Panizza,* and Ignasi Sirés*An invited contribution to a Special Collection dedicated to Trends in Synthetic Diamond for Electrochemical Applications

Table S1. Distribution of chlorinated species after 240 min of electrochemical oxidation of 500 mL of 23.7 mg L^{-1} imidacloprid in simulated water and softened groundwater at pH 9.8 and 25 ºC using a stirred reactor with an SPE cell composed of a Nb/BDD mesh anode and a Ti/RuO2 mesh cathode, at 0.50 A.

Chlorinated species	Concentration (mg L^{-1})	
	Simulated water	Softened groundwater
Cl^-	82.7±2.7 [a]	92.1±2.8 [b]
Active chlorine as ClO^-	69.2±2.5	22.3±0.9
ClO_3^-	435.9±13.1	522.3±22.8
ClO_4^-	346.1±10.7	381.7±14.4

Initial Cl– concentration: [a] 442.8±15.4 mg L^{-1}; [b] 476.8±18.8 mg L^{-1}

Table S2. Apparent rate constant determined for the degradation of imidacloprid in different aqueous matrices at pH 9.8 and 25 ºC using a stirred reactor with an SPE cell composed of a Nb/BDD mesh anode and a Ti/RuO2 mesh cathode under selected conditions.

[Imidacloprid] (mg L^{-1})	Current (mA)	$k1$ (10^{-2} min^{-1})	R^2
Simulated water			
23.7	0.10	2.4±0.1	0.982
	0.25	4.0±0.2	0.992
	0.50	4.2±0.2	0.986
	1.00	6.2±0.2	0.991
	1.50	6.5±0.2	0.994
Softened groundwater			
1.2	0.50	2.1±0.1	0.980
4.8	0.50	1.8±0.1	0.994
11.8	0.50	1.9±0.1	0.989
23.7	0.50	2.0±0.1	0.990
59.2	0.50	2.5±0.2	0.995

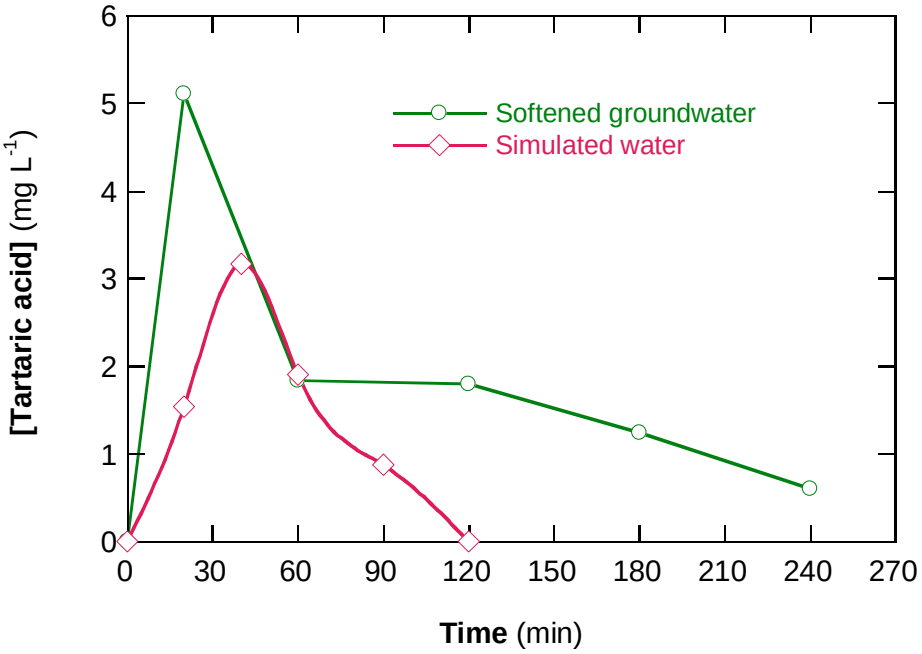

Figure S1. Time course of tartaric acid detected during the electrochemical oxidation of 500 mL of 23.7 mg L^{-1} imidacloprid spiked into simulated water and softened groundwater at pH 9.8 and 25 ºC using an SPE cell with a Nb/BDD mesh anode and a Ti/RuO2 mesh cathode, at 0.50 A.

4.2. Paired electro-oxidation of insecticide imidacloprid and electrodenitrification in simulated and real water matrices

The removal of IMC at a concentration of 0.12 mM (23.7 mg L^{-1}) was carried out by EO, coupled with the ER of nitrate in different water matrices, including simulated water and softened GW. The first process caused the oxidation of the organic pollutant at the anode from: (i) direct anodic oxidation, (ii) mediated oxidation by physisorbed hydroxyl radical generated at the anode surface from water oxidation through an electrocatalytic (i.e., heterogeneous) process, having a high oxidation power; or (iii) mediated oxidation by the active chlorine species, generated through the oxidation of chloride present in solution at the anode surface, through homogeneous catalysis. Two different anode materials, BDD and IrO_2, were used to compare the pesticide removal, employing in both cases an AISI DC01 carbon steel plate as cathode. The use of this cathode material allowed the removal of nitrate present in the solutions by ER, being converted into ammonia and nitrogen. The removal of nitrate with a stainless steel (SS) cathode was studied as well. The area of all electrodes was 10 cm^2.

Four water matrices were employed in the trials: (i) ultrapure water with sodium sulfate as supporting electrolyte, without the organic pollutant; (ii) softened GW, without the organic pollutant; (iii) a synthetic solution mimicking the anion content, in the presence and absence of nitrate, and in the presence of IMC; and (iv) softened GW with IMC spiked into it. Raw and softened GW characterization is shown in **Table 1** (see related paper). Calcium and magnesium concentrations in the natural GW were diminished through a decalcification process based on solution alkalinization. This process consisted in the increase of pH up to a value of 12 with sodium hydroxide, aiming to force the precipitation of these divalent alkaline-earth cations in their hydroxide and carbonate forms. Afterwards, the pH was adjusted to near-neutral to emulate the raw GW initial pH value.

A comparison between the two steel cathodes related to nitrate removal by ER in 150 mL of ultrapure water with 221 mg L^{-1} of nitrate can be seen in **Figure 1**. A superior performance of the AISI DC01 steel was found, removing 83% of the initial nitrate after 240 min, in contrast with the low activity of SS for its abatement (44%). The latter

material led to a lower accumulation of ammonia in the solution, as well as a lower amount of generated N-based volatile compounds (presumably NH_3 due to the pH increase by nitrate ER). **Table 2** shows the results obtained by combining the mild steel cathode with each of the anodes to treat softened GW and the synthetic water matrices, in the presence and absence of nitrate, at different current densities within the range from 5 to 50 mA cm^{-2}. First-order rate constants for the nitrate and chloride removals and the pseudo-first-order rate constant for IMC decay, along with the related percentage of TOC removal at 240 min, were determined. Note that a higher degradation was achieved when a greater current density was used due to the acceleration of the electrode reactions.

The fate of nitrogen and chlorine-based species in the solution over the course of softened GW electrolyses when using the AISI DC01 steel cathode and BDD or IrO_2 as anodes at different current densities was thoroughly assessed, as shown in **Figure 2** and **Figure 3**, respectively. A nitrate removal of 81% was obtained when the cathode was paired with BDD after 240 min when the lowest current density (i.e., 5 mA cm^{-2}) was applied. In contrast, an almost complete abatement was found at 10 and 20 mA cm^{-2}. Higher amount of N-containing volatile compounds, i.e., from 22% to 34% as the current density raised from 5 to 20 mA cm^{-2}, were attained. This can be ascribed to the faster nitrate elimination by ER at the highly active cathode surface and the reaction of the products formed with the active chlorine generated by EO at the anode surface. Although the nitrate reduction mechanism takes place at the cathode surface, the global nitrate ER was much lower when the IrO_2 anode was combined with the cathode, attaining removals of 48%, 64%, 61% and 52% at 5, 10, 20 and 50 mA cm^{-2}, probably due to the re-oxidation of the N-containing intermediates back to nitrate upon continuous reaction with active chlorine via reaction (17). Volatile compounds of 29%, 50%, 52% and 50% were determined, respectively, due to conversion to N_2 via reaction (16). The accumulation of toxic oxychlorine anions was observed regardless of the anode used. High contents of chlorate and perchlorate were produced by the oxidation of the active chlorine in both chloride-containing water matrices (natural and synthetic) when BDD anode was employed. In contrast, when the anode was IrO_2, a much smaller amount of chlorate was accumulated over time. resulting in no perchlorate detection. However, when the experiments were done in the absence of the pesticide, the concentrations of these chlorinated anionic species were higher regardless of the anode. This phenomenon was

caused by the absence of competitive oxidation reactions at the anode surface. It was also observed in these electrolyses that, by using lower current densities, an acceptable nitrate removal was still obtained with the chosen cathode, especially in combination with the BDD anode.

The results depicted in **Figure 4** show a higher performance of the BDD anode for the simultaneous removal of nitrate and IMC in synthetic GW, in comparison with the results obtained when using the IrO_2 anode (**Figure 5**). When comparing the results obtained with the softened GW in the absence of pesticide and the ones obtained in the synthetic GW with IMC, a smaller removal of chloride could be observed in the presence of IMC due to competitive EO of both species. This had also impact on the oxidation products of chloride, such as chlorate and perchlorate, being the latter one only detected when BDD was employed as anode.

The results depicted in **Figure 6** at 5, 10 and 20 mA cm^{-2} in the absence of nitrate evidenced a higher oxidation power employing the BDD anode by increasing the current density, achieving a complete removal of IMC at 240, 180 and 150 min, respectively. In the case of the IrO_2 anode, the total removal of the pesticide was only attained after 180 min at the highest current density of 20 mA cm^{-2}. This demonstrates the higher oxidation power of the physisorbed hydroxyl radical originated at the BDD anode. **Figure 7** shows the total elimination of this contaminant by BDD as anode material at 210 min, with 61% of mineralization. When IrO_2 was used, 79% of the initial IMC was eliminated, only obtaining a mineralization of 8.9% at 240 min, in agreement with its lower oxidation power. The nitrate concentration was reduced by 80% and 33% in the cells equipped with BDD and IrO_2, respectively, at 240 min.

The following heteroaromatic intermediates were detected by GC-MS: 1-[(6-chloro-3-pyridyl)methyl]imidazolidine-2-imine, 2-chloro-5-(4,5-dihydroimidazol-1-ylmethyl)-pyridine, (6-chloro-3-pyridyl)methyl)-(2-imino-ethyliden)-amine, 1-[(6-chloro-3-pyridyl)methyl]imidazolidine-2-oxime, 1-[(6-chloro-3-pyridyl)methyl]imidazolidine-2-one, 6-chloronicotinonitrile, 6-chloronicotinoaldehyde e imidazolidin-2,4,5-trione. From these compounds, the initial reaction sequence for IMC degradation of **Figure 8** was proposed.

Electrochimica Acta 317 (2019) 753–765

Contents lists available at ScienceDirect

Electrochimica Acta

journal homepage: www.elsevier.com/locate/electacta

Paired electro-oxidation of insecticide imidacloprid and electrodenitrification in simulated and real water matrices

Roger Oriol [1], María del Pilar Bernícola, Enric Brillas [1], Pere L. Cabot [1], Ignasi Sirés [*, 1]

Laboratori d'Electroquímica dels Materials i del Medi Ambient, Departament de Química Física, Facultat de Química, Universitat de Barcelona, Martí i Franquès 1-11, 08028, Barcelona, Spain

ARTICLE INFO

Article history:
Received 18 March 2019
Received in revised form
30 April 2019
Accepted 1 May 2019
Available online 9 May 2019

Keywords:
Boron-doped diamond
Dimensionally stable anode
Electrochemical oxidation
Groundwater
Nitrate removal

ABSTRACT

Groundwater is one of the main freshwater resources on the Earth, but its contamination by NO_3^- and pesticides jeopardizes its suitability for consumption. In this work, the simultaneous electro-oxidation of insecticide imidacloprid (IMC) and electroreduction of NO_3^- in softened groundwater containing a large amount of Cl^- has been addressed. The assays were carried out in a stirred undivided tank reactor containing either a boron-doped diamond (BDD) or IrO_2 anode, and Fe cathode, which showed greater electrocatalytic activity than stainless steel to reduce NO_3^-. Comparative assays in simulated water mimicking the anionic composition of groundwater were made to assess the influence of natural organic matter (NOM) on the decontamination process. The BDD/Fe cell had much greater performance than the IrO_2/Fe one, although the former produced larger amounts of ClO_3^- and ClO_4^-. In all cases, the NO_3^-, Cl^- and IMC decays agreed with a (pseudo)-first-order kinetics. In the BDD/Fe cell, total NO_3^- removal was reached at $j \geq 10$ mA cm^{-2} in softened groundwater, at similar rate in the presence and absence of IMC, but it was decelerated using the simulated matrix. The N-products formed upon NO_3^- electroreduction contributed to IMC degradation, but its decay was inhibited by NOM because of the partial consumption of oxidants like hydroxyl radical and active chlorine. Operating at 5 mA cm^{-2} for 240 min, total removal of the insecticide and 61.5% total organic carbon (TOC) decay were achieved, also attaining a low NO_3^- content that was suitable for humans. Eight heteroaromatic products were identified, allowing the proposal of a reaction sequence for IMC degradation in groundwater.

1. Introduction

Regions with high density of pig farming and agricultural land are particularly vulnerable to environmental issues linked to groundwater contamination by NO_3^- ion and pesticides. Groundwater is the largest reservoir of liquid freshwater, providing most of the drinking and irrigation water in arid and semiarid areas [1], but the abovementioned pollutants can cause diseases and serious health problems to human beings and animals. The occurrence of NO_3^-, one of the major contaminants of natural water [1,2], is due to: (i) improper disposal of nitrate-laden wastewater, (ii) acid deposition of atmospheric N_xO_y, and (iii) large use of nitrogen fertilizers, including swine wastewater. As a result of its large stability at ambient conditions, NO_3^- is accumulated in water and reaches concentrations as high as 900 mg L^{-1} [1]. Since the excessive intake of dissolved NO_3^- exerts behavioral and cardiovascular diseases, as well as methaemoglobinaemia [3,4], the World Health Organization (WHO) has established a guideline value of 50 mg L^{-1} NO_3^- for human consumption [4]. However, NO_3^- removal from groundwater is difficult because of its high solubility and poor adsorption or precipitation. Hence, this ion is usually treated by reverse osmosis, electrodialysis and ion exchange [4], but these still are non-destructive, expensive and/or ineffective methods.

On the other hand, neonicotinoids are the most widely employed neuro-active insecticides, being applied to many crops and a large plethora of vegetables and fruits [5,6]. They are very harmful to birds, owing to the reduction in insect population, and honeybee colonies. Relatively high concentrations of neonicotinoids have been detected in natural water [5]. Recent EU regulations have banned the use of several of these compounds due to the environmental risks [7,8]. Imidacloprid (IMC, $C_9H_{10}ClN_5O_2$, *N*-[1-[(6-chloro-3-pyridyl)methyl]-4,5-dihydroimidazol-2-yl]nitramide, $M = 255.66$ g mol^{-1}) has been the most widespread neonicotinoid in agriculture. Its tolerance varies from 0.02 mg kg^{-1} in eggs to 3.0 mg kg^{-1} in hops, causing hepatotoxicity, immunotoxicity, nephrotoxicity and oxidative stress

* Corresponding author.
E-mail address: i.sires@ub.edu (I. Sirés).
[1] Active ISE member.

https://doi.org/10.1016/j.electacta.2019.05.002
0013-4686/

effects in animals [9]. Due to its high resistance to degradation by conventional methods, IMC has been found at concentrations up to 0.36 μg L^{-1} in urban wastewater [10] and 52 μg L^{-1} in agricultural water [11]. This molecule contains five N atoms, which worsens the situation if their transformation into stable NO_3^- is promoted during water treatment.

Recently, a wide range of electrochemical technologies is being developed for the decontamination of both, natural water and urban and industrial wastewater [12–16]. Separation methods such as electrodialysis and electrocoagulation have been reported for NO_3^- removal [17], although most research efforts have been devoted to its destruction by electroreduction [2,4,13,17–23]. The effectiveness of the latter technique is tightly related to the properties of the cathode material, the solution composition and its pH, the applied current density (j) and the cell configuration. Cu-Zn [17], boron-doped diamond (BDD), stainless steel (SS), silicon carbide, graphite and lead [18,19], Cu [20], Fe and Al [21], nano TiO_2 [22,23] and nano zero-valent iron supported on mesoporous carbon [24] have been tested. The electrochemical reduction is aimed to consecutively transform the target ion into NO_2^-, NH_2OH, N_xO_y, N_2 and NH_3, according to the following overall sequence [2,13,18]:

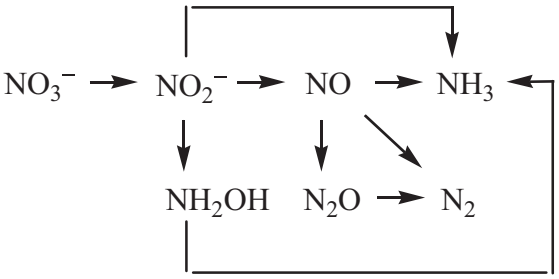

(1)

In the absence of Cl^- ion, that sequence involves overall reactions (2)–(4) [23]:

$$NO_3^- + H_2O + 2e^- \rightarrow NO_2^- + 2OH^- \quad (2)$$

$$NO_2^- + 5H_2O + 6e^- \rightarrow NH_3 + 7OH^- \quad (3)$$

$$2NO_2^- + 4H_2O + 6e^- \rightarrow N_2 + 8OH^- \quad (4)$$

Using undivided reactors, the process is more complicated in the presence of Cl^- ion because active chlorine (Cl_2/HClO/ClO^-) is formed from reactions (5)–(7) [25], further reacting with NH_3 to yield either N_2 by reaction (8) or NO_3^- by reaction (9), or oxidizing NO_2^- to NO_3^- by reaction (10) [19,20,22], which causes a slower NO_3^- removal. Moreover, chloramines can be originated, for example, from reaction (11), which can evolve either to N_2 or N_2O, as shown by reaction (12) [19].

$$2Cl^- \rightarrow Cl_2(aq) + 2e^- \quad (5)$$

$$Cl_2(aq) + H_2O \rightarrow HClO + H^+ + Cl^- \quad (6)$$

$$HClO \leftrightarrows ClO^- + H^+ \quad pK_a = 7.53 \quad (7)$$

$$2NH_3 + 2ClO^- \rightarrow N_2 + 2Cl^- + 2H_2O + 2H^+ + 2e^- \quad (8)$$

$$NH_3 + 4ClO^- \rightarrow NO_3^- + H_2O + H^+ + 4Cl^- \quad (9)$$

$$NO_2^- + ClO^- \rightarrow NO_3^- + Cl^- \quad (10)$$

$$NH_3 + ClO^- \rightarrow NH_2Cl + H_2O \quad (11)$$

$$2NH_2Cl + 2ClO^- \rightarrow N_2O + H_2O + 2H^+ + 4Cl^- \quad (12)$$

The anode material may also have influence. Lacasa et al. [19] compared NO_3^- electroreduction in synthetic solutions using either BDD or a dimensionally stable anode (DSA®). The latter anode was very efficient in highly concentrated sulfate medium, whereas BDD performed better in Cl^- medium because the products formed from cathodic NO_3^- reduction were less prone to adsorption on BDD, thereby minimizing their re-oxidation to yield this ion. The electroreduction process is expected to become less efficient in groundwater due to: (i) the presence of CO_3^{2-} that can cause cathode fouling, (ii) the small NO_3^- content, and (iii) the presence of natural organic matter (NOM) [13].

The efficient removal of several pesticides from synthetic solutions by electrochemical advanced oxidation processes (EAOPs) like electro-oxidation (EO), electro-Fenton (EF) and photoelectro-Fenton (PEF) using BDD or DSA® anodes has been reported [26–33]. In contrast, less is known about the treatment of pesticides in groundwater, since as far as we know only the treatment of lindane and IMC has been reported [34,35]. For IMC, EO [14,35–37] and EF [38–40] processes, along with electrocoagulation [41], have been studied in different water matrices.

EO, the simplest EAOP, involves the attack of the strong oxidant hydroxyl radical (M(•OH)) on organic molecules. The radical is originated from water discharge on an active or non-active anode (M) at high j from reaction (13) [42,43]. The non-active BDD electrode has been found as the most powerful anode, since it yields large quantities of reactive M(•OH) as compared to DSA® [44]. In Cl^- media, the performance of the latter anode is substantially upgraded because of its higher selectivity to produce active chlorine, which then contributes to the oxidative degradation of organics. However, in some cases, BDD anode possesses higher mineralization power even in such media due to its ability to destroy the chlorinated by-products [44].

$$M + H_2O \rightarrow M(\bullet OH) + H^+ + e^- \quad (13)$$

In this work, the simultaneous IMC electro-oxidation and NO_3^- electroreduction in groundwater is assessed for the first time. This aims at ensuring the electrodenitrification of the aqueous matrix, which is related to the decrease of total nitrogen (TN) content. The assays were performed in an undivided cell equipped with a BDD or IrO_2 (i.e., DSA®-O_2) anode and Fe or stainless steel (SS) cathode. The real groundwater was previously softened to minimize the alkaline earth metal ions and carbonate concentrations, and IMC was spiked into it at 10.0 mg dm^{-3} of total organic carbon (TOC). This high concentration was chosen to monitor the degradation and mineralization and to identify the products formed. Comparative assays with pure and simulated water mimicking the anionic composition of the softened groundwater were also made in order to clarify the raw NO_3^- electroreduction process and the role of NOM.

2. Materials and methods

2.1. Chemicals

Analytical standard imidacloprid (PESTANAL®) was provided by Sigma-Aldrich. Analytical grade NaOH (98–100%) and H_2SO_4 (95–98%) were provided by Panreac. Analytical grade KNO_3 (98%) from Panreac, Na_2SO_4 (99.9%) from BDH PROLABO®, and NaCl (99%) from Panreac were used for the preparation of the simulated water matrix. Carboxylic acids and other chemicals were either of analytical or HPLC grade purchased from Fluka, Merck and Probus.

Analytical solutions and the simulated water matrix were prepared with ultrapure water from a Millipore Milli-Q system (resistivity > 18.2 MΩ cm).

2.2. Aqueous matrices

Apart from pure water, the following aqueous matrices were employed to assess the electrodenitrification and EO processes:

(i) A raw groundwater sample, preserved at 4 °C in a refrigerator once collected from a water well located in an agricultural land in the surroundings of Barcelona (Spain). Its characteristics are shown in Table 1: neutral pH, low conductivity, large amount of HCO_3^- and CO_3^{2-} ions yielding a high total carbon (TC) content, as well as of NO_3^-, Cl^- and SO_4^{2-} ions, and alkaline earth metal ions such as Ca^{2+} and Mg^{2+}. Before electrolytic assays, the raw groundwater was pre-treated following three steps: softening by means of alkalinization up to pH 12 with 20% (w/v) NaOH, filtration to remove the hydroxide and carbonate precipitates formed and, finally, pH adjustment to the original value by adding 10% (v/v) H_2SO_4. As can be seen in Table 1, this softened groundwater showed a drastic reduction of the concentration of all alkaline earth metal ions, whereas the Na^+ and SO_4^{2-} concentrations substantially increased as result of the conditioning procedure. It is also noticeable the low conductivity and TOC of the softened sample, whereas TN mainly corresponded to its NO_3^- content.

(ii) Simulated water prepared to mimic the anions content of the softened groundwater. It was prepared with ultrapure water and contained 2.10 mM KNO_3 (130 mg dm^{-3} NO_3^-), 10.30 mM NaCl (365 mg dm^{-3} Cl^-), and 7.04 mM Na_2SO_4 (690 mg dm^{-3} SO_4^{2-}). The pH was adjusted to 6.8 with 1 M NaOH, thus reaching a conductivity of 1.3 mS cm^{-1}. An analogous solution without NO_3^- was also employed for comparison.

2.3. Electrolytic system

The electrolytic experiments were carried out in a classical two-electrode, cylindrical, jacketed glass tank reactor, which contained 150–175 cm^3 of solution kept under vigorous stirring with a magnetic follower at 800 rpm. The solution temperature was maintained at 25 °C thanks to the circulation of thermostated water through the jacket. The anode was either a Si wafer coated with a BDD thin film, purchased from NeoCoat (Le-Chaux-de-Fonds, Switzerland), or an IrO_2 electrode purchased from NMT Electrodes (Pinetown, South Africa). The cathode was an iron (Fe, 99.9%) or a SS (AISI 304) plate. All the electrodes had a geometric area of 10 cm^2 in contact with the solution. The two electrodes were placed in the center of the reactor, at 1.5 mm from each other. The assays were performed under galvanostatic conditions with an Amel 2049 potentiostat-galvanostat to provide the constant current density (j). The potential difference between the electrodes was directly measured on a Demestres 601BR digital multimeter. The trials with IMC were run after spiking the insecticide at 23.7 mg dm^{-3} (10.0 mg dm^{-3} TOC) into the aqueous matrix.

Table 1
Physicochemical characteristics of the raw and softened groundwater.

Parameter (unit)	Raw groundwater	Softened groundwater
pH	6.9 ± 0.2	6.8 ± 0.3
Conductivity (mS cm^{-1})	0.70 ± 0.03	1.30 ± 0.05
TC (mg dm^{-3})	67.2 ± 2.7	13.1 ± 0.4
TOC (mg dm^{-3})	2.6 ± 0.1	1.8 ± 0.1
TN (mg dm^{-3})	29.2 ± 1.2	29.1 ± 1.1
NO_3^- (mg dm^{-3})	130.0 ± 4.3	129.4 ± 4.8
Cl^- (mg dm^{-3})	366.0 ± 14.4	364.5 ± 17.3
SO_4^{2-} (mg dm^{-3})	88.2 ± 3.8	688.3 ± 28.5
Ca^{2+} (mg dm^{-3})	240.1 ± 9.8	14.4 ± 0.6
Mg^{2+} (mg dm^{-3})	55.4 ± 1.8	0.43 ± 0.02
Ba^{2+} (mg dm^{-3})	0.12 ± 0.01	-[a]
K^+ (mg dm^{-3})	4.1 ± 0.2	3.2 ± 0.1
Na^+ (mg dm^{-3})	80.7 ± 3.2	712.8 ± 26.7
S (mg dm^{-3})	31.6 ± 1.4	288.0 ± 10.5
Si (mg dm^{-3})	11.9 ± 0.4	4.1 ± 0.1

[a] Not found.

2.4. Analytical procedures

A Crison 2200 pH-meter was employed to measure the solution pH, and a Metrohm 644 conductometer was used for the conductance determination. Active chlorine was measured by the *N*,*N*-diethyl-*p*-phenylenediamine colorimetric method, using an Unicam UV4 UV/Vis spectrophotometer set at λ = 515 nm [45]. A small volume of thiosulfate solution was added to the 1.5 cm^3 samples withdrawn from the cell to neutralize the low contents of residual active chlorine, thus ensuring that the degradation process of IMC was stopped. Chloramines were determined upon KI addition, according to the standard 4500-Cl G. DPD Colorimetric Method. All the aliquots were then filtered with Whatman 0.45 μm PTFE membrane filters prior to analysis.

Reversed-phase HPLC was used to monitor the IMC concentration. A Waters 600 LC controlled by Empower® software and coupled to a 996 photodiode array detector (PAD) set at λ = 270 nm was utilized. To carry out the analysis, 20 μL aliquots were injected into the LC and the organics were perfectly separated with a Thermo BDS Hypersil C-18 5 μm (250 mm × 4.6 mm (i.d.)) column at 35 °C, upon elution with a 50:50 (v/v) acetonitrile/0.02 M phosphate buffer (pH 3) mixture at 1.2 cm^3 min^{-1}. IMC appeared at retention time (t_r) of 3.2 min, with L.O.Q = 0.298 mg dm^{-3} and L.O.D = 0.090 mg dm^{-3}.

The solution TOC was measured on a Shimadzu VCSN TOC analyzer using the non-purgeable organic carbon (NPOC) method. An aliquot volume of 50 μL was injected into it, and reproducible values with ±1% accuracy were always obtained, with L.O.Q = 0.708 mg dm^{-3} and L.O.D = 0.211 mg dm^{-3}. TN measurements were carried out with a TNM-1 unit coupled to the TOC analyzer.

The concentration of Cl^-, ClO_3^-, ClO_4^-, SO_4^{2-}, NO_2^-, NO_3^- and NH_4^+ ions was determined following the analytical procedures previously reported [46]. The content of metal ions was obtained by inductively coupled plasma with optical emission spectroscopy (ICP-OES) using a Perkin Elmer Optima 8300 spectrometer.

Average values obtained in duplicate assays are reported in this work. The corresponding error bars within a 95% confidence interval are shown for the experimental data shown in figures.

Stable heteroaromatic derivatives from IMC degradation were detected by gas chromatography-mass spectrometry (GC-MS), and their mass spectra were compared with those in the NIST05 database. Treated solutions were collected after 60 min of EO treatment of 23.7 mg dm^{-3} insecticide spiked into the softened groundwater matrix, using either a BDD or IrO_2 anode, at 5 mA cm^{-2}. The organics accumulated in each sample were extracted with CH_2Cl_2 (3 × 15 cm^3) and the organic phase was dried over anhydrous Na_2SO_4, filtered and its volume reduced to about 2 cm^3 under N_2 stream to be analyzed by GC-MS. To do the analysis, the gas chromatograph contained a non-polar Teknokroma Sapiens X5-MS column, and the same procedure previously detailed was applied [47].

3. Results and discussion

3.1. NO_3^- electroreduction in pure water

First, experiments for the selection of the best cathode able to promote the largest NO_3^- electroreduction were carried out. To do this, 150 cm^3 of solutions of 221 mg dm^{-3} NO_3^-, corresponding to 50 mg dm^{-3} $N{-}NO_3^-$, in pure water at pH 6.8 after adjustment with H_2SO_4 (i.e., conductivity of 0.88 mS cm^{-1}), was electrolyzed in an undivided reactor with an IrO_2 anode and either Fe or SS cathode at $j = 50$ mA cm^{-2} for 240 min. At the end of both trials, a slightly greater conductivity of 1.1 ± 0.1 mS cm^{-1} was determined, because of the alkalinization of both solutions to pH near 10.5. This behavior agrees with the reduction of NO_3^- to NO_2^-, NH_3 and N_2 via reactions (2)–(4), which entails an increase of OH^- concentration.

Fig. 1a depicts a gradual decay of $N{-}NO_3^-$ with electrolysis time, much more rapidly using Fe as the cathode. Average final reductions of 72.8% and 44.0% were obtained using Fe and SS, respectively. A practically constant potential difference between the electrodes (E_{cell}) in each cell was found, with average values of 20.6 V with Fe and 26.1 V with SS. The greater E_{cell} using the SS cathode suggests that the cathode potential became much more negative to maintain the required j, thus informing about its lower catalytic activity towards H_2O and NO_3^- reduction. Fig. 1a also reveals the generation of $N{-}NH_4^+$, with maximum values of 9.8 mg dm^{-3} using Fe and 4.6 mg dm^{-3} using SS at 120 min, which were reduced to 4.9 and 0.9 mg dm^{-3}, respectively, at 240 min. The higher $N{-}NH_4^+$ production with the Fe cathode agrees with the quicker $N{-}NO_3^-$ decay, pointing out the higher rate of reaction (3). The drop of $N{-}NH_4^+$ concentration at long electrolysis time informs about a gradual re-oxidation of this ion at the IrO_2 anode surface. In addition, the TN dropped down to 21.0 mg dm^{-3} using Fe and 28.9 mg dm^{-3} using SS, corresponding to a nitrogen loss of 57.6% and 42.2% that can be ascribed to the release of volatile N-compounds such as N_2O and, pre-eminently, N_2 [18] (see sequence (1)). Some loss of gaseous NH_3 cannot be discard either because the final pH near 10.5 favors its preponderance over soluble NH_4^+ ($pK_a = 4.75$). Hence, the predominant NO_3^- electroreduction pathway in both systems involves consecutive reactions (2) and (4).

From the above results, the speciation of the N-containing species in the resulting electrolyzed solutions was determined, as presented in Fig. 1b. Most of the initial NO_3^- was always converted into volatile products and, to a much lesser extent, into NH_4^+, with greater efficiency using the Fe cathode. In this case, a 5.6% of other undetected species remained in solution, which were not formed using SS. This may be accounted for by the accumulation of products formed from NH_4^+ re-oxidation, which takes place to greater extent with Fe. All these findings confirm the superior electrocatalytic activity of Fe to reduce NO_3^- and hence, this cathode was chosen for all trials described below.

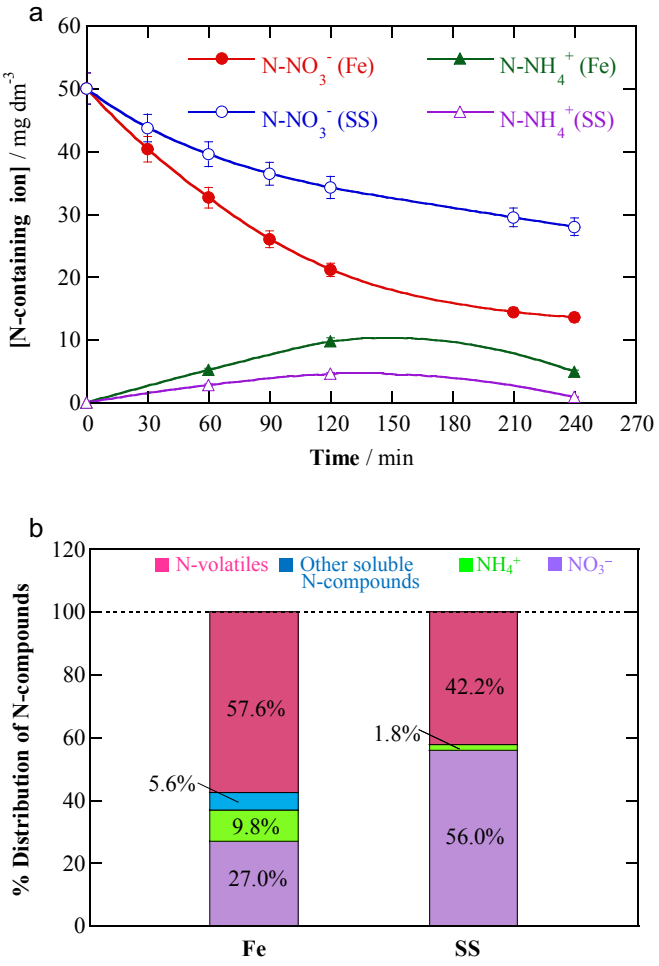

Fig. 1. (a) $N{-}NO_3^-$ concentration removal and $N{-}NH_4^+$ accumulated content during the electrolysis of 150 cm^3 of 221 mg L^{-1} NO_3^- in ultrapure water using a stirred undivided tank reactor with a 10 cm^2 IrO_2 anode and a 10 cm^2 Fe or SS (AISI 304) cathode at a current density (j) of 50 mA cm^{-2} and 25 °C. (b) Percentage distribution of the nitrogen species at the end of the above trials.

3.2. Fate of nitrogen and chlorine species upon electrolysis in softened groundwater

First electrolyses performed with raw groundwater in BDD/Fe and IrO_2/Fe cells revealed a very low decay of NO_3^- and Cl^-, which was attributed to the passivation of the Fe cathode upon precipitation of carbonates and hydroxides/oxides of highly concentrated alkaline metal ions (Ca^{2+} and Mg^{2+}, see Table 1). To overcome this problem, the raw groundwater was conditioned to remove most of these harmful species, following the procedure described in subsection 2.2. Table 1 shows that the resulting softened groundwater kept the initial TOC (related to NOM) and TN (corresponding to NO_3^-), with an insignificant reduction of Cl^- concentration to 365 mg dm^{-3}. The use of this aqueous matrix prevented the cathode passivation in all subsequent electrolyses.

The coupling of Fe cathode with a BDD or IrO_2 anode to reach NO_3^- electroreduction alongside Cl^- electro-oxidation was assessed at j values between 5 and 50 mA cm^{-2}. In all these assays, the solution pH remained at circumneutral pH (between 6.8 and 7.8), whereas conductivity remained practically constant as well. No fluctuation of the E_{cell} value was found at each j value tested, always yielding greater potentials in cells with the BDD anode. For example, at j of 5 and 10 mA cm^{-2}, the E_{cell} was of 7.4 and 10.4 V using the BDD/Fe cell, decreasing to 6.1 and 7.7 V using IrO_2/Fe.

Fig. 2a depicts a faster $N{-}NO_3^-$ decay when j rose from 5 to 20 mA cm^{-2} using BDD. After 240 min of electrolysis, the ion was almost completely removed at 10 and 20 mA cm^{-2}, whereas its concentration was only reduced by 81.0% at the lowest j. Each $N{-}NO_3^-$ decay showed an exponential profile, which can be related to a process under mass-transport control. Fig. 2b illustrates the good fitting to a first-order kinetics for the above concentration abatements, which agrees with an analogous finding by Katsounaros et al. [48] using a tin cathode at high potentials. Table 2 shows that the absolute rate constant ($k(N{-}NO_3^-)$) was 2.70-fold greater upon a 4-fold increase of j, from 5 to 20 mA cm^{-2}. That informs about a gradual loss of the electrocatalytic activity of Fe as j was increased, which can be ascribed to the greater extent of H_2

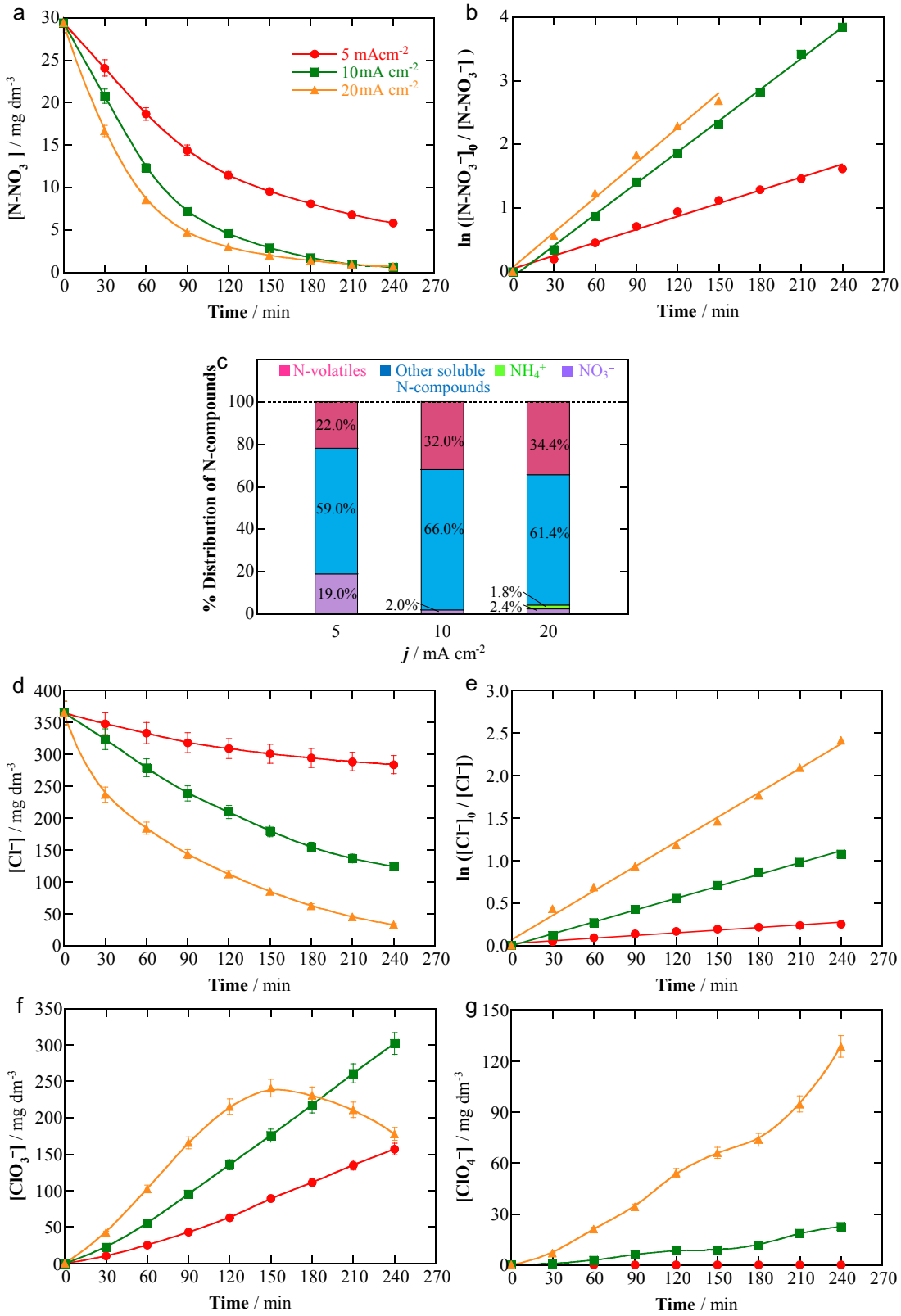

Fig. 2. Effect of current density on the change of the concentrations of (a) N–NO_3^- (129.4 mg dm^{-3} of initial NO_3^-), (d) Cl^- ion (365.0 mg dm^{-3} of initial Cl^-), (f) ClO_3^- ion, and (g) ClO_4^- ion with time during the electrolysis of 175 cm^3 of softened groundwater at pH 6.8 using an undivided tank reactor with a 10 cm^2 BDD anode and a 10 cm^2 Fe cathode at 25 °C. (b,e) First-order kinetic analysis for the data of plots (a) and (d). (c) Percentage distribution of the nitrogen species at the end of the above trials.

Table 2
First-order rate constant for $N{-}NO_3^-$ and Cl^- decays and pseudo-first-order rate constant imidacloprid decay, along with the percentage of TOC removal at the end of the electrolyses. The table includes trials performed with 175 cm^3 of softened groundwater and simulated water matrix, in the presence and absence of the insecticide, at pH 6.8 and 25 °C using an undivided cell with a BDD or IrO_2 anode and a Fe cathode at different current densities.

Anode	[IMC]/mg dm^{-3}	j/mA cm^{-2}	$k(N{-}NO_3^-)/10^{-3}$ min^{-1} (R^2)	$k(Cl^-)/10^{-3}$ min^{-1} (R^2)	k(IMC)/10^{-3} min^{-1} (R^2)	% TOC removal at 240 min
Softened groundwater						
BDD	–	5	6.8 (0.992)	1.0 (0.974)	–	–
	23.7	5	6.4 (0.998)	0.9 (0.993)	14.0 (0.991)	61.5[b]
	–	10	16.3 (0.998)	4.6 (0.998)	–	–
	–	20	18.2 (0.992)	9.6 (0.996)	–	–
IrO_2	–	5	4.4 (0.994)	1.3 (0.999)	–	–
	23.7	5	1.8 (0.985)	0.3 (0.986)	6.7 (0.997)	8.9[b]
	–	20	5.5 (0.995)	1.9 (0.999)	–	–
	–	30	6.6 (0.988)	4.8 (0.994)	–	–
	–	50	5.3 (0.984)	4.3(0.991)	–	–
Simulated water matrix						
BDD	23.7	5	4.8 (0.993)	2.3 (0.982)	23.4 (0.994)	68.2[c]
		20	5.2 (0.982)	11.7 (0.986)	43.5 (0.996)	87.3[c]
		50	16.8 (0.994)	18.8 (0.998)	74.0 (0.980)	89.1[c]
IrO_2	23.7	5	1.3 (0.983)	0.3 (0.992)	9.4 (0.991)	0[c]
		20	1.6 (0.980)	0.8 (0.980)	22.2 (0.993)	0[c]
		50	2.5 (0.996)	1.8 (0.981)	43.5 (0.981)	17.7[c]
Simulated water without NO_3^-						
BDD	23.7	5	–	0.9 (0.982)	22.1 (0.993)	56.8[c]
		10	–	-[a]	31.1 (0.988)	60.8[c]
		20	–	2.1 (0.984)	56.4 (0.992)	71.0[c]
IrO_2	23.7	5	–	-[a]	11.0 (0.997)	-[a]
		10	–	-[a]	15.0 (0.990)	-[a]
		20	–	-[a]	28.6 (0.992)	-[a]

[a] Not determined.
[b] Initial TOC: 11.8 mg dm^{-3}.
[c] Initial TOC: 10.0 mg dm^{-3}.

evolution from H_2O reduction. From the TN values measured at the end of these trials, the speciation of the final N-containing species was determined, as shown in Fig. 2c. A progressively higher amount of volatile N-products from 22.0% to 34.4% was observed as j was increased, as expected from the acceleration of reaction (4) as well as from N_2 release stimulated via reaction (8) upon the oxidation of NH_4^+ by active chlorine. This is supported by the fact that only a small fraction of NH_4^+, formed from consecutive reactions (2) and (3), was found in these reactions. In all cases, unidentified soluble products accounted for the most of the final TN content. Since no NO_2^- and a very low concentration of chloramines (<0.05%) were detected, one can conclude that such final products were pre-eminently intermediates originated during the NO_2^- reduction according to scheme (1), alongside species coming from NH_4^+ re-oxidation.

As deduced from Fig. 2d, the oxidation of Cl^- at the BDD anode surface was also gradually enhanced as j was increased. The content of this ion was finally reduced by 22.2% at 5 mA cm^{-2}, 66.0% at 10 mA cm^{-2} and 91.2% at 20 mA cm^{-2}. Its exponential decay always obeyed a first-order kinetics (see Fig. 2e), in agreement with a mass-transport controlled process. The rate constants ($k(Cl^-)$) for these experiments are summarized in Table 2. At each j value, $k(Cl^-)$ was lower than $k(N{-}NO_3^-)$, highlighting the importance of the competition between Cl^- oxidation via reaction (5) and O_2 evolution occurring from the electrochemical oxidation of BDD(•OH), formed via reaction (13), at the electroactive sites of BDD. For example, a large rise in $k(Cl^-)$, i.e., 4.6-fold, occurred when j was doubled from 5 to 10 mA cm^{-2}, evidencing of a larger enhancement of reaction (5) as compared to O_2 evolution. In contrast, the $k(Cl^-)$ value became exactly twice when j grew from 10 to 20 mA cm^{-2}.

ClO_3^- and ClO_4^- ions were produced at the BDD anode from the consecutive oxidation of ClO^- via reactions (14)–(16) [25,46]:

$$ClO^- + H_2O \rightarrow ClO_2^- + 2H^+ + 2e^- \quad (14)$$

$$ClO_2^- + H_2O \rightarrow ClO_3^- + 2H^+ + 2e^- \quad (15)$$

$$ClO_3^- + H_2O \rightarrow ClO_4^- + 2H^+ + 2e^- \quad (16)$$

Fig. 2f and g shows the time course of the ClO_3^- and ClO_4^- contents for the above trials, respectively. Both ions were more largely accumulated at raising j, with predominance of the former one. It is noticeable that almost no ClO_4^- was formed at the lowest j, whereas at the highest j the accumulation of this ion was greatly enhanced from 150 min of electrolysis (see Fig. 2g) at the expense of ClO_3^- (see Fig. 2f). This suggests a remarkable acceleration of reactions (14)–(16) when j is increased. A mass balance at $j = 20$ mA cm^{-2} reveals that the lost Cl^- was converted into 22.6% of ClO_3^- and 13.7% of ClO_4^-. Since no active chlorine and a very low content of chloramines were found, one can infer that 64% of Cl^- was transformed into gaseous Cl_2.

A lower performance was found for the IrO_2/Fe cell and hence, the electrolyses with the softened groundwater were made up to $j = 50$ mA cm^{-2}. Fig. 3a shows a poor $N{-}NO_3^-$ abatement, which increased from 45.9% to 62.2% at 240 min as j was raised from 5 to 20 mA cm^{-2}. Further increase to 30 and 50 mA cm^{-2} yielded decreasing abatements of 59.5% and 53.7%, respectively. Note that the latter value is much lower than that obtained in ultrapure water (see Fig. 1a). The above trend was corroborated from the $k(N{-}NO_3^-)$ values (see Table 2) determined from the excellent linear plots found for the corresponding first-order kinetic analysis presented in Fig. 3b. As compared to 20 mA cm^{-2}, Table 2 highlights a slightly greater $k(N{-}NO_3^-)$ value at 30 mA cm^{-2} or a similar one at 50 mA cm^{-2}, in agreement with the $N{-}NO_3^-$ decay trends of Fig. 3a that show a more pronounced deceleration from 60 min at the two highest j values. After comparison with the higher rate constants obtained with the BDD/Fe cell (see Table 2), one can conclude that the NO_3^- electroreduction was much less effective using the IrO_2/Fe cell. This can be related to the expected greater production of active

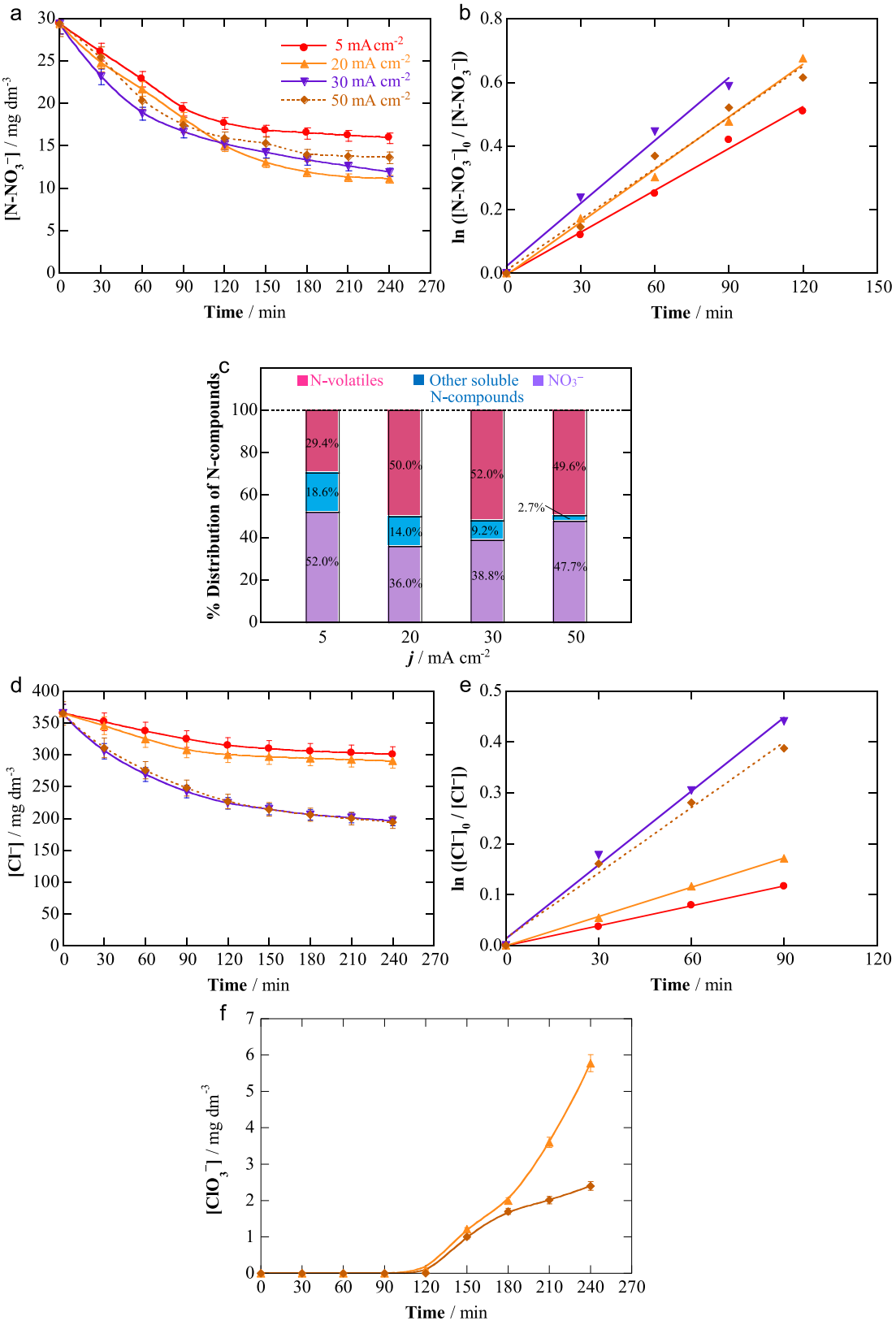

Fig. 3. Influence of current density on the time course of the concentrations of (a) $N-NO_3^-$, (d) Cl^- ion and (f) ClO_3^- ion under the same conditions as those described in Fig. 2, but using a 10 cm^2 IrO_2 anode. (b,e) First-order kinetic analysis for the data of (a) and (d). (c) Percentage distribution of the nitrogen species at the end of the above trials.

chlorine when the IrO_2 anode is employed. Chlorine promotes the oxidation of NH_4^+ to N_2 via reaction (8), alongside the re-oxidation of this ion and NO_2^- to NO_3^- via reactions (9) and (10), respectively. As a result, the overall NO_3^- electroreduction was decelerated, as shown in Fig. 3a. A complementary explanation could be given taking into account the larger ability of IrO_2 to adsorb electroactive species [12,42,43], such as NH_4^+ or NO_2^-, thus favoring their partial conversion into NO_3^-. NO_3^- electroreduction is also slowed down by the competitive reduction of H_2O to H_2, which is expected to be relatively more significant at higher *j*. The production of N-volatiles upon the action of active chlorine, as shown in reaction (8), has been well proven in the literature [19,49]. This aspect was corroborated by determining the speciation of N-containing species at the end of the above assays, on the basis of the TN measured and the absence of NH_4^+, NO_2^- and chloramines in the final solutions. Fig. 3c shows the formation of progressively higher amounts of volatile compounds with increasing *j* from 5 to 30 mA cm^{-2}, being much greater than those determined using the BDD/Fe cell (see Fig. 2c). This agrees with the different production of active chlorine in each system, along with the higher accumulation as *j* was upgraded (see below). Furthermore, the decreasing percentage of undetected soluble N-containing compounds with raising *j*, accumulated to much lesser extent as compared to the BDD/Fe cell (see Fig. 2c), suggests that they were intermediates with larger tendency to be transformed into volatiles. Formation of N_2 via reactions (4) and (8), alongside other volatiles, then seems the pre-eminent route for NO_3^- electroreduction using the IrO_2/Fe cell.

Regarding the fate of Cl^-, Fig. 3d shows a slow removal of this ion with electrolysis time, which was enhanced from 17.8% at 5 mA cm^{-2} to 46.3% at 30 mA cm^{-2} in 240 min, without further

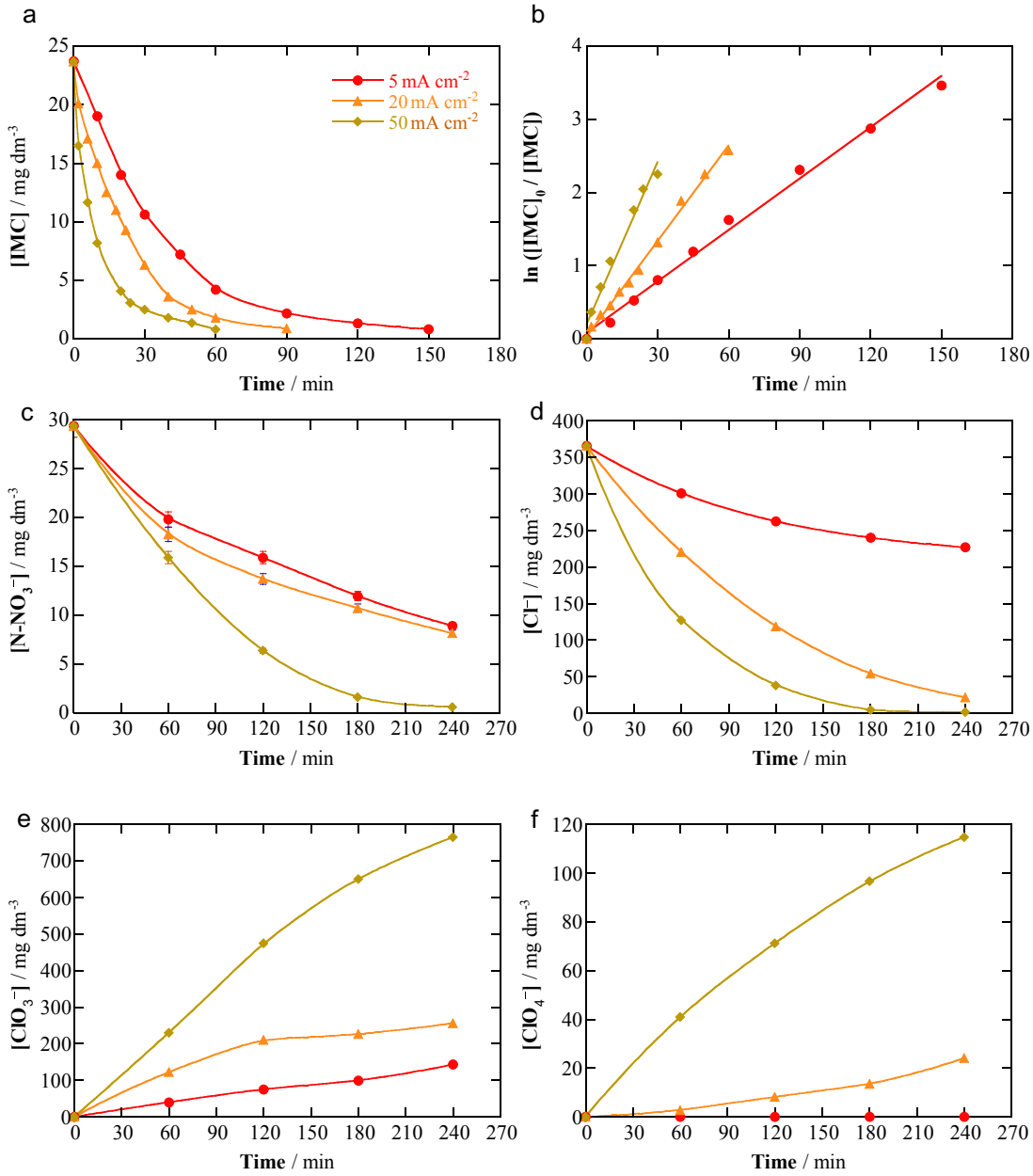

Fig. 4. Effect of current density on the variation of (a) imidacloprid concentration, (b) the corresponding pseudo-first-order kinetics, and the concentrations of (c) $N–NO_3^-$, (d) Cl^- ion, (e) ClO_3^- ion and (f) ClO_4^- ion with electrolysis time for the electrochemical treatment of 175 cm^3 of 23.7 mg dm^{-3} insecticide in the simulated water matrix at pH 6.8 and 25 °C using a BDD/Fe cell.

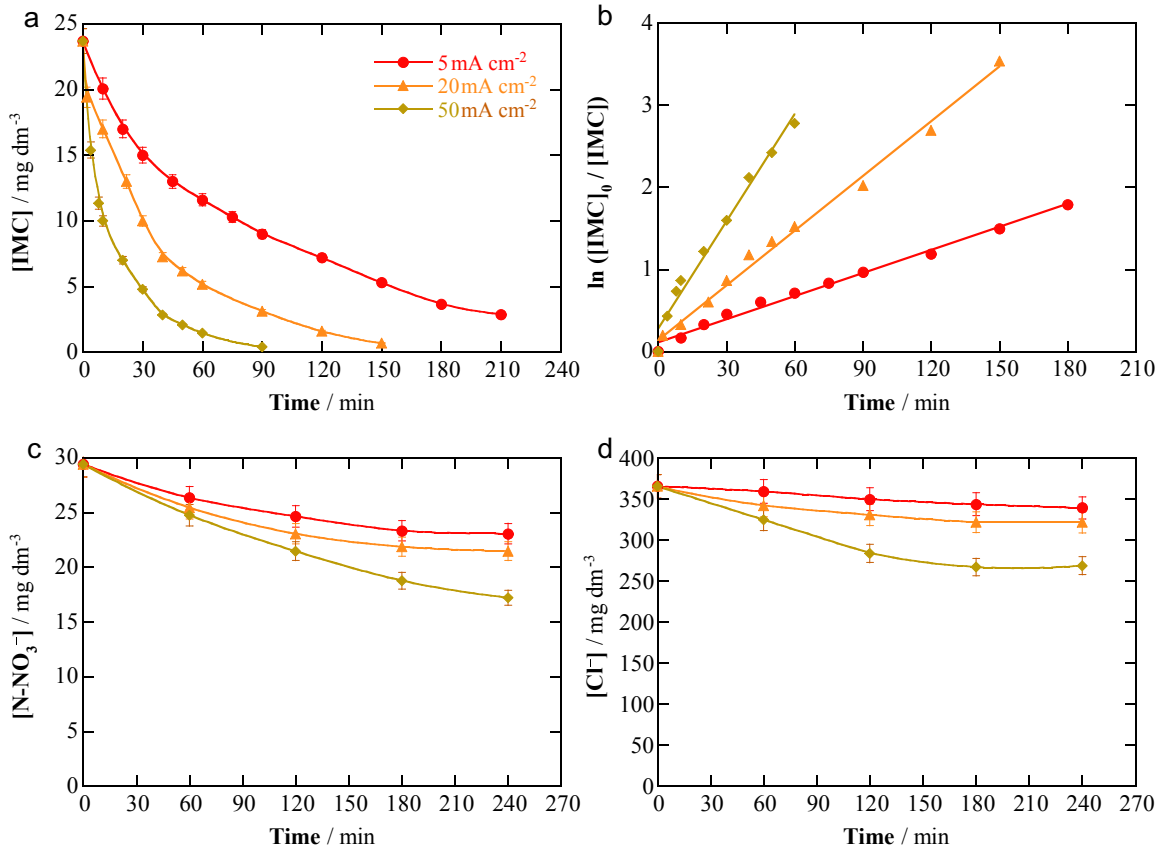

Fig. 5. Influence of current density on the change of (a) imidacloprid concentration, (b) the corresponding pseudo-first-order kinetics, and the concentrations of (c) N–NO_3^- ion and (d) Cl^- ion with electrolysis time under the same conditions of Fig. 4, but using an IrO_2/Fe cell.

acceleration at 50 mA cm^{-2}. Fig. 3e highlights that the concentration decays always obeyed a first-order kinetics, although with $k(Cl^-)$ values much lower than those found with the BDD/Fe cell (see Table 2), particularly at $j \geq 20$ mA cm^{-2}. Fig. 3f reveals the formation of small quantities of ClO_3^- at the two higher j values, whereas no ClO_4^- was detected in solution, in agreement with results reported elsewhere [19]. The lower oxidation power of the IrO_2 anode as compared to BDD can justify the smaller ability of the IrO_2/Fe cell to remove Cl^-. This active anode has higher electroactivity to convert IrO_2(•OH) formed from reaction (13) into O_2, which strongly reduces the extent of Cl^- oxidation as well as the subsequent destruction of active chlorine via reactions (14)–(16), eventually yielding low amounts of ClO_3^-. The above results described for the N–NO_3^- evolution in this cell suggest that most active chlorine is accumulated as ClO^-, which converts the N-species via reactions (8)–(10). In these reactions, Cl^- is regenerated, impeding its fast removal from the solution. Reactions (8)–(10) occur to much lesser extent using the BDD anode because active chlorine is much more rapidly transformed into ClO_3^- and ClO_4^- ions.

3.3. Paired imidacloprid electrochemical oxidation and NO_3^- electroreduction in simulated water

Once clarified the electrochemical behavior of NO_3^- and Cl^- in the softened groundwater matrix, we focus our efforts on the simultaneous EO of IMC. The paired electrolyses were performed in three different matrices: (i) simulated water with the same anionic composition as the softened groundwater, aiming to avoid the influence of NOM, (ii) the same matrix but without NO_3^-, in order to assess the influence of N-containing species over IMC destruction, and (iii) softened groundwater matrix. All the assays were carried out by spiking 23.7 mg dm^{-3} insecticide (10.0 mg dm^{-3} TOC) into each aqueous matrix at pH 6.8, by applying j values ranging between 5 and 50 mA cm^{-2} using the BDD/Fe and IrO_2/Fe cells. In these experiments, similar trends for pH, conductivity and E_{cell} as those described for the electrolyses without IMC (subsection 3.2) were found.

Fig. 4a shows the quicker abatement of IMC when increasing from 5 to 50 mA cm^{-2} using the BDD anode, as a result of its destruction with greater amounts of BDD(•OH) formed from reaction (13) and active chlorine generated from reactions (5)–(7). Total removal was achieved at gradually shorter times, decreasing from 150 to 60 min. Fig. 4b depicts that the concentration decays followed a pseudo-first-order reaction kinetics, as expected for a mass-transport controlled process like EO in which a steady content of oxidants is produced, thus reacting with the insecticide molecules. As can be seen in Table 2, a 3.2-fold increase of the corresponding apparent rate constant (k(IMC)), from 2.34×10^{-2} to 7.40×10^{-2} min^{-1}, was obtained when j changed from 5 to 50 mA cm^{-2}. This suggests a progressively greater concomitant destruction of oxidants due to the acceleration of their parasitic reactions, as for example O_2 evolution from BDD(•OH) oxidation [12,14]. Table 2 also shows that TOC was reduced by 68.2% at 5 mA cm^{-2}, rising up to 89.1% at 50 mA cm^{-2}, which corroborates the remarkable loss of oxidation power. In this case, the production of recalcitrant chloro-derivatives that are hardly destroyed by BDD(•OH) also plays a crucial role regarding the EO efficiency [12].

Fig. 4c shows the effective simultaneous NO_3^- electroreduction that occurs during the above assays, with N–NO_3^- decays increasing as: 69.7% at 5 mA cm^{-2}, 72.5% at 20 mA cm^{-2} and 97.9% at 50 mA

cm^{-2}, after 240 min of electrolysis. The results collected in Table 2 allow inferring the smaller $k(N{-}NO_3^-)$ values obtained in this simulated matrix as compared with those in softened groundwater without insecticide (see also Fig. 2a), despite the feasibility of almost total NO_3^- removal at the highest j value tested. This deceleration of NO_3^- electroreduction could be ascribed with the generation of NO_3^- from the initial N (6.5 mg dm^{-3}) of IMC [39], as well as the re-oxidation of N-containing species derived from oxidation products of this insecticide. On the other hand, Fig. 4d confirms the fast reduction of Cl^- in the simulated matrix, completely disappearing after 180 min at 50 mA cm^{-2}. The $k(Cl^-)$ values under these conditions were even greater than in the absence of the insecticide (see Table 2) due to the enhancement of reaction (5) favored by the attack of produced active chlorine over the organic matter. A good proportionality between $k(Cl^-)$ and j can be observed, informing about a similar efficiency for Cl^- removal. Fig. 4e and f reveal a large conversion of active chlorine into ClO_3^- and ClO_4^-, respectively, except at $j = 5$ mA cm^{-2} that did not yield the latter ion. At the highest j of 50 mA cm^{-2}, the initial Cl^- became completely transformed into oxychlorine ions, with 88.8% of ClO_3^- and 11.2% of ClO_4^-, corroborating the high effectiveness of reactions (14)–(16) to remove active chorine.

From these results, energy consumptions of 52.4 kWh (kg IMC)$^{-1}$ and 41.3 kWh (kg NO_3^-) were determined after 240 min at the lowest j, i.e., 5 mA cm^{-2}, using the BDD/Fe cell. These high values can be explained by the great electrode potential of the BDD anode. In such system, the anode and cathode potentials were +5.2 and −1.6 V/Ag|AgCl, respectively, meaning that the ohmic drop associated to the solution resistance only accounted for 0.6 V.

The results of Fig. 5 inform about the much lower performance of the IrO_2/Fe cell for the paired ICM electro-oxidation and NO_3^- removal. Fig. 5a shows the fast removal of IMC concentration with electrolysis time, which increased as j was raised from 5 to 50 mA cm^{-2} and always obeyed a pseudo-first-order kinetics (see Fig. 5b). However, the resulting k(IMC) values were smaller than those found using a BDD anode (see Table 2). This behavior agrees with the expected lower oxidation power of IrO_2(•OH) as compared to BDD(•OH), despite the aforementioned larger accumulation of active chlorine using the IrO_2 anode. The much smaller oxidation ability of this anode was confirmed by the null or very low mineralization degree achieved at the end of all electrolyses (see Table 2). A deceleration of $N{-}NO_3^-$ removal in the simulated matrix as compared to that in the softened groundwater without organic matter can be easily deduced by comparing the data of Figs. 3d and 5c, as well as the $k(N{-}NO_3^-)$ values given in Table 2. This phenomenon has been explained for the BDD/Fe cell. Moreover, Fig. 5d and the $k(Cl^-)$ values of Table 2 also evidence the smaller removal of Cl^- in this medium. This can be ascribed to its slower oxidation via reaction (5) due to the competitive oxidation of the insecticide on the electroactive sites of the anode.

3.4. Electrochemical oxidation of imidacloprid in simulated aqueous matrix without NO_3^-

Fig. 6a and b shows the decay of an initial concentration of 23.7 mg dm^{-3} IMC, spiked into simulated water with the same anionic composition of the softened wastewater but without NO_3^- content, at pH 6.8, by EO employing the BDD/Fe and IrO_2/Fe cells at j values between 5 and 20 mA cm^{-2}, respectively. By comparing these profiles with those obtained in simulated water with NO_3^- (see Figs. 4a and 5a), one can infer a slower insecticide removal in the case of the BDD/Fe cell. Conversely, using the IrO_2 anode, the absence of NO_3^- in the treated matrix allowed a faster IMC removal. These trends can also be established from the comparison of the k(IMC) values listed in Table 2 for 5 and 20 mA cm^{-2}. With BDD, the data of this table also highlight lower $k(Cl^-)$ values and TOC removals in the absence of NO_3^-. The decrease of the oxidation power of this cell under the latter conditions suggests that, when NO_3^- is present in the medium, some of the N-containing species produced upon NO_3^- electroreduction may attack the insecticide and its oxidation products, thus enhancing their removal and the overall mineralization process. Moreover, such N-products also react with active chlorine, accelerating Cl^- reduction from reaction (5). In contrast, when the IrO_2 anode is alternatively utilized, the greater accumulation of active chlorine in the absence of NO_3^- upgrades its oxidative attack onto ICM. The poor reactivity of IrO_2(•OH) is thus responsible for the preponderant role of active chlorine during IMC removal with IrO_2. This effect was much less significant with BDD because of the much greater oxidation ability of BDD(•OH).

3.5. Paired imidacloprid electrochemical oxidation and NO_3^- electroreduction in softened groundwater

Finally, the treatment of 23.7 mg dm^{-3} IMC was carried out in the softened groundwater (11.8 mg dm^{-3} TOC, which includes IMC and NOM) at pH 6.8 using both electrolytic cells at 5 mA cm^{-2}. This low j value was chosen to prevent the formation of toxic ClO_4^- with the BDD anode. Fig. 7a–c shows the superior IMC, $N{-}NO_3^-$ and Cl^- decays obtained with the BDD/Fe cell, reaching the total insecticide removal at 210 min, in agreement with the results described in subsection 3.3 in the simulated water. Nevertheless, a closer look at Table 2 confirms that the k(IMC), $k(N{-}NO_3^-)$ and $k(Cl^-)$ values obtained with both cells in the softened groundwater were significantly lower than those in the simulated water. The same feature

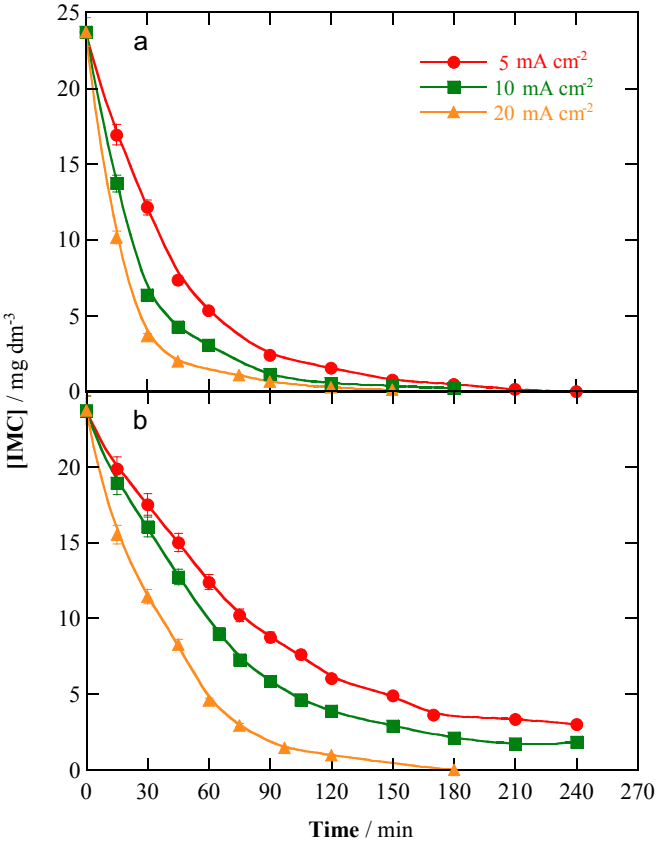

Fig. 6. Effect of current density on imidacloprid concentration vs. electrolysis time for the EO treatment of 175 cm^3 of 23.7 mg dm^{-3} insecticide in the simulated water matrix without NO_3^- at pH 6.8 and 25 °C using a (a) BDD/Fe cell and (b) IrO_2/Fe cell.

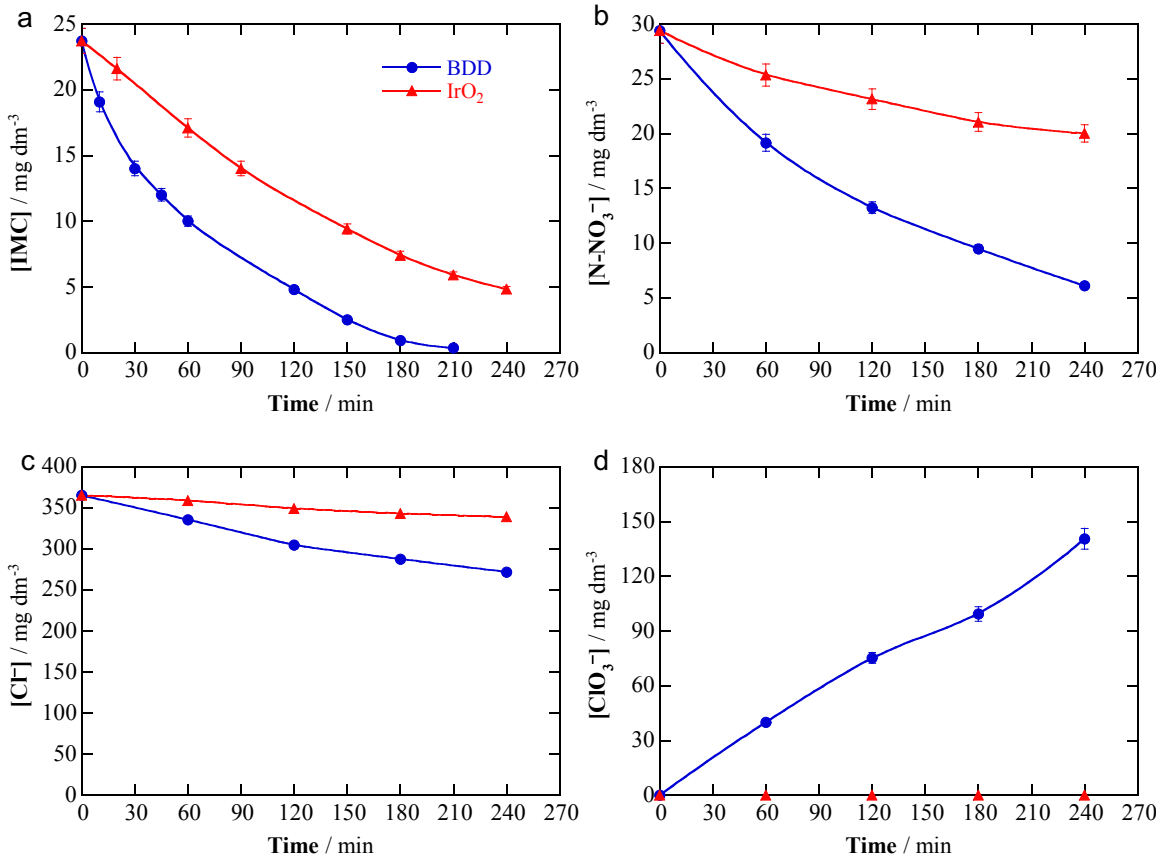

Fig. 7. Time course of (a) imidacloprid, (b) N–NO_3^-, (c) Cl^- and (d) ClO_3^- concentrations for the electrochemical treatment, with BDD or IrO_2 anode, of 175 cm^3 of 23.7 mg dm^{-3} insecticide in softened groundwater at pH 6.8, 25 °C, and $j = 5$ mA cm^{-2}.

can be deduced for the percentage of TOC removed using BDD, although a higher amount of TOC, i.e., 7.3 mg dm^{-3} vs. 6.8 mg dm^{-3}, was destroyed in the former medium because of the concomitant NOM mineralization. This was corroborated by the loss of a small quantity of 1.1 mg dm^{-3} TOC (8.9%) when using the IrO_2 anode, which can be ascribed to the partial destruction of the initial NOM content (1.8 mg dm^{-3}). The lower ability of the cells to remove IMC in the softened groundwater can then be related to the parallel oxidation of NOM, which partly consumes the oxidizing M(•OH) and active chlorine produced. In the case of BDD, however, the NOM oxidation had a small effect on NO_3^- electroreduction and Cl^- electro-oxidation, as deduced from the analogous $k(N–NO_3^-)$ and $k(Cl^-)$ values found in softened groundwater without and with the insecticide (see Table 2). In contrast, much smaller $k(N–NO_3^-)$ and $k(Cl^-)$ values were determined in the presence of IMC using the IrO_2 anode, which can be associated with a great consumption of active chlorine by NOM since the action of IrO_2(•OH) was much milder. All these findings allow concluding the good performance of the BDD/Fe cell to ensure the paired IMC electro-oxidation and NO_3^- electroreduction in actual groundwater. A final content of 27.0 mg dm^{-3} NO_3^- was finally reached (see Fig. 7b), lower than the 50 mg dm^{-3} established by the WHO guideline for human consumption. Under these conditions, ClO_3^- was accumulated in the final solutions attaining 140.5 mg dm^{-3} after 240 min of electrolysis, as shown in Fig. 7d. This accounts for 64.2% of the removed Cl^-.

3.6. Primary oxidation by-products of imidacloprid

Fig. 8 presents a reaction sequence proposed for the initial degradation of IMC (**1**) that includes all the heteroaromatic products detected by GC-MS after 60 min of EO treatment of 23.7 mg dm^{-3} insecticide spiked into the softened groundwater matrix, using a BDD or IrO_2 anode at 5 mA cm^{-2}. The initial attack of M(•OH) over **1** causes: (i) the release of the terminal $-NO_2$ group to yield **2** (1-[(6-chloro-3-pyridyl)methyl]imidazolidine-2-imine, m/z 209 (^{35}Cl)) and (ii) the loss of the $-NH-NO_2$ group to form **3** (2-chloro-5-(4,5-dihydroimidazol-1-ylmethyl)-pyridine, m/z 195 (^{35}Cl)), whose imidazole group is subsequently opened to produce **4** ((6-chloro-3-pyridyl)methyl)-(2-imino-ethylidene)-amine, m/z 182 (^{35}Cl). The terminal =NH group of compound **2** is then oxidized to a $=N^+=O$ one yielding **5** (1-[(6-chloro-3-pyridyl) methyl]imidazolidine-2-oxime, m/z 225 (^{35}Cl)), which undergoes further denitrozation leading to **6** (1-[(6-chloro-3-pyridyl)methyl] imidazolidin-2-one, m/z 211 (^{35}Cl)). Compound **6** can also be produced from direct oxidation of compound **2**. The subsequent degradation of these heteroaromatics involves the cleavage of the imidazole group to yield **7** (6-chloronicotinonitrile, m/z 138 (^{35}Cl)), whose nitrile group is then converted into a carbaldehyde one to yield **8** (6-chloronicotinoaldehyde, m/z 140 (^{35}Cl)). On the other hand, the imidazole group can also be released and oxidized to form **9** (imidazolidine-2,4,5-trione, m/z 114). Note that compound **5** has been identified during the IMC treatment in sulfate medium by EO with Pt or BDD and EF with the same anodes and a carbon felt cathode [39], whereas the formation of compound **6** has been reported for the photo-Fenton and TiO_2 photocatalysis treatment of IMC solutions [50,51]. Chlorinated by-products were not detected and, in case of formation, they would be gradually degraded in the BDD/Fe cell.

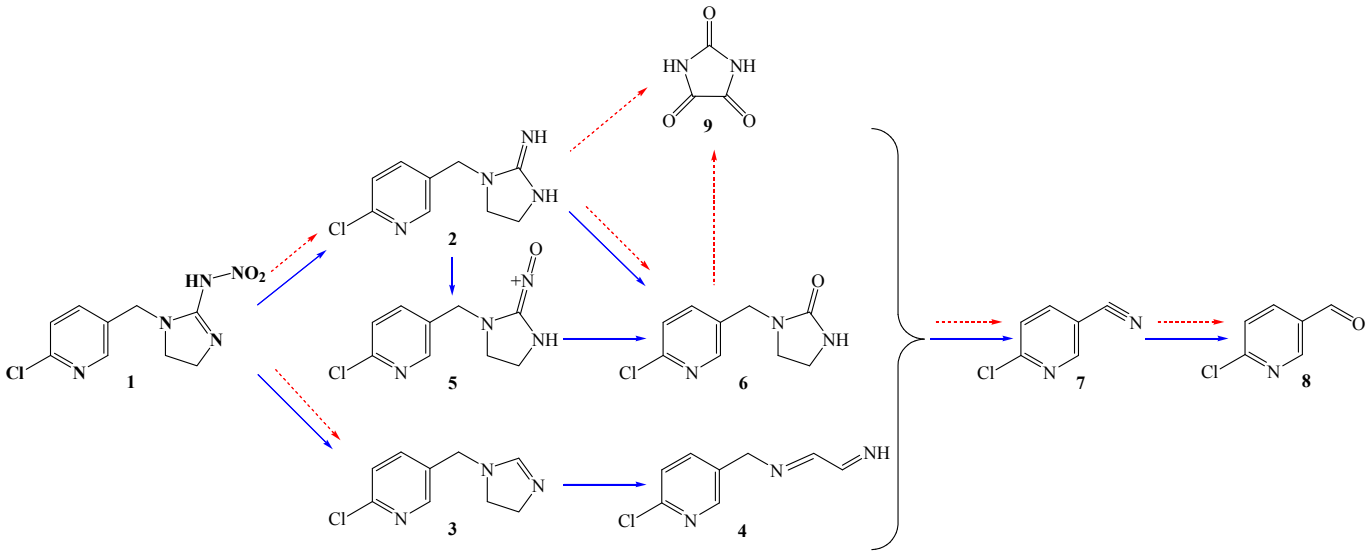

Fig. 8. Reaction sequence for the initial degradation of imidacloprid in softened groundwater. Solid arrows correspond to intermediates found in the BDD/Fe cell, whereas dashed arrows are used for those identified in the IrO_2/Fe cell.

4. Conclusions

The BDD/Fe cell outperformed the IrO_2/Fe one for the paired IMC electro-oxidation and NO_3^- electroreduction in all the aqueous matrices tested. Fe cathode showed greater electrocatalytic activity than SS. The main drawback of cells equipped with BDD anode is the co-generation of ClO_3^- and ClO_4^-, whose concentration may be minimized by working at low j values. The NO_3^- and Cl^- decays agreed with a first-order kinetics, whereas IMC removals followed a pseudo-first-order kinetics. By electrolyzing the softened groundwater without insecticide in the BDD/Fe cell, total NO_3^- removal was already achieved at $j \geq 10$ mA cm^{-2}, with a large conversion into soluble N-compounds and, to lesser extent, into N-volatiles. Similar NO_3^- decays were found in the presence of IMC, indicating that the EO process did not interfere in the electroreduction process. However, a clear influence of NOM was observed, since NO_3^- removal was clearly decelerated in its presence. The decay of 23.7 mg dm^{-3} IMC in the BDD/Fe cell was accelerated in the presence of NO_3^-, since some of the N-products formed from this ion attacked the parent molecule, alongside BDD(•OH) and active chlorine. The presence of NOM caused a slower IMC removal due to partial consumption of oxidants. Under these conditions and operating at a low $j = 5$ mA cm^{-2}, ICM was completely removed in 210 min, whereas after 240 min of electrolysis, 61.5% of TOC was removed and NO_3^- concentration was reduced to 27.0 mg dm^{-3}, becoming suitable for human consumption. The EO process generated 140.5 mg dm^{-3} ClO_3^-. A reaction sequence for the initial IMC degradation in softened groundwater has been proposed.

Acknowledgments

The authors thank the financial support from project CTQ2016-78616-R (AEI/FEDER, EU). R. Oriol acknowledges the FPI grant awarded by MINECO (Spain).

References

[1] M. Gutiérrez, R.N. Biagioni, M.T. Alarcón-Herrera, B.A. Rivas-Lucero, An overview of nitrate sources and operating processes in arid and semiarid aquifer systems, Sci. Total Environ. 624 (2018) 1513–1522.
[2] M. Duca, M.T.M. Koper, Powering denitrification: the perspectives of electrocatalytic nitrate reduction, Energy Environ. Sci. 5 (2012) 9726–9742.
[3] M. Zhou, W. Fu, H. Gu, L. Lei, Nitrate removal from groundwater by a novel three-dimensional electrode biofilm reactor, Electrochim. Acta 52 (2007) 6052–6059.
[4] M. Shrimali, K.P. Singh, J. Greeley, New methods of nitrate removal from water, Environ. Pollut. 112 (2001) 351–359.
[5] E. Herrero-Hernández, M.S. Rodríguez-Cruz, E. Pose-Juan, S. Sánchez-González, M.S. Andrades, M.J. Sánchez-Martín, Seasonal distribution of herbicide and insecticide residues in the water resources of the vineyard region of La Rioja (Spain), Sci. Total Environ. 609 (2017) 161–171.
[6] M.L. Hladik, S. Bradbury, L.A. Schulte, M. Helmers, C. Witte, D.W. Kolpin, J.D. Garrett, M. Harris, Neonicotinoid insecticide removal by prairie strips in row-cropped watersheds with historical seed coating use, Agric. Ecosyst. Environ. 241 (2017) 160–167.
[7] European Commission, First Watch List for Emerging Water Pollutants, https://ec.europa.eu/jrc/en/news/first-watch-list-emerging-water-pollutants (last access, June 7, 2018).
[8] J.C.G. Sousa, A.R. Ribeiro, M.O. Barbosa, M.F.R. Pereira, A.M.T. Silva, A review on environmental monitoring of water organic pollutants identified by EU guidelines, J. Hazard Mater. 344 (2018) 146–162.
[9] Komal, A review: immunological and biochemical studies on imidacloprid toxicity, Pharmaceut. Innovat. 7 (4) (2018) 999–1002.
[10] A.M. Sadaria, R. Sutton, K.D. Moran, J. Teerlink, J.V. Jackson, R.U. Halden, Passage of fiproles and imidacloprid from urban pest control uses through wastewater treatment plants in northern California, USA, Environ. Toxicol. Chem. 36 (2017) 1473–1482.
[11] M.A. Daam, A.C. Santos Pereira, E. Silva, L. Caetano, M.J. Cerejeira, Preliminary aquatic risk assessment of imidacloprid after application in an experimental rice plot, Ecotoxicol. Environ. Saf. 97 (2013) 78–85.
[12] C.A. Martínez-Huitle, M.A. Rodrigo, I. Sirés, O. Scialdone, Single and coupled electrochemical processes and reactors for the abatement of organic water pollutants: a critical review, Chem. Rev. 115 (2015) 13362–13407.
[13] J. Martínez, A. Ortiz, I. Ortiz, State-of-the-art and perspectives of the catalytic and electrocatalytic reduction of aqueous nitrates, Appl. Catal. B: Environ. 207 (2017) 42–59.
[14] F.C. Moreira, R.A.R. Boaventura, E. Brillas, V.J.P. Vilar, Electrochemical advanced oxidation processes: a review on their application to synthetic and real wastewaters, Appl. Catal. B: Environ. 202 (2017) 217–261.
[15] N. Flores, E. Brillas, F. Centellas, R.M. Rodríguez, P.L. Cabot, J.A. Garrido, I. Sirés, Treatment of olive oil mill wastewater by single electrocoagulation with different electrodes and sequential electrocoagulation/electrochemical Fenton-based processes, J. Hazard Mater. 347 (2018) 58–66.
[16] Z. Ye, J.R. Steter, F. Centellas, P.L. Cabot, E. Brillas, I. Sirés, Photoelectro-Fenton as post-treatment for electrocoagulated benzophenone-3-loaded synthetic and urban wastewater, J. Clean. Prod. 208 (2019) 1393–1402.
[17] M. Li, C. Feng, Z. Zhang, X. Lei, R. Chen, Y. Yang, N. Sugiura, Simultaneous reduction of nitrate and oxidation of by-products using electrochemical method, J. Hazard Mater. 171 (2009) 724–730.
[18] E. Lacasa, P. Cañizares, J. Llanos, M.A. Rodrigo, Effect of the cathode material on the removal of nitrates by electrolysis in non-chloride media, J. Hazard Mater. 213–214 (2012) 478–484.
[19] E. Lacasa, J. Llanos, P. Cañizares, M.A. Rodrigo, Electrochemical denitrification with chlorides using DSA and BDD anodes, Chem. Eng. J. 184 (2012) 66–71.
[20] Y.F. Ning, Y.P. Chen, Y. Shen, Y. Tang, J.S. Guo, F. Fang, S.Y. Liu, Directly

determining nitrate under wide pH range condition using a Cu-deposited Ti electrode, J. Electrochem. Soc. 160 (2013) H715–H719.
[21] K. Govindan, M. Noel, R. Mohan, Removal of nitrate ion from water by electrochemical approaches, J. Water Process Eng. 6 (2015) 58–63.
[22] X. Ma, M. Li, C. Feng, W. Hu, L. Wang, X. Liu, Development and reaction mechanism of efficient nano titanium electrode: reconstructed nanostructure and enhanced nitrate removal efficiency, J. Electroanal. Chem. 782 (2016) 270–277.
[23] L. Wang, M. Li, X. Liu, C. Feng, N. Chen, W. Hu, Design and applications of Ti nano-electrode for denitrification of groundwater, Environ. Technol. 38 (2017) 3055–3063.
[24] W. Teng, N. Bai, Y. Liu, Y. Liu, J. Fan, W.-X. Zhang, Selective nitrate reduction to dinitrogen by electrocatalysis on nanoscale iron encapsulated in mesoporous carbon, Environ. Sci. Technol. 52 (2018) 230–236.
[25] J.R. Steter, E. Brillas, I. Sirés, On the selection of the anode material for the electrochemical removal of methylparaben from different aqueous media, Electrochim. Acta 222 (2016) 1464–1474.
[26] I. Sirés, E. Brillas, G. Cerisola, M. Panizza, Comparative depollution of mecoprop aqueous solutions by electrochemical incineration using BDD and PbO_2 as high oxidation power anodes, J. Electroanal. Chem. 613 (2008) 151–159.
[27] N. Borràs, R. Oliver, C. Arias, E. Brillas, Degradation of atrazine by electrochemical advanced oxidation processes using a boron-doped diamond anode, J. Phys. Chem. A 114 (2010) 6613–6621.
[28] A.R.F. Pipi, I. Sirés, A.R. De Andrade, E. Brillas, Application of electrochemical advanced oxidation processes to the mineralization of the herbicide diuron, Chemosphere 109 (2014) 49–55.
[29] F. Gozzi, I. Sirés, A. Thiam, S.C. de Oliveira, A. Machulek Jr., E. Brillas, Treatment of single and mixed pesticide formulations by solar photoelectro-Fenton using a flow plant, Chem. Eng. J. 310 (2017) 503–513.
[30] D.R.V. Guelfi, F. Gozzi, A. Machulek Jr., I. Sirés, E. Brillas, S.C. de Oliveira, Degradation of herbicide S-metolachlor by electrochemical AOPs using a boron-doped diamond anode, Catal. Today 313 (2018) 182–188.
[31] A. Kesraoui, N. Oturan, N. Bellakhal, M.A. Oturan, Remediation of water contaminated with pesticides by indirect electrochemical oxidation process electro-Fenton, J. Adv. Oxid. Technol. 11 (2018) 276–282.
[32] D.R.V. Guelfi, E. Brillas, F. Gozzi, A. Machulek Jr., S.C. de Oliveira, I. Sirés, Influence of electrolysis conditions on the treatment of herbicide bentazone using artificial UVA radiation and sunlight. Identification of oxidation products, J. Environ. Manag. 231 (2019) 213–221.
[33] D.R.V. Guelfi, Z. Ye, F. Gozzi, S.C. de Oliveira, A. Machulek Jr., E. Brillas, I. Sirés, Ensuring the overall combustion of herbicide metribuzin by electrochemical advanced oxidation processes. Study of operation variables, kinetics and degradation routes, Separ. Purif. Technol. 211 (2019) 637–645.
[34] C.M. Dominguez, N. Oturan, A. Romero, A. Santos, M.A. Oturan, Removal of lindane wastes by advanced electrochemical oxidation, Chemosphere 202 (2018) 400–409.
[35] R. Oriol, D. Clematis, E. Brillas, J.L. Cortina, M. Panizza, I. Sirés, Groundwater treatment using a solid polymer electrolyte cell with mesh electrodes, ChemElectroChem 6 (2019) 1235–1243.
[36] M.B. Brahim, H.B. Ammar, R. Abdelhedi, Y. Samet, Electrochemical removal of the insecticide imidacloprid from water on a boron-doped diamond and Ta/PbO_2 anodes using anodic oxidation process, Korean J. Chem. Eng. 33 (2016) 2602–2609.
[37] L.M. Silva, R.P.A. dos Santos, C.C.O. Morais, C.L. Vasconcelos, C.A. Martínez-Huitle, S.S.L. Castro, Anodic oxidation of the insecticide imidacloprid on mixed metal oxide (RuO_2-TiO_2 and IrO_2-RuO_2-TiO_2) anodes, J. Electrochem. Soc. 164 (2017) E489–E495.
[38] H. Zhao, Y. Wang, Y. Wang, T. Cao, G. Zhao, Electro-Fenton oxidation of pesticides with a novel Fe_3O_4@Fe_2O_3/activated carbon aerogel cathode: high activity, wide pH range and catalytic mechanism, Appl. Catal. B: Environ. 125 (2012) 120–127.
[39] M. Turabik, N. Oturan, B. Gözmen, M.A. Oturan, Efficient removal of insecticide "imidacloprid" from water by electrochemical advanced oxidation processes, Environ. Sci. Pollut. Res. 21 (2014) 8387–8397.
[40] H. Zhao, L. Qian, Y. Chen, Q. Wang, G. Zhao, Selective catalytic two-electron O_2 reduction for onsite efficient oxidation reaction in heterogeneous electro-Fenton process, Chem. Eng. J. 332 (2018) 486–498.
[41] M.A. Nasser Ghalwa, B. Nader Farhat, Removal of imidacloprid pesticide by electrocoagulation process using iron and aluminum electrodes, J. Environ. Anal. Chem 2 (2015), 1000154.
[42] B. Marselli, J. Garcia-Gomez, P.A. Michaud, M.A. Rodrigo, C. Comninellis, Electrogeneration of hydroxyl radicals on boron-doped diamond electrodes, J. Electrochem. Soc. 150 (2003) D79–D83.
[43] A. Galia, S. Lanzalaco, M.A. Sabatino, C. Dispenza, O. Scialdone, I. Sirés, Crosslinking of poly(vinylpyrrolidone) activated by electrogenerated hydroxyl radicals: A first step towards a simple and cheap synthetic route of nanogel vectors, Electrochem. Commun. 62 (2016) 64–68.
[44] I. Sirés, E. Brillas, M.A. Oturan, M.A. Rodrigo, M. Panizza, Electrochemical advanced oxidation processes: today and tomorrow. A review, Environ. Sci. Pollut. Res. 21 (2014) 8336–8367.
[45] APWA, AWWA, WEF, Standard methods for the examination of water and wastewater, in: Method Number 4500-Cl Chlorine (Residual)–G. DPD Colorimetric Method, twenty-first ed., American Public Health Association, Washington D.C., 2005, pp. 4–67, and 4–68.
[46] A. Thiam, I. Sirés, J.A. Garrido, R.M. Rodríguez, E. Brillas, Effect of anions on electrochemical degradation of azo dye Carmoisine (Acid Red 14) using a BDD anode and air-diffusion cathode, Separ. Purif. Technol. 140 (2015) 43–52.
[47] J.R. Steter, E. Brillas, I. Sirés, Solar photoelectro-Fenton treatment of a mixture of parabens spiked into secondary treated wastewater effluent at low input current, Appl. Catal. B: Environ. 224 (2018) 410–418.
[48] I. Katsounaros, D. Ipsakis, C. Polatides, G. Kyriacou, Efficient electrochemical reduction of nitrate to nitrogen on tin cathode at very high cathode potentials, Electrochim. Acta 52 (2006) 1329–1338.
[49] A. Kapałka, L. Joss, A. Anglada, C. Comninellis, K.M. Udert, Direct and mediated electrochemical oxidation of ammonia on boron-doped diamond electrode, Electrochem. Commun. 12 (2010) 1714–1717.
[50] A. Agüera, E. Almansa, S. Malato, M.I. Maldonado, A.R. Fernández-Alba, Evaluation of photocatalytic degradation of imidacloprid in industrial water by GC-MS and LC-MS, Analysis 26 (1998) 245–251.
[51] S. Malato, J. Caceres, A. Agüera, M. Mezcua, D. Hernando, J. Vial, A.R. Fernández-Alba, Degradation of imidacloprid in water by photo-Fenton and TiO_2 photocatalysis at a solar pilot plant: a comparative study, Environ. Sci. Technol. 35 (2001) 4359–4366.

4.3. Paired electrochemical removal of nitrate and terbuthylazine pesticide from groundwater using mesh electrodes

The TBZE pesticide, an s-triazine pesticide widely used in Spain, Italy and Portugal, (see details in subsection 1.1.5), has a low solubility in water but a high affinity for the soil, persisting for a long time and being leached into GW and surface water along with its metabolites. Its removal in aqueous matrices was previously studied by non-destructive physical methods and by advanced oxidation methods, both electrochemical and non-electrochemical.

This work was focused on the study of the elimination of TBZE by single EO process, the removal of nitrate by ER and the combined EO/ER process to remove both pollutants simultaneously. The trials were carried out in actual softened GW with around 100 mg L^{-1} of nitrate and in simulated GW mimicking its anion content and/or with TBZE pesticide spiked at 5 mg L^{-1}. Galvanostatic electrolyses were carried out with 500 mL of aqueous solutions at pH ranging from 4.0 to 10.5 in an SCC tank reactor described above, equipped with RuO_2 or BDD anodes and one or two mild DC01 steel cathodes. All of them were mesh electrodes, and a current ranging between 250 and 1000 mA was applied. Mass balances were made for the initial chlorine and nitrogen contents in the solutions. Chlorine was present in the pesticide molecule as well as in the medium in the form of chloride. Nitrogen was also present in the pesticide molecule and also and in the medium in the form of nitrate.

The final speciation of chlorine resulted in chloride, chlorate, perchlorate and active chlorine species. Higher concentration of active chlorine was found when using the RuO_2 anode, whereas when BDD was employed, a lower concentration of active chlorine was accumulated, but accompanied with the production of large amounts of chlorate and perchlorate. In addition, the effect of doubling the cathode area by adding another iron mesh on the overall process was studied. In such experiments, a lower current density but with more electroactive area was applied, which was intended to be beneficial based on the results obtained in the previous study of simultaneous elimination of nitrate and IMC. After the study of all the parameters described above, the system of two iron electrodes as cathodes (70 cm^2) and the BDD electrode as anode (35 cm^2) was chosen,

since they presented a greater capacity for the simultaneous removal of the pesticide. This occurred at the expense of accumulating toxic chlorinated spices, such as chlorate and perchlorate in the solution. An ion-exchange resin based on quaternary amines was used to capture the chlorate and perchlorate anions, releasing chloride into the medium, thus increasing the quality of the final water. Characterization of the raw GW without decalcification, softened GW with pH increased using sodium hydroxide, electrolyzed GW and post-treated GW is summarized in **Table 1** (see the related paper). The results obtained in this work for the kinetic study of nitrate, chloride and TBZE removal, as well as the energy consumption are summarized in **Table 2**. The work is organized based on the main operation parameters: pH (4, 7 and 10.5), applied current (250, 500 and 1000 mA) and the nature of the water matrix (i.e., simulated GW in the absence and presence of chloride anion for nitrate removal; ultrapure water with sodium sulfate as supporting electrolyte spiked with the pesticide; simulated GW in the absence and presence of chloride anion for simultaneous TBZE and nitrate removal by EO/ER; and softened GW for simultaneous TBZE and nitrate removal using the same current density but employing single or double cathode area).

Nitrate removal by ER was assessed first at 500 mA in a chloride-free GW at different pH values between 4 and 10.5, aiming at studying the effect of the anode on the nitrate kinetics. **Figure 1** reveals that the BDD anode yielded relatively similar values within all the pH interval, but RuO_2 showed dramatic differences depending on the initial pH, revealing a much lower activity for nitrate removal at circumneutral pH. The nitrate removal takes place at the cathode surface and using RuO_2, the highest value was achieved at pH = 4. The re-oxidation of the reduced products was faster at pH 7 than 10.5, resulting in a much lower overall denitrification process.

The effect of chloride contained in the simulated GW was studied at different pH values using the same current of 500 mA, using BDD or RuO_2, in a similar way as that described in a chloride free synthetic matrix. **Figure 2** shows that using BDD, the presence of chloride allowed slightly higher decay rates for nitrate, owing to the lower generation of active chlorine. In addition, a small amount of ammonia was accumulated as by-product, promoting N-containing volatile species. In the case of the RuO_2 anode, a higher promotion of active chlorine clearly had a negative effect on the overall nitrate and soluble N-containing species removal, since the re-oxidation of nitrate degradation by-

products occurred (reactions (17), (21) and (22)). With this anode, the change of the initial pH had clear effect on the reactivity with ammonia generated from nitrate ER, because ammonia or ammonium accumulation and the speciation of active chlorine species (reactions (13-15)) depend on pH. The chlorine-containing anions showed similar trends at the different initial pH values, but a large dependence was observed for the current efficiency. The effect of the applied current was assessed for one of the best conditions, with a BDD anode and an initial acidic pH of 4. A greater nitrate removal was determined at higher current, but clearly loosing efficiency by increasing from 250 to 1000 mA. A 4-fold increase of the applied current was accompanied by only a 2-fold rise in the rate constant for nitrate removal. Higher amounts of chlorate ion were gradually oxidized to perchlorate when BDD was used, owing to its higher oxidation power as compared with RuO_2 (**Figure 3**).

Ammonia and nitrate were generated as by-products of TBZE degradation. TBZE-DE as a main aromatic by-product and oxamic, oxalic and cyanuric acids were detected and quantified, as shown in **Figure 4**. The removal of TBZE and nitrate was modified in the presence of both pollutants, and affected the generation of *N*-tert-buthyl-*N'*-[1,3,5]triazin-2,4-diamine by-product as a first step reduction process competing with the destruction of the pesticide by EO (**Figure 5**). Although nitrate removal was lower at pH 4 in the chloride-free aqueous matrix, BDD showed an exceptional performance to degrade TBZE when compared with RuO_2.

Electrolyses of chloride-containing simulated GW, containing spiked TBZE, allowed studying the effect on nitrate and pesticide content removal at different pH (4, 7, 10.5) and current (250, 500 and 1000 mA) values, as can be seen in **Figure 6** and **Figure 7** for the cells with BDD and RuO_2 anodes, respectively. Similar results to those obtained in the absence of TBZE were achieved for nitrate abatement, being slightly worse than those obtained in its presence. With the BDD electrode, both pollutants followed similar trends, decreasing their decay at higher pH and lower current. With the RuO_2 anode, the rise in current dramatically increased the removal rate of the pesticide, regardless of the initial pH of the solution, reaching total abatement in 40 min. This occurred because the main mechanism for TBZE oxidation was its homogeneous reaction with active chlorine species generated at its surface. The overpotential was much lower than that needed with BDD anode, resulting in a larger amount of active chlorine species at the same current.

In the absence of the pesticide, the nitrate removal varied with pH in the order: 4, 10.5 and 7, being always worse than using the BDD anode. The release of N-containing volatile species was much lower than using BDD due to the re-oxidation of nitrate, as pointed out above. The maximum active chlorine accumulation was determined at the beginning of the experiment and increased at greater current in both cells, being the values much higher with RuO_2. In contrast, the amount of chlorate accumulated from the EO of the active chlorine species with the RuO_2 anode did not show any significant change with the initial pH, and it was higher than that achieved with the BDD anode, increasing much more upon current increase. Moreover, when employing the BDD anode, high amounts of toxic perchlorate anion were generated by the EO of chlorate anion. An ion-exchange resin based on quaternary amines showed a great effectiveness to lower the chlorate and perchlorate concentrations of the electrolyzed softened GW, from 59 and 767 mg L^{-1}, respectively, to around 4 mg L^{-1} of chlorate in the final post-treated softened GW. In turn, the chloride concentration rose from 42 to 712 mg L^{-1}.

The electrolyses of the softened GW showed worse nitrate and TBZE removals over time when compared with those attained in the synthetic water matrix. The presence of NOM present in the softened GW, the competitive adsorption of NOM over the cathode surface and the partial scavenging of hydroxyl and hydrogen radicals caused interferences in the ER and EO processes. **Figure 8** depicts the evolution of all the species detected in the simulated GW using 1 BDD anode and two Fe cathodes, along with the results for the treatment of actual GW without TBZE using just one Fe cathode.

The following 10 primary derivatives were detected by GC-MS, as listed in **Table 3** of the related paper: *N*-tert-buthyl-*N'*-[1,3,5]triazin-2,4-diamine, 4-tert-butylamino-6-vinylamino-[1,3,5]triazin-2-ol, desethyl-terbuthylazine (DE-TBZE), *N*-(4-tert-butylamino-6-chloro-[1,3,5]trazin-2-yl)-acetamide, 6-chloro-*N*-ethyl-[1,3,5]triazin-2,4-diamine, 4-amino-6-isopropenylamino-[1,3,5]triazin-2-ol, *N*-(4-tert-butylamino-6-chloro-[1,3,5]trazin-2-yl)-2-hydroxyacetamide, *N*-(4-amino-6-chloro-[1,3,5]trazin-2-yl)-acetamide, 6-chloro-[1,3,5]triazin-2,4-diamine and cyanuric acid. Finally, the initial pathways for TBZE degradation to cyanuric acid using BDD in the presence and absence of chloride are proposed in **Figure 9**. Final short-linear carboxylic acids like oxamic and oxalic acid were also detected and quantified by HPLC.

Electrochimica Acta 383 (2021) 138354

Contents lists available at ScienceDirect

Electrochimica Acta

journal homepage: www.elsevier.com/locate/electacta

Paired electrochemical removal of nitrate and terbuthylazine pesticide from groundwater using mesh electrodes

Roger Oriol[a,1], Enric Brillas[a,1], Pere L. Cabot[a,1], José L. Cortina[b,c], Ignasi Sirés[a,1,*]

[a] Laboratori d'Electroquímica dels Materials i del Medi Ambient, Departament de Química Física, Facultat de Química, Universitat de Barcelona, Martí i Franquès 1-11, 08028 Barcelona, Spain

[b] Chemical Engineering Department, Escola d'Enginyeria de Barcelona Est (EEBE), Universitat Politècnica de Catalunya (UPC)-BarcelonaTECH, Eduard Maristany 10-14, Campus Diagonal-Besòs, 08930 Barcelona, Spain

[c] Barcelona Research Center for Multiscale Science and Engineering, Campus Diagonal-Besòs, 08930 Barcelona, Spain

ARTICLE INFO

Article history:
Received 1 March 2021
Revised 30 March 2021
Accepted 3 April 2021
Available online 9 April 2021

Keywords:
Boron-doped diamond anode
Electrochemical oxidation
Electrodenitrification
Groundwater
Iron cathode

ABSTRACT

Groundwater is one of the main freshwater resources on Earth, but its contamination with NO_3^- and pesticides jeopardizes its viability as a source of drinking water. In this work, a detailed study of single electro-oxidation (EO) and electrodenitrification and paired EO/electrodenitrification processes has been undertaken with simulated and actual groundwater matrices containing 100 mg dm^{-3} NO_3^- and/or 5 mg dm^{-3} terbuthylazine pesticide. Galvanostatic electrolyses were made with 500 cm^3 of solutions at pH 4.0-10.5 and 250-1000 mA in tank reactors with a RuO_2 or boron-doped diamond (BDD) anode and one or two Fe cathodes, all of them in the form of meshes. Most of NO_3^- removals agreed with a pseudo-first-order kinetics. In Cl^--free media, NH_4^+ predominated as electroreduction product. In chloride media, a greater amount of N-volatiles was determined alongside a slower electrodenitrification, especially with RuO_2 due to the partial re-oxidation of electroreduction products like NH_4^+ by active chlorine. The pesticide decays were also fitted to a pseudo-first order kinetics, and its presence led to a smaller release of N-volatiles. Overall, BDD always favored the pesticide degradation thanks to the action of BDD(•OH), whereas RuO_2 was preferred for electrodenitrification under some conditions. The EO/electrodenitrification of groundwater was successful once the matrix was softened to minimize its hardness. The NO_3^- concentration was reduced below the limit established by the WHO. Overall, the BDD/Fe cell was more suitable than the RuO_2/Fe cell because it accelerated the pesticide removal with a simultaneous high degree of NO_3^- electroreduction. However, it produced toxic chlorate and perchlorate. A final post-treatment with an anion exchange resin ensured a significant removal of both ions, thus increasing the viability of the electrochemical approach to treat this type of water. Chromatographic analyses revealed the formation of ten heteroaromatic products like desethyl-terbuthylazine and cyanuric acid, alongside oxalic and oxamic as final short-chain carboxylic acids.

1. Introduction

NO_3^- ion and pesticides are the main pollutants of groundwater resources in regions with high density of livestock and agricultural land. The occurrence of these toxic agents is consistently linked to hazardous health problems and diseases exerted on animals and humans, especially in arid and isolated regions where groundwater is a direct source for irrigation and drinking water supply [1]. The application of highly effective water treatment technologies is therefore a must in such cases, aiming to prevent serious health risks. The atmospheric N_xO_y gases, as well as surplus synthetic nitrogen fertilizers and manure spread on land are the main sources of NO_3^- that is further accumulated in groundwater, attaining contents up to 900 mg L^{-1} due to its weak adsorption and high solubility [1,2]. High contents of this anion may cause methaemoglobinaemia and cardiovascular illnesses [3,4], and for this reason, the World Health Organization (WHO) limits to 50 mg L^{-1} its concentration in groundwater intended for human consumption. Classical separation methods such as ion exchange and reverse osmosis are able to remove NO_3^- from water [4], but lately more attention has been drawn to the electrochemical technologies. Among them, electrocoagulation and electrodialysis have been proven effective as separation methods [5], although there is greater interest in transformation treatments involving electrore-

* Corresponding author.
E-mail address: i.sires@ub.edu (I. Sirés).
[1] Active ISE member.

https://doi.org/10.1016/j.electacta.2021.138354

duction. The latter, which is also called electrodenitrification, consists in the use of an electrocatalytic cathode to increase the activity and/or selectivity of the NO_3^- reduction process. Worth noting, electrodenitrification has been rarely coupled with electrochemical oxidation (EO) [2,4,5–24].

Several factors such as cell configuration, applied current (I), solution composition and pH affect the effectiveness of NO_3^- electroreduction. It has been found that this process becomes faster using electrodes with large overpotential for the H_2 evolution reaction (HER), owing to the comparatively slower rate of H^+ and/or H_2O electroreduction. This has been confirmed from the behavior of metallic and semiconductor cathode surfaces made of Pd-Rd [6,7], Sn [8,9], Cu [10,11], Cu-Zn [5,12], stainless steel (SS) [13,14], boron-doped diamond (BDD), SS, graphite, silicon carbide and Pb [15,16], Sn, Bi, Pb, Al, Zn and In [17], Sn modified Pd [18], Fe, Cu, Ni and carbon foams [19], Cu, Pd, Pt and Rh nanoparticles deposited on reduced graphene [20], Cu-Ni [21], Fe [14,22], TiO_2 nanotubes [23], and Bi-Pd nanoparticles [24]. The electroreduction process is complex and involves the initial transformation of NO_3^- into NO_2^- ion by overall reaction (1), which is subsequently reduced to NH_3 according to reaction (2), via NH_2OH formation, or converted into N_2 gas by reaction (3) through N_xO_y species [2,15,25]:

$$NO_3^- + H_2O + 2e^- \rightarrow NO_2^- + 2OH^- \quad (1)$$

$$NO_2^- + 6H_2O + 6e^- \rightarrow NH_3 + 8OH^- \quad (2)$$

$$2NO_2^- + 4H_2O + 6e^- \rightarrow N_{2(g)} + 8OH^- \quad (3)$$

EO/electrodenitrification pairing using an undivided reactor appears to be an appealing alternative to increase the viability of the electrochemical technologies, since the typical parasitic oxygen evolution reaction (OER) at the anode (M) is replaced by water conversion to adsorbed hydroxyl radical (M($^\bullet$OH)) via reaction (4). This is a strong oxidant that can be directly employed to degrade organic pollutants [26–28]:

$$M + H_2O \rightarrow M(^\bullet OH) + H^+ + e^- \quad (4)$$

In EO, the non-active BDD anode is more powerful than the active dimensionally stable anodes (DSA®) in chloride-free aqueous matrices because it gives large amounts of physisorbed M($^\bullet$OH). In contrast, in Cl^- media the oxidation power of DSA® is considerably improved due to its higher selectivity to produce active chlorine (Cl_2/HClO/ClO^-) via reactions (5)-(7) [28,29]. HClO with $E° = 1.36$ V prevails at pH 3.0-8.0, whereas at pH > 8.0 the milder ClO^- with $E° = 0.89$ V predominates. Once generated, active chlorine can oxidize NH_3 to N_2 from reaction (8) [16,30–33] or to NO_3^- ion from reaction (9) [30,31]. Oxidation of NO_2^- to NO_3^- ion via reaction (10) is feasible [34], thereby reducing the global effectiveness of NO_3^- electroreduction. Active chlorine can be anodically oxidized to yield toxic and undesired ClO_3^- and ClO_4^- ions [14–16], and the process can be further complicated by the formation of chloramines, initiated by reaction (11) [16,35,36]. Chloramines are preferentially formed in acidic medium and can easily evolve to N_2 or N_2O. Reactions (6)-(11) are homogeneous, thus taking place in the solution bulk. Note that reactions (2), (8), (9) and (11) can involve either NH_3 in alkaline medium or its less reactive protonated form NH_4^+ ($pK_a = 9.25$) in acidic and circumneutral media. In the three latter reactions, NH_3/NH_4^+ reacts with active chlorine in the form of ClO^-/HClO, having the higher or lower redox potential of these oxidants a certain influence on the conversion percentage.

$$2Cl^- \rightarrow Cl_{2(aq)} + 2e^- \quad (5)$$

$$Cl_{2(aq)} + H_2O \rightarrow HClO + H^+ + Cl^- \quad (6)$$

$$HClO \rightleftarrows ClO^- + H^+ \rightarrow pK_a = 7.40 \quad (7)$$

$$2NH_3 + 2ClO^- \rightarrow N_{2(g)} + 2Cl^- + 2H_2O + 2H^+ + 2e^- \quad (8)$$

$$NH_3 + 4ClO^- \rightarrow NO_3^- + H_2O + H^+ + 4Cl^- \quad (9)$$

$$NO_2^- + ClO^- \rightarrow NO_3^- + Cl^- \quad (10)$$

$$NH_3 + ClO^- \rightarrow NH_2Cl + OH^- \quad (11)$$

Some authors evaluated the influence of the anode material on the NO_3^- electroreduction, showing that in the presence of Cl^-, BDD becomes more efficient than IrO_2-based DSA® [14,16]. This unexpected behavior has been ascribed to the lower adsorption of the products, arising from cathodic NO_3^- reduction, on BDD surface, which drastically diminishes their eventual re-oxidation. Much less is known about the electrodenitrification process in groundwater, although a smaller efficiency could be expected due to different detrimental factors such as the presence of natural organic matter (NOM), the low NO_3^- concentration and the high hardness that can cause the cathode deactivation, thus blocking the electrocatalytic reduction process [25].

In recent years, our group has shown the excellent oxidation power of EO and other electrochemical advanced oxidation processes to destroy pesticides in synthetic solutions [37–42] and even in groundwater [14,29]. A preliminary study about the treatment of the insecticide imidacloprid in groundwater evidenced a good performance of EO/electrodenitrification using Fe as cathode to simultaneously remove the pesticide and NO_3^- ion [14]. However, more research efforts are required to demonstrate the potential viability of paired electrolysis for groundwater remediation in view of the scarce information available so far.

Terbuthylazine (TBZE, CAS number 5915-41-3, $C_9H_{16}ClN_5$, *N-tert*-butyl-6-chloro-*N'*-ethyl-[1,3,5]triazine-2,4-diamine, $M = 229.71$ g mol^{-1}) belongs to the s-triazine family, and it is one of the most used herbicides in Portugal, Italy and Spain [43]. It is a pollutant of emerging concern because its low solubility in water (about 9 mg dm^{-3} at 25 °C) and high affinity to soil confer large persistence in surface water, groundwater and marine water, where it has reached 0.2 μg L^{-1}, > 5 μg L^{-1} and 84 ng L^{-1} in EU countries, respectively. Note that 0.1 μg L^{-1} is the recommended maximum content in drinking water, according to EU Directives [43,44]. TBZE is very toxic to living beings at low doses due to its ability to bioaccumulate, posing high long-term risks to non-target plants and soil macroinvertebrates, mammals and aquatic organisms [43]. It is decomposed to desethylterbuthylazine (DE-TBZE), which is also largely persistent in water and even more toxic than the parent herbicide [44]. Several works have reported a large removal of TBZE from water by simple separation methods involving adsorption on membranes [45], selective polymeric materials [46], activated carbon and carbon nanotubes [47] and metal-organic frameworks [48]. Transformation techniques including O_3/activated carbon, solar/O_3 and solar/TiO_2/O_3 [47], UV/H_2O_2 [47,49], UV/TiO_2/chitosan [50] and UV/B-doped TiO_2/O_3 [51] have been tested as well. Tasca et al. [52] used a zero-gap cell equipped with a BDD mesh anode, a RuO_2 mesh cathode and a solid polymer electrolyte, to degrade 300 cm^3 of 4 mg dm^{-3} TBZE in deionized water by EO. About 89% and 97% of pesticide removal was attained after 60 min at 100 and 500 mA, respectively, with energy consumptions < 11 kWh m^{-3}. Note that the target herbicide possesses 5 N atoms that can be released to contribute to NO_3^- accumulation.

To gain a better insight on the EO/electrodenitrification process, here we report the simultaneous TBZE electrochemical oxidation and NO_3^- electroreduction in actual groundwater matrix. Key experimental parameters like *I* and pH were systematically assessed. The experiments were carried out with an undivided tank reactor equipped with a BDD or RuO_2 (i.e., DSA®-Cl_2) anode and an Fe cathode. Prior to electrolysis with groundwater matrix, the sample was softened to minimize the content of alkaline earth metal ions, a crucial step to avoid the loss of cathode electroactivity upon precipitation of hydroxides and carbonates. Comparative assays were performed with simulated solutions mimicking the anionic composition of the softened groundwater to clarify the evolution of NO_3^- and generated ions and the role of NOM. TBZE was always spiked into the aqueous matrices at a concentration as high as 5.0 mg dm^{-3} in order to minimize the quantification error of all concentrations, thus providing reliable degradation kinetics data. The total nitrogen (TN) concentration decay in solution was monitored as well. A post-treatment with an ion exchange resin was implemented as a final conditioning step to reduce the impact of the oxychlorine anions produced.

2. Materials and methods

2.1. Chemicals

Analytical standards (PESTANAL®) terbuthylazine and desethylterbuthylazine were purchased from Sigma. The solution pH was regulated with analytical grade H_2SO_4 (95-98%) and NaOH (98-100%) purchased from Panreac. Simulated water matrices were prepared with analytical grade electrolytes, including KCl (> 99%) provided by Sigma-Aldrich, and KNO_3 (98%) and K_2SO_4 (99.9%) supplied by Panreac. Other chemicals and solvents used were either of analytical or high-performance liquid chromatography (HPLC) grade provided by Aldrich, Fluka, Lancaster and Panreac. Ultrapure water (Millipore Milli-Q, p> 18.2 MΩ cm) was used to prepare the analytical solutions and simulated water matrices.

2.2. Aqueous matrices

Actual groundwater was collected from a water well located in an agricultural land in the surroundings of Barcelona (Spain). The sample was softened following three consecutive steps: (i) alkalinization up to pH 11.5 by adding 1 mol dm^{-3} NaOH solution, (ii) sedimentation for 24 h and filtration with regenerated cellulose filter membrane (0.45 μm) to remove the precipitated carbonates and hydroxides and, finally, (iii) acidification with 1 mol dm^{-3} H_2SO_4 solution to reach the desired pH. The resulting softened groundwater was preserved in a refrigerator at 4 °C before usage for electrolytic treatments. Table 1 collects the physicochemical parameters of: (i) the raw groundwater; (ii) the softened groundwater once conditioned at pH 4.0 and with TBZE spiked at a concentration of 5.0 mg dm^{-3}; (iii) that softened groundwater, after an electrochemical treatment for 360 min; and (iv) the solution resulting from such electrolysis, after treatment with a Purolite® A532E resin, a polystyrenic strong base anion gel in the chloride form that is recommended by the provider for perchlorate removal. As can be seen, the softening process led to a drastic reduction of the concentration of all alkaline earth metal ions, whereas the Na^+ and SO_4^{2-} concentrations substantially grew up. This sample showed low conductivity and total organic carbon (TOC), whereas its TN content mainly corresponded to NO_3^-. The final post-treatment with the resin allowed the reduction of the ClO_3^-, NO_3^- and SO_4^{2-} concentrations alongside the complete removal of ClO_4^-, with a concomitant increase in the Cl^- content.

Three simulated water samples were prepared to separately assess the behavior of the main anions contained in the softened groundwater. The conductivity of such solutions at neutral pH was around 1.7-1.8 mS cm^{-1} and their composition was: (i) 10 mmol dm^{-3} K_2SO_4 (980 mg dm^{-3} SO_4^{2-}); (ii) 1.6 mmol dm^{-3} KNO_3 (100 mg dm^{-3} NO_3^-) + 7.6 mmol dm^{-3} K_2SO_4 (745 mg dm^{-3} SO_4^{2-}); and (iii) 10 mmol dm^{-3} KCl (355 mg dm^{-3} Cl^-) + 1.6 mmol dm^{-3} KNO_3 (100 mg dm^{-3} NO_3^-) + 0.8 mmol dm^{-3} K_2SO_4 (78 mg dm^{-3} SO_4^{2-}). The pH of these solutions was adjusted to 4.0, 7.0 and 10.5 and they were electrolyzed, in the absence or presence of 5.0 mg dm^{-3} TBZE, without pH regulation.

2.3. Electrolytic system

The electrolytic assays were performed in an undivided glass tank reactor, which had a jacket to continuously recirculate thermostated water at 25 °C. Each experiment was made with 500 cm^3 of solution, which was kept under stirring with a magnetic follower at 900 rpm. The anode was either a Nb mesh coated with a 5 μm BDD thin film (3,500 ppm B), purchased from Condias, or a RuO_2 mesh purchased from De Nora, whereas a custom iron mesh (Fe, 99.9%) was used as the cathode. The surface of the anode and cathode immersed into the solution had dimensions of 3.5 cm × 7.5 cm. The electrodes were placed in the center of the tank reactor, separated at a distance of 3 mm. In some cases, two Fe cathodes were used, with the anode sandwiched between them keeping a separation of 3 mm with each cathode. The electrolyses were carried out under galvanostatic conditions with an Amel 2051 potentiostat-galvanostat providing a constant current (*I*) of 250, 500 or 1000 mA. A Demestres 601BR digital multimeter was used to monitor the potential difference between the electrodes. Before each experiment, the Fe cathode was consecutively polished with P240 and P800 sandpapers, submerged in a 20% H_2SO_4 solution, rinsed with Milli-Q water and dried at room temperature.

2.4. Analytical procedures

A Metrohm 644 conductometer and a Crison 2200 pH-meter were used to determine the solution conductance and pH, respectively. A periodic withdrawal of 1.5 cm^3 of treated samples from the tank reactor was made for analysis, followed by filtration with Whatman 0.45 μm PTFE membrane filters.

TN measurements were made with a Shimadzu VCSN TOC analyzer coupled to a TNM-1 unit. The nitrogen mass balance at the end of each assay was made considering the NO_2^-, NO_3^- and NH_4^+ concentrations detected, the solution TN value at each time to account for other soluble N-species and the initial TN of the sample to ascertain the quantity of volatiles released. Free chlorine and total chlorine contents were obtained by the *N,N*-diethyl-*p*-phenylenediamine colorimetric method, using an Unicam UV4 UV/Vis spectrophotometer at λ = 515 nm [53]. The concentration of Cl^-, ClO_3^-, ClO_4^-, NO_2^-, NO_3^- and NH_4^+ ions was obtained following the procedures described elsewhere [54]. The content of iron, calcium, magnesium ions and the other elements in solution was determined by inductively coupled plasma with optical emission spectroscopy (ICP-OES) on a Perkin Elmer Optima 8300 spectrometer.

The TBZE concentration was monitored by reversed-phase HPLC using a Waters 600 liquid chromatograph (LC) coupled to a 996 photodiode array detector. Aliquots of 20 μL were injected into the LC and the separation of organics was achieved by means of a Spherisorb® S5 ODS2 5 μm (150 mm × 4.6 mm (i.d.)) column at 35 °C, upon elution with a 60:40 (v/v) acetonitrile/water mixture at 1.0 cm^3 min^{-1}. Using Empower® software for control, the peak for TBZE (λ = 222.9 nm) appeared at retention time (t_r) of 7.8 min, with L.O.Q = 0.32 mg dm^{-3} and L.O.D = 0.11 mg dm^{-3}. The peak for DE-TBZE (λ = 214.7 nm) appeared at t_r = 4.1 min, with L.O.Q = 0.59 mg dm^{-3} and L.O.D = 0.19 mg dm^{-3}.

Table 1
Physicochemical characteristics of the raw groundwater, the softened groundwater after conditioning at pH 4.00 and addition of 5 mg dm^{-3} TBZE, the electrolyzed softened groundwater after 360 min of an EO/electrodenitrification treatment in an undivided stirred BDD/Fe tank reactor at I = 500 mA and 25 °C, and the same final solution once post-treated with Purolite® A532E ion-exchange resin.

Parameter (units)	Raw groundwater	Softened groundwater	Electrolyzed groundwater	Post-treated groundwater
pH	7.19	4.00	10.20	8.31
Conductivity (mS cm^{-1})	1.72	1.93	1.90	2.02
TC (mg dm^{-3})	50.02	- [a]	- [a]	- [a]
TOC (mg dm^{-3})	1.30	3.74	2.43	2.22
TN (mg dm^{-3})	23.89	23.77	16.76	10.58
NO_3^- (mg dm^{-3})	101.32	99.76	33.43	5.26
NO_2^- (mg dm^{-3})	- [b]	- [b]	2.72	- [b]
Cl^- (mg dm^{-3})	363.26	344.26	42.2	712.31
ClO_3^- (mg dm^{-3})	- [b]	- [b]	58.74	3.24
ClO_4^- (mg dm^{-3})	- [b]	- [b]	766.61	- [b]
SO_4^{2-} (mg dm^{-3})	77.52	357.21	358.56	56.91
Ca^{2+} (mg dm^{-3})	99.59	0.87	0.84	1.31
Mg^{2+} (mg dm^{-3})	26.57	0.55	- [b]	- [b]
K^+ (mg dm^{-3})	9.9	10.47	10.67	11.49
Na^+ (mg dm^{-3})	179.90	389.74	384.53	386.30

[a] Not measured. [b] Not found

The same LC was equipped with a Bio-Rad Aminex HPX 87H (300 mm × 7.8 mm (i.d.)) column at 35 °C, its detector selected at λ = 210 and a 4 mmol dm^{-3} H_2SO_4 solution flowing at 0.6 cm^3 min^{-1} as mobile phase, to quantify the produced acids by ion-exclusion HPLC. The acids detected were oxalic (t_r = 7.3 min), oxamic (t_r = 10.3 min) and cyanuric (t_r = 12.6 min).

The experiments were always made in duplicate, and average results are reported. Figures show the corresponding error bars within a 95% confidence interval.

Solutions of 5.0 mg dm^{-3} TBZE spiked into a simulated water matrix at pH 4.0 and 25 °C were electrolyzed for 60 min using a BDD/Fe cell at I = 500 mA. The organics were extracted with CH_2Cl_2 (3 × 50 cm^3). The organic phase was then dried over anhydrous Na_2SO_4, filtered and its volume reduced to ca. 2 cm^3 under N_2 stream for analysis by gas chromatography-mass spectrometry (GC-MS). The analysis was performed by equipping the gas chromatograph with either a polar Agilent HP-INNOWax GC or a non-polar Teknokroma Sapiens X5-MS column, following the same procedures detailed in earlier work [55]. The mass spectra of heteroaromatic products formed from the initial TBZE degradation were compared with those found in the NIST05 database.

3. Results and discussion

3.1. Electrodenitrification of simulated groundwater without herbicide

A first series of experiments was performed to clarify the effect of pH on the NO_3^- electroreduction, in the absence of pesticide. This was made by electrolyzing 500 cm^3 of solutions with 100 mg dm^{-3} NO_3^- + 7.6 mmol dm^{-3} SO_4^{2-} at initial pH of 4.0, 7.0 and 10.5 using BDD/Fe and RuO_2/Fe tank reactors at I = 500 mA. Table 2 shows that the acidic and neutral solutions were strongly alkalinized, attaining final pH values of 10.3-10.8 and 10.1-11.2 in the cells with BDD and RuO_2, respectively, as expected from the OH^- generation upon consecutive reduction of NO_3^- to NO_2^-, NH_3 and N_2 via reactions (1)-(3) [14]. The high OH^- content at initial pH 10.5 can explain the small pH variation (± 0.5 units) found in that medium regardless of the anode used (see Table 2).

Fig. 1a presents the variation of NO_3^- concentration with electrolysis time. Using BDD anode, similar decays can be observed at all pH values, with a reduction of 75%-78% at the end of the treatment. This good result can be related to the poor adsorption of the products originated from NO_3^- electroreduction (e.g., NH_4^+ ion) on the BDD surface regardless of the pH. As a result, their subsequent re-oxidation to the parent anion occurred only to a small extent, which was positive in terms of global nitrate removal [15,16]. In contrast, a fluctuating behavior occurred in the cell with RuO_2 anode, with up to 87% of NO_3^- removal at pH 4.0, 81% at pH 10.5 but only up to 56% at pH 7.0. This means that at the latter pH, the products of NO_3^- electroreduction are more largely adsorbed onto the RuO_2 surface, favoring their faster re-oxidation. According to these findings, the use of BDD is more favorable for electrodenitrification at neutral pH, whereas RuO_2 becomes slightly superior in acidic and alkaline media. Fig. 1b depicts that the above concentration decays obeyed a pseudo-first-order kinetics, and the apparent rate constants ($k(NO_3^-)$) are collected in Table 2. As expected from the trends of Fig. 1, similar $k(NO_3^-)$ values between 4.6 × 10^{-3} and 5.2 × 10^{-3} min^{-1} were obtained in the trials with BDD, which rose up to 6.3 × 10^{-3} min^{-1} for the faster abatement at pH 4.0 using RuO_2.

The accumulated NH_4^+ content increased gradually as the NO_3^- concentration disappeared, as can be seen in Fig. 1c. About 20 mg dm^{-3} as maximal and 12 mg dm^{-3} as minimal of NH_4^+ were finally obtained. A certain TN abatement was found in all the assays, varying between 9.0% and 18%, which can be related to the loss of volatile N-compounds (see Fig. 1d). The speciation of N-containing compounds at the end of all electrolyses shown in Fig. 1e reveals the preeminence of NH_4^+ ion over all the other species, suggesting the leading role of consecutive reactions (1) and (2) in the electrodenitrification process with Fe cathode. The production of volatile N-compounds, like N_xO_y and N_2 via reaction (3) is then a less favorable reduction route. Note that at the final alkaline pH values achieved, the acid/base equilibrium of NH_4^+ ion (pK_a = 9.25) results in the accumulation of its conjugated form, which can contribute to the N-volatiles.

Data of Table 2 also show higher average cell potentials (E_{cell}) using BDD, owing to the higher potential required for water discharge as compared to that needed with RuO_2 [26]. The energy consumption (EC) of the process, calculated as EC = E_{cell} I t / V, was then greater for BDD (45.0-50.4 kWh m^{-3} vs 39.0-41.2 kWh m^{-3}).

The above study was extended to a 100 mg dm^{-3} NO_3^- + 0.8 mmol dm^{-3} SO_4^{2-} + 10 mmol dm^{-3} Cl^- solution to explore the effect of Cl^- oxidation on the NO_3^- electroreduction. These trials were carried out starting at pH 4.0, 7.0 and 10.5 using both cells at I = 500 mA. In addition, with the BDD anode, the effect of I was studied at pH 4.0. After 360 min, Table 2 shows that final pH values with BDD were similar to those mentioned for chloride-free solutions, whereas they tended to be slightly lower (8.4-10.0) using RuO_2. This behavior suggests that the greater production of active

Table 2
Pseudo-first-order rate constant for NO_3^-, Cl^- and terbuthylazine decays, alongside the energy consumption at 360 min of electrolysis, for the treatment of 500 cm^3 of simulated groundwater matrices and softened actual groundwater in the absence and presence of herbicide at different pH values and 25 °C. The assays were made using undivided cells with a BDD or RuO_2 anode and an Fe cathode.

Anode	pH_0 (pH_f)	I / mA	E_{cell} / V	$k(NO_3^-)$ / 10^{-3} min^{-1} (R^2)	$k(Cl^-)$ / 10^{-3} min^{-1} (R^2)	k(TBZE) / 10^{-2} min^{-1} (R^2)	EC / kWh m^{-3}
Simulated groundwater (100 mg dm^{-3} NO_3^- + 7.6 mmol dm^{-3} SO_4^{2-})							
BDD	4.0 (10.3)	500	8.4	4.7 (0.990)	-	-	50.4
	7.0 (10.7)	500	8.3	5.2 (0.988)	-	-	49.8
	10.5 (10.8)	500	7.5	4.6 (0.981)	-	-	45.0
RuO_2	4.0 (10.1)	500	6.7	6.3 (0.987)	-	-	40.2
	7.0 (11.2)	500	6.5	2.5 (0.997)	-	-	39.0
	10.5 (10.0)	500	6.9	5.0 (0.993)	-	-	41.4
Simulated groundwater (100 mg dm^{-3} NO_3^- + 0.8 mmol dm^{-3} SO_4^{2-} + 10 mmol dm^{-3} Cl^-)							
BDD	4.0 (10.3)	250	5.4	3.3 (0.991)	3.4 (0.988)	-	16.2
	4.0 (10.2)	500	8.5	4.3 (0.980)	7.5 (0.994)	-	51.0
	7.0 (10.3)	500	8.6	3.9 (0.993)	5.1 (0.981)	-	51.6
	10.5 (10.4)	500	8.0	3.2 (0.980)	7.0 (0.986)	-	48.0
	4.0 (10.7)	1000	13.5	6.1 (0.988)	12.4 (0.993)	-	162.0
RuO_2	4.0 (8.4)	500	7.5	2.8 (0.997)	1.6 (0.985)	-	45.0
	7.0 (9.8)	500	7.5	2.5 (0.995)	1.7 (0.980)	-	45.0
	10.5 (10.0)	500	7.3	1.8 (0.997)	1.5 (0.991)	-	43.8
Simulated groundwater (5.0 mg dm^{-3} TBZE + 10 mmol dm^{-3} SO_4^{2-})							
BDD	4.0 (4.35)	500	8.3	-	-	9.0 (0.998)	49.8
Simulated groundwater (5.0 mg dm^{-3} TBZE + 100 mg dm^{-3} NO_3^- + 7.6 mmol dm^{-3} SO_4^{2-})							
BDD	4.0 (9.3)	500	8.0	2.2 (0.981)	-	5.7 (0.988)	48.0
RuO_2	4.0 (10.9)	500	7.5	6.5 (0.989)	-	0.63 (0.994)	45.0
Simulated groundwater *(5.0 mg dm^{-3} TBZE + 100 mg dm^{-3} NO_3^- + 0.8 mmol dm^{-3} SO_4^{2-} + 10 mmol dm^{-3} Cl^-)*							
BDD	4.0 (10.6)	250	5.8	2.1 (0.984)	-[a]	4.5 (0.997)	17.4
	4.0 (9.9)	500	9.1	3.6 (0.988)	-[a]	9.9 (0.998)	54.6
	4.0 (10.4)	1000	14.7	4.3 (0.993)	-[a]	12.0 (0.993)	176.4
	7.0 (10.6)	250	6.1	2.5 (0.998)	-[a]	4.3 (0.991)	18.3
	7.0 (10.5)	500	10.4	3.3 (0.982)	-[a]	5.6 (0.991)	62.4
	7.0 (10.0)	1000	16.3	2.8 (0.980)	-[a]	7.2 (0.985)	185.6
	10.5 (9.8)	250	6.7	2.1 (0.983)	-[a]	3.6 (0.995)	20.1
	10.5 (10.4)	500	9.2	4.4 (0.981)	-[a]	5.2 (0.993)	55.2
	10.5 (10.0)	1000	14.2	3.6 (0.982)	-[a]	8.0 (0.995)	170.4
BDD[b]	4.0 (10.6)	1000	8.8	6.6 (0.993)	14.0 (0.990)	16.5 (0.982)	105.6
RuO_2	4.0 (9.6)	250	4.4	3.3 (0.986)	-[a]	3.4 (0.988)	13.2
	4.0 (9.7)	500	8.0	5.9 (0.989)	-[a]	4.7 (0.980)	48.0
	4.0 (10.1)	1000	14.2	5.0 (0.991)	-[a]	11.1 (0.993)	170.4
	7.0 (9.8)	250	5.3	3.0 (0.981)	-[a]	2.4 (0.996)	15.4
	7.0 (9.8)	500	8.3	4.8 (0.995)	-[a]	4.1 (0.993)	49.8
	7.0 (9.3)	1000	14.1	4.4 (0.997)	-[a]	9.1 (0.991)	169.2
	10.5 (10.3)	250	4.9	3.3 (0.998)	-[a]	1.8 (0.991)	14.7
	10.5 (10.3)	500	8.9	4.4 (0.995)	-[a]	3.0 (0.992)	53.4
	10.5 (9.5)	1000	13.4	3.9 (0.998)	-[a]	9.8 (0.998)	160.8
Softened actual groundwater							
BDD[c]	4.0 (9.7)	500	7.1	-[e]	5.7 (0.996)	-[a]	42.6
BDD[b,d]	4.0 (10.2)	1000	8.9	-[e]	13.4 (0.997)	15.6 (0.997)	106.8

[a] Not determined. [b] 2 Fe cathodes. [c] Without and [d] with 5.0 mg dm^{-3} TBZE. [e] Nonlinear correlation.

chlorine with the latter anode resulted in a relevant contribution of reactions (9)-(10), eventually leading to a smaller global electrodenitrification with lower OH^- net production from reactions (1)-(3). This hypothesis is confirmed from the profiles of Fig. 2a, where the NO_3^- concentration decays more slowly using RuO_2. The NO_3^-content was progressively reduced by 79%, 76% and 65% at pH 4.0, 7.0 and 10.5 using BDD, becoming slower until reaching 62%, 60% and 47% removal with RuO_2. Good linear correlations related to a pseudo-first order process were found for all these trends (see Fig. 2b), giving rise to lower $k(NO_3^-)$ values as compared to those determined in the absence of chloride (see Table 2). The loss of efficiency of NO_3^- electroreduction in the chloride medium can be accounted for by the anodic generation of active chlorine (HClO and/or ClO^-) via reactions (5)-(7), which then reacts with NH_4^+ (largely formed from NO_3^- reduction, as shown in Fig. 1c) to originate N_2 gas via reaction (8), regenerate NO_3^- ion via reactions (9) and (10) or produce chloramines via reaction (11). The oxidation of electroreduction products by active chlorine contributed to slow down the global electrodenitrification. Moreover, the progressive deceleration of NO_3^- electroreduction with decrease of $k(NO_3^-)$ was much more remarkable when changing the starting pH from neutral to alkaline (see Fig. 2a and Table 2). This phenomenon can be ascribed to the conversion of HClO to ClO^-, which behaves as a more reactive species, either promoting the oxidation of N-species to NO_3^- or competing with NO_3^- electroreduction. On the other hand, Fig. 2a also shows a more effective electrodenitrification when I was increased from 250 to 1000 mA at pH 4.0 using BDD, with the highest NO_3^- removal of 82% attained upon application of the greatest I. The corresponding $k(NO_3^-)$ values of Table 2 were upgraded from 3.3×10^{-3} to 6.1×10^{-3} min^{-1} (1.85-fold) upon a 4-fold rise of I from 250 to 1000 mA, pointing to a larger influence of NH_4^+ re-oxidation at higher I.

The effect of reactions (8)-(11) on electrodenitrification was confirmed by analyzing the evolution of generated NH_4^+ and TN. No NH_4^+ was detected using the RuO_2 anode. Fig. 2c shows that the amount of this ion accumulated in the medium using the BDD anode depended on the applied I. While NH_4^+ was not found at 250 mA, it was accumulated between 2.2 and 2.9 mg dm^{-3} at 500 mA and much more largely (up to 10.0 mg dm^{-3}) at 1000 mA, in agreement with the faster NO_3^- electroreduction. Much larger TN removals were attained in the chloride medium (see Fig. 2d)

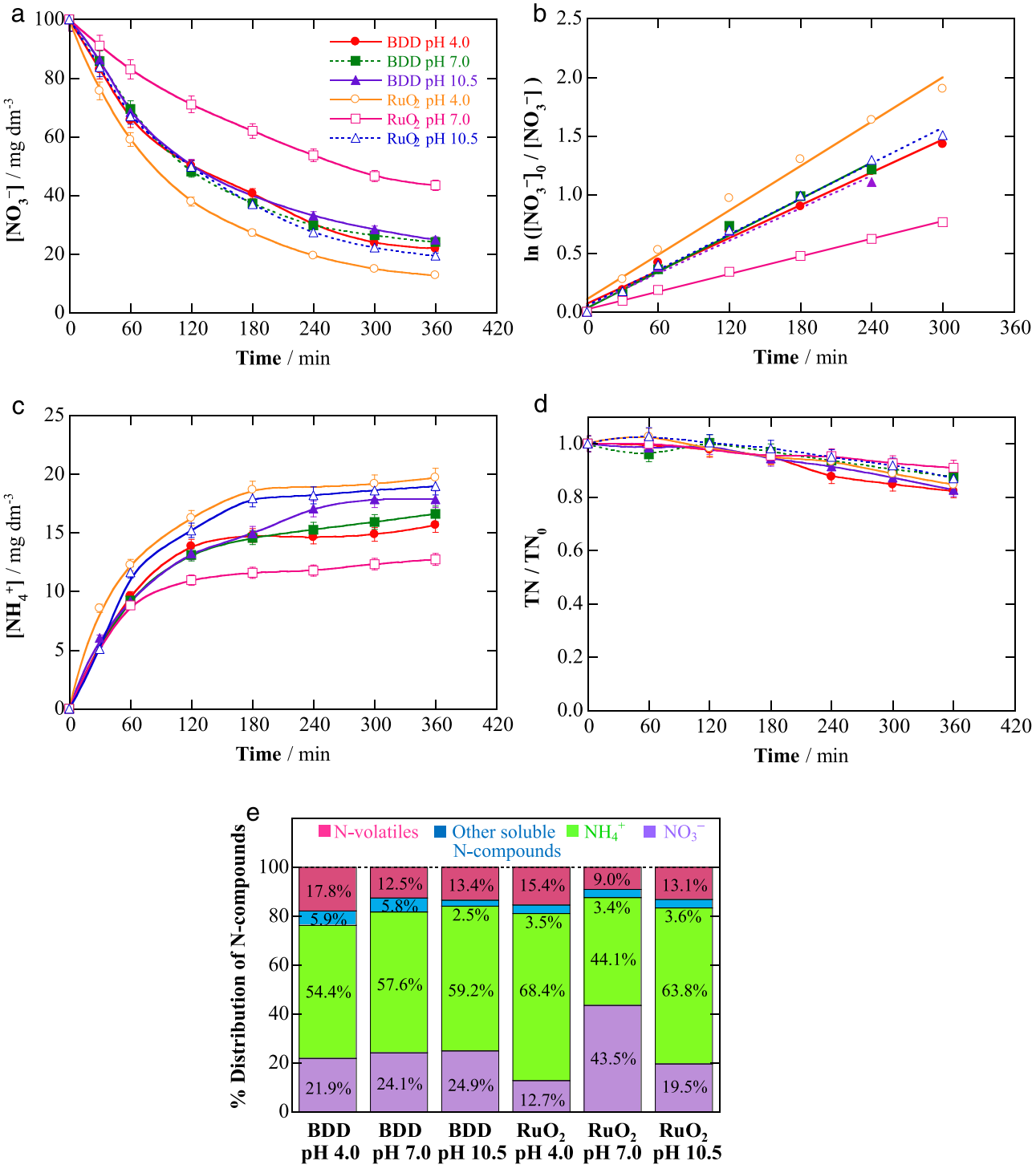

Fig. 1. (a) NO_3^- concentration removal during the electrodenitrification of 500 cm^3 of a solution containing 100 mg dm^{-3} NO_3^- + 7.6 mmol dm^{-3} SO_4^{2-} in ultrapure water at initial pH 4.0, 7.0 and 10.5, using undivided stirred BDD/Fe or RuO_2/Fe tank reactors at 500 mA and 25 °C. (b) Pseudo-first-order kinetic analysis of trends of plot (a), (c) accumulated NH_4^+ contents, (d) normalized total nitrogen decays, and (e) percent distributions of the nitrogen species at the end of the trials.

as compared to those in the chloride-free one (see Fig. 1d), which is explained by the loss of much greater amounts of volatile N-compounds, mainly N_2. For example, up to 65.5% of volatiles was released as maximal at initial pH 7.0 with a BDD anode at 500 mA, much superior to 12.5% found in the absence of chloride. Active chlorine reacts with the generated NH_4^+ via reaction (8), reaching the breakpoint chlorination at a pH at which the HClO and NH_4^+ species have the maximum reactivity, enhancing the production of volatile N-compounds especially at an initial pH of 7.0. At initial pH 10.5, the acid/base equilibrium of NH_4^+ ion (pK_a =9.25) is shifted toward NH_3, the most reactive form with active chlorine, but ClO^- has a lower oxidation power than its acidic counterpart, yielding a lower amount of volatile N-compounds. From these results, the speciation of the final N-compounds is depicted in Fig. 2e. As can be seen, the residual NO_3^- and, more significantly, the volatile N-compounds in most cases were the predominant species. This means that the reduction of NO_3^- to NH_4^+ via reaction (2), followed by the conversion of NH_4^+ to N_2 via reaction

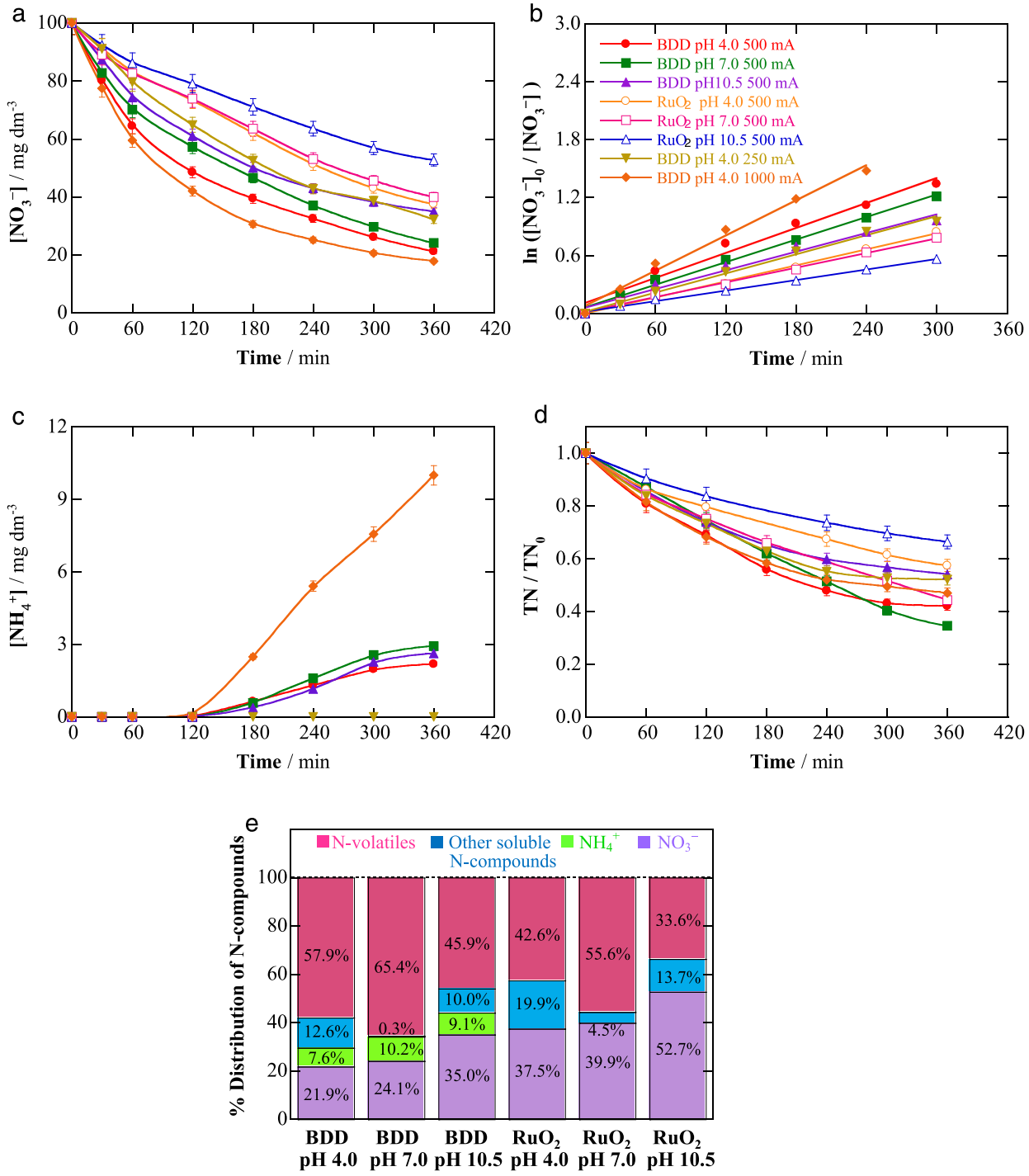

Fig. 2. (a) NO_3^- content decay during the electrodenitrification of 500 cm^3 of a solution containing 100 mg dm^{-3} NO_3^- + 0.8 mmol dm^{-3} SO_4^{2-} + 10 mmol dm^{-3} Cl^{-1} in ultrapure water at different pH values, using undivided stirred BDD/Fe or RuO_2/Fe tank reactors at several *I* values and 25 °C. (b) Pseudo-first-order kinetic analysis of trends of plot (a), (c) N accumulated NH_4^+ contents, (d) normalized total nitrogen decays, and (e) percent distributions of the nitrogen species at the end of the trial at *I* = 500 mA.

(8), are the preferential electrodenitrification steps occurring in the chloride matrix.

Fig. 3a shows the decay of Cl^- concentration for the runs performed in the chloride media. Two trends can be observed: (i) a slow abatement of the ion using RuO_2, achieving close to 47% removal regardless of the pH; and (ii) a faster removal with BDD that was highly dependent on the applied *I*, yielding increasing final removals of 75%, 93% and 96% at 250, 500 and 1000 mA, respectively, at pH 4.0. This agrees with the tendencies of the $k(Cl^-)$ values listed in Table 2 for such assays, obtained from the excellent linear profiles shown in Fig. 3b assuming a pseudo-first-order reaction. The slow Cl^- removal found using RuO_2 is indicative of its main electrodic oxidation via reaction (5). In contrast, its quicker destruction using BDD can be ascribed to the action not only of reaction (5), but also to its reaction with BDD($^\bullet$OH) originated from reaction (4), which is a more powerful oxidant than RuO_2($^\bullet$OH). It is noticeable that for BDD, the rise of $k(Cl^-)$ value showed good proportionality with *I*, changing from 3.4 × 10^{-3} min^{-1} at 250 mA

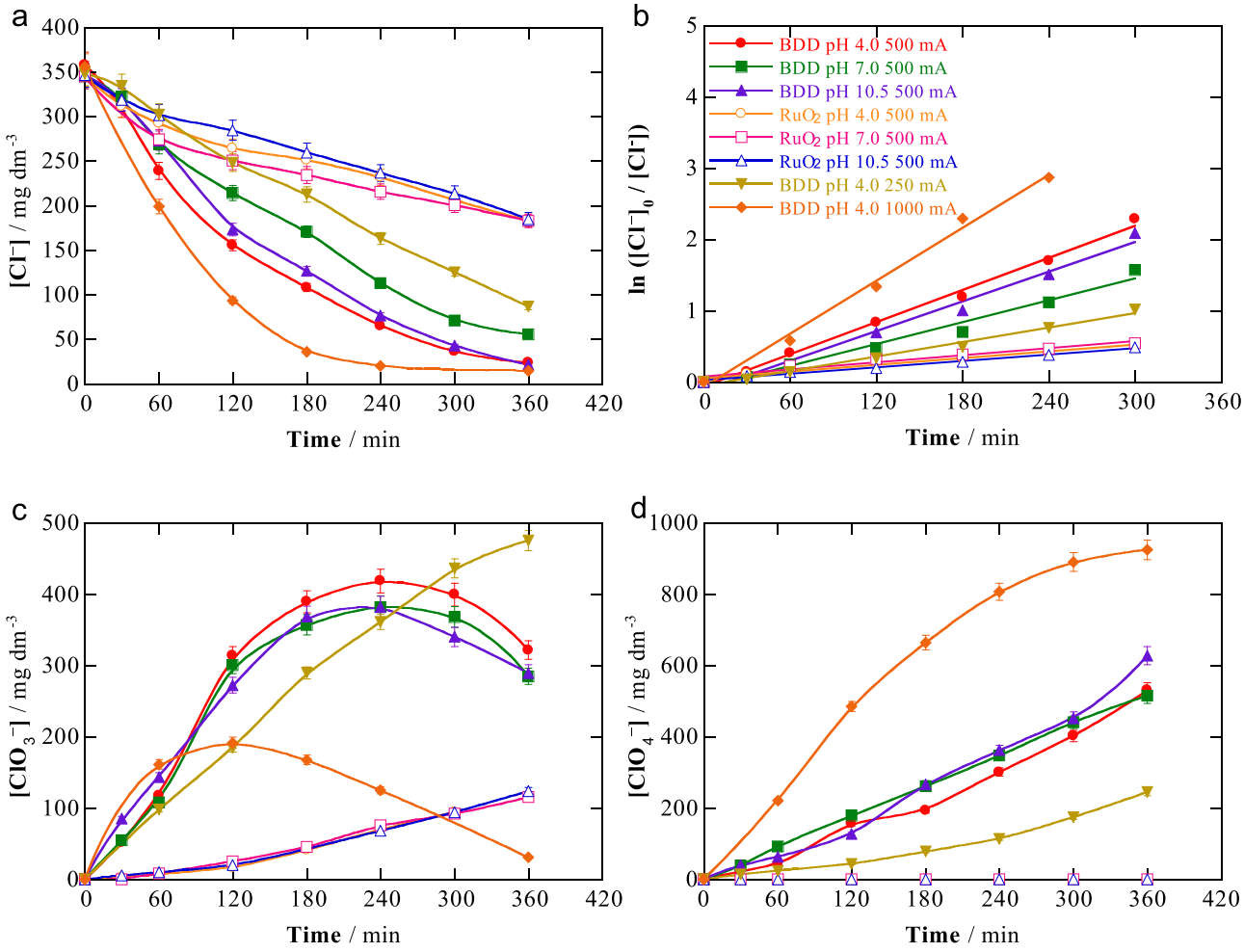

Fig. 3. Change of the concentrations of (a) Cl^- ion (355 mg dm^{-3} of initial Cl^-), (c) ClO_3^- ion, and (d) ClO_4^- ion with electrolysis time for the assays of Fig. 2. (b) Pseudo first-order kinetic analysis for the data of plot (a).

to 1.24 × 10^{-2} min^{-1} at 1000 mA (see Table 2). This suggests an almost linear enhancement of the rate of reactions (4) and (5) to destroy the ion. It is well known that further conversion of Cl^- into active chlorine is complicated with BDD due to the subsequent generation of ClO_3^- and ClO_4^- ions as follows [26]:

$$ClO^- + H_2O \rightarrow ClO_2^- + 2H^+ + 2e^- \quad (12)$$

$$ClO_2^- + H_2O \rightarrow ClO_3^- + 2H^+ + 2e^- \quad (13)$$

$$ClO_3^- + H_2O \rightarrow ClO_4^- + 2H^+ + 2e^- \quad (14)$$

The time course of both ions for the same trials is presented in Fig. 3c and 3d. As can be seen, when a RuO_2 anode was used, low ClO_3^- contents up to 120 mg dm^{-3} were always determined at all pH values, whereas no ClO_4^- was found. This behavior indicates that this anode allowed reactions (12) and (13) to some extent, but reaction (14) was completely inhibited. In contrast, much higher ClO_3^- concentrations were found with BDD, thanks to the parallel reaction with BDD($^\bullet$OH). In fact, Fig. 3c shows a similar ClO_3^- evolution at all pH values and a decay of its accumulated content with raising I due to its fast reaction with BDD($^\bullet$OH) to obtain much greater amounts of ClO_4^- as the electrolysis was prolonging (see Fig. 3d). For example, at the highest I of 1000 mA, a ClO_4^- concentration as high as 925 mg dm^{-3} was determined, being much higher than 35 mg dm^{-3} obtained for ClO_3^- ion. These two ions were the main oxidation products of Cl^- with BDD, since no active chlorine was detected at the end of most treatments.

The similar conductivity of media prepared with and without chloride allowed obtaining an analogous E_{cell} at a given I, giving rise to EC values similar to those mentioned above (see Table 2). As expected, E_{cell} and EC increased dramatically with increasing I, attaining excessively high values of 13.5 V and 162.0 kWh m^{-3} at 1000 mA, although the higher electrodenitrification power could justify the operation at such high input current.

3.2. Electrochemical oxidation of terbuthylazine in sulfate medium

The oxidation ability of the BDD/Fe cell to remove TBZE from 500 cm^3 of a 10 mmol dm^{-3} Na_2SO_4 solution with 5.0 mg dm^{-3} herbicide at pH 4.0 by EO was assessed at 500 mA for 360 min. The solution pH slightly increased, whereas the E_{cell} of 8.3 V was analogous to the above matrices with similar conductivity, resulting in an EC close to 50 kWh m^{-3} (see Table 2).

Fig. 4a highlights the fast herbicide abatement with electrolysis time, completely disappearing from the medium in 80 min. Its concentration followed a pseudo-first-order decay, as depicted in the inset of Fig. 4a, with an apparent rate constant k(TBZE) = 9.0 × 10^{-2} min^{-1}, much greater than that found for Cl^- oxidation (see Fig. 3a and Table 2). This is indicative of a quick reaction of the target herbicide with a constant concentration of BDD($^\bullet$OH) formed from reaction (4).

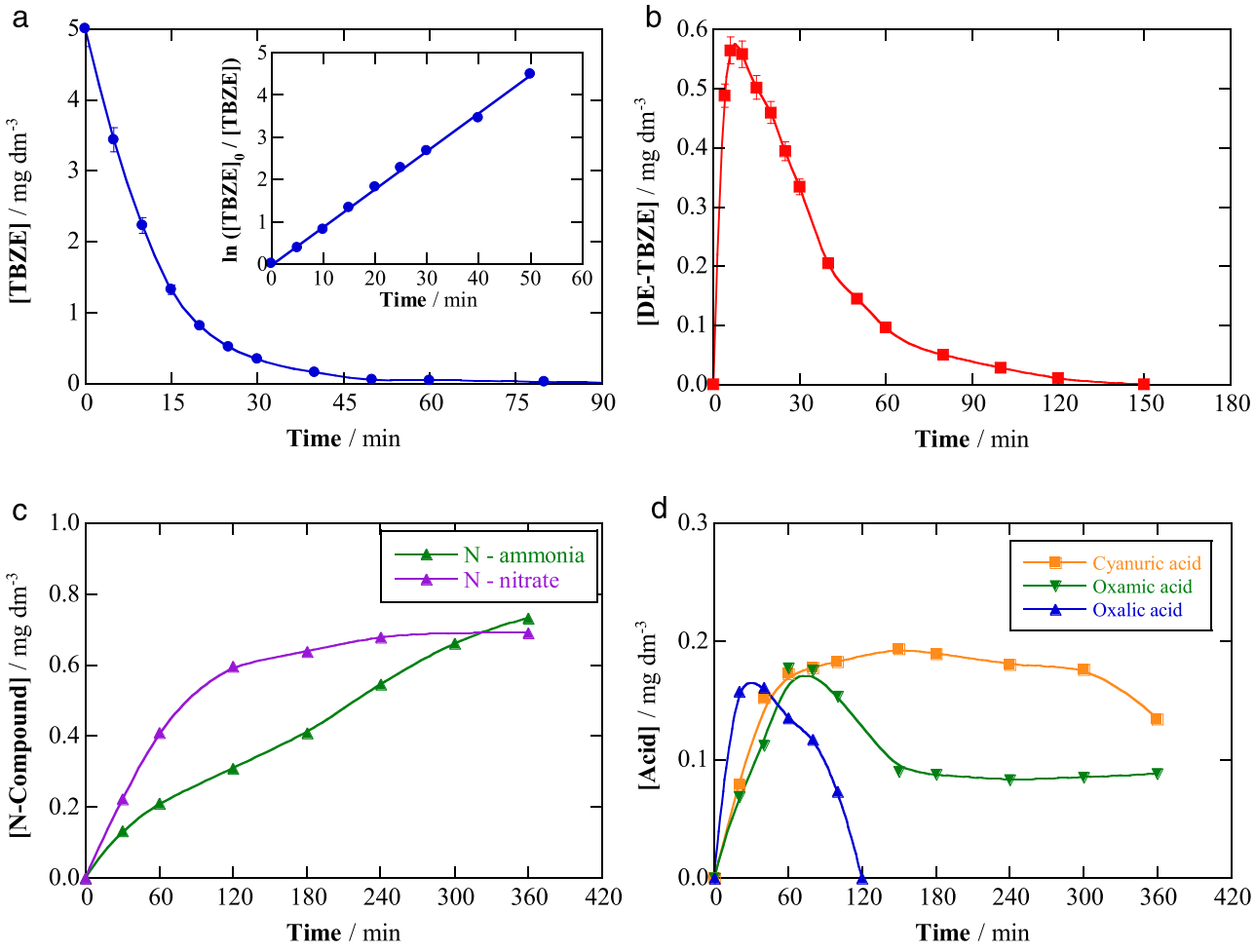

Fig. 4. (a) Time course of terbuthylazine (TBZE) concentration and its pseudo-first-order decay (inset) during the electrochemical oxidation (EO) of 500 cm^3 of a 10 mmol dm^{-3} Na_2SO_4 solution with 5 mg dm^{-3} herbicide in pure water, using an undivided stirred BDD/Fe tank reactor at 500 mA and 25 °C. The content of compounds accumulated during this trial is shown in: (b) desethyl-terbuthylazine (DE-TBZE), (c) inorganic N-compounds ($N\text{-}NH_4^+$ and $N\text{-}NO_3^-$) and (d) final acids.

The intermediates and final products formed during the EO process were analyzed as well. The reversed-phase HPLC chromatograms revealed the production of DE-TBZE as main heteroaromatic byproduct. It was rapidly accumulated up to 0.59 mg dm^{-3} at 10 min, further being completely removed in 150 min (see Fig. 4b). Fig. 4c shows that the NH_4^+ concentration grew continuously up to 0.73 mg N dm^{-3}, while NO_3^- was accumulated up to 0.69 mg N dm^{-3}, accounting for a 47.8% and 45.3% of the 1.525 mg N dm^{-3} contained in the herbicide, respectively. This suggests the presence of other more recalcitrant N-products in the final solution, considering the low ability of BDD to produce N_2 (see Fig. 1e). Oxalic, oxamic and cyanuric acids were identified by ion-exclusion HPLC. The two former carboxylic acids are final byproducts that are directly transformed into CO_2, whereas cyanuric acid is the most stable byproduct in the degradation of s-triazines [56]. As can be seen in Fig. 4d, only oxalic acid was completely removed in 120 min, whereas the other acids were very persistent, thereby impeding the overall mineralization of TBZE.

3.3. Electrochemical oxidation/electrodenitrification process in simulated groundwater

The paired EO/electrodenitrification using the BDD/Fe and RuO_2/Fe tank reactors was studied with a 5.0 mg dm^{-3} TBZE + 100 mg dm^{-3} NO_3^- + 7.6 mmol dm^{-3} SO_4^{2-} solution at pH 4.0 and 500 mA. As in the cases discussed above, the solution pH raised up to ca. 10 after 360 min of electrolysis, the E_{cell} value was slightly superior with the BDD anode, and EC values were similar to those found without the herbicide (see Table 2). Fig. 5a highlights a much faster TBZE removal using BDD. The herbicide was completely abated in 120 min, a time higher than 80 min needed in sulfate medium (see Fig. 4a), suggesting that the anodic oxidation of NH_4^+ diminishes the amount of BDD($^\bullet$OH) available for TBZE destruction. In contrast, the herbicide concentration was reduced by 89% using RuO_2, in agreement with the much smaller oxidation power of RuO_2($^\bullet$OH). This behavior can be confirmed from the corresponding k(TBZE) values, which were 9.0-fold higher using BDD (see Table 2). The intermediate DE-TBZE was not detected with this anode, in contrast to that found in sulfate medium (see Fig. 4b), probably because it was accumulated to a smaller amount during the whole electrolysis. This phenomenon did not occur with RuO_2 due to its lower oxidation ability, and DE-TBZE was largely accumulated without apparent destruction, attaining a steady value 1.49 mg dm^{-3} as can be seen in Fig. 5b. The aforementioned behavior can be confirmed from the NO_3^- abatements shown in Fig. 5c. Using the RuO_2 anode, the content decayed with a $k(NO_3^-)$ value of 6.5 × 10^{-3} min^{-1}. This is similar to that determined in the absence of the herbicide (see Table 2), denoting that EO and electroreduction behave as independent processes using RuO_2. In contrast, the interaction of both processes using BDD caused 0.5-fold drop of $k(NO_3^-)$ in the presence of the herbicide, pointing to the NO_3^- generation during the pesticide degradation.

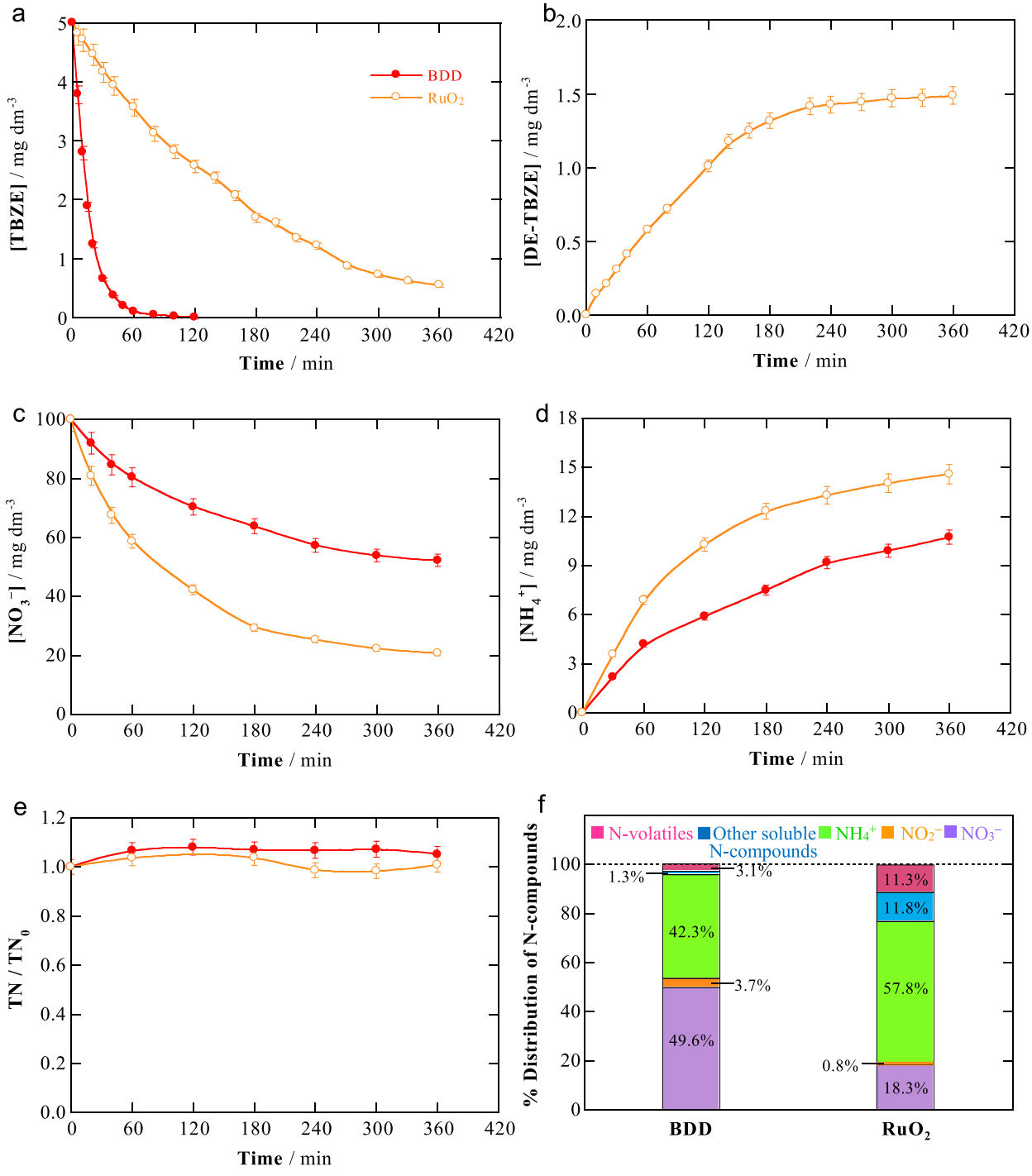

Fig. 5. (a) TBZE content abatement during the paired EO/electrodenitrification of 500 cm^3 of a solution containing 5 mg dm^{-3} herbicide in pure water with 100 mg dm^{-3} NO_3^- + 7.6 mmol dm^{-3} SO_4^{2-} at pH 4.0, using undivided stirred BDD/Fe or RuO_2/Fe tank reactors at 500 mA and 25 °C. (b) Accumulated DE-TBZE concentrations, (c) NO_3^- concentration removal, (d) NH_4^+ accumulated concentrations, (e) normalized total nitrogen decays, and (f) percent distributions of the nitrogen compounds at the end of the trials.

This was confirmed by the fact that in the final solution treated with BDD, small contents of NO_2^- ion were detected alongside a much smaller NH_4^+ accumulation (see Fig. 5d). As in the case of the chloride-free medium without the herbicide, in the presence of this latter pollutant a very low TN removal could be observed (Fig. 5e). Hence, NO_3^- evolved mainly to NH_4^+ via reaction (2) and, to a much smaller extent, to N_2 gas via reaction (3). The speciation of the final N-compounds depicted in Fig. 5f confirms this behavior, showing that the generated NH_4^+ ion and the residual NO_3^- ion were the main N-species regardless of the anode. Note that the N initially contained in the herbicide was not measured with the TN analyzer, but this N (10% of the total TN) appeared gradually as the herbicide byproducts were formed, which justifies the normalized TN values greater than 1.0 in Fig. 5e. This was more significant using BDD due to its greater power to destroy TBZE.

The study was completed with the case of a simulated matrix with chloride (100 mg dm^{-3} NO_3^- + 0.8 mmol dm^{-3} SO_4^{2-} + 10 mmol dm^{-3} Cl^-). TBZE was spiked at a concentration of 5.0 mg

dm^{-3}, and the effect of initial pH from 4.0 to 10.5 and applied *I* from 250 to 1000 mA was evaluated with both cells. Comparison of the data of Table 2 for these assays allows concluding that analogous final pH, E_{cell} and EC values were obtained in the absence and presence of TBZE. As expected, the latter two parameters underwent a progressive rise at higher *I*, with the consequent acceleration of all electrodic reactions.

For the cell with the BDD anode, Fig. 6a shows a gradual deceleration of the herbicide disappearance as the pH was risen from 4.0 to 10.5 at each given *I*, with a concomitant longer time needed for total removal. This tendency can also be deduced from the corresponding *k*(TBZE) values collected in Table 2. For example, at 500 mA, the herbicide disappeared after 50, 60 and 100 min at pH 4.0, 7.0 and 10.5, related to decreasing *k*(TBZE) values of 9.9×10^{-2}, 5.7×10^{-2} and 5.2×10^{-2} min^{-1}. Note that at the best pH of 4.0, a slightly quicker herbicide destruction was attained in the presence of chloride, as compared to sulfate medium (*k*(TBZE) = 9.0×10^{-2} min^{-1}) and chloride-free matrix (*k*(TBZE) = 5.7×10^{-2} min^{-1}). This can be explained by its simultaneous reaction with BDD($^{\bullet}$OH) formed via reaction (4) and active chlorine (HClO) generated via reactions (5) and (6), which accelerated its destruction. The change of this active chlorine form to the weaker oxidant ClO^- can justify the loss of oxidation power when starting at pH 7.0 and 10.5. Fig. 6a also shows that, at each pH, TBZE decayed more rapidly at higher *I*, as result of the greater production of BDD($^{\bullet}$OH) and active chlorine.

The rate of NO_3^- concentration decay in the chloride medium was slightly lower with the herbicide (see Fig. 6b) than in its absence (see Fig. 2a). This trend can also be established from the lower *k*(NO_3^-) values determined in the former case, listed in Table 2. In the presence of TBZE, part of the active chlorine oxidizes the organics, yielding additional amounts of NO_3^- ion. Large decays of TN were obtained in the chloride medium with herbicide, as shown in Fig. 6c, in agreement with the discussion in the absence of organics (subsection 3.1). The process was slightly slower at pH 10.5, although large amounts of volatile products (N_2) were always formed. The analysis of the distribution of final N-species shown in Fig. 6d makes in evidence that up to 57% of volatile products were produced, corroborating that reaction (8) becomes the most important step for NO_3^- removal in the presence of Cl^-. However, a smaller proportion of volatile compounds was detected as compared to the chloride matrix without herbicide (see Fig. 2d), owing to the partial loss of active chlorine resulting from its participation in the degradation of the organic molecules.

Fig. 6e reveals that generated active chlorine was rapidly accumulated up to around 90 mg dm^{-3} as maximal, being subsequently destroyed in all cases after 360 min of electrolysis. Only at pH 10.5 some small amounts persisted working at 250 and 500 mA. Although active chlorine attacks the organics and NH_3, with BDD it is mainly destroyed through direct and/or BDD($^{\bullet}$OH)-mediated oxidation to ClO_3^- and ClO_4^- ions. Fig. 6f shows the rapid formation of ClO_3^- ion, which was more rapidly destroyed at increasing *I* to yield a large amount of the stable ClO_4^- ion (see Fig. 6g). Fig. 6f and 6g highlight that the evolution of both ions only depended on *I*, being quite similar to that determined without organics (see Fig. 3c and 3d).

The results obtained for the EO/electrodenitrification of a solution containing 5.0 mg dm^{-3} TBZE in 100 mg dm^{-3} NO_3^- + 0.8 mmol dm^{-3} SO_4^{2-} + 10 mmol dm^{-3} Cl^{-1} using the RuO_2/Fe tank reactor are presented in Fig.7a-7f. Similar trends to those described for the BDD/Fe cell can be observed, but with notable differences that can be ascribed to the smaller ability of RuO_2($^{\bullet}$OH) to oxidize organics and active chlorine, thus becoming much more effective to remove NO_3^-. Fig. 7e reveals the accumulation of much greater contents of active chlorine as compared to the BDD/Fe cell, up to 322 mg dm^{-3} as maximal, which decreased more largely as *I* grew up. The decay of active chlorine is due to its oxidation to ClO_3^- ion, which is generated to larger extent at higher *I*, as can be seen in Fig. 7f.

Regarding the TBZE abatement using the RuO_2 anode, two tendencies can be observed in Fig. 7a, as compared to the BDD/Fe cell: (i) a lower degradation rate at 250 and 500 mA, with the herbicide being mainly oxidized by RuO_2($^{\bullet}$OH), and (ii) a similar degradation at 1000 mA, when larger amounts of active chlorine act as preeminent oxidant. The change of *k*(TBZE) between these two regions can be seen in Table 2. It can also be deduced that the best abatements were achieved at pH 4.0, regardless of the applied *I*. The greater production of active chlorine with RuO_2 favors the overall oxidation of NH_3 (not detected) to regenerate more NO_3^- ion at long electrolysis time. This can be inferred by comparing the NO_3^- profiles of Fig. 7b using RuO_2 with those of Fig. 6b using BDD. However, the *k*(NO_3^-) values of Table 2 are greater for the RuO_2 anode. This is not surprising because they were only determined during the first 60 min of electrolysis, because at higher time the NO_3^- concentration in the medium was practically stabilized due to its fast regeneration from reaction (9). This phenomenon was not found with the BDD anode, where the NO_3^- concentration decayed gradually and excellent linear $\ln([NO_3^-]_0/[NO_3^-])$ vs. *t* plots were obtained up to 300 min of electrolysis. In the same context, Fig. 7c shows a slower TN abatement using RuO_2 than that obtained with BDD (see Fig. 6c). Despite this, high percentages of generated volatile N-compounds were always determined, as highlights Fig. 7d, corroborating again the fast reaction (8) to produce N_2 gas. The main species in final solutions was the residual NO_3^- ion under all operation conditions. No combined chlorine forming chloramines was detected in both cells at the end of any experiment. This suggests that, if produced, they reacted rapidly either with the NO_2^- ion generated from reaction (1) according to reaction (15), or with the active chlorine present in solution to be oxidized to nitrate.

$$NH_2Cl + NO_2^- + H_2O \rightarrow NO_3^- + NH_4^+ + Cl^- \quad (15)$$

3.4. Electrochemical oxidation/electrodenitrification process in softened actual groundwater

Since the cell equipped with BDD yields faster EO and electrodenitrification than that with RuO_2 in chloride matrices, BDD/Fe cells were chosen to study the paired treatment of 5.0 mg dm^{-3} TBZE spiked into actual softened groundwater (100 mg dm^{-3} NO_3^-) conditioned at pH 4.0. One cell had one Fe cathode and was operated at *I* = 500 mA, whereas another cell had two Fe cathodes sandwiching the BDD anode to work at *I* = 1000 mA. Moreover, to clarify the influence of NOM on the performance of the system, an assay with the latter cell was carried out with the simulated chloride matrix. A significant effect of using two Fe cathodes instead of one at 1000 mA was the notable decay of E_{cell} (8.8 V vs 14.7 V), giving rise to a great reduction of EC (105.6 kWh m^{-3} vs. 176.4 kWh m^{-3}) (see Table 2). Therefore, the number and position of the electrodes plays a crucial role in the optimization of the energy parameters. In contrast, final pH values close to 10.5 were always obtained at the end of the treatment for both systems.

A similar TBZE content decay can be observed in Fig. 8a for the simulated and actual softened groundwater using two Fe anodes, achieving the total removal in 40 min, which suggests that the influence of NOM oxidation was irrelevant. In fact, Table 2 shows that the *k*(TBZE) value for both treatments (about 0.16 min^{-1}) was even greater than 0.10 and 0.12 min^{-1} determined for the cell with one Fe cathode at 500 mA (i.e., the same current density

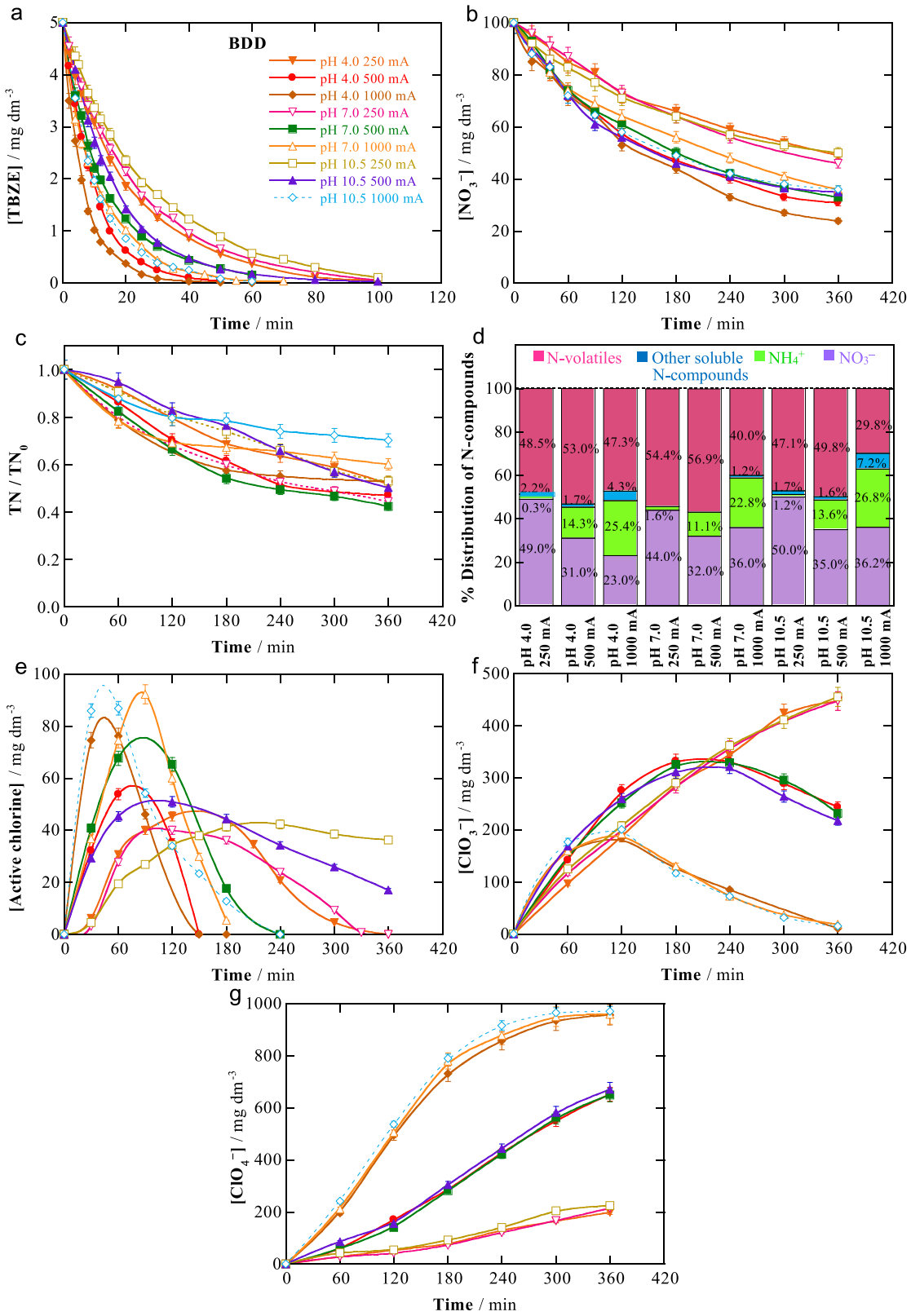

Fig. 6. Influence of pH and current on the time course of (a) TBZE content during the paired EO/electrodenitrification of 500 cm^3 of a solution containing 5 mg dm^{-3} herbicide in pure water with 100 mg dm^{-3} NO_3^- + 0.8 mmol dm^{-3} SO_4^{2-} + 10 mmol dm^{-3} Cl^{-1}, using an undivided stirred BDD/Fe tank reactor at 25 °C. (b) NO_3^- concentrations, (c) normalized total nitrogen decays, (d) percent distribution of the nitrogen species at the end of the trials, (e) active chlorine concentrations, (f) ClO_3^- contents and (g) ClO_4^- concentrations.

Table 3
Products identified by GC-MS after 60 min of EO/electrodenitrification of 500 cm^3 of solutions with 5.0 mg dm^{-3} terbuthylazine in a simulated matrix at pH 4.0 and 25 °C using a BDD/Fe cell at 500 mA.

No.	Chemical name	Molecular structure	Column[a]	t_r / min	Fragments (*m/z*)[b]
1	Terbuthylazine (TBZE)	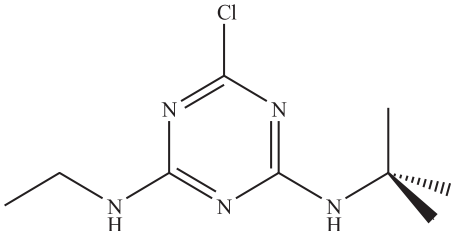	P [c, d] NP [c, d]	40.71 30.73	229 214 (- CH_3) 173 (- $C(CH_3)_3$ + H) 158 (173 - CH_3)
2	*N-tert*-butyl-*N'*-[1,3,5]triazine-2,4-diamine[a,b]	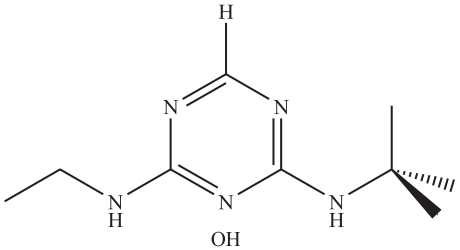	P [c] NP [c, d]	33.93 26.92	195 180 (- CH_3) 139 (- ($C(CH_3)_3$ + H)) / - CH_3-CH_2-NH-C-)
3	4-*tert*buthylamino-6-vinylamino-[1,3,5]triazine-2-ol	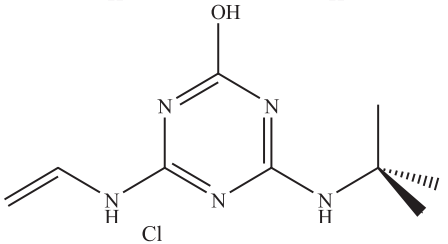	P [d] NP [d]	40.47 29.84	209 194 (- CH_3) 152 (- $C(CH_3)$ / 194 - $C(CH_3)_2$) 125 (152 - $CH{=}CH_2$)
4	(Desethyl-terbuthylazine), *N-tert*-butyl-6-chloro-[1,3,5]triazine-2,4-diamine (DE-TBZE)	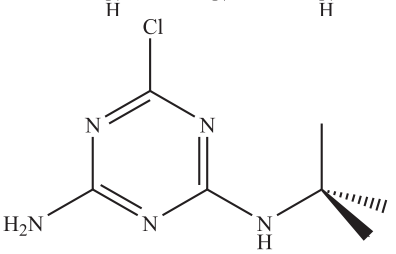	P [c]	43.98	201 186 (- (NH_2 + H)) 145 (- ($C(CH_3)_3$ + H)) 173 (- $C(NH_2)$-) 138 (173 -Cl)
5	*N*-(4-*tert*-butylamino-6-chloro-[1,3,5]triazine-2-yl)-acetamide	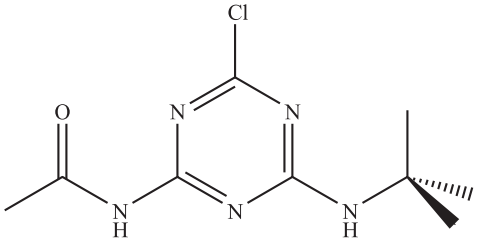	P [c,] NP [d]	45.31 33.23	243 228 (- CH_3) 200 (- (CO-CH_3)) 186 (-$C(CH_3)_3$)
6	6-chloro-*N*-ethyl-[1,3,5]triazine-2,4-diamine	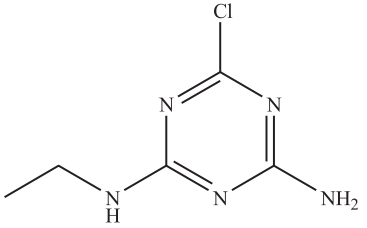	P [c, d] NP [c, d]	47.42 28.36	173 158 (- (NH_2 + H) / - CH_3) 145 (- (CH_2-CH_3 + H)) 110 (145 -Cl)

(*continued on next page*)

Table 3 (*continued*)

No.	Chemical name	Molecular structure	Column[a]	t_r / min	Fragments (*m/z*)[b]
7	4-amino-6-isopropenylamino-[1,3,5]triazine-2-ol	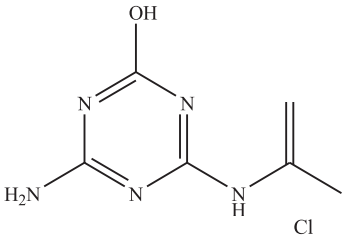	P [d]	36.56	167 152 (- CH_3) 111 (- NH-C(CH_2)-CH_3)
8	*N*-(4-*tert*-butylamino-6-chloro-[1,3,5]triazine-2-yl)-2-hydroxy-acetamide	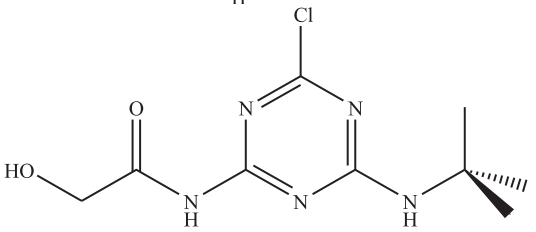	P [c,]	42.60	259 185 (- NH-C(O)-CH_2OH) 129(185 –(C(CH_3)$_3$ +H))
9	*N*-(4-amino-6-chloro-[1,3,5]triazine-2-yl)-acetamide	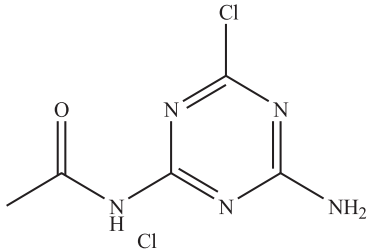	P [c]	45.48	187 172 (- CH_3) 145 (- (C(O)-CH_3 +H)) 110 (145 - Cl)
10	6-chloro-[1,3,5]triazine-2,4-diamine	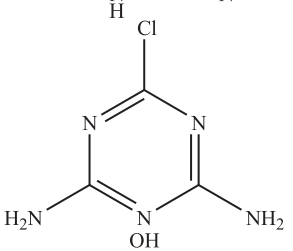	P [d]	41.89	145
11	Cyanuric acid	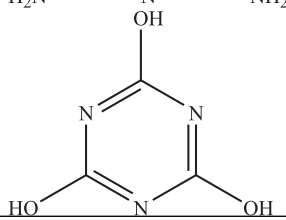	P [c]	30.27	129 115 (- N-) 98 (115 - OH) 87 (129 – (N-C(OH)- + H)) 73 (87 - N-)

[a] P: polar column, NP: Nonpolar column. [b] The mass (*m*) of chlorinated fragments considered the isotope ^{35}Cl. [c] Medium: 100 mg dm^{-3} NO_3^- + 7.6 mmol dm^{-3} SO_4^{2-}. [d] Medium: 100 mg dm^{-3} NO_3^- + 0.8 mmol dm^{-3} SO_4^{2-} + 10 mmol dm^{-3} Cl^-.

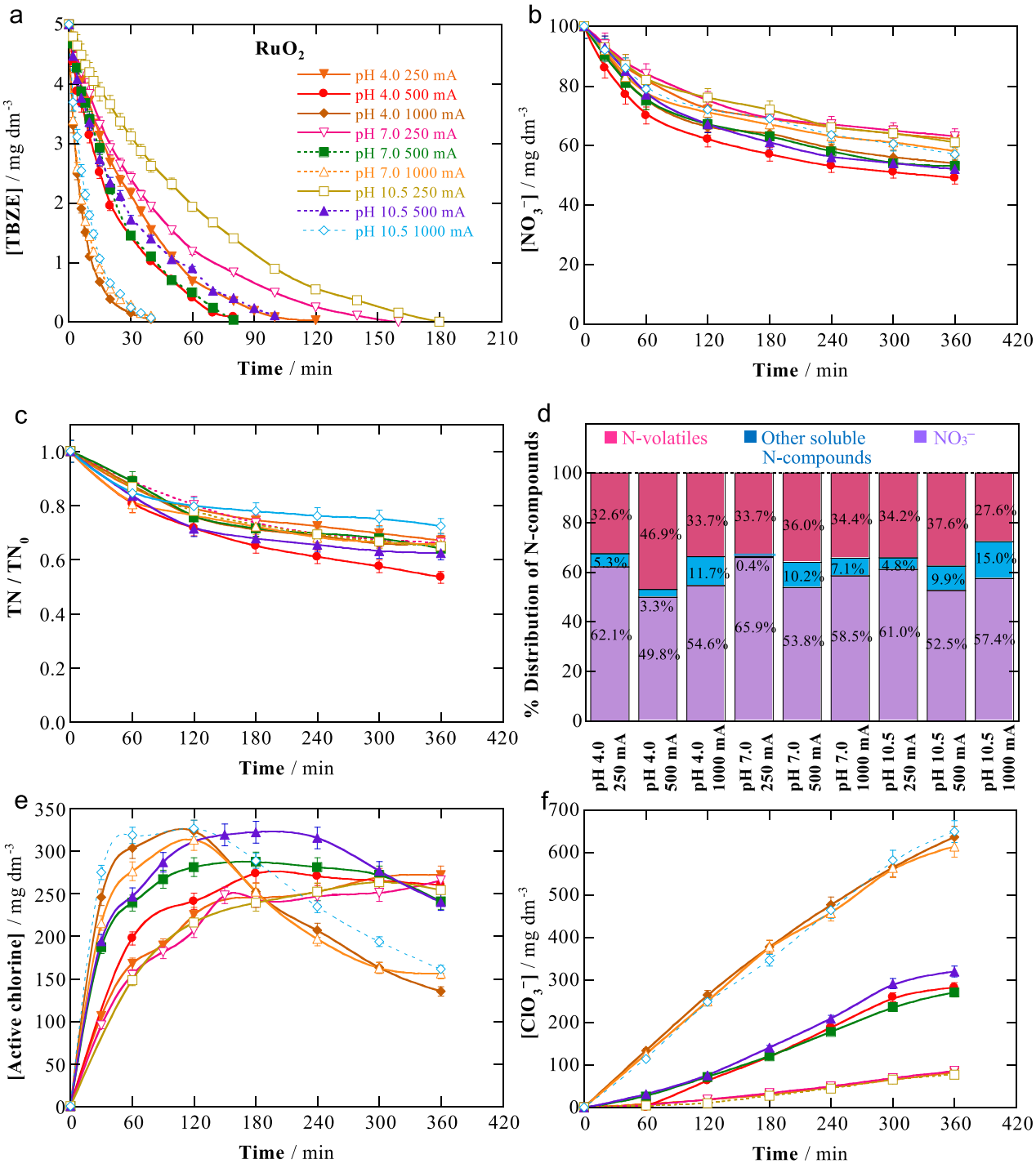

Fig. 7. Effect of pH and current under the conditions described in Fig. 6, but using an undivided stirred RuO_2/Fe tank reactor.

than using two Fe cathodes at 1000 mA) and 1000 mA, thus being the TBZE degradation faster and more efficient. In contrast, Fig. 8b depicts a slower destruction of the intermediate DE-TBZE in the actual groundwater after reaching a maximal of 0.26 mg dm^{-3}, which can be ascribed to the loss of oxidizing agents that are partly consumed by NOM. The effect of the organic matter was also evaluated for the evolution of NO_3^-, NH_4^+ and TN. Fig, 8c and 8e show a very fast NO_3^- and TN decay in the simulated groundwater with two Fe cathodes, much more rapid than using one Fe cathode at the same *I* (see Figs. 6b and 6c). These figures also show a strong inhibition of both parameters in the actual groundwater, which can be explained by the fouling effect of NOM and residual Mg on the cathode surface and a small formation of NO_3^- ion from the degradation of NOM. This influence of the organic matter was also evident for the NO_3^- content removal when using the cell with one Fe cathode at $I = 500$ mA to treat the actual groundwater (see Fig. 8c), but it was irrelevant for TN decay as compared to the trial with two Fe cathodes (see Fig. 8e). Fig. 8d reveals the expected greater accumulation of NH_4^+ ion in the three treatments as a greater NO_3^- concentration was abated.

A different behavior was observed for the time course of Cl^-, ClO_3^- and ClO_4^- ions, mainly depending on the applied *I* and

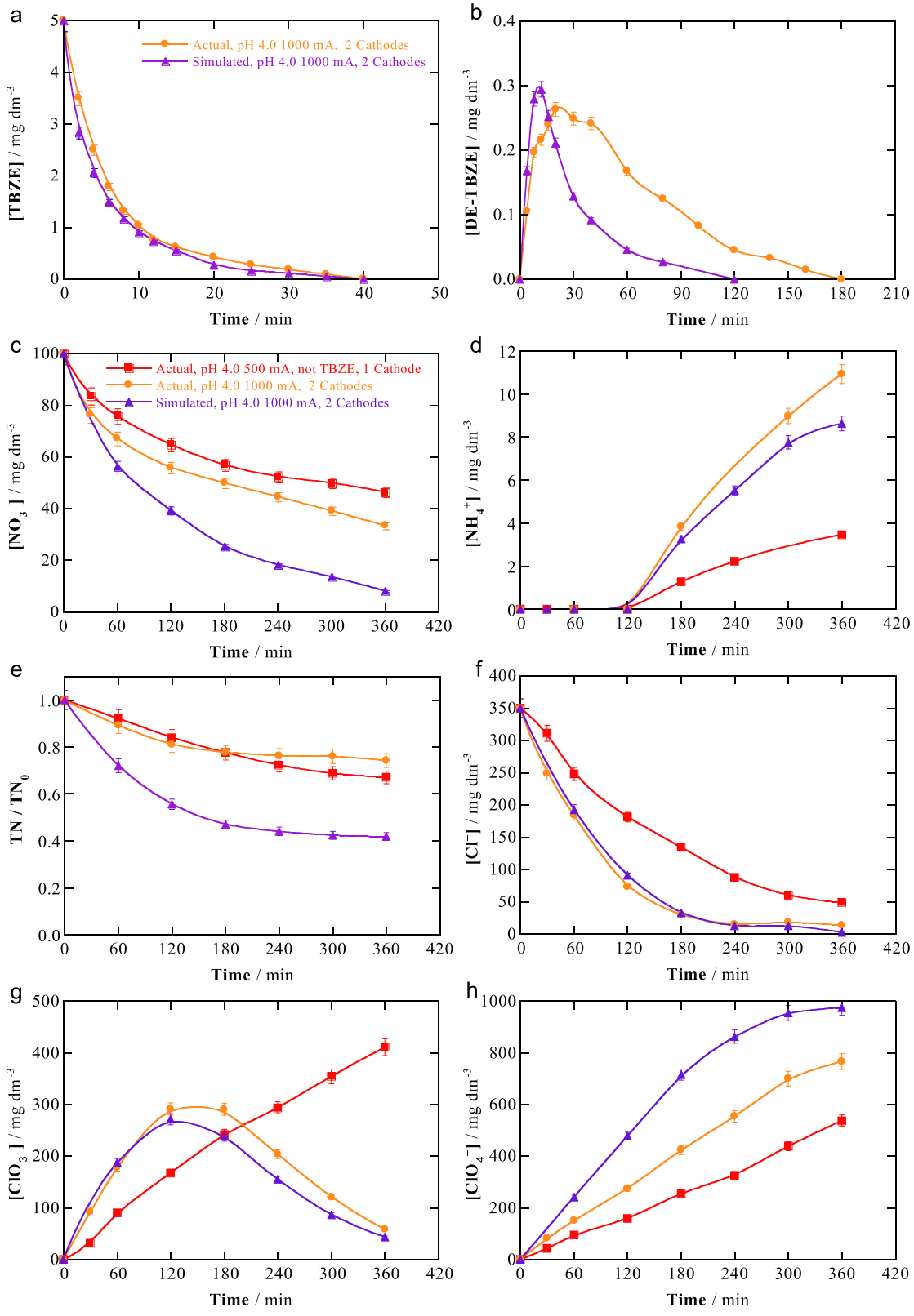

Fig. 8. Change of the concentrations of: (a) TBZE, (b) DE-TBZE, (c) NO_3^-, (d) NH_4^+, (e) normalized total nitrogen, (f) Cl^-, (g) ClO_3^- and (h) ClO_4^- during the paired EO/electrodenitrification of 500 cm^3 of the simulated groundwater (100 mg dm^{-3} NO_3^- + 0.8 mmol dm^{-3} SO_4^{2-} + 10 mmol dm^{-3} Cl^-) or softened actual groundwater containing 5 mg dm^{-3} herbicide, using 1 BDD anode and 2 Fe cathodes. For comparison, the results for the treatment of actual groundwater without TBZE using 1 Fe cathode are also shown.

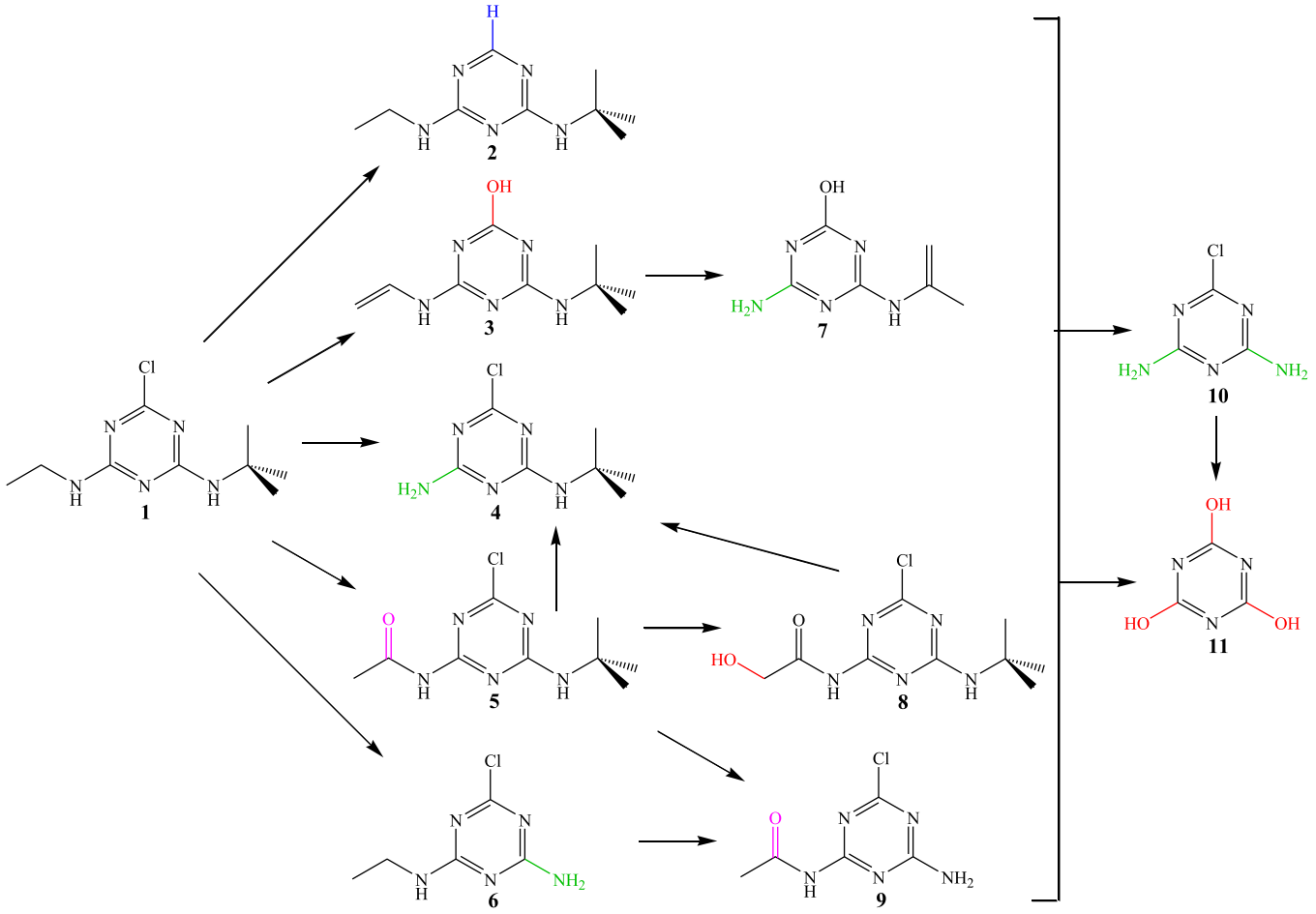

Fig. 9. Initial reaction pathway for terbuthylazine degradation in groundwater by EO with a BDD/Fe cell.

with little influence of the number of Fe cathodes, as can be seen in Figs. 8f-8h. Total Cl^- removal was reached in 240 min using two Fe cathodes, with similar $k(Cl^-)$ values of 1.32-1.40 × 10^{-2} min^{-1}, very close to 1.24 × 10^{-2} min^{-1} determined with one Fe cathode (see Table 2). The lower I of 500 mA with two Fe cathodes yielded an 88% reduction of Cl^- content in 360 min, with $k(Cl^-)$ = 5.7 × 10^{-3} min^{-1}, slightly lower than 7.5 × 10^{-3} min^{-1} found with one Fe cathode (see Table 2). All the active chlorine produced from Cl^- oxidation was then transformed into ClO_3^-, which was converted into ClO_4^-, to larger extent at higher I. For the actual groundwater at I = 1000 mA, 59 mg dm^{-3} of ClO_3^- and 767 mg dm^{-3} of ClO_4^- were finally obtained. The latter content was smaller than 975 mg dm^{-3} determined in the simulated groundwater, which can be due to the loss of active chlorine by reaction with the organic matter. The ClO_3^- and ClO_4^- concentrations after electrolysis of the actual groundwater need to be removed before disposal or reuse. Aiming at evaluating the viability of the technology for future scale-up, a post-treatment was applied by employing a commercial ion-exchange resin. Table 1 shows that this resin allowed the overall removal of ClO_4^- and NO_2^- anions, most of the residual ClO_3^- ion and partial removal of NO_3^- and SO_4^{2-} ions.

3.5. Identification of heteroaromatic byproducts and proposal of initial reaction sequence

Table 3 summarizes the chemical name, molecular structure, type of column, retention time and fragments for the stable heteroaromatic byproducts of TBZE (**1**) identified after 60 min of electrolysis of simulated matrices with and without chloride containing 5.0 mg dm^{-3} herbicide. For this, the BDD/Fe tank reactor was operated at I = 500 mA. Although different byproducts were identified in each medium due to the different oxidation environments, any organochlorine derivative was found despite the formation and attack of active chlorine in the chloride matrix, as pointed out above. This surprising finding can be explained by the rapid destruction of such chloro-compounds by the strong oxidant BDD(•OH). As can be seen in Table 3, ten heteroaromatics were identified related to: (i) the release of either the Cl atom with hydrogenation (compound **2**) or hydroxylation (compound **3**), the lateral ethyl group (compound **4**), the lateral *tert*-butyl group (compound **6**) or both lateral groups (compound **10**); (ii) the carbonylation of the ethyl group (compounds **5, 8** and **9**); (iii) the oxidation of the *tert*-butyl group (compound **7**); and (iv) the overall hydroxylation (compound **11**) of these products. Note that compounds **4**-**6** have been previously reported by other authors for **1** degradation [52,57]. Compounds **4** (DE-TBZE) and **11** (cyanuric acid) have been also detected and quantified in this work by reversed-phase and ion-exclusion HPLC, respectively.

Based on the identified heteroaromatics, an initial route for **1** destruction by EO with a BDD anode is proposed in Fig. 9. In this pathway, BDD(•OH) is assumed as the main oxidant. The initial attack of this radical over **1** leads to 5 compounds: (i) **2** with hydrogenation and Cl loss, (ii) **3** with hydroxylation and Cl release, (iii) **4** with release of the ethyl group, (iv) **5** with carbonylation of the ethyl group and (v) **6** with loss of the *tert*-butyl group. The subsequent release of the ethenyl group with oxidation of the *tert*-butyl group of **3** yields **7**, whereas the hydroxylation of **5** gives **8** and the

carbonylation of **6** produces **9**. Transformation of **5** and **8** into **4**, as well as that of **5** into **9**, is feasible. Compounds **4**-**6, 8** and **9** can then evolve to **10** and all products to **11** as final heteroaromatic.

4. Conclusions

This study has presented a comprehensive set of EO, electroreduction and EO/electroreduction trials in simulated and actual groundwater matrices with only NO_3^-, only TBZE or NO_3^- + TBZE, in the absence and presence of Cl^-. The BDD/Fe and RuO_2/Fe cells showed a very high effectiveness to simultaneously remove nitrate and pesticide from the solutions. From our results, it can be concluded that an effective treatment of groundwater polluted with nitrate and TBZE pesticide requires a sequence of three steps: (i) Softening to minimize the Ca^{2+} and Mg^{2+} content that block the electocatalytic nitrate electroreduction; (ii) EO/electrodenitrification with a BDD/Fe or RuO_2/Fe cell, preferably with two Fe cathode because the greater exposed surface favored the occurrence of electrocatalysis; and (iii) post-treatment with an anion-exchange resin to minimize the chlorate and perchlorate concentrations and achieve an additional nitrate removal. The NOM contained in the groundwater had no negative influence on TBZE removal, but it decelerated the nitrate removal. All removals became faster as the applied current was increased from 250 to 1000 mA. Once demonstrated that the paired electrolysis of nitrate + pesticide solutions can be highly effective with BDD/Fe and RuO_2/Fe cells at small scale, further work is being carried out in our laboratory to scale-up the treatment using a flow reactor.

CReDiT author statement

Roger Oriol: Conceptualization, Formal analysis, Investigation, Methodology; **Enric Brillas**: Data curation, Formal analysis, Writing-original draft, Writing-review & editing; **Pere L. Cabot**: Funding acquisition, Validation; **José L. Cortina**: Resources, Validation; **I. Sirés**: Conceptualization, Funding acquisition, Project administration, Supervision, Writing-original draft, Writing-review & editing.

Declaration of Competing Interest

The authors declare that they have no known competing financial interests or personal relationships that could have appeared to influence the work reported in this paper.

Acknowledgements

The authors thank the financial support from project PID2019-109291RB-I00 (AEI, Spain). R. Oriol acknowledges the FPI grant awarded by MINECO (Spain).

References

[1] M. Gutiérrez, R.N. Biagioni, M.T. Alarcón-Herrera, B.A. Rivas-Lucero, An overview of nitrate sources and operating processes in arid and semiarid aquifer systems, Sci. Total Environ. 624 (2018) 1513–1522.
[2] M. Duca, M.T.M. Koper, Powering denitrification: the perspectives of electrocatalytic nitrate reduction, Energy Environ. Sci. 5 (2012) 9726–9742.
[3] M. Zhou, W. Fu, H. Gu, L. Lei, Nitrate removal from groundwater by a novel three-dimensional electrode biofilm reactor, Electrochim. Acta 52 (2007) 6052–6059.
[4] M. Shrimali, K.P. Singh, J. Greeley, New methods of nitrate removal from water, Environ. Poll. 112 (2001) 351–359.
[5] M. Li, C. Feng, Z. Zhang, X. Lei, R. Chen, Y. Yang, N. Sugiura, Simultaneous reduction of nitrate and oxidation of by-products using electrochemical method, J. Hazard. Mater. 171 (2009) 724–730.
[6] H. Cheng, K. Scott, P.A. Christensen, Paired electrolysis in a solid polymer electrolyte reactor-simultaneously reduction of nitrate and oxidation of ammonia, Chem. Eng. J. 108 (2005) 257–268.
[7] H. Cheng, K. Scott, Christensen P.A, Application of a solid polymer electrolyte reactor to remove nitrate ions from wastewater, J. Appl. Electrochem. 35 (2005) 551–560.
[8] I. Katsounaros, G. Kyriacou, Influence of the concentration and the nature of the supporting electrolyte on the electrochemical reduction on tin cathode, Electrochim. Acta 52 (2007) 6412–6420.
[9] I. Katsounaros, G. Kyriacou, Influence of nitrate concentration on its electrochemical reduction on tin cathode: identification of reaction intermediates, Electrochim. Acta 53 (2008) 5477–5484.
[10] D. Reyter, D. Bélanger, L. Roué, Study of the electroreduction of nitrate on copper in alkaline solution, Electrochim. Acta 53 (2008) 5977–5984.
[11] W. Huang, M. Li, B. Zhang, C. Feng, X. Lei, B. Xu, Influence of operating conditions on electrochemical reduction of nitrate in groundwater, Water Environ. Res. 85 (2013) 224–231.
[12] M. Li, C. Feng, Z. Zhang, Z. Shen, N. Sugiura, Electrochemical reduction of nitrate using various anodes and a Cu/Zn cathode, Electrochem. Commun. 11 (2009) 1853–1856.
[13] B. Talhi, F. Monette, A. Azzouz, Effective and selective nitrate electroreduction into nitrogen through synergistic parameter interactions, Electrochim. Acta 58 (2011) 276–284.
[14] R. Oriol, M.P. Bernícola, E. Brillas, P.L. Cabot, I. Sirés, Paired electrooxidation of insecticide imidacloprid and electrodenitrification in simulated and real water matrices, Electrochim. Acta 317 (2019) 753–765.
[15] E. Lacasa, P. Cañizares, J. Llanos, M.A. Rodrigo, Effect of the cathode material on the removal of nitrates by electrolysis in non-chloride media, J. Hazard. Mater. 213-214 (2012) 478–484.
[16] E. Lacasa, J. Llanos, P. Cañizares, M.A. Rodrigo, Electrochemical denitrificacion with chlorides using DSA and BDD anodes, Chem. Eng. J. 184 (2012) 66–71.
[17] M. Dortsiu, I. Katsounaros, C. Polatides, G. Kyriacou, Influence of the electrode and the pH on the rate and the product distribution of the electrochemical removal of nitrate, Environ. Technol. 34 (2013) 373–381.
[18] Y.Y. Birdja, J. Yang, M.T.M. Koper, Electrocatalytic reduction of nitrate on tin–modified palladium electrodes, Electrochim. Acta 140 (2014) 518–524.
[19] L. Rajic, D. Berroa, S. Gregor, S. Elbakri, M. MacNeil, A.N. Alshawabkeh, Electrochemically-induced reduction of nitrate in aqueous solution, Int. J. Electrochem. Sci 12 (2017) 5998–6009.
[20] C. Sun, F. Li, H. An, Z. Li, A.M. Bond, J. Zhang, Facile electrochemical co-deposition of metal (Cu, Pd, Pt, Rh) nanoparticles on reduced graphene oxide for electrocatalytic reduction of nitrate/nitrite, Electrochim. Acta 269 (2018) 733–741.
[21] Y. Zhang, Y. Zhao, Z. Chen, L. Wang, P. Wu, F. Wang, Electrochemical reduction of nitrate via Cu/Ni composite cathode paired with Ir-Ru/Ti anode: high efficiency and N_2 selectivity, Electrochim. Acta 291 (2018) 151–160.
[22] L. Wu, Y. Shi, C. Su, H. Cao, G. Zheng, Efficient electrochemical reduction of high concentration nitrate by a stepwise method, Catal. Lett. 149 (2019) 1216–1223.
[23] D.E. Kim, D. Pak, Ti plate with TiO_2 nanotube arrays as a novel cathode for nitrate reduction, Chemosphere 228 (2019) 611–618.
[24] I. Sanjuán, L. García-Cruz, J. Solla-Gullón, E. Expósito, V. Montiel, Bi-Sn nanoparticles for electrochemical denitrification: activity and selectivity towards N_2 formation, Electrochim. Acta 340 (2020) 135914.
[25] J. Martínez, A. Ortiz, I. Ortiz, State-of-the-art and perspectives of the catalytic and electrocatalytic reduction of aqueous nitrates, Appl. Catal. B: Environ. 207 (2017) 42–59.
[26] J.R. Steter, E. Brillas, I. Sirés, On the selection of the anode material for the electrochemical removal of methylparaben from different aqueous media, Electrochim. Acta 222 (2016) 1464–1474.
[27] S. Lanzalaco, I. Sirés, A. Galia, M.A. Sabatino, C. Dispenza, O. Scialdone, Facile crosslinking of poly(vinylpyrrolidone) by electro-oxidation with IrO_2-based anode under potentiostatic conditions, J. Appl. Electrochem. 48 (2018) 1343–1352.
[28] G. Daniel, Y. Zhang, S. Lanzalaco, F. Brombin, T. Kosmala, G. Granozzi, A. Wang, E. Brillas, I. Sirés, C. Durante, Chitosan-derived nitrogen-doped carbon electrocatalyst for a sustainable upgrade of oxygen reduction to hydrogen peroxide in UV-assisted electro-Fenton water treatment, ACS Sustain. Chem. Eng. 8 (2020) 14425–14440.
[29] R. Oriol, D. Clematis, E. Brillas, J.L. Cortina, M. Panizza, I. Sirés, Groundwater treatment using a solid polymer electrolyte cell with mesh electrodes, ChemElectroChem 6 (2019) 1235–1243.
[30] L. Li, Y. Liu, Ammonia removal in electrochemical oxidation: mechanism and pseudo-kinetics, J. Hazard. Mater 161 (2009) 1010–1016.
[31] G. Pérez, J. Saiz, R. Ibañez, A.M. Urtiaga, I. Ortiz, Assessment of the formation of inorganic oxidation by-products during the electrocatalytic treatment of ammonium from landfill leachates, Water Res. 46 (2012) 2579–2590.
[32] C. Zhang, D. He, J. Ma, D. Waite, Active chlorine mediated ammonia oxidation revisited: reaction mechanism, kinetic modelling and implications, Water Res. 145 (2018) 220–230.
[33] P. Mandal, M.K. Yadav, A.K. Gupta, B.K. Dubey, Chlorine mediated indirect electro-oxidation of ammonia using non-active PbO_2 anode: influencing parameters and mechanism identification, Sep. Purif. Technol. 247 (2020) 116910.
[34] D.G. Wahman, G.E. Speitel Jr, Relative importance of nitrite oxidation by hypochlorous acid under chloramination conditions, Environ. Sci. Technol. 46 (2012) 6056–6064.
[35] J. Chen, H. Shi, J. Lu, Electrochemical treatment of ammonia in wastewater by RuO_2-IrO_2-TiO_2/Ti electrodes, J. Appl. Electrochem. 37 (2007) 1137–1144.

[36] A. Kapalka, A. Katsaounis, N.L. Michels, A. Leonidova, S. Souentie, C. Comninellis, K.M. Udert, Ammonia oxidation to nitrogen mediated by electrogenerated active chlorine on Ti/PtOx-IrO_2, Electrochem. Commun. 12 (2010) 1203–1205.
[37] I. Sirés, E. Brillas, G. Cerisola, M. Panizza, Comparative depollution of mecoprop aqueous solutions by electrochemical incineration using BDD and PbO_2 as high oxidation power anodes, J. Electroanal. Chem. 613 (2008) 151–159.
[38] A.R.F. Pipi, I. Sirés, A.R. De Andrade, E. Brillas, Application of electrochemical advanced oxidation processes to the mineralization of the herbicide diuron, Chemosphere 109 (2014) 49–55.
[39] F. Gozzi, I. Sirés, A. Thiam, S.C. de Oliveira, A, Machulek Jr., E. Brillas, Treatment of single and mixed pesticide formulations by solar photoelectro-Fenton using a flow plant, Chem. Eng. J. 310 (2017) 503–513.
[40] D.R.V. Guelfi, F. Gozzi, A. Machulek Jr., I. Sirés, E. Brillas, S.C. de Oliveira, Degradation of herbicide S-metolachlor by electrochemical AOPs using a boron–doped diamond anode, Catal. Today 313 (2018) 182–188.
[41] D.R.V. Guelfi, E. Brillas, F. Gozzi, A. Machulek Jr., S.C. de Oliveira, I. Sirés, Influence of electrolysis conditions on the treatment of herbicide bentazon using artificial UVA radiation and sunlight. Identification of oxidation products, J. Environ. Manage. 231 (2019) 213–221.
[42] D.R.V. Guelfi, Z. Ye, F. Gozzi, S.C. de Oliveira, A. Machulek Jr., E. Brillas, I. Sirés, Ensuring the overall combustion of herbicide metribuzin by electrochemical advanced oxidation processes. Study of operation variables, kinetics and degradation routes, Sep. Purif. Technol. 211 (2019) 637–645.
[43] A.L. Tasca, M. Puccini, A. Fletcher, Terbuthylazine and desethylterbuthylazine: recent occurrence, mobility and removal techniques, Chemosphere 202 (2018) 94–104.
[44] P. Bottoni, P. Grenni, L. Lucentini, A. Barra Caracciolo, Terbuthylazine and other triazines in Italian water resources, Microchem. J. 108 (2013) 136–142.
[45] E. Drazevic, K. Kosutic, S. Fingler, V. Drevenkar, Removal of pesticides from the water and their adsorption on the reverse osmosis membranes of defined porous structure, Des. Water Treat. 1-3 (2011) 161–170.
[46] S. Ronka, M. Kujawska, H. Juskiewicz, Triazines removal by selective polymeric adsorbent, Pure Appl. Chem. 11 (2014) 1755–1769.
[47] P.M. Álvarez, D.H.. Quiñones, I. Terrones, A. Rey, F.J. Beltrán, Insights into the removal of terbuthylazine from aqueous solution by several treatment methods, Water Res. 98 (2016) 334–343.
[48] L. Liang, X. Wang, Y. Sun, P. Ma, X. Li, H. Piao, Y. Jiang, D. Song, Magnetic solid-phase extraction of triazine herbicides from rice using metal-organic framework MIL-101(Cr) functionalized magnetic particles, Talanta 179 (2018) 512–519.
[49] S. Sorlini, F. Gialdini, M. Stefan, UV/H_2O_2 oxidation of arsenic and terbuthylazine in drinking water, Environ. Monit. Assess. 186 (2014) 1311–1316.
[50] A.F. Tchicaya, S.B. Wognin, I.A.A. Aka, Y.M. Kouassi, A.L.M. N'Guessan, Photocatalytic degradation of the herbicide terbuthylazine: preparation, characterization and photoactivity of the immobilized thin layer of TiO_2/chitosan, J. Photochem. Photobiol. A 309 (2015) 22–29.
[51] D.H. Quiñones, A. Rey, P.M. Álvarez, F.J. Beltrán, G.L. Puma, Boron doped TiO_2 catalysts for photocatalytic ozonation of aqueous mixtures of common pesticides: diuron, o-phenylphenol, MCPA and terbuthylazine, Appl. Catal. B: Environ. 178 (2015) 74–81.
[52] A.L. Tasca, M. Puccini, D. Clematis, M. Panizza, Electrochemical removal of terbuthylazine: boron-doped diamond anode coupled with solid polymer electrolyte, Environ. Pollut. 251 (2019) 285–291.
[53] AWWA APWA, Standard WEF, Methods for the Examination of Water and Wastewater, 21st ed., Method Number 4500-Cl Chlorine (residual)–G. DPD Colorimetric Method, American Public Health Association, Washington D.C, 2005 pp. 4-67 and 4–68.
[54] A. Thiam, I. Sirés, J.A. Garrido, R.M. Rodríguez, E. Brillas, Effect of anions on electrochemical degradation of azo dye Carmoisine (Acid Red 14) using a BDD anode and air-diffusion cathode, Sep. Purif. Technol. 140 (2015) 43–52.
[55] J.R. Steter, E. Brillas, I. Sirés, Solar photoelectro-Fenton treatment of a mixture of parabens spiked into secondary treated wastewater effluent at low input current, Appl. Catal. B: Environ. 224 (2018) 410–418.
[56] N. Borràs, R. Oliver, C. Arias, E. Brillas, Degradation of atrazine by electrochemical advanced oxidation process using boron-doped diamond anode, J. Phys. Chem. 114 (2010) 6613–6621.
[57] S.V. Pereira, T. Reis, B.S. Souza, R.F. Dantas, D.A. Azevedo, M. Dezotti, C. Sans, S. Esplugas, Oestrogenicity assessment of *s*-triazines by products during ozonation, Environ. Technol. 36 (2014) 1–25.

4.4. Characterization of mass transport regime in a rotating cylinder electrode reactor used for electrochemical denitrification

The RCE reactor drastically promotes the mass transport towards the working electrode by generating a turbulent flow at low rotation rates of the central cylinder. This reactor has been mostly used for metal recovery through electrodeposition, although its characteristics are suitable to study the electrodenitrification when an appropriated mild steel cathode is used as the cathode, aiming to establish whether the nitrate ER process is ruled by a charge transfer, mass transport or a mixed regime. In this study, the controlling regime for the nitrate ER process was characterized employing a system formed by a central RCE and six concentric Ti|IrO_2 anode plates, as can be seen in **Figure 1** (see related paper). Given the complexity of the nitrate ER removal mechanism and the high number of parameters and considerations involved in the electrodenitrification, the investigation was carried out with a synthetic solution. First, a fundamental study of the NRR using a mild steel (which had shown good result in the previous works described above) was made. For this purpose, linear sweep voltammetry (LSV) was performed with a rotating disk electrode (RDE). From these analyses at different rotation rates of the RDE, an analysis based on the Koutecky-Levich (KL) relationship (equations (33) and (34)) was performed, allowing determining the number of electrons involved in the reaction, as well as the heterogeneous charge transfer constants of the limiting step of the reaction at different applied potentials. Potentiostatic electrolyses were carried out in a 3-electrode system with 400 mL of a synthetic solution, with 500 mM of sodium sulfate as supporting electrolyte and 10 mM of potassium nitrate as electroactive species. The trials were performend at different rotation rates of the central electrode (100, 200, 300, 400 and 500 rpm) and applied cathodic potentials (E_{cath} of -1.65, -1.8, -1.7, -1.9 and -2.2 V vs Hg|Hg_2SO_4|K_2SO_4 (sat.)). The kinetic results obtained for such potentiostatic nitrate removal study were analysed through a complex mathematic relationship. As a result, the mass transport coefficients were found, establishing a relationship of dimensionless numbers that is foreseen as a key tool for future scale-up.

Two different iron-based materials, AISI 1018 steel and AISI 316 stainless steel, were used as cathodes and graphite as the anode for the fundamental study by LSV, employing custom-made RDEs for the characterization. **Figure 2** depicts the cathodic

linear sweep voltammograms recorded with different nitrate concentrations (0, 2, 5 and 10 mM), and the peaks associated with the nitrate electrocatalytic reduction were assigned for the AISI 1018 steel cathode. When the AISI316 stainless steel was employed, no activity was observed for NRR. This different behaviour of iron-based materials can be related to the different composition of the steels. Using the RDE at different rotation rates from 100 to 3000 rpm, the K-L analysis allowed the determination of a number of electrons (n) equal to 8 for the nitrate ER on the mild steel cathode. **Figure 3** presents the EPR spectra of the DMPO-H adduct formed between the generated hydrogen radical ($^{\bullet}$H) and the spin-trapping agent (DMPO). It clearly shows the pattern formed by 9 signals with a 1:1:2:1:2:1:2:1:1 distribution, in agreement with the theoretically provided. The $^{\bullet}$H was generated at the mild steel material upon application of E_{cath}, whereas it was not produced at the stainless steel during the polarization. This radical seems to be the cause of the activity of mild steel towards nitratereduction, since it is a high reducing agent that can act as an electrochemical mediator.

Electrolyses employing the RCE reactor with a mild steel as central electrode (cathode) were made at different E_{cath} values at a constant rotation rate of 300 rpm. **Figure 4** shows a first-order kinetics for nitrate removal with higher rate constants at higher E_{cath} values. The predominant by-product was ammonia with a maximum accumulation around 60 min, which was more evident when the applied current was more negative. Lower Faradaic efficiency (FE) was found with more negative E_{cath} values and decreased over time due to the enhancement of the hydrogen evolution as parasitic reaction (reactions (49) and (50)). Moreover, lower energy consumption (EC) was found for greater FE. The first-order rate constant (k_1) at each E_{cath} is listed in **Table 1**, alongside the corresponding heterogeneous charge transfer constants (k_h). With these two values, the mass transport coefficient (k_m) was found (equation 42) to calculate the Damköhler dimensionless number (Da) (equation (39)), eventually establishing the effectiveness factor (η) value at each applied E_{cath},

Maintaining a constant E_{cath} = -1.80 V vs $Hg|Hg_2SO_4|K_2SO_4$ (sat.) and varying the rotation rate of the RCE, the effect of an increased mass transport was then assessed. **Figure 5** reveals the improvement of the nitrate removal when increasing the rotation of the central electrode, following always a first-order kinetics with generation of ammonia as main by-product. For each experiment, the ammonia concentration gradually decreased

more rapidly as it was more highly formed. By running blank experiments without current with an analogous amount of ammonia to the initial amount of nitrate at initial pH 12.0 (i..e, similar pH to that found after some minutes in the degradation trials, owing to alkalinization), a higher loss of N-containing compounds from the solution upon rise of the rotation rate of the central electrode was found. These results agreed with those obtained by electrolyzing nitrate at different rotation rates. It can then be assumed that the selectivity for ammonia as nitrate ER by-product is around 100%. Combining the k_1 obtained at different rotation rates at the same E_{cath} with its associated k_h values with the equations mentioned above, the k_m and *Da* values were calculated and collected in **Tables 1** and **2.**

The representation of η, calculated from the *Da*-values, against the cathodic overpotential and against *Re* revealed that under the selected electrolytic conditions, the system was always controlled by a mixed regime. **Figure 6** shows that the system presented a larger dependence on charge transfer when increasing the rotation rate, whereas a greater overpotential enhanced the mass transport dependence. The *Sh* value was determined from the calculated k_m and an empiric correlation was established (equation (46)), where $\gamma = 0.356$ is characteristic of the RCE reactor configuration and $\alpha = 0.70$ and $\beta = 0.46$. The mass transport correlation with dimensionless numbers of **Figure 7** opens the door to the scale-up of the electrochemical nitrate removal with the RCE, when developing suitable conditions for high mass transport contribution with a better electrocatalyst in the near future.

The effect of the supporting electrolyte concentration is depicted in **Figure 8**. It was shown that the migration contributed negatively to the nitrate ER for high transport index of this ion, since it tends to move towards the anode due to the electric field, but it can be adsorbed and further reduced at the cathode.

Journal of Environmental Chemical Engineering 10 (2022) 108839

Contents lists available at ScienceDirect

Journal of Environmental Chemical Engineering

journal homepage: www.elsevier.com/locate/jece

Diffusion-charge transfer characterization of a rotating cylinder electrode reactor used for the complete electrocatalytic removal of nitrate from water

Roger Oriol [a], José L. Nava [b,*], Enric Brillas [a], Ignasi Sirés [a,*]

[a] Laboratori d'Electroquímica dels Materials i del Medi Ambient, Departament de Ciència de Materials i Química Física, Secció de Química Física, Facultat de Química, Universitat de Barcelona, Martí i Franquès 1–11, 08028 Barcelona, Spain

[b] Departamento de Ingeniería Geomática e Hidráulica, Universidad de Guanajuato, Av. Juárez 77, Zona Centro, C.P 36000 Guanajuato, Mexico

ARTICLE INFO

Keywords:
Electrochemical denitrification
Electroreduction
Groundwater treatment
Hydrogen radical
Rotating cylinder electrode

ABSTRACT

Groundwater nitrate contamination is an emerging threat in stressed regions under intensive farming although, lately, efforts to valorize such residues are highly encouraged. Here, electrochemical nitrate removal has been investigated as a versatile strategy for this purpose, using a reactor equipped with a cheap central Fe-based rotating cylinder electrode (RCE) as cathode and six concentric Ti|IrO_2 plates as anodes. The study of the effect of E_{cath} and rotational speed (ω) on NO_3^- electroreduction from a synthetic aqueous solution with high conductivity revealed the feasibility of complete nitrate removal, which only required 100–120 min at E_{cath} = −1.80 V vs Hg|Hg_2SO_4|sat. K_2SO_4 within the ω-range of 100–500 rpm. The concentration decays agreed perfectly with a first-order kinetics. NH_3 was accumulated as main product, being partly volatilized due to the quick solution alkalization, whereas NO_2^- was not found. Linear sweep voltammetries demonstrated the high electrocatalytic activity of carbon steel RCE as compared to inactive stainless steel. Koutecky-Levich analysis showed that the reduction process with carbon steel at E_{cath} from −1.80 V involved 8 electrons. The participation of H radical in the reduction mechanism was ascertained by electron paramagnetic resonance. The mass transport and charge transfer of the RCE reactor were characterized under turbulent flow by means of the dimensionless Damköhler (*Da*) number, as well as from the Sherwood-Reynolds-Schmidt (*Sh-Re-Sc*) analysis. A mixed regime with a prevalence of mass transport control was determined at E_{cath} from −1.8 V. The $Sh = 0.70Re^{0.46}Sc^{0.356}$ correlation obtained for this reactor may serve to guide the scale-up of electrochemical NO_3^- removal as more electrocatalytic cathode materials are developed. Successful NO_3^- elimination from solutions with low conductivity that mimicked groundwater is finally reported.

1. Introduction

Nitrate removal from surface water and groundwater has attracted increasing attention in recent years, since its progressive accumulation critically endangers freshwater reservoirs worldwide [1–3]. Recent transnational reports [4] have documented that the main sources for nitrate accumulation in groundwater are the leaching of the nitrogen-based fertilizers used in intensive agriculture and the livestock manure spreading on land, whereas surface water is mostly polluted by discharge of wastewater that contains high concentration of nitrogen species. Biotic and abiotic processes cause the conversion of these species into nitrate [5], which shows great stability and solubility in water alongside poor adsorption or precipitation. The removal of this toxic ion from aqueous matrices has been investigated by several physicochemical processes like adsorption [6], biological denitrification [7], coagulation [8], chemical reduction [9] and catalytic reduction [10], as well as electrocoagulation [11,12], bioelectrochemical [13,14] and electroreduction [15,16] methods. The latter approach has led to sound results, which combines with its operational simplicity, although the mechanism involved is complex and not fully understood yet. The effect of different parameters on NO_3^- electroreduction has been studied, including the cathode material [17,18], the electrolyte concentration [19], the electrolyte composition [20–22], the pH [23] and the cell configuration (i.e., single- or double-chamber cell) [24,25].

The NO_3^- electroreduction is an electrocatalytic process that involves several species with nitrogen valence number varying from +V to -III [26]. Several mechanisms, involving either direct or indirect pathways, have been proposed for this process depending on the cathode material

* Corresponding authors.
E-mail addresses: jlnm@ugto.mx (J.L. Nava), i.sires@ub.edu (I. Sirés).

https://doi.org/10.1016/j.jece.2022.108839
Received 12 September 2022; Received in revised form 18 October 2022; Accepted 21 October 2022
Available online 21 October 2022

and the applied cathode potential (E_{cath}) [27]. In the direct pathway, which is typical for diluted nitrate solutions (< 1 M) at near-neutral or alkaline pH, adsorbed NO_3^- ions are reduced by electrons supplied to the cathode. In the mediated or indirect route, NO_3^- reacts with adsorbed atomic hydrogen (or hydrogen radical) originated as an intermediate of the hydrogen evolution reaction (HER) (1) [28]. The NO_3^- electroreduction yields the adsorbed NO_2^- from reaction (2), which can be the rate-determining step of the process, involving 2 electrons. The subsequent NO_2^- electroreduction yields NH_3 or N_2 (6-electron steps) via reactions (3) and (4), respectively. Worth noting, some authors have reported lower energetic barriers for the indirect hydrogen radical (•H) mechanism leading to NH_3 [28].

$$2H_2O + 2e^- \rightarrow H_2 + 2OH^- \quad (1)$$

$$NO_3^- + H_2O + 2e^- \rightarrow NO_2^- + 2OH^- \quad (2)$$

$$NO_2^- + 5H_2O + 6e^- \rightarrow NH_3 + 7OH^- \quad (3)$$

$$2NO_2^- + 4H_2O + 6e^- \rightarrow N_2 + 8OH^- \quad (4)$$

The distribution of final by-products strongly depends on the selectivity of the cathode material for the NO_3^- conversion, being usually NO_2^- and NH_4^+/NH_3 the main nitrogen species accumulated in the treated solution. However, there are other parameters that can also affect the final speciation of those products, such as the nitrate and electrolyte concentration [19], the electrolyte composition, the pH, the temperature, the cell configuration and the residence time [19–25]. It has been reported that cathodes containing iron minimize the NO_2^- accumulation [17,21,29]. NH_3 can be easily removed from the solution due to its high volatility at alkaline pH or, alternatively, it can be recovered as a value-added product. This introduces a paradigm shift, turning water decontamination into a waste valorization strategy [30]. High selectivity for conversion into molecular N_2 could also be of interest, since it is non-hazardous and can be accumulated in the atmosphere, but it is not easy to demonstrate its predominance over other gaseous nitrogen products such as NH_3 or N_xO_y. Some density functional theory (DFT) calculations combined with experimental data reveal that the NH_3 generation is more kinetically favored due to lower energy barriers [28,31,32].

Figures of merit such as faradaic efficiency (FE) and energy consumption (EC) change notably depending on the reactor design [33,34]. The interplay between the applied E_{cath} and the system hydrodynamics determines the operational conditions needed to establish a charge transfer-controlled regime, mass transport-controlled regime or mixed regimes. The hydrodynamics becomes relevant when the pollutant removal kinetics is partially or totally controlled by the supply of the electroactive species to the electrocatalytic surface and hence, increasing the mass transport coefficient at a fixed E_{cath} leads to a more efficient decontamination with lower energy consumption.

Different electrochemical reactor configurations have been used for NO_3^- electroreduction, in batch or in continuous mode. Planar electrodes have shown unexpectedly high efficiencies at low current, whereas fluidized beds of inert particles enhance the mass transport and the FE [35]. Membrane flow-through [36] and thin-layer [37] reactors have also been considered. Conversely, the rotating cylinder electrode (RCE) reactor has been mostly used for mass transport-controlled cathodic processes like metal recovery in the electroplating sector [38–41], as well for erosion and corrosion studies since they allow a turbulent flow at low Reynold's (*Re*) numbers from 100 [42]. This reactor enhances the mass transport of the electroactive species toward the cathode at a relatively low rotational speed [43,44], and its characterization has been made by correlation of dimensionless numbers that predict the mass transport rates for several electroactive species under a range of hydrodynamic conditions [45,46]. To our knowledge, only a single paper has addressed the electrochemical removal of nitrate with this type of reactor, employing an activated copper RCE and operating under periodic potential reversal to ensure the reactivation of the cathode surface, thus obtaining a high FE and selectivity for NH_3 [47]. However, the mass transport has not been specifically characterized for NO_3^- electroreduction in an RCE reactor.

The electrochemical denitrification opens a window of opportunity for NO_3^- elimination from polluted freshwater resources like groundwater below 50 mg L^{-1}, the threshold value established by the World Health Organization (WHO) [48]. Devices with high removal efficiency, ease of operation and low overall cost are under investigation [49]. In this context, the development and characterization of RCE reactors is required because they easily promote the turbulence and hence, the mass transport, eventually enhancing the efficiency of the denitrification treatment.

This work is focused on the characterization of the mass transport and charge transfer of an RCE reactor used for the overall NO_3^- electroreduction from a synthetic aqueous solution with high conductivity. Stainless steel and carbon steel have been considered as cheap cathode materials to compare their effectiveness to remove NO_3^- by linear sweep voltammetry (LSV). The effect of E_{cath} and rotational speed (ω) on the process performance has been studied. From these results, the RCE reactor has been characterized under turbulent flow regime by means of the dimensionless Damköhler (*Da*) number, as well as from the Sherwood-Reynolds-Schmidt (*Sh-Re-Sc*) correlation for NO_3^- removal. Finally, preliminary promising results to remove NO_3^- under galvanostatic conditions using solutions with low conductivity, mimicking a groundwater treatment, are reported. The novelty of the work lies in demonstrating the high electrocatalytic activity of a cheap carbon steel RCE to remove nitrate from water, also showing the positive effect of mass transport promotion. Moreover, a thorough characterization of this reactor is provided through the effectiveness factor, being possible to predict the nitrate removal rate once the charge transfer kinetics is elucidated.

2. Materials and methods

2.1. Reagents

Sodium hydroxide (> 99% purity), potassium nitrate (> 99% purity) and potassium sulfate (99.5% purity) were purchased from Fermont. Sodium sulfate (99.0% purity), sulfuric acid (analytical grade, 95–98% purity) and tri-distilled water were provided by Karal. 5,5-Dimethy-l,1-pyrroline N-oxide (DMPO) used for electron paramagnetic resonance (EPR) analysis, as well as phthalic acid (99.5% purity) and tris (hydroxymethyl)aminomethane (99.8% purity) as mobile phase reagents for ion chromatography (IC), were purchased from Sigma-Aldrich. Analytical grade sodium nitroprusside dihydrate from Merck, phenol (> 99% purity) from Sigma-Aldrich and EDTA (> 99% purity) from Karal were used for ammonium/ammonia colorimetric determination.

2.2. Electrochemical setup

The RCE reactor consisted of a rotating cylinder cathode surrounded by 6 anode plates, as shown in Fig. 1. Two rotating cylinders with dimensions of 14.00 cm height × 3.80 cm of diameter, made of AISI 1018 carbon steel or AISI 316 stainless steel (SS316), were built as working electrodes (WE). Commercial Ti|IrO_2 (DSA-O_2, NMT Electrodes) anodes were used as counter electrode (CE). The total cathode and anode areas were similar (~100 cm^2), being the exposed surface limited by polyester tape. The good stability of the electrolytic system was confirmed by the good reproducibility of data, which was ensured upon cleaning of the RCE surface before each run. To do this, the cylinder surface was submerged in 20% H_2SO_4 for 30 s, rinsed with tri-distilled water and, finally, dried with paper.

The experiments were carried out by electrolyzing 400 mL of solutions containing 10 mM $NaNO_3$ + 0.50 M Na_2SO_4 in tri-distilled water

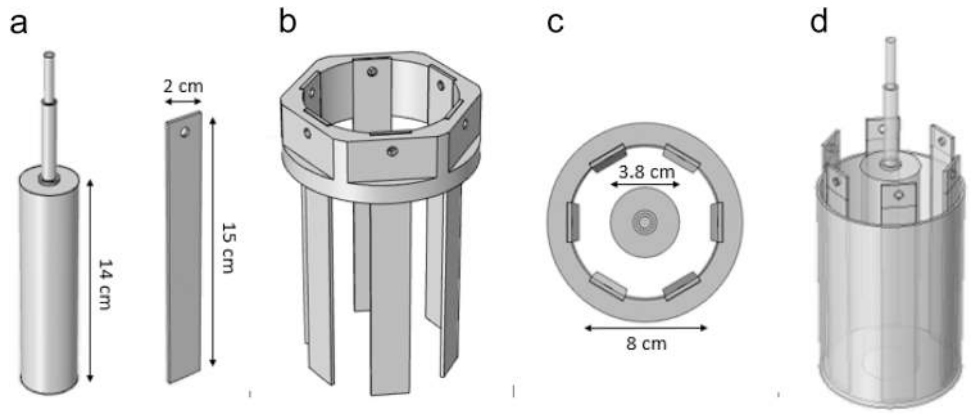

Fig. 1. Sketch of the rotating cylinder electrode (RCE) reactor setup. (a) Rotating cylinder cathode and static planar anode, (b) anodic module consisting of six equidistant anodes fixed to a plastic holder, (c) zenithal view and (d) isometric view.

at natural pH 6.5, placed in a jacketed open glass cell with temperature fixed at 25 ºC by recirculating thermostated water. Most trials were made in potentiostatic mode at constant E_{cath}, controlled by a double junction saturated mercury-mercurous sulfate electrode (MSE) (E^o = +0.64 V vs SHE) as reference electrode (RE), using a Biologic SP-150 power supply equipped with a Biologic VMP3B-10 booster. Some specific assays in low conductivity medium were performed under galvanostatic conditions at constant current (I) with the same instruments. The potentiostatic electrolytic trials were made in a three-electrode cell to study the effect of E_{cath} between −1.6 and −2.2 V and that of rotational speed (ω) between 100 and 500 rpm, all of them with a duration of 120 min. The final pH in these assays was approximately 12.5. The galvanostatic electrolytic trials were made at current density (j) of -12 mA cm^{-2} for 120 min in a two-electrode cell, studying the effect of the Na_2SO_4 concentration between 0.01 and 0.50 M. Some blank experiments were performed to assess the extent of ammonia volatilization.

2.3. Analytical and electrochemical characterization

The solution pH was measured with a HI 3221 pH/ORP/ISE meter from Hannah Instruments. Nitrate concentration was determined by injecting 20 μL aliquots into a Perkin Elmer ion chromatograph coupled to an Adept Cecil CE4710 conductivity detector controlled by Chromera software. A Shim-Pack IC-A1 anion column with dimensions of 100 mm × 4.6 mm (i.d.), at 25 ºC, was used. The mobile phase was a solution composed of 2.4 mM tris(hydroxymethyl)aminomethane + 2.6 mM phthalic acid (pH 4), which was eluted at 1.5 mL min^{-1}, displaying the nitrate peak at 4.6 min. The ammonia concentration was obtained by means of the standard indophenol blue colorimetric method, which required the measure of the absorbance at 645 nm using a PerkinElmer Lambda 35 UV/Vis spectrophotometer.

LSV was performed with a Biologic SP-150 potentiostat controlled by EC-LAB v11.10 software. A rotating disk electrode (RDE) made of AISI 1018 steel or SS316 with 4.5 mm diameter was used as WE. The CE was a graphite bar and the RE was the saturated Hg|Hg_2SO_4 electrode mentioned above. The solutions contained up to 10 mM KNO_3, with 0.50 M Na_2SO_4 as supporting electrolyte, and the voltammograms were recorded starting from the open circuit potential (E_{OCP} = −1.050 V vs MSE), at a scan rate of 5 mV s^{-1}.

The possible generation of hydrogen radical during the nitrate electrocatalytic reduction was assessed by EPR using DMPO as the spin-trapping agent. AISI 1018 steel and SS316 plates of 5 cm^2 were used as cathode, at E_{cath} = −1.80 V. A Pt plate with analogous surface area was used as counter electrode. The in-situ electrogeneration of the adsorbed $^{\bullet}$H, in the form of DMPO-H adduct, was carried out in 15-mL solutions in the presence and absence of 10 mM nitrate after addition of 16.90 μL of 10 mM DMPO, using a single-chamber cell (SCC) under continuous magnetic stirring. 2.0 mL of samples were collected and placed in plastic tubes at 0, 5 and 20 min, immediately frozen by contact with dry ice and further, thawed and introduced into a quartz tube to be analyzed, always after the same time period from initial sampling. The EPR spectra were recorded in a Bruker ESP300E spectrometer at room temperature, fixing the following parameters: resonance frequency of 9.79 GHz, microwave power of 2 mW, modulation amplitude of 1.0 G, sweep width of 100 G (3450–3550), time constant of 40.96, sweep time of 83.97, and receiver gain of 2 × 10^4.

2.4. Theory and calculations

The faradaic efficiency (FE) for nitrate electroreduction and the energy consumption per nitrate gram (EC) were calculated by the following expressions [50]:

$$\mathrm{FE} = \frac{nF(C_0 - C_t)V}{Q_t} = \frac{nF(C_0 - C_t)V}{It} \quad (5)$$

$$\mathrm{EC}\left(W\,h\,g^{-1}\right) = \frac{E_{cell}Q_t}{3600(C_0 - C_t)MV} = \frac{E_{cell}It}{3600(C_0 - C_t)MV} \quad (6)$$

where n is the global number of electrons transferred according to consecutive reactions (2) and (3), accounting for the complete reduction of nitrate to ammonia (n = 8), F is the Faraday constant (96,485 C mol^{-1}), C_0 is the initial nitrate concentration (0.010 M) and C_t is the nitrate concentration at given time (in M), V is the solution volume (0.4 L), M is the nitrate molar mass (62 g mol^{-1}) and Q_t is the charge at the same time (in C).

The Koutecky-Levich (K-L) Eq. (7) and its derived Eq. (8) were applied to analyze the linear sweep voltammograms recorded with an RDE as WE [50]:

$$\frac{1}{I_c} = \frac{1}{I_k} + \frac{1}{I_l} \quad (7)$$

$$\frac{1}{I_c} = \frac{1}{nFAk_hC^*} + \frac{1}{0.62nFAD_t^{2/3}\nu^{-1/6}\omega^{1/2}C^*} \quad (8)$$

where I_c is the measured current, I_k is its kinetic term (in the absence of mass transport), I_l is the limiting diffusion current, n is the number of electrons involved in the nitrate electroreduction, A is the electrode area, D_t is the diffusion coefficient of nitrate ion, ω is the rotational speed, ν is the kinematic viscosity and C^* is the nitrate bulk concentration (10^{-2} M). The heterogeneous charge transfer constant (k_h) can then be obtained from the independent term of the linear regression at infinite ω.

The effectiveness factor (η) for the heterogeneous electroreduction

process is described by Eq. (9) [51]:

$$\eta = \frac{R}{R^*} = \frac{k_1 C}{k_1 C^*} = \frac{C}{C^*} \tag{9}$$

where R is the reaction rate involving an electroactive species at concentration C, whereas R^* is that of an ideal process considering the bulk concentration C^* . In Eq. (9), it is assumed that R is described as $dC/dt = -k_1 C$ where k_1 is the global reaction rate. This means that under steady-state conditions, the species arriving by mass transport to the electrocatalytic surface disappears according to a heterogeneous charge transfer rate constant $k_h a$ [51–53], where a is the volumetric area (here, ratio between the area A of the RCE and the solution volume V inside the reactor), thereby verifying Eqs. (10)-(12):

$$k_m a(C^* - C) = k_h a C \tag{10}$$

$$C = \frac{1}{1 + \frac{k_h a}{k_m a}} C^* \tag{11}$$

$$R = \eta R^* = \eta k_h a C^* \tag{12}$$

where k_m is the mass transport coefficient (m s^{-1}). The dimensionless Damköhler number (Da), which relates the charge transfer rate (intrinsic reaction) to the convective mass transport, is then defined by Eq. (13):

$$Da = \frac{k_h a}{k_m a} \tag{13}$$

As a result, the isothermal effectiveness factor η can be expressed in terms of the Damköhler dimensionless number Da from Eq. (14) [51–54]:

$$\eta = \frac{1}{1 + \frac{k_h a}{k_m a}} = \frac{1}{1 + Da} \tag{14}$$

Furthermore, R can be expressed by Eq. (15), leading to Eq. (16), which relates $k_h a$, $k_m a$ and k_1.

$$R = \frac{k_h a}{1 + Da} C^* = \frac{k_h a}{1 + \frac{k_h a}{k_m a}} C^* = \frac{1}{\frac{1}{k_h a} + \frac{1}{k_m a}} C^* \tag{15}$$

$$k_1 = \frac{1}{\frac{1}{k_h a} + \frac{1}{k_m a}} \tag{16}$$

3. Results and discussion

3.1. Comparative electrocatalytic performance of cathode materials for nitrate removal

First, the AISI 1018 steel and SS316 cathodes were electrochemically characterized by LSV to assess their electrocatalytic activity for NO_3^- electroreduction. The voltammograms were recorded in an SCC, with one of the above materials embedded in a cylindrical PTFE case to become an RDE employed as WE; a graphite bar and Hg|Hg_2SO_4 |sat. K_2SO_4 served as CE and RE, respectively, operating at a scan rate of 5 mV s^{-1}. The assays were made with 400 mL of solutions containing 0, 2, 5 and 10 mM NO_3^- under static conditions, followed by trials made with 400 mL of 10 mM NO_3^- solutions at ω values from 100 to 3000 rpm, always using 0.50 M Na_2SO_4 as supporting electrolyte. Under static conditions, Fig. 2a highlights a well-defined wave with half-wave potential ($E_{1/2}$) of −1.58 V vs RE when using the 1018 steel cathode, which can be attributed to the NO_3^- reduction. This was confirmed by the fact that the height of the wave raised proportionally as the NO_3^- concentration in the medium was increased, suggesting that the mechanism involves the reaction (2) as rate-determining step, followed by faster successive reduction steps. In contrast, only the background signal can be observed in Fig. 2a using the SS316 cathode, being the current related to the HER because the same profile was recorded in the absence of NO_3^-. This means that this ion cannot be efficiently electroreduced on this cathode material, probably because the process is inhibited by the passivating chromite present on its surface.

Fig. 2b depicts the progressive rise in height of the reduction wave when the rotational speed of the RDE made with 1018 steel increased from 100 to 3000 rpm, owing to the gradual enhancement of the NO_3^-

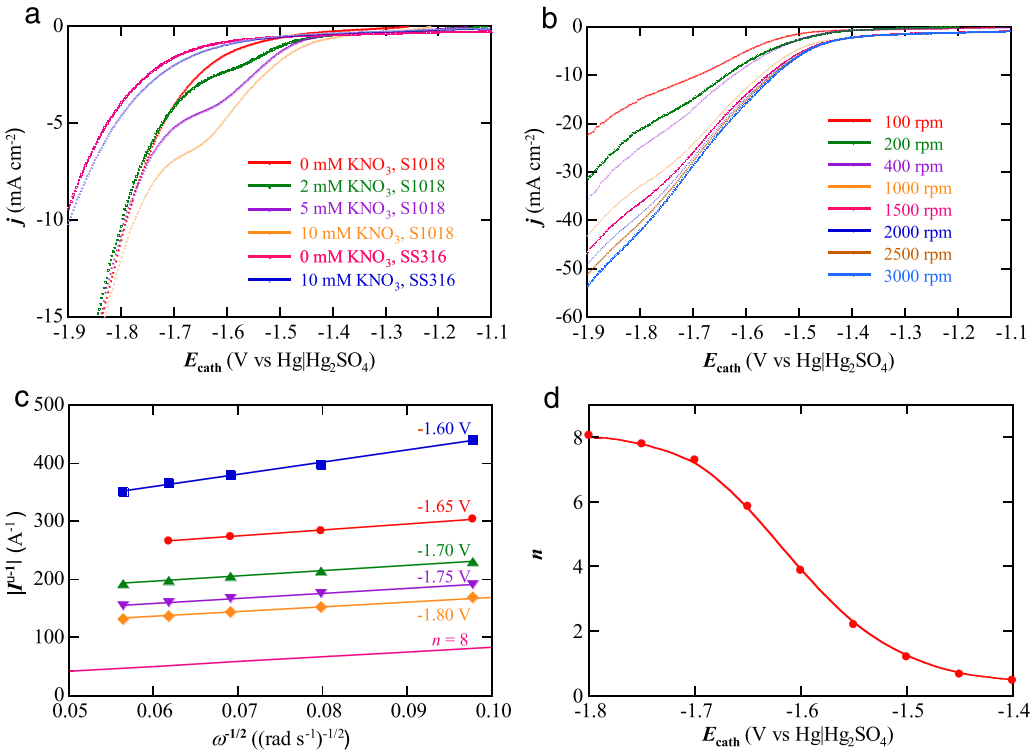

Fig. 2. Linear sweep voltammograms of nitrate reduction obtained using 400 mL of nitrate solutions in 0.50 M Na_2SO_4 at 25 °C, with a 0.181 cm^2 AISI 1018 steel or SS316 RDE as WE, recorded from −1.1 to −1.9 V at a scan rate of 5 mV s^{-1}. A graphite bar was used as CE and Hg|Hg_2SO_4 |sat. K_2SO_4 (E^o = +0.64 V vs SHE) as RE. (a) Effect of the nitrate concentration under static conditions. (b) Effect of the RDE rotational speed (ω) from 100 to 3000 rpm using a 1018 steel cathode in a 10 mM KNO_3 solution, (c) the corresponding Koutecky-Levich (K-L) plots at different E_{cath} values, and (d) number total of electrons involved in nitrate electroreduction obtained from the slope of the linear K-L regressions.

mass transport towards the diffusion boundary layer adjacent to the electrocatalytic surface. However, a clear plateau was not achieved in any case, as also reported for the same reaction on copper cathode [47]. This behavior can be ascribed to the partial overlapping of the wave of NO_3^- electroreduction with the slightly more negative background signal of HER (see Fig. 2a), causing a disturbance that makes it difficult to corroborate that the process under study is only controlled by mass transport. The data of Fig. 2b were then analyzed at each E_{cath} value to obtain the corresponding I^{-1} vs $\omega^{-1/2}$ relationships (K-L plot) [55], some of which (i.e., potentials between −1.60 and −1.80 V) are presented in Fig. 2c. Excellent linear correlations were found in the E_{cath} interval between −1.45 and −1.85 V, with decreasing slopes varying from 10, 115 to 867 $rad^{1/2}\ s^{-1/2}\ A^{-1}$ and $R^2 > 0.983$. This allowed the calculation of the total number of electrons n involved in the NO_3^- electroreduction. Fig. 2d shows a reverse sigmoidal profile of n vs E_{cath}, which is typical of a sluggish reaction. In this case, the n value increased gradually at higher E_{cath}, up to a value close to 8 at −1.80 V and beyond. This can be confirmed from Fig. 2c, where the linear regression depicted at $E_{cath} = -1.80$ V is parallel to the theoretical trend assuming $n = 8$. This number of transferred electrons corresponds to the selective conversion of NO_3^- to NH_3 via the global reaction (17), which is the sum of reactions (2) and (3). This full reduction of the NO_3^- with an oxidation state of (+V) to NH_3 nitrogen (-III) can be associated to successive faster rate steps after the two-electron rate-limiting reaction (2) of the adsorbed NO_3^- to NO_2^-, occurring on the 1018 steel cathode electrocatalytic surface.

$$NO_3^- + 6H_2O + 8e^- \rightarrow NH_3 + 9OH^- \quad (17)$$

From the above K-L analysis, the k_h resulting at given E_{cath} values was determined from Eq. (8), as has been collected in Table 1. For this calculation, the diffusion coefficient of NO_3^- ($D_{NO3} = 1.90 \times 10^{-5}$ $cm^2\ s^{-1}$) and the kinematic viscosity of the solution ($\nu = 0.0088$ $cm^2\ s^{-1}$) were used [35].

Fig. 3a shows the EPR spectra recorded with DMPO acting as the spin trap to detect the adsorbed •H generated on the electrocatalytic surface of the 1018 steel cathode. The signal intensity increased with electrolysis time because of the larger production of •H, with a larger accumulation of DMPO-•H. In the presence of NO_3^-, a lower signal intensity was found. This means that •H may certainly play an important role in the NO_3^- electroreduction, since it is generated in large amounts as an intermediate of the HER. The high surface mobility of •H favors its reaction with either adsorbed NO_3^- or partially reduced nitrogen intermediates, since atomic hydrogen is an efficient reducing agent. In contrast, DMPO-•H adduct was not detected when the SS316 cathode was used, as deduced from the overlapping spectrum with that of the blank solution before electrolysis. The EPR spectra from the trials with 1018 steel show the typical DMPO-•H pattern composed of 9 peaks, and Fig. 3b reveals an intensity ratio of 1:1:2:1:2:1:2:1:1 with measured hyperfine coupling constant values of $a_N = 16.52$ G and $a_H = 22.58$ G for the nitrogen and the 2 equivalent hydrogen atom nuclei, respectively, in agreement with those determined in the literature [56].

Table 1
First-order rate constant (k_1) determined from Fig. 4b with RCE at $\omega = 300$ rpm, heterogeneous charge transfer constants (k_h) obtained from the Koutecky-Levich analysis with RDE from Fig. 2c, and *Da* values determined upon combination of Eqs. (13) and (16).

E_{cath} (V vs $Hg\|Hg_2SO_4$)	k_1 (10^{-4} s^{-1})	k_h (10^{-3} cm s^{-1})	*Da*
-1.60	n.d.	3.1	0.9
-1.65	1.9	3.7	1.1
-1.70	3.9	5.0	1.5
-1.75	n.d.	6.7	2.0
-1.80	6.5	8.1	2.4
-1.85	n.d.	10.8	3.2
-1.90	7.5	12.8	3.8
-2.20	7.7	n.d.	n.d.

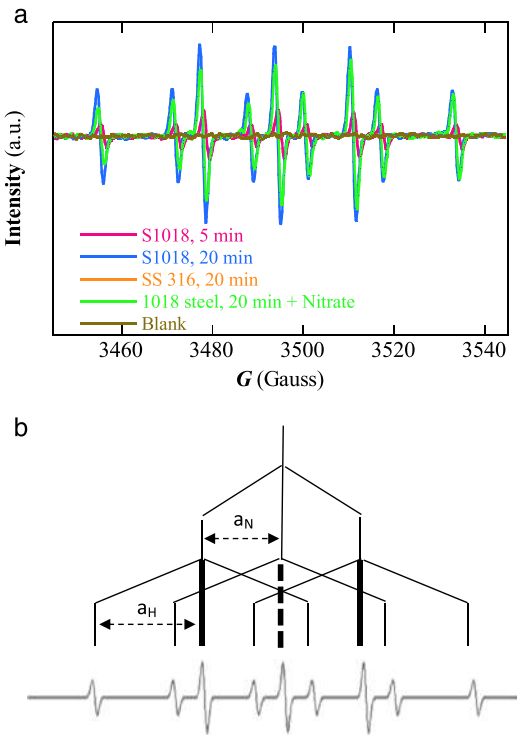

Fig. 3. (a) EPR spectra of the DMPO-H adduct generated during the galvanostatic electrolysis of solutions of 15 mL containing 10 mM DMPO + 0.050 M Na_2SO_4 using a single-chamber cell with a 5 cm^2 AISI 1018 steel or SS316 cathode and a 5 cm^2 Pt foil anode, at $E_{cath} = -1.80$ V vs $Hg|Hg_2SO_4|$sat. K_2SO_4 for 20 min (b) Interpretation of a DMPO-H spectrum.

3.2. Potentiostatic nitrate removal using an RCE reactor

The NO_3^- removal was subsequently studied employing a 100 cm^2 1018 steel cathode as WE in an RCE reactor. Fig. 4a depicts the effect of the E_{cath}, from −1.65 to −2.2 V, applied to the cathode for the treatment of 400 mL of solutions containing 10 mM KNO_3 + 0.50 M Na_2SO_4 at 25 °C and $\omega = 300$ rpm. As expected, a more negative E_{cath} accelerated the NO_3^- electroreduction and 100% removal was achieved after 100–120 min of electrolysis from E_{cath} − 1.80 V. This is due to the increase of the applied overpotential, which enhances the charge transfer kinetics for the rate-limiting reaction (2), achieving the complete NO_3^- removal at $E_{cath} = -1.80$ V with $n = 8$ (see Fig. 2d), i.e., when all the ion is selectively converted into N-ammonia. Therefore, This E_{cath} value was selected as optimal for subsequent trials. The kinetic analysis of the above concentration decays revealed that they obeyed a first-order reaction, as expected if the electrode reaction (2) is the rate-determining step. The good linear plots obtained in this analysis are shown in Fig. 4b and the corresponding k_1-values with excellent fittings ($R^2 > 0.996$) are summarized in Table 1. The k_1-value grew 4.1 times when E_{cath} varied between −1.65 and −2.20 V (i.e., 1.9×10^{-4} s^{-1} vs 7.7×10^{-4} s^{-1}), suggesting that the electrocatalytic activity of the cathode was maintained in all the trials.

The concentration of generated N-ammonia was measured during the trials of Fig. 4a, and its normalized accumulation over the initial N-nitrate concentration (10 mM) is given in Fig. 4c. The accumulated N-ammonia increased at more negative E_{cath}, attaining similar profiles for the fastest trials (E_{cath} from −1.80 V). However, maximum accumulation values of 67–72% at 60 min of electrolysis were obtained under these conditions, very far from 100% expected for total conversion of NO_3^- into NH_3. This apparent discrepancy can be explained by the gradual volatilization of NH_3 from the solution at alkaline pH, since the pK_a of its acidic form NH_4^+ is 9.26. Note that during the electrolysis, the solution pH changed from an initial value of 6.5 to a final value of 12.5

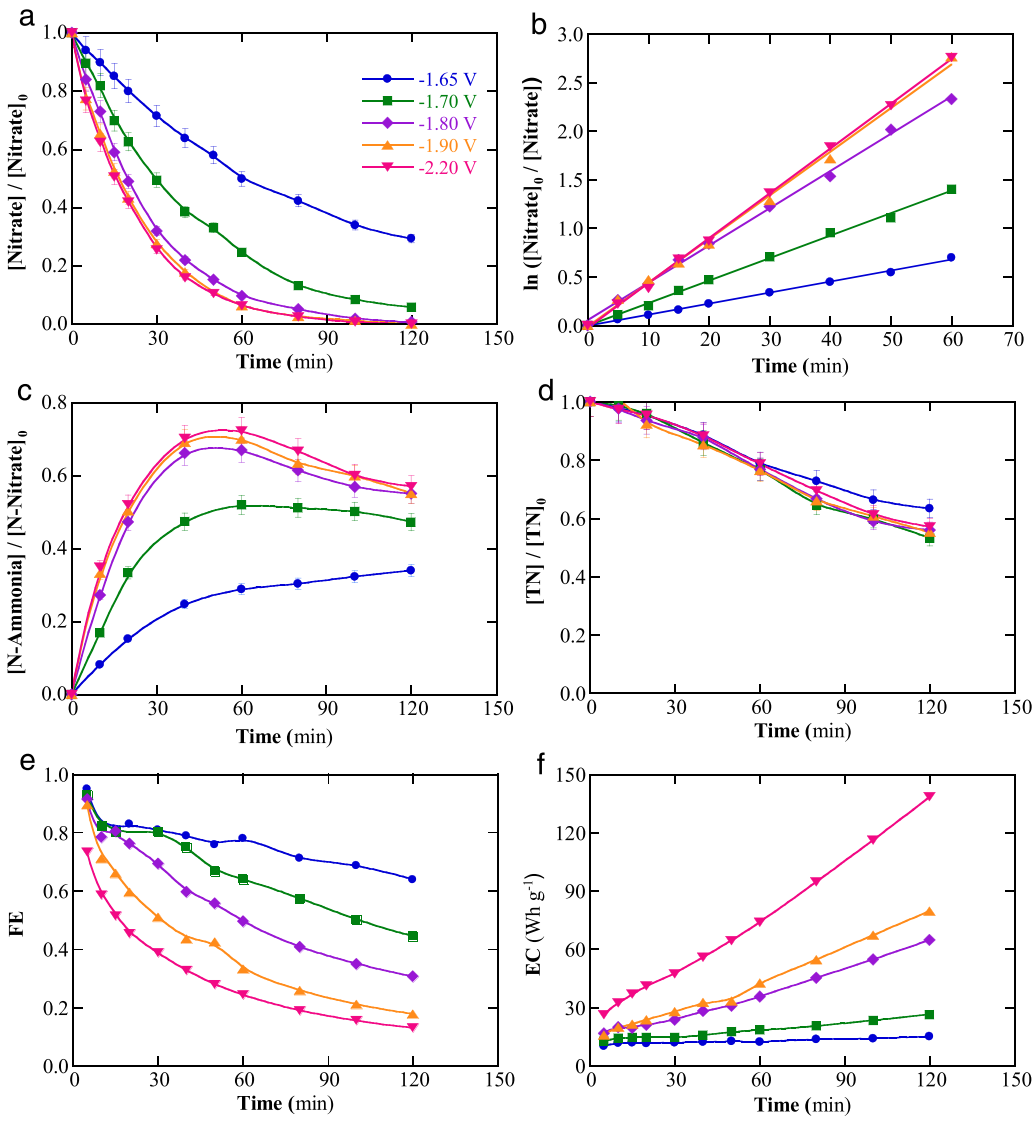

Fig. 4. Influence of E_{cath}, from −1.65 to −2.2 V, on the (a) normalized nitrate concentration decay, (b) first-order kinetics for nitrate removal, (c) normalized N-ammonia accumulation, (d) normalized TN content, (e) faradaic efficiency and (f) energy consumption per gram of nitrate ion. These trials involved the potentiostatic electrolysis of 400 mL solutions of 10 mM KNO_3 + 0.50 M Na_2SO_4 at 25 °C, using a 100 cm^2 AISI 1018 steel RCE as WE at ω = 300 rpm for 120 min. Commercial Ti|IrO_2 anodes of analogous total surface were employed as CE, and Hg|Hg_2SO_4 |sat. K_2SO_4 as RE.

as result of the positive global balance of OH^- ions generated for each NO_3^- molecule removed (reaction (17)). This means that, after 60 min of treatment, the solution became highly alkaline and NH_3 loss was evidenced, thus dropping its accumulation in the medium. This explains the progressive decay of accumulated N-ammonia in Fig. 4c at $E_{cath} \geq -1.80$ V at times longer than 60 min, reaching 55% of accumulation at 120 min. To confirm the NH_3 loss during the assays, the total nitrogen (TN), i.e., the sum of soluble N-nitrate and N-ammonia, of the electrolyzed solutions was calculated. As can be seen in Fig. 4d, TN underwent a slow and gradual abatement regardless of the applied E_{cath}, losing a 37% at $E_{cath} = -1.60$ V and up to 45–47% at $|E_{cath}| \geq -1.80$ V, i.e., when larger amount of N-ammonia was produced. This decay in TN justifies the progressive volatilization of the final NH_3 due to the solution alkalinization during electrolysis. If needed, this loss might be avoided by regulating the pH around its initial value of 6.5, although this should be explored in a focused work.

The FE and EC values during the above experiments were calculated from Eqs. (5) and (6), respectively, only considering the change in NO_3^- concentration. Fig. 4e highlights that FE dropped with rising E_{cath}, reaching decreasing values of 64%, 44%, 31%, 18% and 12% after 120 min of electrolysis at −1.65, −1.70, −1.80, −1.90 and −2.20 V, respectively. Consequently, the highest FE was achieved at $E_{cath} = -1.65$ V. The opposite trend followed by EC can be observed in Fig. 4 f, with increasing maximum values of 15.2, 26.5, 65.8, 79.6 and 134.8 Wh g^{-1}. This loss of performance is attributable to the smaller NO_3^- coverage on the cathode surface, which is necessary for further electroreduction, and can be explained by three main reasons: (i) the progressive loss of NO_3^- concentration as the electrolysis is prolonged, (ii) the competitive electroreduction of nitrogen by-products that are fully converted into NH_3, also causing a FE decay and EC rise at longer time, and (iii) the increase in rate of the parasitic HER, taking place in a greater number of active sites, eventually causing a drop in efficiency at higher E_{cath}.

Next study aimed at assessing the influence of ω on the NO_3^- electroreduction process. To do this, 400 mL of solutions with 10 mM KNO_3 + 0.50 M Na_2SO_4 at 25 °C were electrolyzed at $E_{cath} = -1.80$ V, with ω values from 100 to 500 rpm using the 1018 steel RCE. Fig. 5a makes in evidence a greater NO_3^- removal as ω raised due to the promotion of the diffusion-convection that enhances the mass transport of the ion toward the cathode. While 98% removal was achieved after 120 min at ω = 100 rpm, overall electroreduction was obtained at the same time at ω = 300 rpm and even at shorter time of 100 min at ω = 500 rpm. This tendency can also be deduced from the excellent first-order kinetics followed by the concentration decays, as depicted in Fig. 5b. The k_1-value thus determined progressively grew from 4.5×10^{-4} s^{-1} at ω = 100 rpm to 7.8×10^{-4} s^{-1} at ω = 500 rpm. These findings are

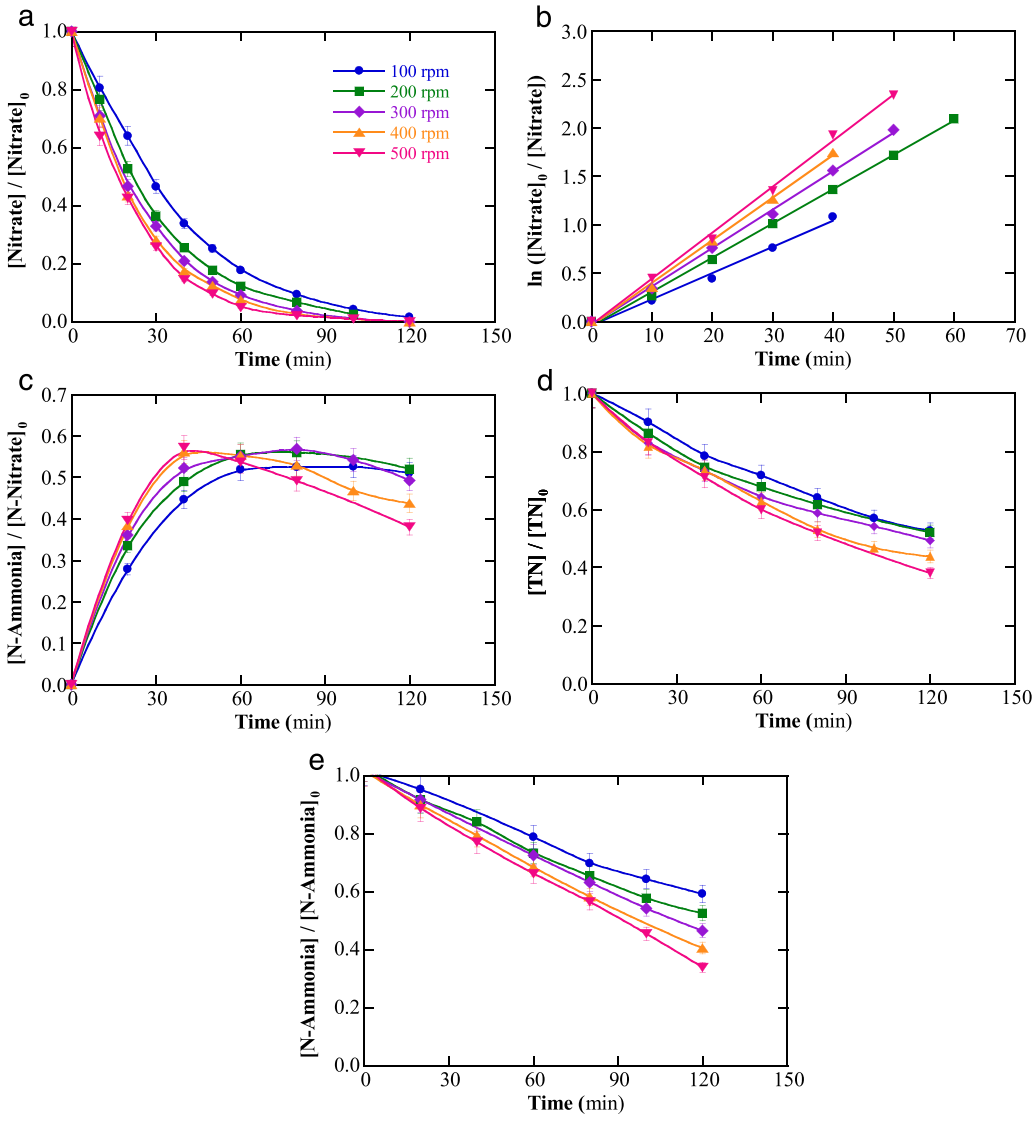

Fig. 5. Effect of the ω value, from 100 to 500 rpm, of the RCE on the (a) normalized nitrate concentration decay, (b) resulting first-order kinetics, (c) normalized N-ammonia accumulation and (d) normalized TN content under the same conditions described in Fig. 4, at $E_{cath} = -1.80$V for 120 min (e) Influence of ω on the time course of ammonia concentration during the electrolysis of a 5 mM $(NH_4)_2SO_4$ + 0.50 M Na_2SO_4 solution at pH 12.0, using the same RCE reactor but with the SS316 cylinder.

indicative of the process improvement at higher rotation.

The profiles related to the NH_3 accumulation upon change of ω are shown in Fig. 5c. A maximum accumulation close to 56–57% was always reached, regardless of the applied ω. This maximum value was attained after 40 min at 400 and 500 rpm, and at progressively longer times of 60, 80 and 100 min when ω decreased from 300 to 200 and 100 rpm, owing to the worsen diffusion-convection that led to a slower NO_3^- electroreduction, as stated above. Once the maximum NH_3 was accumulated, its volatilization predominated over its accumulation, giving rise to a gradual loss of its concentration from 51% at $\omega = 100$ rpm to 38% at $\omega = 500$ rpm. The occurrence of a quicker NH_3 concentration abatement at higher ω was expected in the alkalinized medium, as typically observed for volatiles retained in aqueous media. This behavior can be confirmed from the calculated TN variations presented in Fig. 5d. While 48% of TN was reduced after 120 min at 100 and 200 rpm, higher and increasing TN decays of 51%, 56% and 62% were found at 300, 400 and 500 rpm as result of the gradual greater formation and volatilization of NH_3 due to the quicker NO_3^- electroreduction. These results agree with those pointed out above in Fig. 4d.

A last series of experiments was made with 400 mL of solutions containing 5 mM $(NH_4)_2SO_4$ (i.e., 10 mM of NH_4^+) + 0.50 M Na_2SO_4 at pH 12.0, using a SS316 cylinder in a RCE reactor with rotation between 100 and 500 rpm, but without current supply. These non-electrochemical blank trials were made to confirm the NH_3 volatilization under the alkaline conditions tested. Fig. 5e reveals quite similar profiles for the loss of N-ammonia concentration to those shown in Fig. 5c. Thus, after 120 min, Fig. 5e shows that the NH_3 concentration was progressively reduced by 41%, 47%, 54%, 69% and 66% operating at 100, 200, 300, 400 and 500 rpm. These values are slightly higher than those found for the loss of N-ammonia in Fig. 5c because of the higher initial NH_3 used. Hence, these findings corroborate the occurrence of a quicker volatilization of NH_3 at higher ω, favored by a more turbulent flow ($8592 \leq Re \leq 42{,}959$), which impedes an accurate calculation of the yield rate for converting nitrate to ammonium.

3.3. Mass transport characterization of nitrate removal

The assays described above allowed the determination of the k_1-values corresponding to the NO_3^- electroreduction process from a 10 mM NO_3^- + 0.50 M Na_2SO_4 solution using a 1018 steel RCE. The data obtained at different E_{cath} values at $\omega = 300$ rpm are collected in Table 1, whereas those found at $E_{cath} = -1.80$ V and different ω values are summarized in Table 2. These results make in evidence that the system operates under diffusion-convection conditions, being insignificant the migration of NO_3^- ions due the high concentration of supporting electrolyte. On the other hand, the k_h-values under the same conditions were

Table 2
First-order rate constants (k_1) obtained from Fig. 5b at $E_{cath} = -1.80$ V, mass transport coefficient (k_m) obtained from Eq. (16), and dimensionless *Re*, *Sh* and *Da* numbers obtained from Eqs. (18) and (19) and (9), respectively.

ω (rpm)	u (cm s^{-1})	k_1 (10^{-4} s^{-1})	k_m (10^{-3} cm s^{-1})	*Re*	*Sh*	*Da*
100	19.9	4.5	2.0	8592	408	4.0
200	39.8	5.9	2.9	17,184	576	2.8
300	59.7	6.5	3.4	25,775	676	2.4
400	79.6	7.3	3.9	34,367	785	2.1
500	99.5	7.8	4.3	42,959	860	1.9

determined from the aforementioned K-L analysis and hence, those corresponding to different E_{cath} values at $\omega = 300$ rpm are listed in Table 1. Based on all these data, the k_m-values of the assays were calculated from Eq. (16) considering a volumetric area of $a = 0.25$ cm^{-1} (i.e., A (100 cm^2) /V (400 cm^3)). Table 2 shows the k_m-values calculated for trials at different ω values and $E_{cath} = -1.80$ V.

Once determined the k_h and k_m parameters for each assay, the dimensionless Damköhler number was obtained from Eq. (9), and the values obtained are given in Tables 1 and 2. This parameter is very relevant because, from the effectiveness factor η calculated by Eq. (14) that must range between 0 and 1 [52], it informs about the regime that controls the process. So, for high *Da* values, the effectiveness factor will tend to 1/*Da* and hence, to 0, meaning that the process is under mass transport control regime and $k_1 = k_m a$. In contrast, for small *Da* values, η will tend to 1, picturing that the process is controlled by charge transfer and $k_1 = k_h a$. In intermediate situations, the process will be under a mixed regime with no predominance of neither mass transport nor charge transfer. In the present RCE reactor, Fig. 6a and 6b show the change of η with the overpotential in absolute value ($|E_{cath} - E_{OCP}|$) and with the dimensionless Reynolds (*Re*) number, respectively. The latter term was calculated by Eq. (18) [52]:

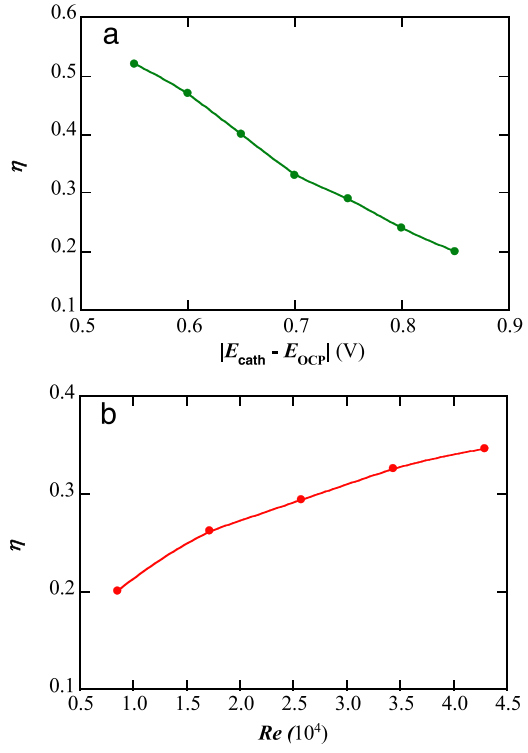

Fig. 6. Representation of the effectiveness factor (η) versus (a) the overpotentials (in absolute value) studied in the assays of Fig. 4, and (b) the Reynolds dimensionless number corresponding to the assays of Fig. 5.

$$Re = \frac{ud}{v} \tag{18}$$

where u is the peripheral velocity ($= \pi\omega d$); in this relationship, ω is expressed in rev s^{-1}, and d is the RCE diameter.

Fig. 6a shows a uniform decay of η from 0.52 to 0.20 when the absolute value of the cathodic overpotential was increased from 0.55 to 0.85 V (considering the E_{cath} data of Fig. 4 at constant $\omega = 300$ rpm). Since the NO_3^- electroreduction process is limited by the slowest phenomenon, the trend of Fig. 6a means that the increase of the overpotential in absolute value enhanced the charge transfer kinetics, thus making the system gradually more dependent on the mass transport. Fig. 6b highlights a rise of the effectiveness factor from 0.20 to 0.35 for *Re* varying from 8592 to 42959 (see assays of Fig. 5a at $E_{cath} = -1.80$ V). As the rotation of the RCE is increased, the fluid becomes more turbulent and the mass transport toward the cylindric electrode is enhanced (i.e., the Nernst diffusion layer becomes thinner), thus increasing the relevance of the charge transfer rate. Based on the intermediate values obtained for η (i.e., between 0.20 and 0.35) in the selected ranges of E_{cath} and ω, it can be concluded that the system is under mixed control regime [53]. It is worth mentioning that the effectiveness factor is an indicator of how efficient is the mass transport; i.e., if a very fast charge transfer process exists, an efficient mass transport will be required to have $k_h a = k_m a$, and therefore, $Da \to 1$ with $\eta \to 0.5$. The RCE is suitable to achieve such condition because of the resulting turbulence; just for comparison, the η values would tend to zero in a parallel plate electrochemical reactor because the inertia of the fluid does not generate the high turbulence promoted in an RCE. From the data obtained here, the electrochemical NO_3^- reduction on the electrocatalytic 1018 steel (at $E_{cath} = -1.80$ V) occurs under excellent mass transport. NO_3^- electroreduction is thus substantially dependent on the charge transfer kinetics although, under certain experimental conditions, it is revealed to be shifted toward a larger mass transport control.

Eq. (16) makes it possible to treat the mass transport coefficient separately, by obtaining an additional correlation that describes its dependence on the hydrodynamics imposed by the RCE. The reactor characterization described in previous subsections allowed determining the dimensionless Sherwood (*Sh*) and Schmidt (*Sc*) values as follows [46]:

$$Sh = \frac{k_m d}{D} \tag{19}$$

$$Sc = \frac{v}{D} \tag{20}$$

The *Sh* number correlates convective mass transport with pure diffusion, whereas the *Sc* number correlates momentum diffusivity with molecular diffusion. The *Sh*-values obtained from the trials of Fig. 5 are collected in Table 2. These parameters accomplish the following correlation [46]:

$$Sh = \alpha Re^{\beta} Sc^{\gamma} \tag{21}$$

where α is a coefficient related to the reactor dimensions, shape of the electrode and electrolyte properties, β is associated with the hydrodynamic regime, and $\gamma = 0.356$ is characteristic of the RCE reactor configuration [42,43,46]. Fig. 7 shows the good linear ln (Sh /$Sc^{0.356}$) vs ln *Re* plot obtained from the assays of Fig. 5, yielding values of $\alpha = 0.70$ and $\beta = 0.46$ for our system, with an interelectrode gap of 2.1 cm. Rivera et al. [46] reported quite similar values of $\alpha = 0.89$ and $\beta = 0.43$ using an interelectrode gap of 2.4 cm to study the I_3^-/I^- process with an SS304 RCE. In contrast, Arredondo et al. [39] obtained very different values of $\alpha = 0.11$ and $\beta = 0.99$ using an SS316 RCE for Ag deposition, suggesting that the values are strongly dependent on the nature of the reduced electroactive species. Based on these evidences, it is evident that the mass transport correlations must be experimentally obtained for each particular electrochemical system.

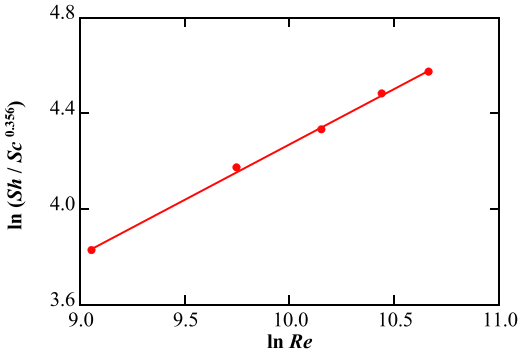

Fig. 7. Mass transport correlation for nitrate electroreduction evaluated from the trials of Fig. 5b, using Eq. (16).

3.4. Preliminary assessment of the RCE reactor for groundwater treatment

A crucial conclusion from results reported in previous sections is that, knowing the *Sh-Re-Sc* correlation and the k_h values for NO_3^- electroreduction on a given cathode, the removal rates of this ion would be fully predictable for treating actual wastewater with sufficient conductivity that enables the operation under convection-diffusion conditions. This is feasible, for example, when NO_3^--polluted effluents are pretreated with ion exchange resins, further generating rinsing solutions highly concentrated with desorbed NO_3^-. In such cases, the electroreduction process in a scaled-up RCE reactor would be fully controlled. To assess the possibility of treating NO_3^- in less conductive media (e.g., groundwater) than that studied so far, model solutions with lower concentrations of supporting electrolyte were prepared. Electrolytic trials were performed in galvanostatic mode because of its greater simplicity, envisaging a future application.

The effect of the supporting electrolyte concentration (10–500 mM Na_2SO_4) over the electroreduction of 400 mL of 10 mM NO_3^- solutions was then studied in the same RCE system described above but applying a current of −1.2 A ($j = -12$ mA cm^{-2}) at $\omega = 300$ rpm ($Re = 25{,}775$). At such j, the potential was $-1.8 < E_{cath} < -1.6$ V to favor the nitrate reduction minimizing the HER. Fig. 8a shows that NO_3^- was more rapidly removed as the Na_2SO_4 concentration was risen, i.e., at higher conductivity that enhances the diffusion-convection regime and mass transport. After 120 min of electrolysis, 94%, 95% and 97% reduction of NO_3^- was achieved at 10, 100 and 500 mM Na_2SO_4, respectively. The kinetic analysis of Fig. 8b corroborates that NO_3^- decay obeyed a first-order kinetics, yielding rising k_1-values of 3.5×10^{-2}, 4.0×10^{-2} and 5.4×10^{-2} s^{-1} with excellent fittings ($R^2 > 0.99$). The FE values presented in Fig. 8c highlight a higher efficiency with increasing the supporting electrolyte concentration, pre-eminently at the beginning of the process when the migration is more relevant, mitigating this detrimental phenomenon as the supporting electrolyte concentration is risen. For the most efficient system (0.50 M Na_2SO_4) the FE drops from 88% to a final value of 34%, owing to the loss of NO_3^- content and the increase of the parallel reduction of water (i.e., HER) and nitrogen by-products formed. Also, the migration term becomes less important and at 120 min, the FE value is 34% regardless of the Na_2SO_4 concentration. Fig. 8d depicts a high EC decrease from 98.2 to 46.9 and 35.8 Wh g^{-1} as the Na_2SO_4 concentration increases from 10 to 100 and 500 mM, mainly due to the decay of cell voltage from 9.0 to 4.6 and 3.6 V due to the progressive rise of conductivity.

These results are promising and open the door to the application of a 1018 steel cathode in an RCE reactor for NO_3^- electroreduction in groundwater and wastewater with low conductivity. Nevertheless, strategies to increase the conductivity of the solution to be treated are welcome, since it favors the mass transport to the cathode surface by diffusion-convection, as the natural NO_3^- migration toward the anode is detrimental for its efficient abatement.

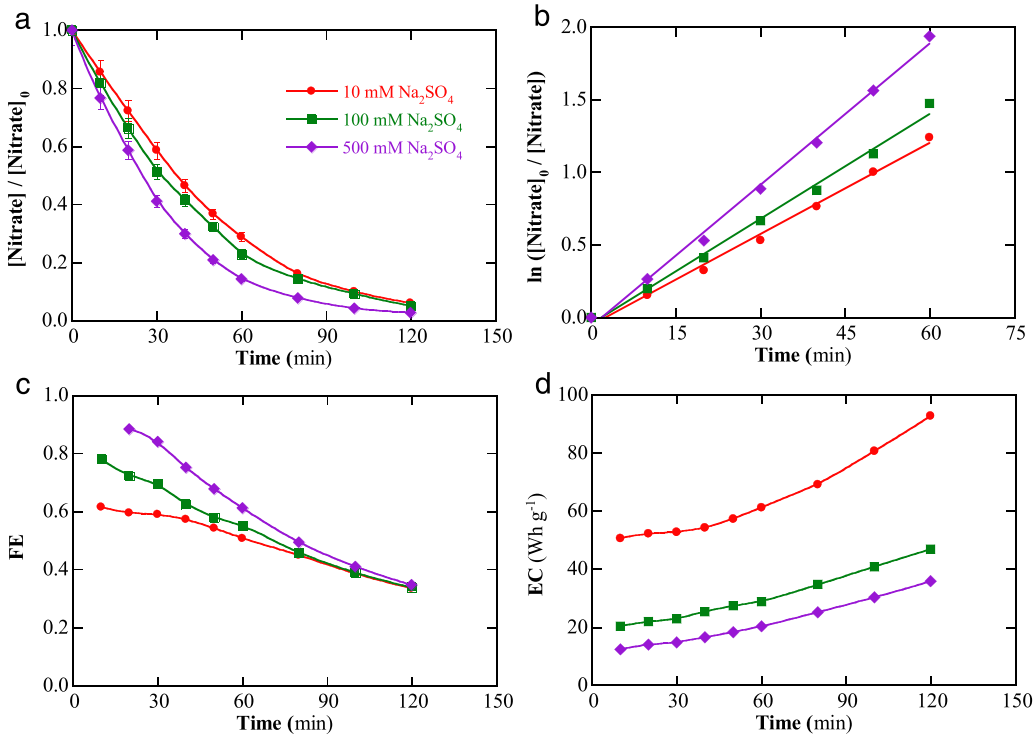

Fig. 8. Effect of the supporting electrolyte concentration on the evolution of (a) the normalized nitrate concentration decay and (b) the resulting first-order kinetics, (c) faradaic efficiency and (d) energy consumption per gram of nitrate ion. Galvanostatic trials were made with 400 mL solutions containing 10 mM KNO_3 + 10, 100 or 500 mM Na_2SO_4, using a 1018 steel RCE as the WE at $\omega = 300$ rpm and $j = -12$ mA cm^{-2} for 120 min.

4. Conclusions

It has been shown that conductive solutions with 10 mM NO_3^- + 0.50 M Na_2SO_4 can be efficiently treated using a 1018 steel RCE under potentiostatic conditions, achieving the complete and selective conversion of NO_3^- into NH_3 via an 8-electron global reaction that involves $^•H$ as mediator. Conversely, the process is inhibited when an SS316 cathode is used. The NO_3^- decay always obeyed a first-order reaction kinetics, in agreement with an initial two-electron reduction of NO_3^- to NO_2^- as the rate-determining step, allowing the determination of the k_1-values. Due to the spontaneous solution alkalinization, NH_3 is partially released to the atmosphere. FE values near 56% were obtained at the beginning of the process, whereas the increase of cathodic overpotential and ω accelerated the electroreduction process. From the LSV analysis and bulk electrolysis, the k_h and k_m values were determined, respectively. The diffusion-charge transfer of the RCE reactor was characterized upon calculation of the *Da* and η values, showing that it operates under a mixed regime. Key dimensionless parameters like *Re*, *Sh* and *Sc* have also been calculated, yielding a useful mass transport correlation (under turbulent flow, $8592 \leq Re \leq 42{,}959$) for the scale-up of the process in the absence of migration. Finally, promising preliminary results have been obtained for the NO_3^- electroreduction in solutions with low conductivity using the same RCE system, thus paving the way for future studies with actual wastewater or groundwater.

CRediT authorship contribution statement

Roger Oriol: Data curation, Investigation, Methodology, Writing – original draft, Writing – review & editing. **Enric Brillas:** Data curation, Writing – original draft, Writing – review & editing; **José L. Nava:** Conceptualization, Data curation, Formal analysis, Funding acquisition, Project administration, Resources, Supervision, Validation, Writing – original draft, Writing – review & editing. **Ignasi Sirés:** Conceptualization, Data curation, Formal analysis, Funding acquisition, Project administration, Resources, Supervision, Validation, Writing – original draft, Writing – review & editing.

Declaration of Competing Interest

The authors declare that they have no known competing financial interests or personal relationships that could have appeared to influence the work reported in this paper.

Data availability

Data will be made available on request.

Acknowledgments

The authors gratefully acknowledge financial support from projects PID2019-109291RB-I00 (MCIN/AEI/10.13039/501100011033, Spain) and CIIC 203/2022 (University of Guanajuato, Mexico), as well as the FPI PhD scholarship awarded to R.O. (BES-2017-080095, MINECO, Spain).

References

[1] D. Han, M.J. Currell, G. Cao, Deep challenges for China's war on water pollution, Environ. Pollut. 218 (2016) 1222–1233, https://doi.org/10.1016/j.envpol.2016.08.078.
[2] European Comission, The nitrate directive, 2021, https://ec.europa.eu/environment/water/water-nitrates/index_en.html
[3] E.P.A., Estimated nitrate concentrations in groundwater used for drinking, 2017. https://www.epa.gov/nutrient-policy-data/estimated-nitrate-concentrations-groundwater-used-drinking.
[4] Euronews, How nitrate water pollution is posing a threat to people and ecosystems in Spain. 2022. https://www.euronews.com/2022/02/25/save-our-water-the-devastating-impact-of-nitrate-pollution-in-spain (accessed on 2 August 2022).
[5] E.E. Stüeken, M.A. Kipp, M.C. Koehler, R. Buick, The evolution of Earth's biogeochemical nitrogen cycle, Earth Sci. Rev. 160 (2016) 220–239, https://doi.org/10.1016/j.earscirev.2016.07.007.
[6] H. Zhou, Y. Tan, W. Gao, Y. Zhang, Y. Yang, Selective nitrate removal from aqueous solutions by a hydrotalcite-like absorbent FeMgMn-LDH, Sci. Rep. 10 (2020) 16126, https://doi.org/10.1038/s41598-020-72845-3.
[7] A. Kapoor, T. Viraraghavan, Nitrate removal from drinking water-A review, J. Environ. Eng. 123 (1997) 371–380, https://doi.org/10.1061/(ASCE)0733-9372(1997)123:4(371).
[8] A.A. Aghapour, S. Nemati, A. Mohammadi, H. Nourmoradi, S. Karimzadeh, Nitrate removal from water using alum and ferric chloride: a comparative study of alum and ferric chloride efficiency, Environ. Eng. Manag. J. 3 (2016) 69–73, https://doi.org/10.15171/ehemj.2016.03.
[9] C. Huang, H. Wang, P. Chiu, Nitrate reduction by metallic iron, Water Res 32 (1998) 2257–2264, https://doi.org/10.1016/S0043-1354(97)00464-8.
[10] X. Huo, D.J. Van Hoomissen, J. Liu, S. Vyas, T.J. Strathmann, Hydrogenation of aqueous nitrate and nitrite with ruthenium catalysts, Appl. Catal. B: Environ. 211 (2017) 188–198, https://doi.org/10.1016/j.apcatb.2017.04.045.
[11] E. Lacasa, P. Cañizares, C. Sáez, F.J. Fernández, M.A. Rodrigo, Removal of nitrates from groundwater by electrocoagulation, Chem. Eng. J. 171 (2011) 1012–1017, https://doi.org/10.1016/j.cej.2011.04.053.
[12] M. Guo, L. Feng, Y. Liu, L. Zhang, Electrochemical simultaneous denitrification and removal of phosphorus from the effluent of a municipal wastewater treatment plant using cheap metal electrodes, Environ. Sci.: Water Res. Technol. 6 (2020) 1095, https://doi.org/10.1039/D0EW00049C.
[13] S. Ghafari, M. Hasan, M.K. Aroua, Bio-electrochemical denitrification - a review, Bioresour. Technol. 99 (2008) 3965–3974. ⟨https://www.researchgate.net/publication/285876442⟩.
[14] G. Puiggioni, S. Milia, E. Dessi, V. Unali, N. Pous, M.D. Balanguer, S. Puig, A. Carucci, Combining electro-bioremediation of nitrate in saline groundwater with concomitant chlorine production, Water Res 206 (2021), 117736, https://doi.org/10.1016/j.watres.2021.117736.
[15] V. Rosca, M. Duca, M.T. De Groot, M.T.M. Koper, Nitrogen cycle electrocatalysis, Chem. Rev. 109 (2009) 2209–2244, https://doi.org/10.1021/cr8003696.
[16] J. Gao, N. Shi, Y. Li, B. Jiang, T. Marhaba, W. Zhang, Electrocatalytic upcycling of nitrate wastewater into an ammonia fertilizer via an electrified membrane, Environ. Sci. Technol. (2022), https://doi.org/10.1021/acs.est.1c08442.
[17] R. Oriol, M.P. Bernícola, E. Brillas, P.L. Cabot, I. Sirés, Paired electro-oxidation of insecticide imidacloprid and electrodenitrification in simulated and real water matrices, Electrochim. Acta 317 (2019) 753–765, https://doi.org/10.1016/j.electacta.2019.05.002.
[18] A.S. Fajardo, P. Westerhoff, C.M. Sanchez-Sanchez, S. Garcia-Segura, Earth-abundant elements a sustainable solution for electrocatalytic reduction of nitrate, Appl. Catal. B: Environ. 281 (2021), 119465, https://doi.org/10.1016/j.apcatb.2020.119465.
[19] I. Katsounaros, G. Kyriacou, Influence of nitrate concentration on its electrochemical reduction on tin cathode: Identification of reaction intermediates, Electrochim. Acta 53 (2008) 5477–5484, https://doi.org/10.1016/j.electacta.2008.03.018.
[20] I. Katsounaros, G. Kyriacou, Influence of the concentration and the nature of the supporting electrolyte on the electrochemical reduction of nitrate on tin cathode, Electrochim. Acta 52 (2007) 6412–6420, https://doi.org/10.1016/j.electacta.2007.04.050.
[21] W. Huang, M. Li, B. Zhang, C. Feng, X. Lei, B. Xu, Influence of operating conditions on electrochemical reduction of nitrate in groundwater, Water Environ. Res. 85 (2013) 224–231, https://doi.org/10.2175/106143012×13418552642047.
[22] R. Oriol, E. Brillas, P.L. Cabot, J.L. Cortina, I. Sirés, Paired electrochemical removal of nitrate and terbuthylazine pesticide from groundwater using mesh electrodes, Electrochim. Acta 383 (2021), 138354, https://doi.org/10.1016/j.electacta.2021.138354.
[23] M. Dortsiou, I. Katsounaros, C. Polatides, G. Kyriacou, Influence of the electrode and the pH on the rate and the product distribution of the electrochemical removal of nitrate, Environ. Technol. 34 (2013) 373–381, https://doi.org/10.1080/09593330.2012.696722.
[24] J. Ding, W. Li, Q.L. Zhao, K. Wang, Z. Zheng, Y.Z. Gao, Electroreduction of nitrate in water: role of cathode and cell configuration, Chem. Eng. J. 271 (2015) 252–259, https://doi.org/10.1016/j.cej.2015.03.001.
[25] W. Li, C. Xiao, Y. Zhao, Q. Zhao, R. Fan, J. Xue, Electrochemical reduction of high-concentrated nitrate using Ti/TiO_2 nanotube array anode and Fe cathode in dual-chamber cell, Catal. Lett. 146 (2016) 2585–2595, https://doi.org/10.1007/s10562-016-1894-3.
[26] D. Xu, Y. Li, L. Yin, Y. Ji, J. Niu, Y. Yu, Electrochemical removal of nitrate in industrial wastewater, Front. Environ. Sci. Eng. 12 (2018) 9, https://doi.org/10.1007/s11783-018-1033-z.
[27] Y. Wang, C. Wang, M. Li, Y. Yu, B. Zhang, Nitrate electroreduction: mechanism insight, in situ characterization, performance evaluation, and challenges, Chem. Soc. Rev. 50 (2021) 6720, https://doi.org/10.1039/D1CS00116G.
[28] J. Li, G. Zhan, J. Yang, F. Quan, C. Mao, Y. Liu, B. Wang, F. Lei, L. Li, A.W.M. Chan, L. Xu, Y. Shi, Y. Du, W. Hao, P.K. Wong, J. Wang, S. Dou, L. Zhang, J.C. Yu, Efficient ammonia electrosynthesis from nitrate on strained ruthenium nanoclusters, J. Am. Chem. Soc. 142 (2020) 7036–7056, https://doi.org/10.1021/jacs.0c00418.
[29] B.P. Dash, S. Chaudhari, Electrochemical denitrificaton of simulated ground water, Water Res 39 (2005) 4065–4072, https://doi.org/10.1016/j.watres.2005.07.032.

[30] P.H. van Langevelde, I. Katsounaros, M.T.M. Koper, Electrocatalytic nitrate reduction for sustainable ammonia production, Joule 5 (2021) 290–294, https://doi.org/10.1016/j.joule.2020.12.025.
[31] J. Gao, B. Jiang, C. Ni, Y. Qi, X. Bi, Enhanced reduction of nitrate by noble metal-free electrocatalysis on P doped three-dimensional Co_3O_4 cathode: mechanism exploration from both experimental and DFT studies, Chem. Eng. J. 382 (2020), 123034, https://doi.org/10.1016/j.cej.2019.123034.
[32] Y. Wang, W. Zhou, R. Jia, Y. Yu, B. Zhang, Unveiling the activity origin of a copper-based electrocatalyst for selective nitrate reduction to ammonia, Angew. Chem. Int. Ed. 59 (2020) 5350–5354, https://doi.org/10.1002/anie.201915992.
[33] C.A. Martínez-Huitle, M.A. Rodrigo, I. Sirés, O. Scialdone, Single and coupled electrochemical processes and reactors for the abatement of organic water pollutants: a critical review, Chem. Rev. (2015) 13362–13407, https://doi.org/10.1021/acs.chemrev.5b00361.
[34] C.A. Martínez-Huitle, M.A. Rodrigo, O. Scialdone, Electrochemical Water and Wastewater Treatment, Elsevier, First ed., Oxford, UK, 2018.
[35] M. Paidar, K. Bouzek, H. Bergmann, Influence of cell construction on the electrochemical reduction of nitrate, Chem. Eng. J. 85 (2002) 99–109, https://doi.org/10.1016/S1385-8947(01)00158-9.
[36] P. Gayen, J. Spataro, S. Avasarala, A.M. Ali, J.M. Cerrato, B.P. Chaplin, Electrocatalytic reduction of nitrate using Magnéli phase TiO_2 reactive electrochemical membranes doped with Pd-based catalysts, Environ. Sci. Technol. 52 (2018) 9370–9379, https://doi.org/10.1021/acs.est.8b03038.
[37] M.A. Hasnat, S. Ben Aoun, M.M. Rahman, A.M. Asiri, N. Mohammed, Lean Cu–immobilized Pt and Pd films/–H^+ conducting membrane assemblies: relative electrocatalytic nitrate reduction activities, J. Ind. Eng. Chem. 28 (2015) 131–137, 1 https://doi.org/0.1016/j.jiec.2015.02.008.
[38] F.F. Rivera, J. González, J.L. Nava, Copper removal from an effluent generated by a plastics chromium-plating industry using a rotating cylinder electrode (RCE) reactor, Environ. Technol. 29 (2008) 817–825, https://doi.org/10.1080/09593330801987327.
[39] J.L. Arredondo, F.F. Rivera, J.L. Nava, Silver recovery from an effluent generated by plating industry using a rotating cylinder electrode (RCE), Electrochim. Acta 147 (2014) 337–342, https://doi.org/10.1016/j.electacta.2014.09.127.
[40] J.E. Terrazas-Rodriguez, S. Gutierrez-Granados, M.A. Alatorre-Ordaz, C. Ponce de Leon, F.C. Walsh, The use of a rotating cylinder electrode to selective recover palladium from acid solutions used to manufacture automotive catalytic converters, J. Appl. Electrochem 41 (2011) 89–97, https://doi.org/10.1016/10.1007/s10800-010-0212-9.
[41] M. Rosales, J.L. Nava, Simulations of turbulent flow, mass transport, and tertiary current distribution on the cathode of a rotating cylinder electrode reactor in continuous operation mode during silver deposition, J. Electrochem. Soc. 164 (2017) E3345–E3353, https://doi.org/10.1149/2.0351711jes].
[42] F.C. Walsh, G. Kear, A.H. Nahlé, J.A. Warton, L.F. Arenas, The rotating cylinder electrode for studies of corrosion engineering and protection of metals - An illustrated review, Corr, Sci 123 (2017) 1–20, https://doi.org/10.1016/j.corsci.2017.03.024.
[43] D.R. Gabe, G.D. Wilcox, J. Gonzalez-Garcia, F.C. Walsh, The rotating cylinder electrode: its continued development and application, J. Appl. Electrochem 28 (1998) 759–780, https://doi.org/10.1023/A:1003464415930.
[44] C.T.J. Low, C. Ponce de León, F.C. Walsh, The rotating cylinder electrode (RCE) and its application to the electrodeposition of metals, Aust. J. Chem. 58 (2005) 246–262, https://doi.org/10.1149/2.0351711jes.
[45] M. Eisenberg, C.W. Tobias, C.R. Wilke, Ionic mass transfer and concentration polarization at rotating electrode, J. Electrochem. Soc. 101 (1954) 306–320, https://doi.org/10.1149/1.2781252.
[46] F.F. Rivera, J.L. Nava, M.T. Oropeza, A. Recéndiz, G. Carreño, Mass transport studies at rotating cylinder electrode: Influence of the inter-electrode gap, Electrochim. Acta 55 (2010) 3275–3278, https://doi.org/10.1016/j.electacta.2009.12.060.
[47] O. González Pérez, J.M. Bisang, Removal of nitrate using an activated rotating cylinder electrode, Electrochim. Acta 194 (2016) 448–453, https://doi.org/10.1016/j.electacta.2016.02.114.
[48] World Health Organization, Guidelines for drinking-water quality, Fourth ed., 2017.
[49] R. Oriol, D. Clematis, E. Brillas, J.L. Cortina, M. Panizza, I. Sirés, Groundwater treatment using a solid polymer electrolyte cell with mesh electrodes, ChemElectroChem 6 (2019) 1235–1243, https://doi.org/10.1002/celc.201801906.
[50] A.J. Bard, L.R. Faulkner, Electrochemical Methods, John Wiley & Sons, Second ed., New York, USA, 2001. https://doi.org/10.1016/B978–0-12–381373-2.00056–9.
[51] G. Cassiere, J.J. Carberry, The interphase catalytic effectiveness factor: activity, yield and non-isothermality, Chem. Eng. Educ. 1 (1973) 22–26.
[52] J.L. Nava, E. Sosa, C. Ponce de León, M.T. Oropeza, Effectiveness factors in an electrochemical reactor with rotating cylinder electrode for the acid-cupric/copper cathode interface process, Chem. Eng. Sci. 2 (56) (2001) 2695–2702, https://doi.org/10.1016/S0009-2509(00)00514-5.
[53] J.L. Nava, E. Sosa, G. Carreño, C. Ponce-de-León, M.T. Oropeza, Modelling of the concentration–time relationship based on global diffusion-charge transfer parameters in a flow-by reactor with a 3D electrode, Electrochim. Acta 51 (2006) 4210–4217, https://doi.org/10.1016/j.electacta.2005.12.002.
[54] J.J. Carberry, Chemical and Catalytic Reaction Engineering. Mc Graw Hill. New York, USA, 1976.
[55] S. Bae, K.L. Stewart, A. Gewirth, Nitrate adsorption and reduction on Cu(100) in acidic solution, J. Am. Chem. Soc. 129 (2007) 10171–10180, https://doi.org/10.1021/ja071330n.
[56] H. Uchiyama, Q. Zhao, M.A. Hassan, G. Andocs, N. Nojima, K. Takeda, K. Ishikawa, M. Hori, T. Kondo, EPR-spin trapping and flow cytometric studies of free radicals generated using cold atmospheric argon plasma and X-ray irradiation in aqueous solutions and intracellular milieu, PLoS One 10 (2015), e0136956, https://doi.org/10.1371/journal.pone.0136956.

4.5. Modeling hydrodynamics, mass transport and current distribution for nitrate removal in a rotating cylinder electrode reactor

After the diffusion-convection characterization of the RCE reactor for the electrochemical removal of nitrate controlled by a charge transfer and mass transport mixed regime employing a suitable material as the central cathode, the system was studied by CFD. A mathematical model was first proposed by defining the state equations that govern the hydrodynamics, mass transport and current distribution in the RCE reactor. Solving these equations employing COMSOL 5.5 Multiphysics® software allowed simulating the electrochemical nitrate removal on the rotating cathode surface, resulting in the overall nitrate concentration abatement.

Galvanostatic electrolyses employing the RCE reactor described above were carried out in a 2-electrode system with 400 mL of a synthetic solution with 500 mM of sodium sulfate as supporting electrolyte and 10, 20 or 40 mol L^{-1} of potassium nitrate as the electroactive species. The trials were carried out at different rotation rates (ω) of the RCE, from 300 to 1000 rpm, imposing a cathodic current density (j) on the RCE from 26 to 45 mA cm^{-2} (see **Table 1** in the related paper). The evolution of nitrate removal obtained from the galvanostatic electrolyses was compared with the concentration profiles obtained by the simulations.

An isometric view of the simulated domain representing the water body on the RCE reactor, and its upper view are depicted in **Figure 1**. The mesh employed consisted of 2.17×10^6 tetrahedral elements. It can be observed that the element density near the rotating electrode is higher, as its rotating walls are the source of the fluid motion. The mesh was selected from a sensitivity analysis (**Figure 1c**), which allowed verifying that more elements converged within the same solution. The electrolyte properties and the kinetic parameters for the electrochemical reactions, needed to solve the mass transport and the simultaneous current and potential distribution, were obtained by the Tafel analysis of the voltammograms for nitrate ER, HER and OER (**Figure S1**), which are shown in **Table 2**.

Figure 2a shows a clockwise rotation of the RCE on the *xy* plane given by the boundary condition, and the velocity field of a transversal section of the domain at z = 4 obtained at ω = 300. This shows a higher velocity of the fluid near the rotating cathode that decreases when getting closer to the static outer wall, being minimum near the corners of the anodes. **Figure 2b** depicts the isometric view of the velocity field on the surface of the domain. Five relevant isosurfaces are observed in **Figure 2c**, where the three lowest velocity-zones are confirmed (*z* = 0, 2.9 and 5.4 cm), as well as two Taylor vortices (*z* = 2.9 and 8 cm) and the increasing velocity of the fluid when getting closer to the RCE.

The streamlines within the RCE reactor account for three distinct zones generated by the two Taylor vortices at ω = 300. The lower speed regions were the result of the chaotic pattern generated by these vortices, as shown in **Figure 3**. This figure also shows the transversal *xz* plane in which the Taylor vortices can be clearly seen. **Figure 3b** shows the change on the velocity when getting away from the RCE (at *z* = 2.9 and 4 cm) due to the loss of inertial force in the anodes-cathode interelectrode gap, being *x/W* the normalized distance between electrodes ranging between 0 (anode surface) and 1 (cathode surface).

The mass transport is closely related to hydrodynamics, since the species in the reactor are carried towards the electrode surface due to inertial forces. The influence of the rotation rate on the concentration field within the RCE reactor at different ω (300 and 1000 rpm) after *t* = 300 s is depicted in **Figure 4**. It can be noticed that the nitrate concentration at one of the corners of each anode is lower than in the bulk due to the low velocity, thereby making more difficult the back-mixing of these volume elements with the bulk, although near the anodes the concentration value is the highest. However, in the inner part of the aqueous domain, the concentration has a homogeneous value of 8.45 and 1.2 mol m^{-3}, respectively, due to the continuous stirred tank behaviour. In the cathode vicinity (*x/W* = 1), the concentration of nitrate is the lowest in the domain; it increases towards the anodic direction until reaching the homogeneous region due to the higher velocity field there, which drags the nitrate towards the cathode, where it reacts.

The current distribution is a relevant parameter to assess electrochemical reactors in order to have a homogeneous distribution that ensures the same activity of the different regions of the electrodes, preventing leakage currents that cause undesired reactions or a

non-controlled electrode activity. The normalized current density distribution field in the RCE reactor at ω = 300 is observed on **Figure 5a**. While the anodes showed border effects with high current distribution, the RCE surface had small variation between the most active regions situated right in front of the anodes and the regions of the RCE in front of the inter-anodic spaces. The normalized current distribution as a function of the normalized arc length is uniform on the RCE surface, keeping values between $0.998 < j_c/j_{c,AVE} < 1.002$, as seen in the **Figure 5b.**

The influence of ω on the nitrate concentration abatement and first-order kinetic assessment are illustrated in **Figure 6**, comparing the experimental (symbols) and the simulation (continuous lines) values. The mathematical model behaved very well, providing excellent predictions. The nitrate ER was faster as ω and j increased, which is more evident from the evaluation of the first-order rate constant; this showed excellent linear regressions, being six-fold the first-order kinetic constant obtained at the highest j and ω in comparison with the lowest ones, which confirms that the faster the nitrate is dragged towards the RCE, the faster nitrate ER occurs on the cathode surface. The main detected and quantified by-product was ammonia, in good agreement with near 100% conversion demonstrated in the Thesis when using this cathode material. **Figure 7** revealed the influence of ω on normalized ammonia accumulation, total nitrogen abatement, and EC during the nitrate ER. The maximum value of ammonia accumulation was around 80% at $\omega \geq 800$, owing to a faster nitrate removal rate. As the rotation rate raised from 600 to 1000 rpm, the ammonia accumulation reached maximum values at 45, 30, and 15 min operating at 600, 800, and 1000 rpm. TN values coincided with the nitrogen mass balance done with nitrate and ammonia. The significant influence of ω on the loss of volatile N-species as the TN depletes over the electrolysis time is observed in **Figure 7b**, reaching final values of 30%, 35%, 42%, 46%, and 55% at 300, 400, 600, 800, and 1000 rpm, respectively. Regarding the EC depicted in **Figure 7c**, at $t < 15$ min, the lowest value in comparison with the other trials is attained at the highest ω due to higher mass transport and j. Moreover, at $t > 15$ min, the trend showed that the higher rotation rates yield higher EC values due to parasitic reactions, in good agreement with the large abatement of the nitrate concentration.

Several electrolyses were carried out at the highest j and ω (45 mA cm^{-2} and 1000 rpm) employing a different nitrate initial concentration (10, 20 and 40 mmol L^{-1}), in order

to assess their effect and validate the model, as depicted in **Figure 8** and **Figure 9**. The plots are analogous to those shown in **Figure 6** and **Figure 7**. In this case, a complete removal was reached after 20, 60, and 75 min at 10, 20, and 40 mmol L^{-1}, respectively. Similar trends to those commented above were obtained for ammonia and TN.

Chronologically, this was the last work made in this Thesis, and a final and very valuable conclusion is the excellent agreement between the theoretical and experimental results. This confirms that the proposed nitrate ER model is valid to predict the treatment outcome in an RCE reactor equipped with a mild steel cathode.

Chemical Engineering Journal

Modeling hydrodynamics, mass transport and current distribution for nitrate removal in a rotating cylinder electrode reactor

--Manuscript Draft--

Manuscript Number:	CEJ-D-23-13591
Article Type:	Research Paper
Section/Category:	Environmental Chemical Engineering
Keywords:	Ammonia production; Computational Fluid Dynamics; Electrochemical reactor; Nitrate electroreduction; Rotating cylinder electrode
Corresponding Author:	Ignasi Sires Universitat de Barcelona Barcelona, Spain
First Author:	Roger Oriol, P
Order of Authors:	Roger Oriol, P
	José Nava, PhD
	Enric Brillas, PhD
	Oscar Cornejo, PhD
	Ignasi Sires
Abstract:	In this study, computational fluid dynamics (CFD) simulations have been employed to investigate the transport phenomena occurring in an electrochemical reactor, equipped with an AISI 1018 carbon steel rotating cylinder electrode (RCE), during nitrate electroreduction. A model that resulted from solving the fundamental transport equations that govern the hydrodynamics, mass transport, and current distribution is proposed to assess the behavior of the RCE reactor when addressing the nitrate removal. The results obtained from the simulations offered a wider understanding of the selected electroreduction process. It was determined that the six surrounding Ti|IrO2-based anodes acted as deflectors that promoted the presence of two Taylor vortices, giving rise to three distinct velocity zones inside the reactor. This fact had an impact on mass transport, since the appearance of low concentration zones was associated with a greater velocity. Furthermore, a slight current distribution was observed at the RCE, which was caused by the existence of the anodic gaps. Nevertheless, homogeneous current density distributions (0.998 < jc/ jc,AVE < 1.002) at the RCE were attained because the nitrate reduction was limited by mass transport. The model was validated by performing a series of nitrate electroreduction experiments in an RCE reactor filled with solutions of 400 mL, corroborating that it is sufficiently robust to predict the nitrate concentration decay. At 1000 rpm, operating at 447 A m-2 to ensure mass transport control conditions, 90% nitrate removal from a 10 mM KNO3 + 500 mM K2SO4 solution was achieved in only 30 min, with a low electrochemical energy consumption of 42.5 Wh g–1.

Graphical Abstract

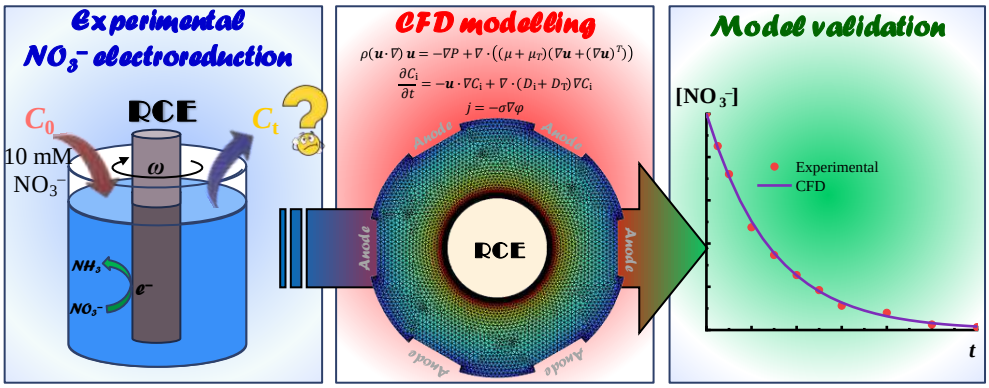

Highlights

▶ Computational fluid dynamics used for the first time to model NO_3^- electroreduction

▶ Experimental NO_3^- removal at different U and [NO_3^-] in RCE reactor validated the model

▶ CFD characterization revealed two Taylor vortices and $j_c/j_{ave} \sim 1$

▶ Conversion of NO_3^- mainly to ammonia (n = 8 e^-) at the carbon steel RCE surface

▶ Fast NO_3^- removal (10-40 mM) in short time, with low energy consumption

Modeling hydrodynamics, mass transport and current distribution for nitrate removal in a rotating cylinder electrode reactor

Roger Oriol [a], José L. Nava [b], Enric Brillas [a], Oscar M. Cornejo [a,c,**], Ignasi Sirés [a,*]

[a] *Laboratori d'Electroquímica dels Materials i del Medi Ambient, Departament de Ciència de Materials i Química Física, Secció de Química Física, Facultat de Química, Universitat de Barcelona, Martí i Franquès 1-11, 08028 Barcelona, Spain*

[b] *Departamento de Ingeniería Geomática e Hidráulica, Universidad de Guanajuato, Av. Juárez 77, Zona Centro, 36000 Guanajuato, Guanajuato, Mexico*

[c] *Facultad de Ciencias Químicas, Benemérita Universidad Autónoma de Puebla, Mexico*

Paper submitted for publication in *Chemical Engineering Journal*

Corresponding author: * E-mail: i.sires@ub.edu (I. Sirés)

** E-mail: om.cornejo@ub.edu (O.M. Cornejo)

Abstract

In this study, computational fluid dynamics (CFD) simulations have been employed to investigate the transport phenomena occurring in an electrochemical reactor, equipped with an AISI 1018 carbon steel rotating cylinder electrode (RCE), during nitrate electroreduction. A model that resulted from solving the fundamental transport equations that govern the hydrodynamics, mass transport, and current distribution is proposed to assess the behavior of the RCE reactor when addressing the nitrate removal. The results obtained from the simulations offered a wider understanding of the selected electroreduction process. It was determined that the six surrounding Ti|IrO_2-based anodes acted as deflectors that promoted the presence of two Taylor vortices, giving rise to three distinct velocity zones inside the reactor. This fact had an impact on mass transport, since the appearance of low concentration zones was associated with a greater velocity. Furthermore, a slight current distribution was observed at the RCE, which was caused by the existence of the anodic gaps. Nevertheless, homogeneous current density distributions ($0.998 < j_c/ j_{c,AVE} < 1.002$) at the RCE were attained because the nitrate reduction was limited by mass transport. The model was validated by performing a series of nitrate electroreduction experiments in an RCE reactor filled with solutions of 400 mL, corroborating that it is sufficiently robust to predict the nitrate concentration decay. At 1000 rpm, operating at 447 A m^{-2} to ensure mass transport control conditions, 90% nitrate removal from a 10 mM KNO_3 + 500 mM K_2SO_4 solution was achieved in only 10 min, with a low electrochemical energy consumption of 14.3 Wh g^{-1}.

Keywords: Ammonia production; Computational fluid dynamics; Electrochemical reactor; Nitrate electroreduction; Rotating cylinder electrode

1. Introduction

Nitrate water pollution is a pressing environmental issue that threatens people and ecosystems. Although nitrates are naturally present in nature, being an absolutely essential nitrogen source for plant growth, excessive levels are known cause severe health and environmental concerns, putting at risk the future of entire populations [1-3].

Several human activities, particularly agriculture and livestock farming, are the primary source for NO_3^- discharge into water bodies [4,5]. The expansive use of synthetic fertilizers and the spread of livestock manure on agricultural land eventually results in nitrate leaching or in-situ generation, thereby ending in groundwater and surface water bodies. Consequently, drinking water sources fed with such polluted streams may exceed the nitrate threshold values established by the law, posing serious health hazards [4-7]. Furthermore, improper disposal or inadequate treatment of industrial waste adds to nitrate discharge into nearby water bodies, exacerbating the pollution problem.

The health implications of long-term water pollution by NO_3^- are subject to discussion, although there is consensus on the worrisome consequences derived from its presence in freshwater and drinking water, particularly for vulnerable people such as infants and pregnant women [7]. Once ingested, nitrates can be converted into nitrites within the body, which bind to hemoglobin in the blood reducing the oxygen transport efficiency [7-9]. This condition, so-called methemoglobinemia, can cause oxygen depletion, leading to severe health complications and, in some extreme cases, death.

These concerns bring about the urgent need to address NO_3^- removal from water. A set of methods has been developed for this purpose so far, including chemical and biological approaches, but electrochemical approaches have gradually gained attention among the

former due to their effectiveness, cost-efficiency, simple operation and environmental compatibility [2,10-13]. In NO_3^- electroreduction, the cathode material, the applied cathodic potential (E_{cath}) or cathodic current density (j_c), and solution pH have impact on the process mechanism, which can be either direct or indirect [14,15]. In dilute NO_3^- solutions (< 1 M) at neat-neutral or alkaline pH, the direct path is favored because the absorbed NO_3^- is reduced by the electrons supplied at the cathode surface. Conversely, in the indirect path, NO_3^- reacts with adsorbed atomic hydrogen, an intermediate of hydrogen evolution reaction (HER) (1), yielding the absorbed NO_2^- species according to reaction (2), which is known to be the rate-determining step of the overall electrochemical nitrate electroreduction process [14-16]. Afterward, further reduction of NO_2^- on the cathode surface yields NH_3 or N_2 via reactions (3) and (4), respectively. The electrochemical nitrate reduction has been widely studied in recent years, showing outstanding results regarding the removal percentage and the possibility of accumulating less hazardous products or even valorizing them [16-21].

$$2H_2O + 2e^- \rightarrow H_2 + 2OH^- \quad (1)$$

$$NO_3^- + H_2O + 2e^- \rightarrow NO_2^- + 2OH^- \quad (2)$$

$$NO_2^- + 5H_2O + 6e^- \rightarrow NH_3 + 7OH^- \quad (3)$$

$$2NO_2^- + 4H_2O + 6e^- \rightarrow N_2 + 8OH^- \quad (4)$$

A critical element to consider in the NO_3^- electroreduction is the cell configuration, which significantly affects the efficiency of the process, since the electrode arrangement as well as the flow pattern or hydrodynamics affect the mass transport and the current distribution inside the cell [18,22,23]. In this context, the rotating cylinder electrode (RCE) reactor has been suggested as a viable system to promote the fast and complete electroreduction of NO_3^- [24,25]. The RCE reactor has been widely used in electrochemical

engineering, being especially noticeable its use in metal recovery [26-28]. The mass transport is dramatically enhanced by the central RCE rotation, upgrading the supply of electroactive species to the electrode, which results in high reaction rates and current efficiencies [26-30]. The latter can be explained by the fact that, at a low Reynolds number (Re > 100), the RCE already develops a turbulent flow [27].

Despite the well-known experimental functioning of the RCE reactor, it is now essential to understand the complex phenomena that occur inside it, aiming to transfer the knowledge to a quite new application field like nitrate treatment. Recently, computational fluid dynamics (CFD) tools have arisen as an efficient strategy to elucidate the hydrodynamics, mass transport, and potential-current distribution inside different electrochemical reactor designs [22,23,31-34]. By solving the state equations linked to each phenomenon, which considers the deviation of the fluid ideality by CFD, a more intricate and insightful comprehension of the overall performance of the reactor can be attained [23]. CFD models have been used to characterize several reactor configurations, achieving results able to replicate the actual reactor performance [31-34]. The modeling of the RCE reactor through CFD has been addressed by several scholars, but always in the context of metal recovery and electrocoagulation process [28,34-36], therefore existing a gap related to nitrate removal.

Most of the published works dealing with nitrate electroreduction focused on assessing the performance of different cathode materials or optimizing the operation parameters to improve the process efficiency [14,15,18-20]. Nonetheless, to the authors knowledge, the development of a mathematical model and CFD tools to describe the nitrate reduction in an electrochemical reactor has not been performed yet.

In this article, a CFD model has been developed to simulate the hydrodynamic pattern, mass transport phenomena, and current distribution within an RCE reactor applied to nitrate

electroreduction. The transport equations of momentum, mass, and charge (under turbulent flow conditions) were solved by the finite element method using a commercial code. The CFD model was used to validate the influence of peripheral velocity and NO_3^- initial concentration on the pollutant removal rate in a 400-mL RCE reactor. Through this modeling study, it is expected that a better understanding of electrochemical nitrate removal mechanisms is attained, thereby inspiring new ways to optimize the performance. The main products generated during nitrate reduction have been quantified as well.

2. Experimental

2.1. Chemicals

The solutions used in this work were prepared with analytical grade electrolytes, including KNO_3 (98%) and K_2SO_4 (99.9%) provided by Panreac. Phthalic acid (99.5%) and tris(hydroxymethyl)aminomethane (99.8%) used to prepare the mobile phase for nitrate quantification by ion chromatography were of analytical grade from Panreac. Analytical grade sodium nitroprusside dihydrate from Merck, phenol (> 99%) from Sigma-Aldrich, and EDTA (> 99%) from Panreac were used for the ammonia colorimetric determination. All solutions employed in this work were prepared with ultrapure water (Millipore Milli-Q system with ρ > 18.2 MΩ cm at room temperature).

2.2. Experimental setup

The RCE reactor consisted of a jacketed glass vessel (13.0 cm height × 8.0 cm diameter). It comprised an AISI 1018 carbon steel RCE (14.0 cm height × 3.8 cm diameter) placed in the center of the vessel and surrounded by six commercial Ti|IrO_2-based anode plates (15.0 cm height × 2.0 cm wide) from NMT Electrodes. These plates were fixed in a polylactic acid

plastic holder, whereas the cathode was insulated at the bottom by means of a polypropylene cap. The gap between the cathode and each anode was kept at 1.9 cm, being the total cathode and anode area exposed to the solution similar in all trials (~ 100 cm^2 each). The reproducibility of the trials was ensured by cleaning the steel RCE after each electrolysis with a 20% H_2SO_4 solution, followed by further polishing of the surface with 280 and 800 grit sheet sandpaper. The RCE reactor was operated in batch mode. A variable rotation electric motor RW 20 from IKA allowed fixing the rotation rate of the RCE, whereas a GVD310 power supply from GRELCO provided the constant applied current. More details about the RCE reactor setup can be found elsewhere [25].

The NO_3^- electroreduction was performed in the RCE reactor containing 400 mL of a 500 mM K_2SO_4 solution at natural pH (~ 6.5), assessing the influence of the rotation rate (ω) in the range 300-1000 rpm, and nitrate initial concentration within 10-40 mM range. Since nitrate is a negatively charged ion, its spontaneous migration would take place towards the anode due to electrostatic attraction, thus negatively affecting the required mass transport towards the cathode where its electroreduction is expected. To neglect such negative contribution during the electrolytic trials, a sufficiently high concentration of supporting electrolyte (i.e., K_2SO_4) was added. This caused a decrease in the nitrate transport number ($t_{NO_3^-}$) below 0.01, calculated from $t_{NO_3^-} = \frac{\lambda_{NO_3^-} C_{NO_3^-}}{\sum \lambda_i C_i}$, where λ_i is the ion molar conductivity, and C_i is the concentration of each ion species in the solution.

The current density to be applied in the trials was determined from a dimensionless number correlation (Eq. (5)) obtained experimentally in our recently published work [25], which informs about the hydrodynamic regime and the overall properties of the solution. Since the Sherwood number (*Sh*) correlates the convective mass transport with molecular

diffusion ($Sh = k_m d_{RCE}/D_{NO_3^-}$) and, in turn, the mass transport coefficient (k_m) can be correlated to the limiting current density (j_L) for NO_3^- electroreduction through $k_m = j_L/nFC_{NO_3^-}$. Eq. (5) can be rewritten as Eq. (6) to finally calculate the limiting current density for nitrate electroreduction under mass transport control.

$$Sh = 0.7Re^{0.46}Sc^{0.356} \quad (5)$$

$$j_L = \frac{0.7nFC_{NO_3^-}D_{NO_3^-}}{d_{RCE}}Re^{0.46}Sc^{0.356} \quad (6)$$

where j_L is in A m^{-2}, n is the number of electrons transferred in the global reduction reaction (= 8), F is the Faraday constant (96485 C mol^{-1}), $C_{NO_3^-}$ is the nitrate concentration (in mol m^{-3}), $D_{NO_3^-}$ is the nitrate diffusion coefficient (in m^2 s^{-1}), and d_{RCE} is the diameter of the RCE (0.038 m), whereas Re and Sc are the Reynolds ($Re = Ud_{RCE}/v$, where v is the kinematic viscosity of the fluid) and Schmidt ($Sc = v/D_{NO_3^-}$ = 463) dimensionless numbers, respectively. Table 1 shows the j_L values required at each peripheral velocity.

The overall energy consumption (EC) of the electrolysis per gram of nitrate removed, was calculated as follows:

$$\text{EC (Wh g}^{-1}) = \frac{E_{cell}It}{3600(C_0 - C_t)MV} \quad (7)$$

where C_0 is the initial nitrate concentration, C_t is the nitrate concentration at each sampling time, V is the volume of the treated solution, I is the applied current (in A), t is the electrolysis time (in s), E_{cell} is the cell voltage (in V), and M is the molecular mass of nitrate ion (62 g mol^{-1}). It is worth mentioning that the duration of each trial was of 2 h and each of them was performed twice. Error bars are shown in the required figures.

172 *2.3. Analytical methods*

173 Nitrate concentration was quantified by ion chromatography using a Shimadzu 10Avp
174 liquid chromatograph that comprised a Shim-Pack IC-A1 anion column, with dimensions of
175 100 mm × 4.6 mm (i.d.), kept at 40 °C and coupled to a Shimadzu CDD 10 Avp conductivity
176 detector. This analysis was carried out by injecting 20 μL of the sample upon elution of a
177 mobile phase composed of a 2.4 mM *tris*(hydroxymethyl)aminomethane solution at pH 4 +
178 2.6 mM phthalic acid solution at 1.5 mL min^{-1}. The ammonia concentration (in the form of
179 ammonium ion) was determined via the standard indophenol blue colorimetric method,
180 which allowed measuring the absorbance at λ = 645 nm in a UV4 Unicam UV/Vis
181 spectrophotometer [16,17]. Total nitrogen (TN) measurements were performed in the TNM-
182 1 unit coupled to a Shimadzu VCSN TOC analyzer. The electrochemical characterization of
183 nitrate reduction and oxygen evolution reaction (OER) was performed by linear sweep
184 voltammetry (LSV) in a standard three-electrode cell connected to an Autolab PGSTAT100
185 potentiostat. The working electrode was either an AISI 1018 steel or a Ti|IrO_2-based piece,
186 for cathodic and anodic sweeps, respectively. A Pt rod and Ag|AgCl (3 M KCl) served as the
187 counter and reference electrodes.

188 **3. Formulation of the numerical simulation**

189 The modeling and simulation of NO_3^- electroreduction in an RCE reactor compels to
190 address the most critical aspects of this electrochemical system to obtain reliable results for
191 hydrodynamics, mass transport and current distribution behavior. Thus, the governing
192 equations for each phenomenon must be solved by proposing boundary conditions that
193 accurately describe the motion of the central cylinder and the main properties of the solution.
194 Moreover, the electrochemical process must be well understood, since the electrochemical

reactions depend on the kinetic parameters arising from the current applied to the specific electrocatalytic materials used as electrodes, as well as on the composition of the solution.

3.1. Electrochemical process

Nitrate electroreduction consists of two steps: (i) The two-electron reduction reaction (2) that converts nitrate to adsorbed NO_2^- on the cathode surface; and (ii) the subsequent six-electron complex cascade mechanism that reduces NO_2^- to either NH_3 from reaction (3) or N_2 from reaction (4). Since reaction (2) is established as the rate-determining step, the subsequent electron transfer to the adsorbed NO_2^- is comparatively fast. On this basis, NO_3^- electroreduction can be actually considered an eight-electron process, which in the case of carbon steel cathode results in the complete conversion to ammonia according to the global Eq. (8) [16,17]. At Ti|IrO_2-based anodes, the OER (reaction (9)) occurs concomitantly, without ammonia reoxidation [16,17].

$$NO_3^- + 6H_2O + 8e^- \rightarrow NH_3 + 9OH^- \quad (8)$$

$$4H_2O \rightarrow 2O_2 + 8H^+ + 8e^- \quad (9)$$

The overall reaction (8) can then be considered for simulation purposes, allowing to model the quick reduction of nitrate into ammonia on the cathode surface.

3.2. Turbulent model

RCE reactors favor turbulence at $Re \geq 100$, promoting fluid instability and generation of eddies, which require solving a set of equations that correctly describe turbulent behavior. The Reynolds-averaged Navier-Stokes (RANS) equations coupled with a κ-ε turbulence model have been widely used to solve CFD models for the RCE reactor, obtaining outstanding theoretical trends that simulated very well the experimental results [35,36].

Therefore, the hydrodynamic model consisted in finding the solution of the RANS and continuity Eqs. (10) and (11) [37]. The electrolyte is an incompressible fluid, and the modeling considers isothermal and steady-state conditions. The κ-ε turbulence model is implemented in the RANS equations through the turbulent viscosity (μ_T) by Eq. (12), which relates the rate of the turbulent kinetic energy (κ) with the dissipation rate of the turbulent energy (ε) [37]. Both κ and ε are described by Eqs. (13) and (14), which must be solved in the turbulent model:

$$\rho(\boldsymbol{u}\cdot\nabla)\boldsymbol{u} = -\nabla P + \nabla\cdot\left((\mu+\mu_T)(\nabla\boldsymbol{u}+(\nabla\boldsymbol{u})^T)\right) \quad (10)$$

$$\nabla\cdot\boldsymbol{u} = 0 \quad (11)$$

$$\mu_T = \rho C_\mu \frac{k}{\varepsilon} \quad (12)$$

$$\rho(\boldsymbol{u}\cdot\nabla)\kappa = \nabla\cdot\left(\left(\mu+\frac{\mu_T}{\sigma_\kappa}\right)\nabla\kappa\right) + P_\kappa - \rho\varepsilon \quad (13)$$

$$\rho(\boldsymbol{u}\cdot\nabla)\varepsilon = \nabla\cdot\left(\left(\mu+\frac{\mu_T}{\sigma_\varepsilon}\right)\nabla\varepsilon\right) + C_{\varepsilon1}\frac{\varepsilon}{\kappa}P_\kappa - C_{\varepsilon2}\rho\frac{\varepsilon^2}{\kappa} \quad (14)$$

where $\boldsymbol{u}$ is the average velocity vector, P is the averaged pressure, ρ is the density of the fluid, μ is the dynamic viscosity of the fluid, μ_T is the turbulent viscosity, and P_κ is an energy production term, whereas C_μ, $C_{\varepsilon1}$, $C_{\varepsilon2}$, σ_κ and σ_ε are dimensionless empirical constants of the model [37].

In a turbulent regime, in the region close to the wall, the velocity of the fluid exponentially decreases as it approaches the viscous zone, where the turbulent model begins to disagree because it is strictly valid for high *Re* numbers. In this scenario, wall functions are often introduced to ensure that the simulation is done in the turbulent zone of the fluid. The most used wall function in the κ-ε turbulence model is described by Eq. (15).

$$u^+ = \frac{1}{k}\ln y^+ + 5.5 \quad (15)$$

where u^+ is the dimensionless velocity normal to the wall, *k* is the von Karman constant, and y^+ is the dimensionless distance from the wall to the turbulent zone [33,37].

In the RCE batch reactor, the solution motion is attributed solely to the RCE rotation; hence, to solve Eqs. (10)-(14), the following boundary conditions were set:

- At the RCE, the cathode rotation was chosen as a normal stress derived from the tangential velocity vector at the RCE surface, $[(\mu + \mu_T)(\nabla \cdot \boldsymbol{u} + (\nabla \cdot \boldsymbol{u})^T)]\boldsymbol{n} = -\rho \frac{u_\tau}{u^+}\boldsymbol{u}_{tang}$, where $u_\tau = C_\mu^{0.25}\sqrt{\kappa}$, $\boldsymbol{u}_{tang} = \boldsymbol{u} - \frac{\boldsymbol{u}_\omega - (\boldsymbol{u}_\omega \cdot \boldsymbol{n})\boldsymbol{n}}{\|\boldsymbol{u}_\omega - (\boldsymbol{u}_\omega \cdot \boldsymbol{n})\boldsymbol{n}\|}\|\boldsymbol{u}_\omega\|$, and $\boldsymbol{u}_\omega$ is the velocity vector of the moving RCE given by $2\pi\omega r_{RCE}$, where ω is in rev s^{-1}.
- At the fluid surface, a decreasing shear stress is set to restrain the free movement of the fluid, $[(\mu + \mu_T)(\nabla \cdot \boldsymbol{u} + (\nabla \cdot \boldsymbol{u})^T)]\boldsymbol{n} = 0$, $u \cdot \boldsymbol{n} = 0$, as the RCE reactor is open to the atmosphere.
- In all the remaining walls, a dimensionless velocity u^+ was considered at a y^+ distance according to Eq. (15).

3.3 Mass transport

In turbulent regime in the absence of migration, ensured by the addition of a supporting electrolyte that allowed neglecting that term in the Nernst-Planck equation, the nitrate transport towards the RCE can be assessed by solving the time-dependent diffusion-convection Eq. (16) considering a turbulent diffusion coefficient (D_T):

$$\frac{\partial C_{NO_3^-}}{\partial t} = -\boldsymbol{u} \cdot \nabla C_{NO_3^-} + \nabla \cdot \left(D_{NO_3^-} + D_T\right)\nabla C_{NO_3^-} \quad (16)$$

where $\boldsymbol{u}$ is the average velocity vector obtained by solving Eqs. (10)-(14). The value of D_{T} can be calculated from the turbulent Schmidt number ($Sc_{\mathrm{T}} = \mu_{\mathrm{T}}/\rho D_{\mathrm{T}}$). For this, the Kays-Crawford model of Eq. (17) was used.

$$Sc_T = \left\{\frac{1}{2Sc_{T\infty}} + \frac{0.3\mu_T}{\sqrt{Sc_{T\infty}}\rho D} - \left(\frac{0.3\mu_T}{\rho D}\right)^2 \left[1 - exp\left(-\frac{\rho D}{0.3\mu_T\sqrt{Sc_{T\infty}}}\right)\right]\right\}^{-1} \quad (17)$$

where $Sc_{\mathrm{T}\infty}$ = 0.85 was included during the simulation of the diffusion-convection Eq. (16), to obtain D_{T} considering the local values of Sc_{T} and μ_{T}.

Although the current density at each rotation rate was calculated considering mass transport control, i.e., the concentration at the cathode surface is zero, the turbulent phenomena affecting the mass transport near the wall cannot be neglected. In this scenario, the Launder-Spalding model describes the concentration near the wall through a dimensionless concentration (C^+) at a distance y^+ by Eqs. (18) and (19), linking the viscous region with the turbulent zone [33,36]:

$$C^+_{\mathrm{NO_3^-}} = Sc_{\mathrm{T}}\left(\frac{1}{\mathrm{k}}\ln y^+ + 5.5 + P_{\mathrm{c}}\right) \quad (18)$$

$$C^+_{\mathrm{NO_3^-}} = \frac{\left(C_{\mathrm{NO_3^-,w}} - C_{\mathrm{NO_3^-}}\right)C_{\mu}^{0.25}\kappa^{0.5}}{N_{\mathrm{NO_3^-,w}}} \quad (19)$$

where $C^+_{\mathrm{NO_3^-}}$ is the dimensionless nitrate concentration, $C_{\mathrm{NO_3^-,w}}$ is the nitrate concentration in the region near the wall, $N_{\mathrm{NO_3^-,w}}$ is the nitrate flux towards the RCE wall, and P_{c} is a factor that describes the resistances near the wall by Eq. (20):

$$P_{\mathrm{c}} = A\left[\left(\frac{Sc}{Sc_{\mathrm{T}}}\right)^{0.75} - 1\right] \quad (20)$$

where A is an empirical constant (= 1) fitted to adjust the experimental data. The mass transport wall function was employed to describe the rate of nitrate transport towards the RCE.

The corresponding boundary conditions to solve Eq. (16) were set as follows:

- At the RCE, a nitrate flux expressed as $-D_{\mathrm{NO_3^-}}\frac{\partial C_{\mathrm{NO_3^-}}}{\partial \xi} = N_{\mathrm{NO_3^-}} = \frac{j_{0,\mathrm{NO_3^-}}\left(\frac{C_{\mathrm{NO_3^-},w}}{C_{\mathrm{NO_3^-}}}\right)\exp\left(\frac{\eta_{\mathrm{NO_3^-}}}{\mathrm{b}_{\mathrm{NO_3^-}}}\right)}{nF}$, where $j_{0,\mathrm{NO_3^-}}$ is the exchange current density for nitrate reduction, $\mathrm{b}_{\mathrm{NO_3^-}}$ is the Tafel slope for nitrate reduction, and $\eta_{\mathrm{NO_3^-}}$ is the nitrate reduction overpotential.
- In all the remaining walls, a zero-flux condition is set.

The initial condition to solve Eq. (16) is stated as follows:

- At t = 0, $C_{\mathrm{NO_3^-}} = C_{\mathrm{NO_3^-}}(t = 0)$, i.e., the initial nitrate concentration.

3.4 Tertiary current in the RCE reactor

In an electrochemical process, the reactions are conditioned by the current density and the potential applied to the electrode. The Laplace equation describes the electric potential distribution in the solution from Eq. (21). Conversely, the electrode local current density can be calculated through the Ohm's law of ionic conductance, Eq. (22).

$$\nabla\varphi^2 = 0 \tag{21}$$

$$\boldsymbol{j} = -\sigma\nabla\varphi \tag{22}$$

where φ is the electric potential, j is the current density vector, and σ is the ionic conductivity of the solution.

Eq. (21) is solved by considering the following boundary conditions:

- At the RCE, an overall cathodic current density is set, including the nitrate reduction as well as the HER, $-\sigma\frac{\partial\varphi}{\partial\xi} = j_c = j_{0,\mathrm{NO_3^-}}\left(\frac{c_{\mathrm{NO_3^-,w}}}{c_{\mathrm{NO_3^-}}}\right)\exp\left(\frac{\eta_{\mathrm{NO_3^-}}}{\mathrm{b}_{\mathrm{NO_3^-}}}\right) + j_{0,\mathrm{HER}}\exp\left(\frac{\eta_{\mathrm{HER}}}{\mathrm{b}_{\mathrm{HER}}}\right)$, where $\mathrm{b}_{\mathrm{HER}}$ and η_{HER} are the Tafel slope and overpotential attributed to HER, respectively. Both reactions are considered because of the co-occurrence of nitrate electroreduction [25].
- At the anodes, Tafel approach is defined as $-\sigma\frac{\partial\varphi}{\partial\xi} = j_a = j_{0,\mathrm{OER}}\exp\left(\frac{\eta_{\mathrm{OER}}}{\mathrm{b}_{\mathrm{OER}}}\right)$, where $j_{0,\mathrm{OER}}$, $\mathrm{b}_{\mathrm{OER}}$ and η_{OER} are the exchange current density, Tafel slope and overpotential attributed to OER, respectively.
- At the remaining insulating walls, a zero-flux condition is set.

Noticeably, the concentration overpotential $\left(\frac{c_{\mathrm{NO_3^-,w}}}{c_{\mathrm{NO_3^-}}}\right)$ is present in the boundary conditions related to the RCE in Eqs. (16) and (21) because mass transport and potential distribution depend on each other. The dependence on the nitrate concentration near the wall in both state equations compels the simultaneous solution of the mass transport and current distribution models.

3.5 Simulations

The state equations described in this model were solved by means of the finite element method, employing COMSOL Multiphysics® 6.0 software on a computer with two Intel® Xeon™ 2.30 GHz processors (96 RAM, 64-bit operating system). The hydrodynamics model was solved with an iterative GMRES method with a relative tolerance of 1×10^{-3} in a stationary state. On the other hand, the mass transport and the potential distribution models

were solved simultaneously using the same iterative method in a time-dependent solver. Simulations of hydrodynamics took ca. 180 min, whereas the time-dependent model could be solved in 120 min for a total simulation time of approximately 300 min per simulation. Table 2 shows the electrolyte properties and electrochemical kinetic parameters needed for the simulations. It is worth mentioning that the exchange current densities and Tafel slopes used in this work were obtained through LSV analysis carried out with the specific electrode materials, as shown in Fig. S1.

Fig. 1a shows an isometric view of the simulation domain, i.e., the RCE reactor, with the field of element quality throughout the domain. The mesh consisted of 2.43×10^6 tetrahedral elements with an average quality above 0.66. Fig. 1b shows the upper view of the simulation domain with the electrode arrangement employed in the simulations; the RCE is placed at the center and six anode plates surround it. Fig. 1c shows the sensitivity analysis performed for the NO_3^- electroreduction considering its concentration at 5 min of simulation time at 300 rpm. Several simulations were performed by changing the element size to improve the accuracy of simulations; optimum reproducibility of results was achieved with a mesh consisting of 2,178,025 elements. Nonetheless, the mesh consisting in 2,436,728 elements was selected to obtain a more detailed solution in the region near the RCE, requiring similar computation times of 290 and 300 min, respectively.

4. Results and discussion

4.1. Simulation of the turbulent regime

By solving the state equations that govern the momentum transport, Eqs. (10)-(14), both the overall behavior and local values of velocity can be obtained. Fig. 2a shows an upper view of a set of 58 surface arrows that was obtained at z = 4 cm (i.e., in the middle of the

reactor length) that inform about the rotation of the fluid elements in a clockwise direction. This can be explained by the tangential velocity boundary condition set on the RCE surface simulating the movement of the liquid towards the center of the reactor. The latter can be confirmed by the fact that the velocity tends to increase near the RCE and has a homogeneous profile around the perimeter of the electrode. On the other hand, due to the clockwise rotation, low-velocity zones are noticed in the corners of each anode, since the elements of the fluid are slowly dragged into the bulk.

Moreover, Fig. 2b shows an isometric view of the velocity field on the surface of the RCE reactor. It can be observed that in the upper part of the reactor, the velocity values are higher when compared to the cut at the center of the reactor. Moreover, two low-velocity zones can be distinguished on the reactor outer walls at z = 0 and 5.4 cm. The presence of such lower velocity zones can be accounted for by the presence of two Taylor vortices, as can be seen in Fig. 2c, at z values of 2.9 and 8.0 cm. These toroidal vortices are generated because the anodes act as deflectors of the fluid within the reactor, thus modifying the trajectory of the fluid elements into a more chaotic and unstable pattern. Fig. 2c shows a set of five isosurfaces from the slowest to the highest velocity inside the reactor, which confirms the presence of the low-velocity zones as well as the Taylor vortices, and the increasing velocity as the fluid is closer to the RCE surface. The number of Taylor vortices in an RCE reactor depends on the geometrical aspects (height and diameter), the reactor volume, and the surface boundary condition set (closed or open to the atmosphere). Usually, for RCE reactors operating in batch mode, one, two or three Taylor vortices are reported. In a work reported by Rivero et al. [35], an RCE reactor with similar geometry (d_{RCE} = 3.8 cm) was employed to describe Cu deposition. In that work, three Taylor vortices promoted by the RCE were observed. In contrast, in a work published by Villalobos et al. [38], only two

Taylor vortices were distinguished in an RCE reactor simulated with a non-fully submerged RCE, i.e., the electrode was over the bottom of the vessel. Even though RCE reactors can be geometrically similar, the phenomena occurring within them can be influenced by small variations, such a wider/narrower gap between electrodes, RCE positioning and reactor volume. Nonetheless, all reported works agree with the higher capacity of RCE reactors to promote turbulence and enhance the efficiency of electrochemical processes.

Fig. 3a shows a set of 50 streamlines within the RCE reactor, highlighting that the presence of the Taylor vortices at z values of 2.9 and 8.0 cm promotes the appearance of three distinct zones within the RCE reactor. Near the RCE, it can be observed that the elements of the fluid move around it. On the other hand, as the fluid gets closer to the anodes, a back mixing starts to develop as the anodes act as fluid deflectors. The first two zones can be attributed to this phenomenon caused by the first Taylor vortex. In contrast, the third zone can be correlated with the collision of the chaotic behavior generated by both vortices. The velocity profile from the anode surface ($x = 0$) to the RCE one ($x = W = 2.1$ cm), being x/W the normalized distance between electrodes ranging between 0 and 1 for the anode and cathode positions, respectively, can be obtained at different heights on the z-coordinate to elucidate the velocity evolution in the anode-cathode gap. Fig. 3b shows the velocity profile in the electrode gap at z values of 2.9 and 4.0 cm, which correspond to the position of the first Taylor vortex and the center of the reactor, respectively, at different rotation rates. At $z = 2.9$ cm, the velocity increases steadily across the anode-to-cathode gap due to the increased acceleration promoted by the Taylor vortex, with a steeper increment at $x/W = 0.85$, where the inertial force of the RCE is more prominent. On the other hand, at $z = 4.0$ cm, the velocity of the fluid remains practically unchanged between $0.1 < x/W < 0.9$ due to the homogeneous velocity field promoted at the reactor center and between both Taylor vortices. Nonetheless,

similarly to the behavior observed at z = 2.9 cm, the velocity increases exponentially at x/W = 0.9 due to the forced convection imposed by the RCE.

4.2. Mass transport and tertiary current distribution simulations

As discussed above, mass transport is closely linked to the hydrodynamic pattern, since the species in the reactor reach the electrode surface due to inertial forces. In turn, the potential distribution is affected by the movement of the species within the reactor. In an RCE reactor, the contribution of the convective term in Eq. (16) is higher than that of the diffusion term. Fig. 4a and 4b show the nitrate concentration field at 300 and 1000 rpm after 5 s of simulation time. It can be noticed that in the corner of each anode, the nitrate concentration is lower than in the bulk due to the low velocity, which makes difficult for the nitrate to reach these zones by back mixing. Moreover, in the inner part of the reactor, the concentration has an almost unchanged value of 9.98 and 9.60 mol dm^{-3}, respectively, resulting from the stirred tank behavior, which favors the homogeneity of the properties in the bulk.

Additionally, as the fluid approaches the RCE, the concentration value decreases. It is worth noticing the presence of six notorious forms around the RCE, which arise from the deflector-like pattern produced by the anodes, accelerating the fluid in the clockwise rotation. These zones penetrate more into the bulk volume at 1000 rpm, since the higher rotation rate, the more chaotic and faster the fluid becomes, which also accelerates the concentration decay at the cathode surface. The latter can be assessed in Fig. 4c, where it can be observed that, at 300 rpm, the concentration follows a quite linear path from the bulk near the anode to a distance x/W = 0.8, where the concentration depletes faster on the RCE surface. On the other hand, Fig. 4d elucidates the more chaotic concentration profile as the RCE is approached. A

slight increase of the nitrate concentration is attained near the anode surface, which then continuously depletes until the anion reaches the RCE surface. These trends are in good agreement with the faster dragging of nitrate toward the cathode when the rotation rate is increased in the RCE reactor.

The current distribution is a crucial parameter to assess in electrochemical reactors, since it is highly desirable that the current values are equal at any point of the electrode surface. Commonly, the current distribution is reported as a ratio between the local current (j) and the average current (j_{AVE}) on the electrode surface and, if $j/j_{,AVE} \sim 1$, it means that the current is distributed homogeneously on the whole electrode. In this context, the current distribution on the six anodes shows a homogeneous current distribution in the center of each plate. Nonetheless, at the edges of each anode, a current distribution up to $j_a/j_{a,AVE} = 1.7$ is observed, which can be explained by the lack of an insulating barrier that restricts the current leakage, which would diminish the border effect on the anodes. On the contrary, the RCE shows a lower current distribution of $j_c/j_{c,AVE} = 0.998$ in the areas where the electrode is not facing an anode. In contrast, as long as the RCE faces an anodic plate, the current becomes homogeneous ($j_c/j_{c,AVE} \sim 1$) along all the cylinder. Fig. 5b shows the normalized current distribution at z = 8.0 cm as a function of the normalized arc length ($s/\pi d_{RCE}$) for the range of $300 < \omega < 1000$ rpm. This distribution is uniform on the RCE surface, ranging as $0.998 < j_c/j_{c,AVE} < 1.002$. Although the current distribution is uniform around the RCE surface, the minor variations in the value are due to the particular electrode configuration that results in a slight current distribution when facing the anode gaps. The latter finding agrees with that attained in a previous paper on the simulation of current distribution at the RCE during copper electrodeposition [39].

4.3. Nitrate electroreduction

The experimental nitrate electroreduction trials were carried out in a 400-mL RCE reactor, assessing the influence of the rotation rate (300-1000 rpm) and the initial nitrate concentration (10-40 mM). The applied current density in each trial was between 26 and 45 mA cm^{-2}, directly depending on the rotation rate established by Eq. (6) as summarized in Table 1. The electrochemical process is under mass transport control regime at high rotation, whereas at low and moderate rotations (i.e., current values), the system is controlled by a charge transfer and mass transport mixed regime [25]. The results of all electrolytic trials regarding the nitrate concentration were fitted with the results predicted by the mathematical model developed as explained in Section 3. Fig. 6a shows the influence of the rotation rate of the RCE on nitrate reduction. The faster the RCE rotates, the quicker the nitrate removal from the solution. At 300 rpm, the nitrate is removed in 120 min, whereas at 1000 rpm, 90% of the nitrate in the solution is removed in 10 min. The accelerated electroreduction of nitrate as the rotation rate increases is more evident upon evaluation of the first-order kinetic constant (k_1). This parameter reached values of 3.37×10^{-2} min^{-1} (R^2 = 0.996), 6.26×10^{-2} min^{-1} (R^2 = 0.999), 12.16×10^{-2} min^{-1} (R^2 = 0.994), 13.99×10^{-2} min^{-1} (R^2 = 0.990), and 22.47×10^{-2} min^{-1} (R^2 = 0.995) at 300, 400, 600, 800, and 1000 rpm, respectively. The k_1-value obtained at 1000 rpm is six-fold the one obtained at the lowest velocity, which confirms that when the nitrate is more quickly dragged toward the RCE, the electroreduction is favored at the electrode surface. At high rotations, the nitrate is continuously dragged toward the electroactive surface of the RCE, resulting in a higher amount of nitrate near the electrode interface. This accelerates the occurrence of the rate-determining step (reaction (2)) and the subsequent cascade sequence that begins with reaction (3). It is worth mentioning that the nitrate profile obtained at 300 rpm is similar to that reported upon use of the RCE under

potentiostatic conditions (E_{cath} = –1.8 V vs. SHE) at 300 rpm [25]. Furthermore, an excellent fitting between the experimental results and data simulated from the model proposed in Section 3 was achieved. Moreover, at t < 30 min, the calculated current efficiency for nitrate electroreduction was over 90%, confirming the good performance of the RCE reactor to carry out the decontamination treatment.

Apart from the faster nitrate elimination attained at higher rotation rates due to resulting higher applied current densities and improved mass transport towards the cathode, the simultaneous assessment of the products generated is of particular interest. Fig. 7a shows the normalized profiles related to the NH_3 accumulation at each of the assessed ω values. The maximum accumulations attained were near 80% at $\omega \geq 800$ rpm due to the quicker release of NH_3 into the bulk from the nitrate electroreduction, which is enhanced on the RCE surface. In addition, it can be observed that as the rotation rate rises from 600 to 1000 rpm, the maximum of the NH_3 accumulation appears in shorter times and has a steep depletion after 45, 30, and 15 min at 600, 800, and 1000 rpm, respectively. This abrupt depletion of NH_3 is explained by the increasing release of the generated NH_3 to the atmosphere at alkaline medium, since the volatilization of NH_3 is promoted according to Henry's law. The maximum values attained were 75%, 80%, and 76%, which dropped at the end of the electrolysis to 49%, 43%, and 33% at 600, 800, and 1000 rpm, respectively. On the other hand, at $\omega \leq 400$ rpm, a steady and lower accumulation of NH_3 attaining values of 49% and 54% at 300 and 400 rpm, respectively, was found due to the slower kinetics of the nitrate electroreduction leading to lower accumulations of NH_3 into the bulk. Moreover, the volatilization of the NH_3 at $\omega \leq 400$ was diminished by the hydrodynamics inside the RCE reactor, with final NH_3 values of 46% and 49% at 300 and 400 rpm, respectively. The increased release of N-species to the atmosphere as ω increases can be corroborated with the

profiles of total nitrogen over the electrolysis time. Fig. 7b confirms the significant influence of ω on the volatilization of the N-species, since total nitrogen content decays steadily throughout the electrolysis time, reaching values of 30%, 35%, 4%2, 46%, and 55% at 300, 400, 600, 800, and 1000 rpm, respectively.

Fig. 7c shows the EC values attained solely considering to the nitrate electroreduction according to Eq. (8). It is noticeable in that figure that, at t < 15 min, the lower values were attained at the higher rotation rates. Nonetheless, at t > 15 min, the trends show that higher rotation rates yield greater EC values. These results can be justified by the low residual nitrate concentration throughout the electrolysis, which also favors secondary reactions such as HER.

Fig. 8a highlights the influence of the initial nitrate concentration on its electroreduction profile. As the initial concentration of nitrate increased, its complete removal required longer time, reaching its total disappearance after ca. 20, 60, and 75 min at 10, 20, and 40 mM NO_3^-, respectively. The k_1-values determined from the slopes of Fig. 8b were 22.5×10^{-2}, 7.9×10^{-2}, and 4.6×10^{-2} min^{-1}, respectively. Although the process is mostly controlled by a mass transport regime, increasing the initial pollutant value in a highly efficient mass transport system like the RCE reactor resulted in a relatively slower nitrate removal process (i.e., lower k_1), although this entailed an enhanced overall nitrate removal rate. A first-order kinetic constant is not expected to depend on the concentration of the reactant when the electrolyses are performed at constant current (447 A m^{-2} in this case), but such k_1 decay was actually observed as the initial concentration of the electroactive species was increased. Note also that although the selected cathode material is proven to yield the total removal of nitrate even at high concentrations, other more electrocatalytic materials could be investigated to face the

sluggish kinetics of nitrate electroreduction [25]. It is especially important to highlight that the theoretical and experimental results showed a good agreement, evidencing the robustness of the proposed nitrate electroreduction model to predict the process behavior in an RCE reactor equipped with an AISI 1018-type steel cathode.

The NH_3 accumulation is shown in Fig. 9a. It is noticeable that as the NO_3^- initial concentration increased, it hindered the accumulation of NH_3 with maximum accumulation attained of 76%, 71%, and 48% at 20, 45, and 60 min, respectively, at each increasing nitrate concentration. Also, the relative volatilization of N-species was slowed down as the nitrate initial concentration increased, owing to higher absolute accumulation rates. The overall percentage of NH_3 remaining at the end of the electrolysis was 33%, 37%, and 32% at 10, 20, and 40 mM NO_3^-, respectively. The latter is confirmed in Fig. 9b because when the initial nitrate concentration increased, the volatilization of N-species was slower, reaching final TN removals of 55%, 52%, and 49% as the nitrate concentration was risen from 10 to 40 mM NO_3^-.

Furthermore, the EC values shown in Fig. 9c increase linearly through the electrolysis time, reaching values of 39.8, 40.0, and 39.8 Wh g^{-1} for the abatement of 99% of nitrate after 30, 60 and 120 min at 10, 20, and 40 mM NO_3^-, respectively.

5. Conclusions

The modeling and simulation of an electrochemical reactor equipped with an AISI 1018 carbon steel RCE used for nitrate electroreduction was performed successfully. The solution of the momentum equations gave rise to two Taylor vortices inside the RCE reactor due to the influence of the surrounding electrodes acting as deflectors and modifying the flow pattern, which created three distinct zones with a homogeneous velocity in each one.

Moreover, the solution of the mass transport equations yielded six zones where the concentration of nitrate decreased quickly, caused by the acceleration of the fluid by the anodes. It was also determined that the RCE had a homogeneous current distribution ($j_c/j_{c,AVE}$ ~ 1), showing a slight distribution deviation only when the cylinder was not directly facing a counter electrode. The model proposed was validated by adjusting the theoretical nitrate electroreduction with experimental results, reaching a good agreement between the two sets of data. Therefore, the model can replicate the behavior of the RCE reactor for electrochemical nitrate removal controlled by mass transport at different rotation rates (i.e., cathodic current values) of the RCE and different initial concentration values.

The fastest nitrate removal was achieved in a solution containing 10 mM NO_3^- + 500 mM K_2SO_4 at 1000 rpm and 25 °C, requiring 10 min for >90% removal with an EC of 14.3 Wh g^{-1}. Additionally, the final product detected in the electrolysis was ammonia, which favored the volatilization of the N-species in the bulk achieving the removal of 55% of the total nitrogen in the trial. The results obtained here show that electroreduction in an RCE reactor is a promising technology to address nitrate contamination, which can be further expanded to a single-step configuration to take a step forward into the real application.

Acknowledgments

Financial support from projects PID2019-109291RB-I00 (MCIN/AEI/10.13039/501100011033, Spain) and CIIC 025/2023 (University of Guanajuato, Mexico), as well as from FPI PhD scholarship awarded to R.O. (BES-2017-080095, MINECO, Spain) and postdoctoral scholarship awarded to O.M.C. (708693, CONACYT, Mexico), is kindly acknowledged.

References

[1] B. Singh, E. Caswell, Fertilizers and nitrate pollution of surface and ground water: an increasingly pervasive global problem, SN Appl. Sci. 3 (2021) 518. https://doi.org/10.1007/s42452-021-04521-8

[2] E. Abascal, L. Gómez-Coma, I. Ortiz, A. Ortiz, Global diagnosis of nitrate pollution in groundwater and review of removal technologies, Sci. Total Environ. 810 (2022) 152233. https://doi.org/10.1016/j.scitotenv.2021.152233

[3] S. Singh, A.G. Anil, V. Kumar, D. Kapoor, S. Subramanian, J. Singh, P.C. Ramamurthy, Nitrates in the environment: A critical review of their distribution, sensing techniques, ecological effects and remediation, Chemosphere 287 (2022) 131996. https://doi.org/10.1016/j.chemosphere.2021.131996

[4] O. Rahmati, A.N. Samani, N. Mahmoodi, M. Mahdavi, Assessment of the contribution of N-fertilizers to nitrate pollution of groundwater in western Iran (Case study: Ghorveh–Dehgelan aquifer), Water Qual. Expo. Health 7 (2015) 143-151. https://doi.org/10.1007/s12403-014-0135-5

[5] J. Nemčić-Jurec, A. Jazbec, Point source pollution and variability of nitrate concentrations in water from shallow aquifers, Appl. Water Sci. 7 (2017) 1337-1348. https://doi.org/10.1007/s13201-015-0369-9

[6] A. Menció, J. Mas-Pla, N. Otero, O. Regàs, M. Boy-Roura, R. Puig, J. Bach, C. Domènech, M. Zamorano, D. Brusi, A. Folch, Nitrate pollution of groundwater; all right…, but nothing else?, Sci. Total Environ. 539 (2016) 241-251. https://doi.org/10.1016/j.scitotenv.2015.08.151

[7] N. Adimalla, H. Qian, Groundwater chemistry, distribution and potential health risk appraisal of nitrate enriched groundwater: A case study from the semi-urban region of

South India, Ecotox. Environ. Safe. 207 (2021) 111277. https://doi.org/10.1016/j.ecoenv.2020.111277

[8] Y. Zhai, Y. Lei, J. Wu, Y. Teng, J. Wang, X. Zhao, X. Pan, Does the groundwater nitrate pollution in China pose a risk to human health? A critical review of published data, Environ. Sci. Pollut. Res. 24 (2017) 3640-3653. https://doi.org/10.1007/s11356-016-8088-9

[9] S.M.K. Alam, P. Li, M. Fida, Groundwater nitrate pollution due to excessive use of N-fertilizers in rural areas of Bangladesh: Pollution status, health risk, source contribution, and future impacts, Expos. Health (2023). https://doi.org/10.1007/s12403-023-00545-0

[10] Y. Fan, J. Zhuang, M. Essington, S. Jagadamma, J. Schwartz, J. Lee, Global significance of substrates for nitrate removal in denitrifying bioreactors revealed by meta-analysis, Eng. 21 (2023) 214-226. https://doi.org/10.1016/j.eng.2022.08.017

[11] Y. Pang, J. Wang, Various electron donors for biological nitrate removal: A review, Sci. Total Environ. 794 (2021) 148699. https://doi.org/10.1016/j.scitotenv.2021.148699

[12] Y. Liu, X. Zhang, J. Wang, A critical review of various adsorbents for selective removal of nitrate from water: Structure, performance and mechanism, Chemosphere 291 (2022) 132728. https://doi.org/10.1016/j.chemosphere.2021.132728

[13] S. Meng, Y. Ling, M. Yang, X. Zhao, A.I. Osman, A.H. Al-Muhtaseb, D.W. Rooney, P.S. Yap, Recent research progress of electrocatalytic reduction technology for nitrate wastewater: A review, J. Environ. Chem. Eng. 11 (2023) 109418. https://doi.org/10.1016/j.jece.2023.109418

[14] J. Theerthagiri, J. Park, H.T. Das, N. Rahamathulla, E.S.F. Cardoso, A.P. Murthy, G. Maia, D.V.N. Vo, M.Y. Choi, Electrocatalytic conversion of nitrate waste into ammonia:

a review, Environ. Chem. Lett, 20 (2022) 2929-2949. https://doi.org/10.1007/s10311-022-01469-y

[15] I. Katsounaros, On the assessment of electrocatalysts for nitrate reduction, Curr. Opinion Electrochem. 28 (2021) 100721. https://doi.org/10.1016/j.coelec.2021.100721

[16] R. Oriol, E. Brillas, P.L. Cabot, J.L. Cortina, I. Sirés, Paired electrochemical removal of nitrate and terbuthylazine pesticide from groundwater using mesh electrodes, Electrochim. Acta 383 (2021) 138354. https://doi.org/10.1016/j.electacta.2021.138354

[17] R. Oriol, M.P. Bernícola, E. Brillas, P.L. Cabot, I. Sirés, Paired electro-oxidation of insecticide imidacloprid and electrodenitrification in simulated and real water matrices, Electrochim. Acta 317 (2019) 753-765. https://doi.org/10.1016/j.electacta.2019.05.002

[18] J. Ding, W. Li, Q.L. Zhao, K. Wang, Z. Zheng, Y.Z. Gao, Electroreduction of nitrate in water: Role of cathode and cell configuration, Chem. Eng. J. 271 (2015) 252-259. https://doi.org/10.1016/j.cej.2015.03.001

[19] Z. Liu, C. Wang, C. Chen, C. Li, C. Guo, Selective electroreduction of nitrate to ammonia with high Faradaic efficiency on nanocrystalline silver, Electrochem. Commun. 131 (2021) 107121. https://doi.org/10.1016/j.elecom.2021.107121

[20] X. Zhang, Y. Wang, C. Liu, Y. Yu, S. Lu, B. Zhang, Recent advances in non-noble metal electrocatalysts for nitrate reduction, Chem. Eng. J. 403 (2021) 126269. https://doi.org/10.1016/j.cej.2020.126269

[21] J. Sun, S. Garg, J. Xie, C. Zhang, T.D. Waite, Electrochemical reduction of nitrate with simultaneous ammonia recovery using a flow cathode reactor, Environ. Sci. Technol. 56 (2022) 17298-17309. https://doi.org/10.1021/acs.est.2c06033

[22] O.M. Cornejo, M.F. Murrieta, L.F. Castañeda, J.L. Nava, Characterization of the reaction environment in flow reactors fitted with BDD electrodes for use in

621 electrochemical advanced oxidation processes: A critical review, Electrochim. Acta 331
622 (2020) 135373. https://doi.org/10.1016/j.electacta.2019.135373
623 [23] F.F. Rivera, T. Pérez, L.F. Castañeda, J.L. Nava, Mathematical modeling and simulation
624 of electrochemical reactors: A critical review, Chem. Eng. Sci. 239 (2021) 116622.
625 https://doi.org/10.1016/j.ces.2021.116622
626 [24] O. González Pérez, J.M. Bisang, Removal of nitrate using an activated rotating cylinder
627 electrode, Electrochim. Acta 194 (2016) 448-453.
628 https://doi.org/10.1016/j.electacta.2016.02.114
629 [25] R. Oriol, J.L. Nava, E. Brillas, I. Sirés, Diffusion-charge transfer characterization of a
630 rotating cylinder electrode reactor used for the complete electrocatalytic removal of
631 nitrate from water, J. Environ. Chem. Eng. 10 (2022) 108839.
632 https://doi.org/10.1016/j.jece.2022.108839
633 [26] J.R. Hernández-Tapia, J. Vazquez-Arenas, I. González, Electrochemical reactor with
634 rotating cylinder electrode for optimum electrochemical recovery of nickel from plating
635 rinsing effluents, J. Hazard. Mater. 262 (2013) 709-716.
636 https://doi.org/10.1016/j.jhazmat.2013.09.029
637 [27] J.L. Arredondo, F.F. Rivera, J.L. Nava, Silver recovery from an effluent generated by
638 plating industry using a rotating cylinder electrode (RCE), Electrochim. Acta 147 (2014)
639 337-342. https://doi.org/10.1016/j.electacta.2014.09.127
640 [28] J.A. Barragan, M. Tesillo-Perales, J.R. Alemán-Castro, E.R. Larios-Durán, E.P. Rivero,
641 Optimization of a rotating cylinder electrode electrochemical reactor for metal recovery:
642 An innovative approach and method combining CFD and response surface methodology,
643 Electrochim. Acta 435 (2022) 141335. https://doi.org/10.1016/j.electacta.2022.141335

644 [29] O.M. Cornejo, I. Sirés, J.L. Nava, Cathodic generation of hydrogen peroxide sustained
645 by electrolytic O_2 in a rotating cylinder electrode (RCE) reactor, Electrochim. Acta 404
646 (2022) 139621. https://doi.org/10.1016/j.electacta.2021.139621
647 [30] A.H. Abbar, R.H. Salman, A.S. Abbas, Studies of mass transfer at a spiral-wound woven
648 wire mesh rotating cylinder electrode, Chem. Eng. Process.: Process Intensif. 127 (2018)
649 10-16. https://doi.org/10.1016/j.cep.2018.03.013
650 [31] E.P. Rivero, M.R. Cruz-Díaz, F.J. Almazán-Ruiz, I. González, Modeling the effect of
651 non-ideal flow pattern on tertiary current distribution in a filter-press-type
652 electrochemical reactor for copper recovery, Chem. Eng. Res. Des. 100 (2015) 422-433.
653 https://doi.org/10.1016/j.cherd.2015.04.036
654 [32] J. Valentín-Reyes, J.L. Nava, Modeling of a novel cascade-type electrocoagulation
655 reactor using iron electrodes. Characterization of bubbling flow and coagulant dosage,
656 Chem. Eng. Process.: Process Intensif. 189 (2023) 109411.
657 https://doi.org/10.1016/j.cep.2023.109411
658 [33] M.F. Murrieta, J.L. Nava, Electrosynthesis of hypochlorous acid in a filter-press
659 electrolyzer and its modeling in dilute chloride solutions, J. Electroanal. Chem. 892
660 (2021) 115286. https://doi.org/10.1016/j.jelechem.2021.115286
661 [34] A.D. Villalobos-Lara, T. Pérez, A.R. Uribe, J.A. Alfaro-Ayala, J.J. Ramírez-Minguela,
662 J.I. Minchaca-Mojica, CFD simulation of biphasic flow, mass transport and current
663 distribution in a continuous rotating cylinder electrode reactor for electrocoagulation
664 process, J. Electroanal. Chem. 858 (2020) 113807.
665 https://doi.org/10.1016/j.jelechem.2019.113807
666 [35] E.P. Rivero, P. Granados, F.F. Rivera, M. Cruz, I. González, Mass transfer modeling
667 and simulation at a rotating cylinder electrode (RCE) reactor under turbulent flow for

668 copper recovery, Chem. Eng. Sci. 65 (2010) 3042-3049.
669 https://doi.org/10.1016/j.ces.2010.01.030
670 [36] M. Rosales, J.L. Nava, Simulations of turbulent flow, mass transport, and tertiary current
671 distribution on the cathode of a rotating cylinder electrode reactor in continuous
672 operation mode during silver deposition, J. Electrochem. Soc. 164 (2017) E3345-E3353.
673 https://iopscience.iop.org/article/10.1149/2.0351711jes
674 [37] H.K Versteeg, W. Malalasekera, An Introduction to Computational Fluid Dynamics:
675 The Finite Volume Method, Second ed., Prentice Hall, London, 1995.
676 [38] A.D. Villalobos-Lara, B. Castillo, F.F. Rivera, J. Vázquez-Arenas, Model accounting
677 for the Cr(III) electroprecipitation kinetics in an electrochemical reactor based on CFD
678 and mass transport contributions, J. Electroanal. Chem. 928 (2023) 117057.
679 https://doi.org/10.1016/j.jelechem.2022.117057
680 [39] T. Pérez, J.L. Nava, Numerical simulation of the primary, secondary and tertiary current
681 distributions on the cathode of a rotating cylinder electrode cell. Influence of using plates
682 and a concentric cylinder as counter electrodes. J. Electroanal. Chem. 719 (2014) 106-
683 112.

Figure captions

Figure 1. (a) Isometric view of the simulation domain with the field of element quality in the mesh. (b) Upper view of the simulation domain with the position of each electrode. (c) Mesh sensitivity analysis performed by determining the nitrate concentration at 5 min of simulation time. Simulation parameters: 10 mM NO_3^- at 25 °C, operating and 300 rpm.

Figure 2. (a) Velocity field inside the RCE reactor in the *xy*-plane at $z = 4.0$ cm. (b) Isometric view of the velocity field on all boundaries of the RCE reactor. (c) Five levels of isosurface within the RCE reactor. Simulation parameters: water at 25 °C, operating at 300 rpm.

Figure 3. (a)Set of 50 streamlines and plane cut of the RCE reactor. (b) Velocity profiles evaluated between an anode and the RCE, at two heights (z): 2.9 and 4.0 cm. Simulation parameters: water at 25 °C, operating at 300 rpm.

Figure 4. Influence of the rotation rate on the nitrate concentration field within the RCE reactor: (a) 300 rpm and (b) 1000 rpm. Concentration profile from the anode to the RCE, at (c) 300 rpm and (d) 1000 rpm. Simulation parameters: 10 mM NO_3^- at 25 °C. Data obtained at 5 s of simulation time.

Figure 5. (a) Normalized current density distribution field on the RCE and the six anodes. The same simulation parameters as those of Fig. 4 at 300 rpm were used. (b) Normalized current density distribution along the RCE normalized arc length at $z = 8.0$ cm, at different rotation rates.

Figure 6. Influence of the rotation rate on (a) nitrate electroreduction and (b) the resulting first-order kinetics. Experimental results and simulations are compared. Solution: 10 mM

705 KNO_3 + 500 mM K_2SO_4 at 25 °C. The applied densities are linked to each rotation rate (see
706 Table 1) to guarantee mass transport control.

707 **Figure 7.** Influence of the rotation rate on (a) normalized ammonia accumulation, (b)
708 normalized total nitrogen depletion, and (c) energy consumption during the nitrate
709 electroreduction process. The same experimental parameters as in Fig. 6 were used.

710 **Figure 8.** Influence of nitrate initial concentration on (a) normalized nitrate depletion and (b)
711 the resulting first-order kinetics. Experimental results and simulations are compared. All
712 electrolyses were made in 500 mM K_2SO_4, at 25 °C and 1000 rpm (i.e., j_L = 447 A m^{-2}).

713 **Figure 9.** Influence of nitrate initial concentration on (a) normalized ammonia accumulation,
714 (b) normalized total nitrogen depletion, and (c) energy consumption during the nitrate
715 electroreduction process. The same experimental parameters as in Fig. 8 were used.

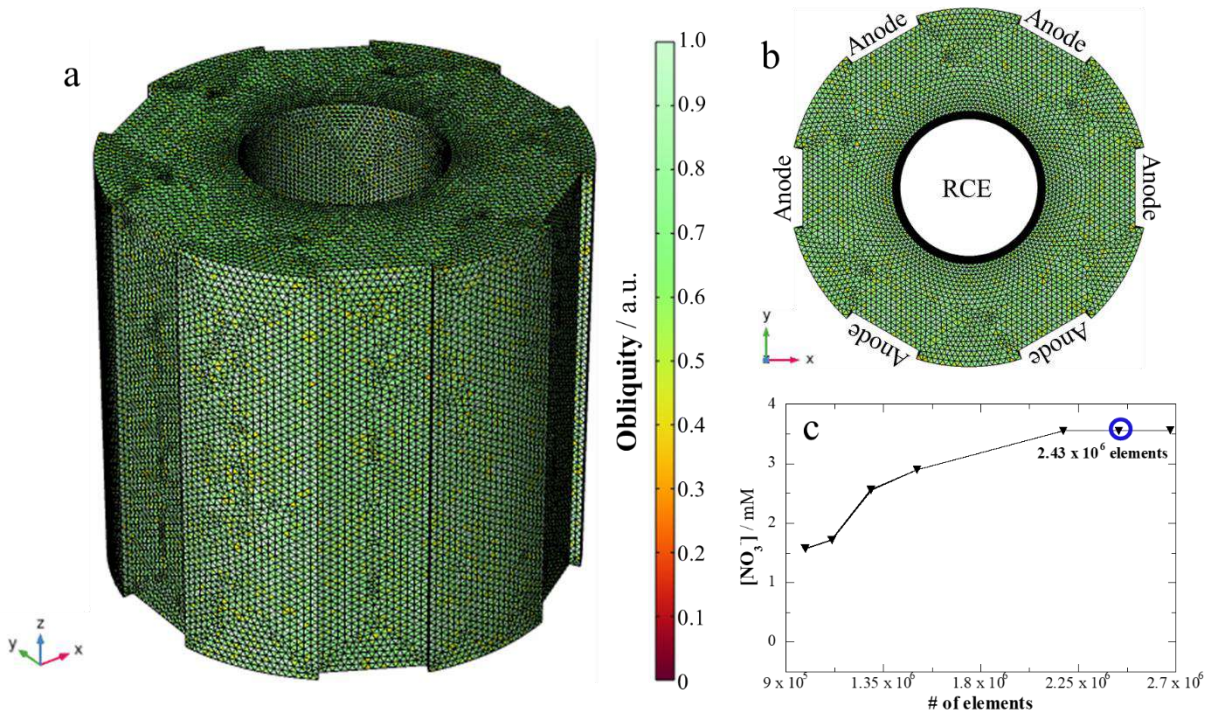

716

717

718 **Figure 1**

719

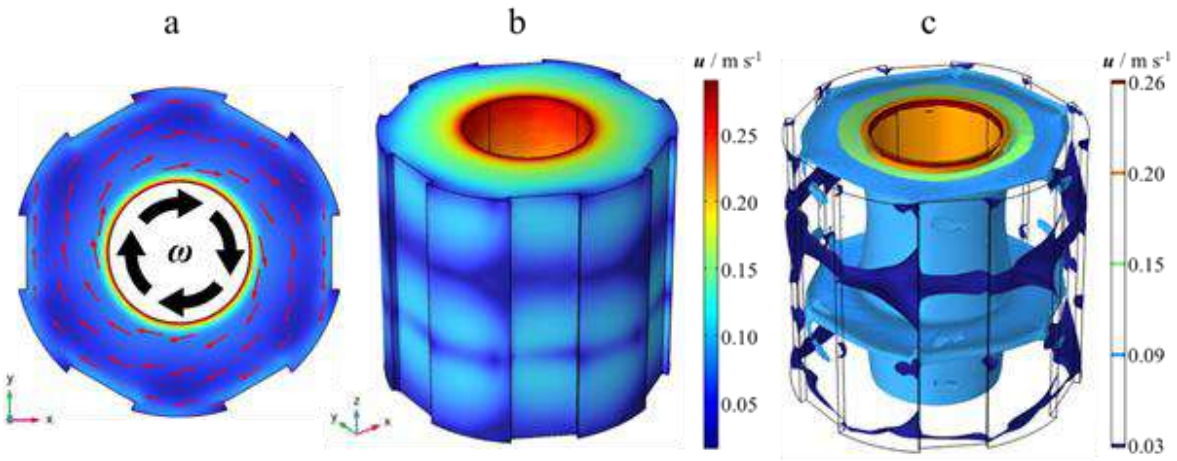

720

721 **Figure 2**

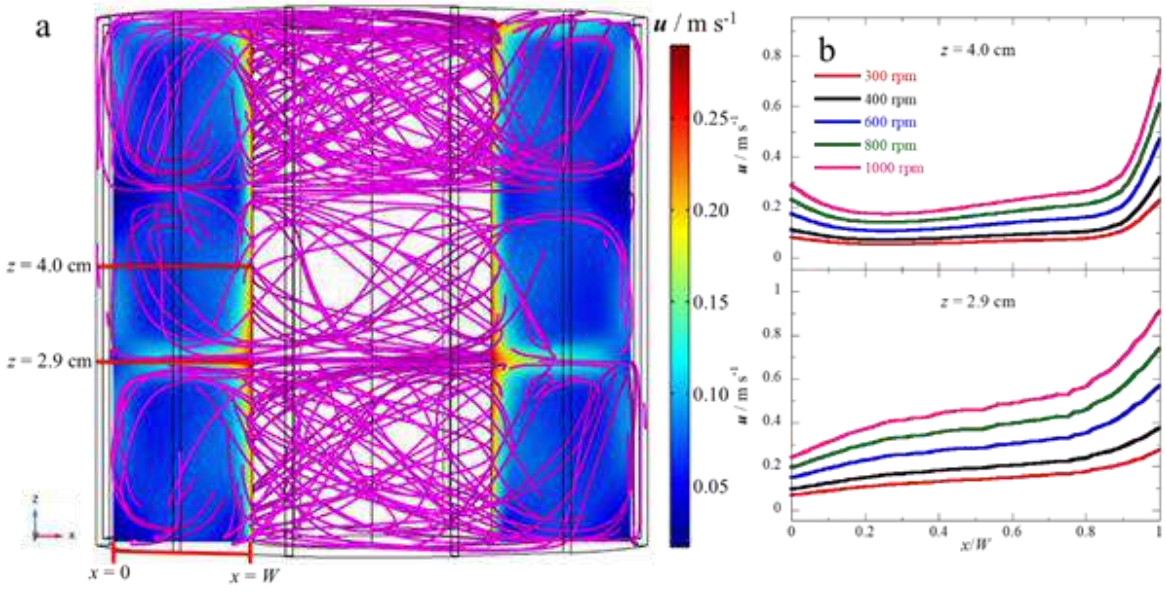

722

723

724 **Figure 3**

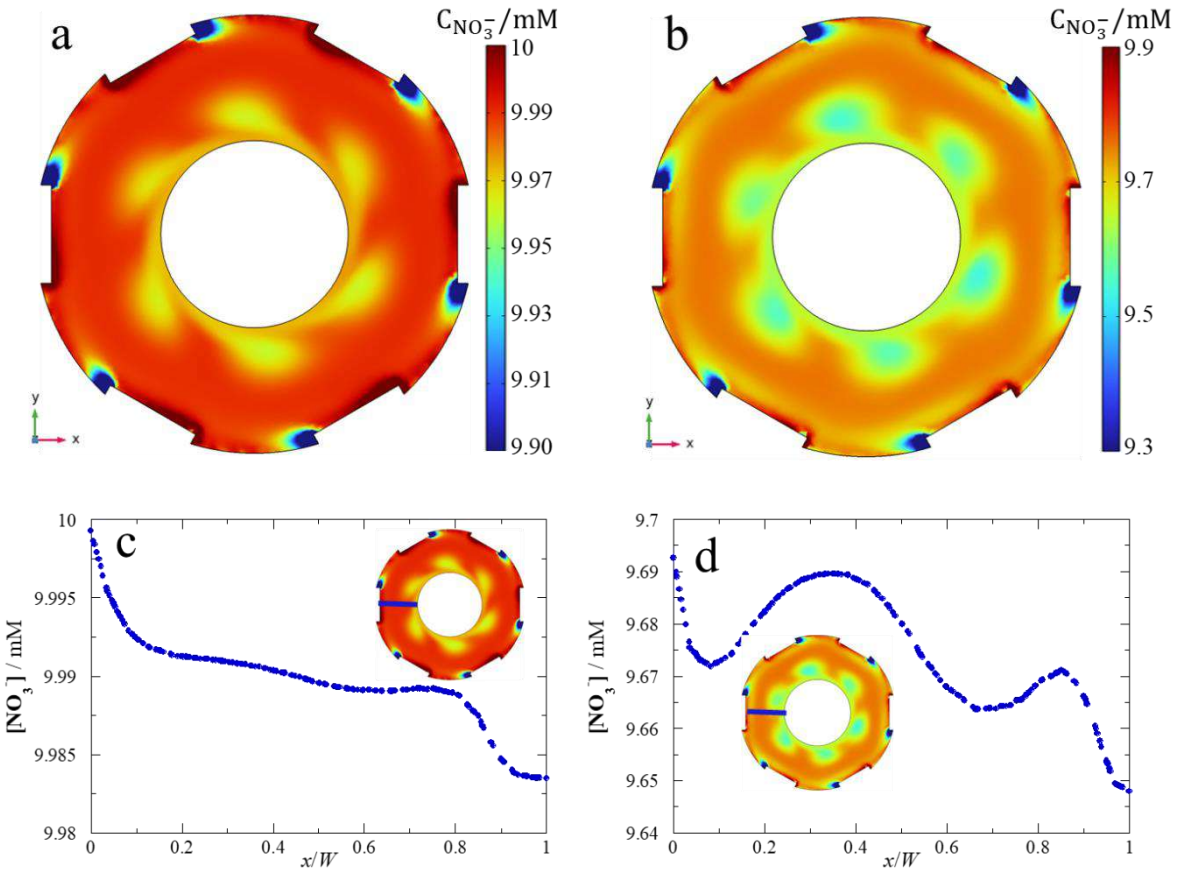

725

726

727 **Figure 4**

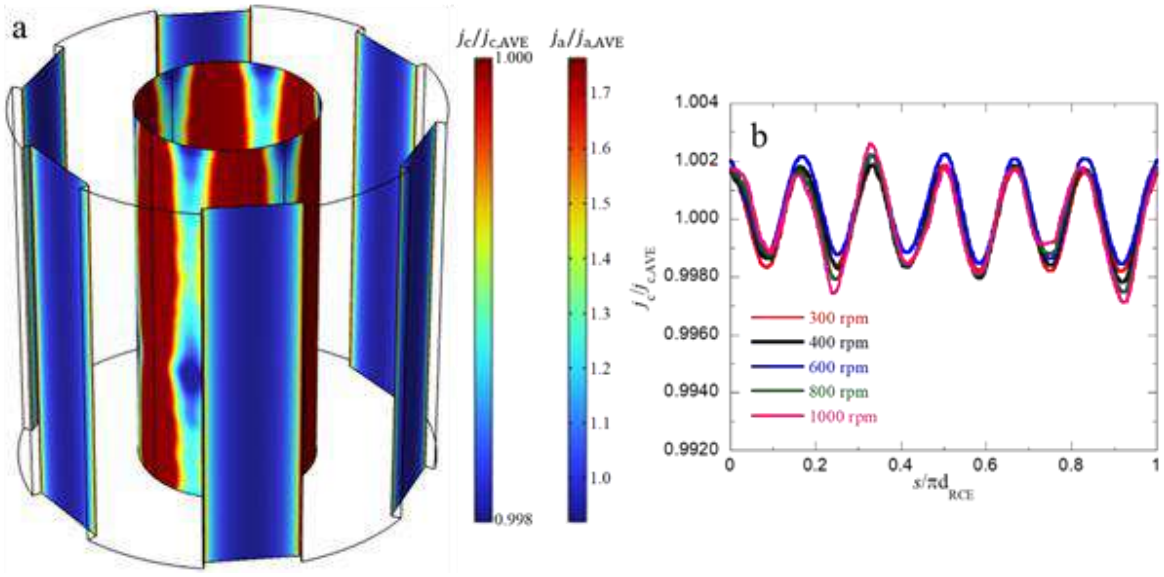

728

729

730 **Figure 5**

731

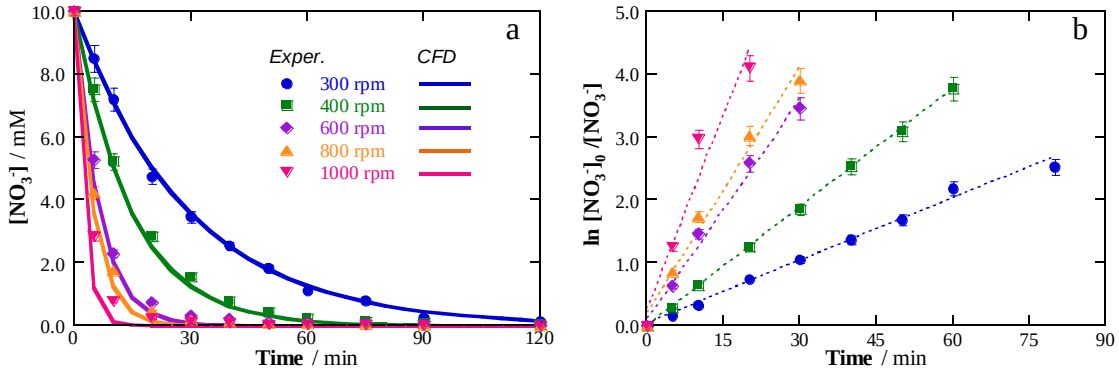

732

733 **Figure 6**

734

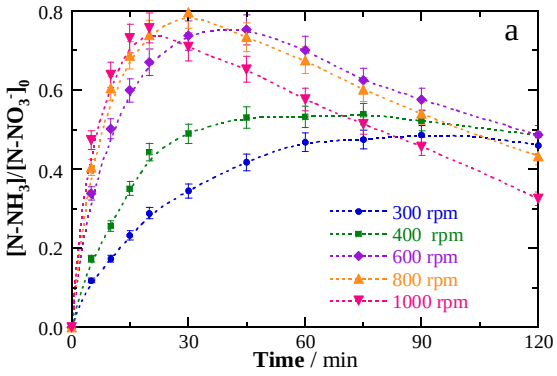

735

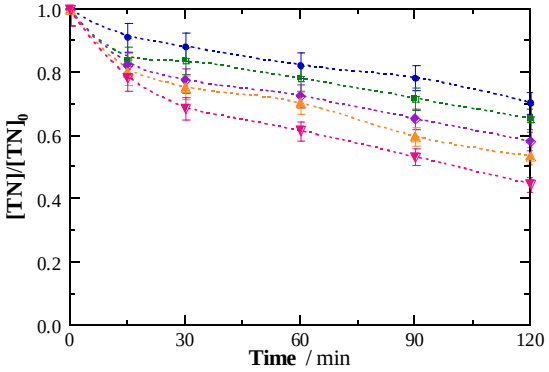

736

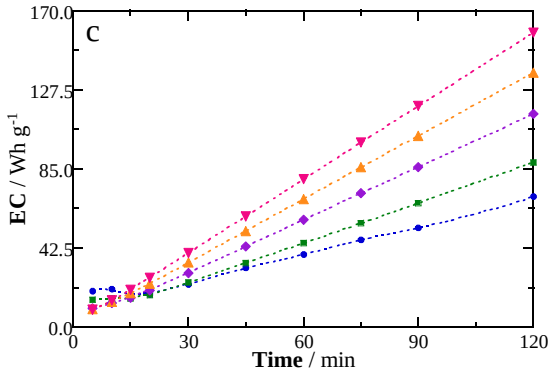

737

738 **Figure 7**

739

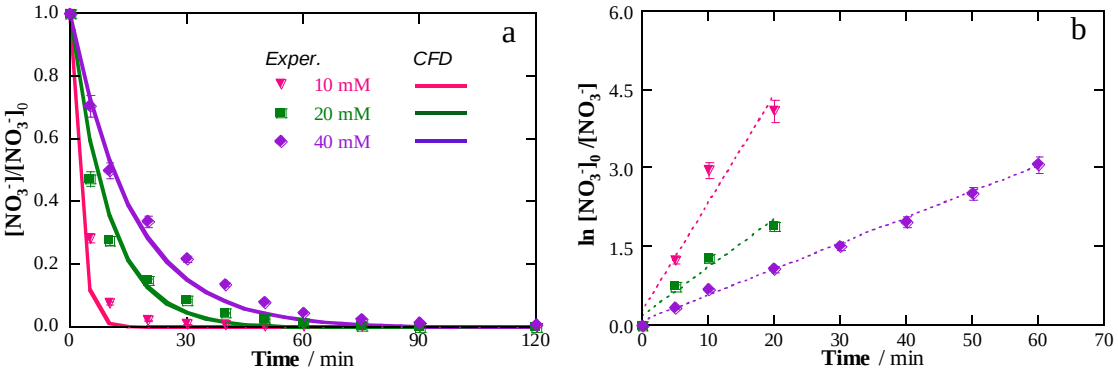

740

741 **Figure 8**

742

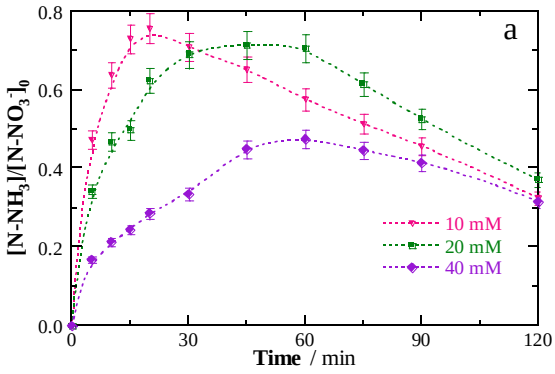

743

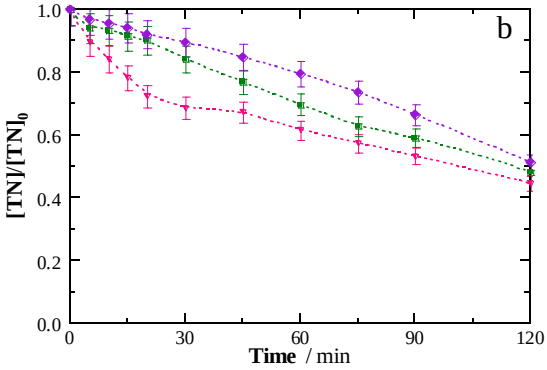

744

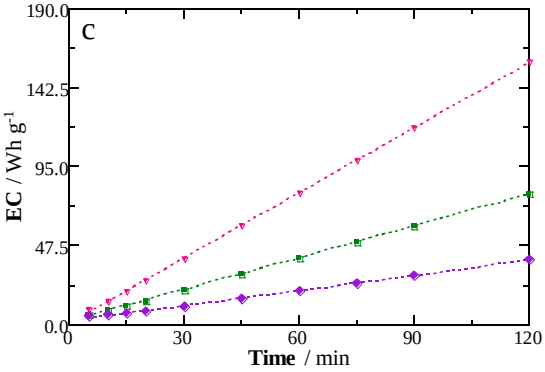

745 **Figure 9**

746 **Table 1**

747 Peripheral velocities, Reynolds numbers and limiting current densities (calculated through
748 Eq. (6)) for each rotation rate.

ω / rpm	U / cm s^{-1}	Re	j_L / A m^{-2}
300	59.7	25775	257
400	79.6	34367	293
600	119.4	51550	353
800	159.2	68733	403
1000	198.9	85873	447

749

Table 2

Electrolyte properties and kinetic parameters employed in the simulation of nitrate electroreduction in the RCE reactor.

Parameter	**Symbol**	**Value**	**Unit**
Fluid density	ρ	1000	kg m^{-3}
Fluid dynamic viscosity	μ	0.001	Pa s
Fluid kinematic viscosity	ν	1×10^{-6}	m^2 s^{-1}
Solution conductivity	σ	5.0	S m^{-1}
Nitrate diffusion coefficient	$D_{NO_3^-}$	1.9×10^{-13}	m^2 s^{-1}
Cathodic open circuit potential	OCP_c	-0.63	V (vs. SHE)
Anodic open circuit potential	OCP_a	0.68	V (vs. SHE)
Nitrate exchange current density	j_{0,NO_3^-}	0.67	A m^{-2}
HER exchange current density	j_{0,H_2}	0.18	A m^{-2}
OER exchange current density	$j_{0,OER}$	$5.6\ 10^{-7}$	A m^{-2}
Nitrate Tafel slope	$b_{NO_3^-}$	0.217	V
HER Tafel slope	b_{HER}	0.127	V
OER Tafel slope	b_{OER}	0.069	V

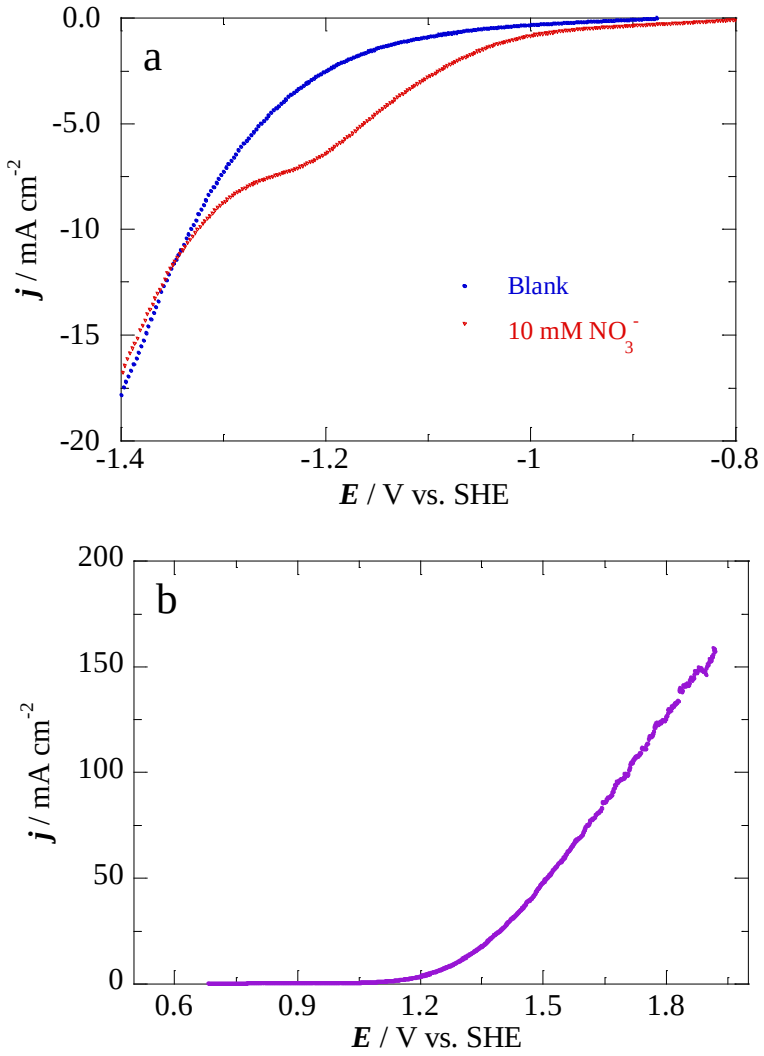

Fig. S1. Linear sweep voltammograms of: (a) Nitrate reduction obtained using 400 mL of a 500 mM K_2SO_4 solution with and without 10 mM KNO_3 at 25 ºC, using AISI 1018 steel as working electrode, sweeping from the OCP at a scan rate of 5 mV s^{-1}. The 3-electrode cell comprised a Pt rod and Ag|AgCl (3 M KCl) as counter and reference electrodes, respectively. (b) O_2 evolution obtained under the same conditions using the solution without NO_3^- and a Ti|IrO_2-based electrode, sweeping from 0.68 V (vs. SHE).

CHAPTER 5

CONCLUSIONS AND PERSPECTIVES

CHAPTER 5. Conclusions and perspectives

5.1. Conclusions

As stated in Chapter 2, the main goal of this Thesis was to investigate the electrochemical removal of pesticides and nitrate from actual GW. Considering each general objective (GO) and specific goal (SG) fulfilled along the five sections of Chapter 4, several conclusions have can be drawn:

Regarding Chapter 4.1 (GO1 and SG1-4):

- The SPE cell is a potentially viable device to electrolyze low-conductivity water matrices, allowing the treatment of conditioned GW. Moreover, an effective GW softening pre-treatment has been devised, based on the valorisation of industrial fly ashes, which led to the decrease of GW hardness by 95%; this allowed diminishing and stabilizing the E_{cell} by preventing cathode fouling.
- The pesticide IMC could be removed by EO with a BDD anode thanks to the high oxidation power of the physisorbed $^{\bullet}OH$. The pseudo first-order kinetics for its decay and the mineralization degree were enhanced by applying a higher current, achieving high TOC removals up to 87%. In contrast, the greatest MCE values were reached operating at low current. The anodic oxidation of IMC competes with that of chloride ion, resulting in a lower MCE due to the partial scavenging of the physisorbed $^{\bullet}OH$ with chloride and the generated active chlorine species. In turn, active chlorine acts as mediator for homogeneous IMC oxidation in the bulk, thereby yielding toxic chlorate and perchlorate ions.
- The heteroatoms contained in the IMC structure were converted to anionic species during the mineralization process. Nitrate and chloride were generated from the nitrogen and chlorine atoms, respectively. Chloride was further oxidized to active chlorine, chlorate and perchlorate.
- The ultrapure water matrix showed the fastest IMC and TOC removals, with the highest MCE. The presence of NOM in GW slowed down the IMC degradation, since that matter reacted with the main oxidants, $^{\bullet}OH$ and active chlorine species. The scavenging role of NOM increased as the pesticide concentration

decreased, giving rise to a less efficient treatment. The IMC degradation rates under comparable conditions depended on the employed water matrix, decreasing in the order: ultrapure water > synthetic matrix > softened GW.

Regarding Chapter 4.2 and 4.3 (GO2 and SG5-11):

- The BDD anode showed a much better performance than the IrO_2- and RuO_2-based ones for the complete degradation of IMC and TBZE pesticides, yielding high mineralization degrees. However, the greater oxidation power of this anode favoured the conversion of active chlorine to chlorate and a large amount of perchlorate. In contrast, the RuO_2-based DSA showed high activity to accumulate active chlorine species with low conversion to chlorate.
- For nitrate ER using a suitable cathode material like mild steel (DC01) in synthetic water matrices, the electrolyte composition (i.e., presence and absence of chloride) had a clear effect on the speciation of the N-containing compounds accumulated in solution and on the generation of volatile N-containing compounds. This was influenced by the anode material employed and its activity and selectivity to oxidize the chlorinated species, since the resulting compounds may react with nitrate ER by-products. In the absence of such chlorine species, the anode may have an important role depending on its activity for re-oxidizing nitrate degradation by-products back to nitrate again, decreasing the global nitrate removal rate. A high ratio of active chlorine species to N-containing by-products like ammonia caused the re-oxidation of the latter back to nitrate in the bulk.
- The initial pH had a strong effect on the nitrate ER due to the different ability of the system to re-oxidize nitrate ER by-products back to nitrate in the absence of chloride. In the presence of this anion, the speciation of the active chlorine, which depends on pH, varies its reactivity with the N-containing by-products, leading to different speciation of the N-containing volatile compounds or re-oxidized N-containing by-products.
- The simultaneous removal of nitrate and organics had a slightly positive effect on the former due to the lower anodic re-oxidation of N-containing by-products. However, the generation of small organic molecules slightly interfered in the

nitrate ER. The nitrogen heteroatoms of the pesticide molecules ended up in their maximum oxidation state, i.e., nitrate, decelerating the global nitrate removal.

- The NOM in actual GW inhibited the electrochemical removal of the pesticides selected as model compounds and became competitor in the mineralization of their intermediate by-products.
- The precipitation of calcium and magnesium as carbonates and hydroxides on the cathode surface blocked its catalytic activity for nitrate ER; moreover, this phenomenon caused an increase in E_{cell} that led to a higher energy consumption with its consequent increasing cost.
- The degradation pathways for the EO treatment of TBZE and IMC, which included the primary by-products detected with the powerful BDD anode, have been proposed.
- An ion-exchange resin based on quaternary amines allowed the reduction of chlorate and perchlorate anions concentrations down to acceptable levels, releasing chloride into the medium.

Regarding Chapter 4.4 (GO3 and SG12-14):

- Iron-based materials like mild steels (DC01) were proven suitable for nitrate ER through a complex heterogeneous mechanism involving $^{\bullet}H$ as reductant. Conversely, AISI 316 stainless steel did not show any activity for nitrate ER, which can be correlated with its ability to promote the HER.
- The K-L analysis using an RDE allowed determining the number of electrons (n = 8) transferred during nitrate ER at high cathode potentials, in good agreement with the complete reduction of nitrate to ammonia.
- The study of nitrate removal kinetics allowed determining the k_1 and k_h values in the absence of migration using an RCE reactor at different ω values of the central cylinder and E_{cath}. In combination with the fundamental electrochemical characterization of the reaction over RDE made of the same material, it was possible to fully characterize the mass transport in the diffusion-convection system by determining the corresponding k_m values.

- The nitrate removal in RCE reactor was controlled by a mixed regime. The determination of η from *Da* allowed quantifying whether the system was controlled by mass transport or a charge transfer, depending on ω and E_{cath}.
- The electrochemical nitrate removal kinetics was improved by lowering the nitrate transport number because of the minimized migration towards the anode.
- The combination of the results obtained by studying the NRR and the nitrate ER at a mild steel RDE and RCE allowed the full characterization of the diffusion-convection mass transport at the reactor, thereby being feasible to establish the following correlation: $Sh = 0.70Re^{0.46}Sc^{0.356}$. This correlation will be useful for the future scale-up of the RCE reactor for electrochemical nitrate removal following the methodology described in this work. The behaviour of an analogous reactor employing a different cathode material could then be easily predicted.

Regarding Chapter 4.5 (GO4 and SG15-16):

- A model for nitrate ER in an RCE reactor was developed and further solved and simulated by CFD using a multiphysics software. Although the velocity field changed with the different applied ω, the hydrodynamic patters remained constant, showing two Taylor vortices. Nitrate abatement agreed with a first-order kinetics, with a strong dependence of the charge transfer reaction. The current distribution at the RCE was homogeneous, with a slightly positive or negative deviation depending on the relative position of the anodes.
- The model was validated by comparing the simulations at different current and ω values with the corresponding experimental nitrate decay profiles, resulting in an excellent overlapping of the concentration trends.

5.2. Perspectives

The imperious need of incorporating a softening pre-treatment method to decrease the content of alkaline-earth cations, as well as a simple post-treatment in order to remove undesired by-products like chlorate and perchlorate, has been discussed in this Thesis. Alternative or complementary pre- and post-treatments could be assessed to increase the viability of the electrochemical step.

Although the nitrogen chemistry is complex and may be sensitive to the composition of the treated effluents, it is clear that some ions like chloride may be used for reaching the chlorination breaking point by the generation of active chlorine species on the anode surface by EO, thus removing soluble N-containing compounds. Nevertheless, the electrochemical characterization of the cathode materials employed for nitrate ER is necessary to be able to propose a viable technology for GW remediation. ER may be combined with other technologies in order to obtain freshwater from GW polluted by nitrate employing a hybrid ER/EO technology. The deep understanding of the nitrate ER mechanism and the search of new electrocatalysts with high activity and selectivity towards N_2, NH_3 or both products, with good corrosion resistance, is mandatory for the scale-up of the RCE reactor.

This work is a clear example of how different technologies can be combined to take advantage of their synergies, being possible to remove pollutants of different nature due to their specific reactivity at the same time. The integration of EO and ER in a single unit allows reducing the operation cost because of the increased efficiency of the system. The hybrid EO/ER technology to remove nitrate from GW using the RCE reactor has been carried out, although the results have not been included in this Thesis. Those results serve to stimulate the future investigation of simultaneous removal of organic compounds and nitrate in the RCE reactor.

It would also be interesting to evaluate the performance of the RCE reactor in continuous operation mode, aiming at demonstrating that it is possible to provide a continuous supply of freshwater that meets the WHO standards in terms of nitrate content. Some studies with this RCE configuration have been initiated in our research group.

CFD is confirmed as a great tool to simulate, when properly modelled, the outcome of an electrochemical reactor. This Thesis provides the mathematical model for nitrate ER with some requirements: high conductivity to disregard the negative transport by migration; use of an electrocatalyst with a clear RDS; and absence of homogeneous reactions such as re-oxidation by active chlorine species. This complexity could be further added to the existing model in order to widen its applicability.

The electrochemical GW treatment should be carried out ensuring the highest current efficiency and lowest energy consumption to make it viable in practice. Coupling to renewable energy sources would be of interest to determine the operation costs of a scaled-up system. A complete system for GW treatment should be modular, including pre- and post-treatment units, both to condition the raw GW and to remove potentially toxic by-products.

References

[1] P. H. Gleick, Water in crisis: A guide to the world's fresh water resources (Oxford University Press, 1993).

[2] Groundwater: Information on Earth's water. https://www.ngwa.org/what-is-groundwater/About-groundwater/information-on-earths-water (accessed June 18, 2023).

[3] Water is found everywhere on earth, so why is it important? https://www.australianenvironmentaleducation.com.au/education-resources/what-is-water/ (accessed June 18, 2023).

[4] European Comission, Groundwater protection in Europe: the new groundwater directive: consolidating the EU regulatory framework. (2008). https://ec.europa.eu/environment/water/water-framework/groundwater/pdf/brochure/en.pdf (accessed January 9, 2023).

[5] IGRAC, International Groundwater Resources Assesment Centre. (2017). https://www.un-igrac.org/ (accessed January 11, 2023).

[6] N. B. Bhatti, A. A. Siyal, A. L. Qureshi, G. S. Solangi, N. A. Memon, I. A. Bhatti, Impact of Small Dam's Construction on Groundwater Quality and Level Using Water Quality Index (WQI) and GIS: Nagarparkar Area of Sindh, Pakistan. *Hum Ecol Risk Assess*, 26 (**2020**) 2586–2607. https://doi.org/10.1080/10807039.2019.1674634

[7] Ş. Arslan, Ç. Yücel, S. S. Çallı, M. Çelik, Assessment of Heavy Metal Pollution in the Groundwater of the Northern Develi Closed Basin, Kayseri, Turkey. *Bull Environ Contam Toxicol*, 99 (**2017**) 244–252. https://doi.org/10.1007/s00128-017-2119-1

[8] World Health Organization, Drinking-water. (2022). https://www.who.int/news-room/fact-sheets/detail/drinking-water (accessed January 10, 2023).

[9] N. Mancosu, R. L. Snyder, G. Kyriakakis, D. Spano, Water Scarcity and Future Challenges for Food Production. *Water*, 7 (**2015**) 975–992. https://doi.org/10.3390/w7030975

[10] C. J. Vörösmarty, P. B. McIntyre, M. O. Gessner, D. Dudgeon, A. Prusevich, P. Green, S. Glidden, S. E. Bunn, C. A. Sullivan, C. R. Liermann, P. M. Davies, Global Threats to Human Water Security and River Biodiversity. *Nature*, 467 (**2010**) 555–561. https://doi.org/10.1038/nature09440

[11] Food and Agriculture Organization of the United Nations, Coping with Water Scarcity: An action framework for agriculture and food security (Rome, 2012). https://doi.org/10.1097/00010694-199203000-00010

[12] World Health Organization, Guidelines for drinking-water quality, 4th Ed (2022).

[13] United Nations Sustainable Development Goals. https://sdgs.un.org/ (2023).

[14] UNESCO, Groundwater: Making the invisible visible in 2022 and beyond. https://www.unesco.org/en/articles/groundwater-making-invisible-visible-2022-and-beyond (accessed January 10, 2023).

[15] The World Bank, Annual freshwater withdrawals. (2019). https://data.worldbank.org/indicator/ (accessed January 11, 2023).

[16] J. Lewandowski, K. Meinikmann, S. Krause, Groundwater–Surface Water Interactions: Recent Advances and Interdisciplinary Challenges. *Water*, 12 (**2020**) 1–7. https://doi.org/https://doi.org/10.3390/w12010296

[17] International Atomic Energy Agency, Groundwater. (2013). https://www.iaea.org/topics/groundwater (accessed January 5, 2023).

[18] B. M. Saalidong, S. A. Aram, S. Otu, P. O. Lartey, Examining the Dynamics of the Relationship between Water pH and other Water Quality Parameters in Ground and Surface Water Systems. *PLoS One*, 17 (**2022**) e0262117. https://doi.org/10.1371/journal.pone.0262117

[19] P. Li, D. Karunanidhi, T. Subramani, K. Srinivasamoorthy, Sources and Consequences of Groundwater Contamination. *Arch. Environ. Contam. Toxicol.*, 80 (**2021**) 1–10. https://doi.org/10.1007/s00244-020-00805-z/figures/2

[20] M. Mon, R. Bruno, J. Ferrando-Soria, D. Armentano, E. Pardo, Metal–organic Framework Technologies for Water Remediation: towards a Sustainable Ecosystem. *J. Mater. Chem. A.*, 6 (**2018**) 4912–4947.

https://doi.org/10.1039/c8ta00264a

[21] B. J. Selck, G. T. Carling, S. M. Kirby, N. C. Hansen, B. R. Bickmore, D. G. Tingey, K. Rey, J. Wallace, J. L. Jordan, Investigating Anthropogenic and Geogenic Sources of Groundwater Contamination in a Semi-Arid Alluvial Basin, Goshen Valley, UT, USA. *Water Air Soil Pollut*, 229 (**2018**) 186.

https://doi.org/10.1007/s11270-018-3839-5

[22] T. H. Goodsell, G. T. Carling, Z. T. Aanderud, S. T. Nelson, D. P. Fernandez, D. G. Tingey, Thermal Groundwater Contributions of Arsenic and other Trace Elements to the Middle Provo River, Utah, USA. *Environ. Earth Sci.*, 76 (**2017**) 1–12.

https://doi.org/10.1007/s12665-017-6594-9

[23] S. Savci, An Agricultural Pollutant: Chemical Fertilizer. *International Journal of Environmental Science and Development*, 3 (**2012**) 73–80.

https://doi.org/10.7763/ijesd.2012.v3.191.

[24] C. Giraldez, G. Fox, An Economic Analysis of Groundwater Contamination from Agricultural Nitrate Emissions in Southern Ontario. *Canadian Journal of Agricultural Economics/Revue canadienne d'agroeconomie*, 43 (**1995**) 387–402.

https://doi.org/10.1111/j.1744-7976.1995.tb00130.x

[25] A. H. Mahvi, J. Nouri, A. A. Babaei, & R. Nabizadeh, Agricultural Activities Impact on Groundwater Nitrate Pollution. *Int J Environ Sci Technol (Tehran)*, 2 (**2005**) 41–47.

https://doi.org/https://doi-org.sire.ub.edu/10.1007/bf03325856

[26] H. R. Powley, H. H. Dürr, A. T. Lima, M. D. Krom, & P. Van Cappellen, Direct Discharges of Domestic Wastewater are a Major Source of Phosphorus and Nitrogen to the Mediterranean Sea. *Environ. Sci. Technol.*, 50 (**2016**) 8722–8730.

https://doi.org/10.1021/acs.est.6b01742

[27] BOE-A-2001-14276 Real Decreto Legislativo 1/2001, de 20 de julio, por el que se aprueba el texto refundido de la Ley de Aguas.

https://www.boe.es/eli/es/rdlg/2001/07/20/1/con (accessed June 18, 2023).

[28] Hydrographic demarcations in Spain. https://www.miteco.gob.es/es/agua/temas/estado-y-calidad-de-las-aguas/tabla1-masas-de-agua-subterranea-825-marco_tcm30-527535.jpg (accessed June 18, 2023).

[29] Masas de agua declaradas en riesgo. https://www.miteco.gob.es/es/agua/temas/estado-y-calidad-de-las-aguas/aguas-subterraneas/masas-de-agua-declaradas-en-riesgo/ (accessed June 18, 2023).

[30] Acuíferos al límite: España daña gravemente sus reservas subterráneas de agua. https://especiales.datadista.com/medioambiente/acuiferos-sobrexplotados-contaminados-espana/ (accessed June 18, 2023).

[31] J. E. Casida, Neonicotinoids and Other Insect Nicotinic Receptor Competitive Modulators: Progress and Prospects. *Annu. Rev. Entomol.*, 63 (**2018**) 125–144. https://doi.org/10.1146/annurev-ento-020117-043042

[32] M. Ihara, K. Matsuda, Neonicotinoids: Molecular Mechanisms of Action, Insights into Resistance and Impact on Pollinators. *Curr. Opin. Insect. Sci.*, 30 (**2018**) 86–92. https://doi.org/10.1016/j.cois.2018.09.009

[33] M. L. Hladik, S. Bradbury, L. A. Schulte, M. Helmers, C. Witte, D. W. Kolpin, J. D. Garrett, M. Harris, Neonicotinoid Insecticide Removal by Prairie Strips in Row-cropped Watersheds with Historical Seed Coating Use. *Agric Ecosyst Environ*, 241 (**2017**) 160–167. https://doi.org/10.1016/j.agee.2017.03.015

[34] E. Herrero-Hernández, M. S. Rodríguez-Cruz, E. Pose-Juan, S. Sánchez-González, M. S. Andrades, M. J. Sánchez-Martín, Seasonal Distribution of Herbicide and Insecticide Residues in the Water Resources of the Vineyard Region of La Rioja (Spain). *Sci. Total Environ.*, 609 (**2017**) 161–171. https://doi.org/10.1016/j.scitotenv.2017.07.113

[35] Yamamoto Izuru, Nicotinoid Insecticides and the Nicotinic Acetylcholine Receptor (Springer Japan, 1999). https://doi.org/10.1007/978-4-431-67933-2

[36] S. Kagabu, K. Yokoyama, K. Iwaya, M. Tanaka, Imidacloprid and Related Compounds: Structure and Water Solubility of N-Alkyl Derivatives of Imidacloprid. *Biosci. Biotechnol. Biochem.*, 62 (**1998**) 1216–1224.

https://doi.org/10.1271/bbb.62.1216

[37] P. Gautam S. Kumar Dubey, Biodegradation of imidacloprid: Molecular and Kinetic Analysis. *Bioresour. Technol.*, 350 (**2022**) 126915.

https://doi.org/10.1016/j.biortech.2022.126915

[38] A. M. Sadaria, R. Sutton, K. D. Moran, J. Teerlink, J. V. Brown, R. U. Halden, Passage of Fiproles and Imidacloprid from Urban Pest Control Uses Through Wastewater Treatment Plants in Northern California, USA. *Environ. Toxicol. Chem.*, 36 (**2017**) 1473–1482.

https://doi.org/10.1002/etc.3673

[39] C. A. Hallmann, R. P. B. Foppen, C. A. M. van Turnhout, H. de Kroon, E. Jongejans, Declines in Insectivorous Birds Are Associated with High Neonicotinoid Concentrations. *Nature*, 511 (**2014**) 341–343.

https://doi.org/10.1038/nature13531

[40] Conclusion on the Peer Review of the Pesticide Risk Assessment of the Active Substance Terbuthylazine. *EFSA Journal*, 9 (**2011**) 1969.

https://doi.org/10.2903/j.efsa.2011.1969

[41] European Comission, First Watch List for Emerging Water Pollutants.

https://ec.europa.eu/jrc/en/news/first-watch-list-emerging-water-pollutants (accessed June 7, 2018).

[42] J. C. G. Sousa, A. R. Ribeiro, M. O. Barbosa, M. F. R. Pereira, A. M. T. Silva, A Review on Environmental Monitoring of Water Organic Pollutants Identified by EU Guidelines. *J. Hazard. Mater.*, 344 (**2018**) 146–162.

https://doi.org/10.1016/j.jhazmat.2017.09.058

[43] A. Komal, A Review: Immunological and Biochemical Studies on Imidacloprid Toxicity. *The Pharma Innovation Journal*, 7 (**2018**) 1008–1011.

[44] Y. Yin, X. Huang, W. Wang, X. Liu, Carbon and Oxygen co-Doped Phosphotungstate for High Performance Photocatalytic Degradation of Imidacloprid. *Solid State Sci*, 136 (**2023**) 107109.

https://doi.org/10.1016/j.solidstatesciences.2023.107109

[45] H. Wamhoff, V. Schneider, Photodegradation of Imidacloprid. *J. Agric. Food Chem.*, 47 (**1999**) 1730–1734.

https://doi.org/10.1021/jf980820j

[46] P. N. Moza, K. Hustert, Feicht, A. Kettrup, Photolysis of Imidacloprid in Aqueous Solution. *Chemosphere*, 3 (**1998**) 497–502.

https://doi.org/10.1016/s0045-6535(97)00359-7

[47] M. Bourgin, F. Violleau, L. Debrauwer, J. Albet, Ozonation of Imidacloprid in Aqueous Solutions: Reaction Monitoring and Identification of Degradation Products. *J. Hazard. Mater.*, 190 (**2011**) 60–68.

https://doi.org/10.1016/j.jhazmat.2011.02.065

[48] X. Wang, Z. Chen, Y. He, X. Yi, C. Zhang, Q. Zhou, X. Xiang, Y. Gao, M. Huang, Activation of Persulfate-based Advanced Exidation Processes by 1T-MoS_2 for the Degradation of Imidacloprid: Performance and Mechanism. *Chem. Eng. J.*, 451 (**2023**).

https://doi.org/10.1016/j.cej.2022.138575

[49] Y. Ma, L. Wu, P. Li, L. Yang, L. He, S. Chen, Y. Yang, F. Gao, X. Qi, Z. Zhang, A Novel, Efficient and Sustainable Magnetic Sludge Biochar Modified by Graphene Oxide for Environmental Concentration Imidacloprid Removal. *J. Hazard. Mater.*, 407 (**2021**).

https://doi.org/10.1016/j.jhazmat.2020.124777

[50] S. Singh, S. Kaushal, J. Kaur, G. Kaur, S. K. Mittal, P. P. Singh, CaFu MOF as an Efficient Adsorbent for Simultaneous Removal of Imidacloprid Pesticide and Cadmium Ions from Wastewater. *Chemosphere*, 272 (**2021**).

https://doi.org/10.1016/j.chemosphere.2021.129648

[51] N. A. Ahmad Zubairi, H. Takaijudin, A. Ab Ghani, H. W. Goh, W. A. Day, Assessment of Imidacloprid Removal from Agricultural Runoff by the Bioretention Treatment Train System. *Environmental Advances*, 7 (**2022**) 100156.

https://doi.org/10.1016/j.envadv.2021.100156

[52] L. Ferreira, E. Rosales, A. S. Danko, M. A. Sanromán, M. M. Pazos, Bacillus Thuringiensis a Promising Bacterium for Degrading Emerging Pollutants. *Process Saf Environ Prot*, 101 (**2016**) 19–26.

https://doi.org/10.1016/j.psep.2015.05.003

[53] C. Segura, C. Zaror, H. D. Mansilla, M. A. Mondaca, Imidacloprid Oxidation by Photo-Fenton reaction. *J. Hazard. Mater.*, 150 (**2008**) 679–686.

https://doi.org/10.1016/j.jhazmat.2007.05.018

[54] F. C. Moreira, R. A. R. Boaventura, E. Brillas, V. J. P. Vilar, Electrochemical Advanced Oxidation Processes: A Review on their Application to Synthetic and Real Wastewaters. *Appl. Catal. B*, 202 (**2017**) 217–261.

https://doi.org/10.1016/j.apcatb.2016.08.037

[55] R. Oriol, D. Clematis, E. Brillas, J. L. Cortina, M. Panizza, I. Sirés, Groundwater Treatment Using a Solid Polymer Electrolyte Cell with Mesh Electrodes. *ChemElectroChem*, 6 (**2019**) 1235–1243.

https://doi.org/10.1002/celc.201801906

[56] L. M. Silva, R. P. A. dos Santos, C. C. O. Morais, C. L. Vasconcelos, C. A. Martínez-Huitle, S. S. L. Castro, Anodic Oxidation of the Insecticide Imidacloprid on Mixed Metal Oxide (RuO_2-TiO_2 and IrO_2-RuO_2-TiO_2) Anodes . *J. Electrochem. Soc.*, 164 (**2017**) E489–E495.

https://doi.org/10.1149/2.1871713jes

[57] M. ben Brahim, H. B. Ammar, R. Abdelhédi, Y. Samet, Electrochemical Removal of the Insecticide Imidacloprid from Water on a Boron-doped Diamond and Ta/PbO2 Anodes Using Anodic Oxidation Process. *Korean J Chem Eng*, 33 (**2016**) 2602–2609.

https://doi.org/10.1007/s11814-016-0128-0

[58] W. Yu, F. Lai, J. He, K. He, R. Wang, D. Li, Q. Chen, Catalytic Performances and Leaching Behavior of Typical Natural Iron Minerals as Electro-Fenton Catalysts for Mineralization of Imidacloprid. *J Ind Eng Chem*, 118 (**2023**) 132–146.

https://doi.org/10.1016/j.jiec.2022.10.052

[59] H. Zhao, Y. Wang, Y. Wang, T. Cao, G. Zhao, Electro-Fenton oxidation of Pesticides with a Novel Fe_3O_4@Fe_2O_3/Activated Carbon Aerogel Cathode: High Activity, Wide pH Range and Catalytic Mechanism. *Appl Catal B*, 125 (**2012**) 120–127. https://doi.org/10.1016/j.apcatb.2012.05.044

[60] M. Turabik, N. Oturan, B. Gözmen, M. A. Oturan, Efficient Removal of Insecticide "Imidacloprid" from Water by Electrochemical Advanced Oxidation Processes. *Environ. Sci. Pollut. Res.*, 21 (**2014**) 8387–8397. https://doi.org/10.1007/s11356-014-2788-9

[61] H. Zhao, L. Qian, Y. Chen, Q. Wang, G. Zhao, Selective Catalytic Two-electron O_2 Reduction for Onsite Efficient Oxidation Reaction in Heterogeneous Electro-Fenton Process. *Chem. Eng. J.*, 332 (**2018**) 486–498. https://doi.org/10.1016/j.cej.2017.09.093

[62] O. Iglesias, J. Gómez, M. Pazos, M. Á. Sanromán, Electro-Fenton Oxidation of Imidacloprid by Fe Alginate Gel Beads. *Appl. Catal. B*, 144 (**2014**) 416–424. https://doi.org/10.1016/j.apcatb.2013.07.046

[63] N. Ghalwa MA, Nader B Farhat, Removal of Imidacloprid Pesticide by Electrocoagulation Process Using Iron and Aluminum Electrodes. *J Environ Anal Chem*, 2 (**2015**) 154. https://doi.org/10.4172/2380-2391.1000154

[64] A. L. Tasca, M. Puccini, A. Fletcher, Terbuthylazine and Desethyl-terbuthylazine: Recent Occurrence, Mobility and Removal Techniques. *Chemosphere*, 202 (**2018**) 94–104. https://doi.org/10.1016/j.chemosphere.2018.03.091

[65] P. Bottoni, P. Grenni, L. Lucentini, A. B. Caracciolo, Terbuthylazine and Other Triazines in Italian Water Resources. *Microchemical Journal*, 107 (**2013**) 136–142. https://doi.org/10.1016/j.microc.2012.06.011

[66] A. F. Hernández, Food Safety: Pesticides. *Encyclopedia of Human Nutrition* (Elsevier, **2023**) 375–388. https://doi.org/10.1016/b978-0-12-821848-8.00042-1

[67] L. Marutescu, M. C. Chifiriuc, Molecular Mechanisms of Pesticides Toxicity. *New Pesticides and Soil Sensors* (Elsevier, **2017**) 393–435.

https://doi.org/10.1016/b978-0-12-804299-1.00012-6

[68] M. Ghisari, M. Long, A. Tabbo, E. C. Bonefeld-Jørgensen, Effects of Currently Used Pesticides and their Mixtures on the Function of Thyroid Hormone and Aryl Hydrocarbon Receptor in Cell Culture. *Toxicol. Appl. Pharmacol.*, 284 (**2015**) 292–303.

https://doi.org/10.1016/j.taap.2015.02.004

[69] E. Swedenborg, I. Pongratz, J. Å. Gustafsson, Endocrine Disruptors Targeting ERβ Function. *Int J Androl* (**2010**) 288–297.

https://doi.org/10.1111/j.1365-2605.2009.01025.x

[70] J. Olivero-Verbel, A. Guerrero-Castilla, & N. R. Ramos, Biochemical Effects Induced by the Hexachlorocyclohexanes. *Rev Environ Contam Toxicol*, 212 (**2011**)1–28.

https://doi.org/10.1007/978-1-4419-8453-1_1

[71] J. S. Taylor, B. M. Thomson, C. N. Lang, F. Y. T. Sin, E. Podivinsky, Estrogenic Pyrethroid Pesticides Regulate Expression of Estrogen Receptor Transcripts in Mouse Sertoli Cells Differently from 17-estradiol. *J. Toxicol. Environ. Health Part A*, 73 (**2010**) 1075–1089.

https://doi.org/10.1080/15287394.2010.482915

[72] V. R. Beasley, Direct and Indirect Effects of Environmental Contaminants on Amphibians. *Reference Module in Earth Systems and Environmental Sciences* (Elsevier, **2020**).

https://doi.org/10.1016/b978-0-12-409548-9.11274-6.

[73] J. N. Perry, L. G. Firbank, G. T. Champion, S. J. Clark, M. S. Heard, M. J. May, C. Hawes, G. R. Squire, P. Rothery, I. P. Woiwod, J. D. Pidgeon, Ban on Triazine Herbicides Likely to Reduce but Not Negate Relative Benefits of GMHT Maize Cropping. *Nature*, 428 (**2004**) 313–316.

https://doi.org/10.1038/nature02374

[74] P. M. Álvarez, D. H. Quiñones, I. Terrones, A. Rey, F. J. Beltrán, Insights into the Removal of Terbuthylazine from Aqueous Solution by Several Treatment Methods. *Water Res.*, 98 (**2016**) 334–343.

https://doi.org/10.1016/j.watres.2016.04.026

[75] L. Liang, X. Wang, Y. Sun, P. Ma, X. Li, H. Piao, Y. Jiang, D. Song, Magnetic Solid-phase Extraction of Triazine Herbicides from Rice Using Metal-organic Framework MIL-101(Cr) Functionalized Magnetic Particles. *Talanta*, 179 (**2018**) 512–519

https://doi.org/10.1016/j.talanta.2017.11.017

[76] S. Ronka, M. Kujawska, H. Juśkiewicz, Triazines Removal by Selective Polymeric Adsorbent. *Pure and Applied Chemistry* 86 (**2014**) 1755–1769.

https://doi.org/10.1515/pac-2014-0722

[77] E. Dražević, K. Košutić, S. Finglerb, V. Drevenkar, Removal of Pesticides from the Water and their Adsorption on the Reverse Osmosis Membranes of Defined Porous Structure. *Desalination Water Treat.*, 30 (**2011**) 161–170.

https://doi.org/10.5004/dwt.2011.1959

[78] D. H. Quiñones, A. Rey, P. M. Álvarez, F. J. Beltrán, & G. Li Puma, Boron-doped TiO_2 Catalysts for Photocatalytic Ozonation of Aqueous Mixtures of Common Pesticides: Diuron, o-Phenylphenol, MCPA and Terbuthylazine. *Appl. Catal. B*, 178 (**2015**) 74–81.

https://doi.org/10.1016/j.apcatb.2014.10.036

[79] J. le Cunff, V. Tomašić, O. Wittine, Photocatalytic Degradation of the Herbicide Terbuthylazine: Preparation, Characterization and Photoactivity of the Immobilized Thin Layer of TiO_2/Chitosan. *J. Photochem. Photobiol. A*, 309 (**2015**) 22–29.

https://doi.org/10.1016/j.jphotochem.2015.04.021

[80] A. L. Tasca, M. Puccini, D. Clematis, M. Panizza, Electrochemical Removal of Terbuthylazine:Boron-doped Diamond Anode Coupled with Solid Polymer Electrolyte. *Environ. Pollut.*, 251 (**2019**) 285–291.

https://doi.org/10.1016/j.envpol.2019.04.134

[81] C. Yanze Kontchou, N. Gschwind, Mineralization of the Herbicide Atrazine in Soil Inoculated with a Pseudomonas Strain. *J. Agric. Food Chem.*, 43 (**1995**) 2291–2294.

https://doi.org/10.1021/jf00056a061

[82] S. Rani, D. Sud, Role of Enhanced Solar Radiation for Degradation of Triazophos Pesticide in Soil Matrix. *Solar Energy*, 120 (**2015**) 494–504.
https://doi.org/10.1016/j.solener.2015.07.050

[83] Y. Mu, G. Zhan, C. Huang, X. Wang, Z. Ai, J. Zou, S. Luo, L. Zhang, Dechlorination-Hydroxylation of Atrazine to Hydroxyatrazine with Thiosulfate: A Detoxification Strategy in Seconds. *Environ. Sci. Technol.*, 53 (**2019**) 3208–3216.
https://doi.org/10.1021/acs.est.8b06351

[84] C. B. Breckenridge, J. W. Simpkins, *Hayes' Handbook of Pesticide Toxicology*, 3rd Edition (Elsevier, 2010).
https://doi.org/10.1016/c2009-1-03818-0

[85] G. Balacco, G. D. Fiorese, & M. R. Alfio, Assessment of Groundwater Nitrate Pollution Using the Indicator Kriging Approach. *Groundw Sustain Dev*, 21 (2023) 100920.
https://doi.org/10.1016/j.gsd.2023.100920

[86] Nitrate/Nitrite Toxicity: What Are the Health Effects from Exposure to Nitrates and Nitrites?
https://www.atsdr.cdc.gov/csem/nitrate-nitrite/health_effects.html (accessed June 18, 2023).

[87] J. P. van der Hoek, A. Klapwijk, Nitrate Removal from Groundwater. *Water Res.*, 21 (**1987**) 989–997.
https://doi.org/10.1016/s0043-1354(87)80018-0

[88] A. Kapoor, T. Viraraghavan, Nitrate Removal from Drinking Water Review. *J Environ Eng*, 123 (**1997**) 371–380.
https://doi.org/10.1061/(asce)0733-9372(1997)123:4(371)

[89] J. Pelley, Nitrate Eyed as Endocrine Disrupter. *Environ. Sci. Technol.*, 37 (**2003**) 162A.
https://doi.org/10.1021/es032437n

[90] A. M. Fan & V. E. Steinberg, Health Implications of Nitrate and Nitrite in Drinking Water: An Update on Methemoglobinemia Occurrence and Reproductive and Developmental Toxicity. *Regul. Toxicol. Pharmacol.*, 23 (**1996**) 35–43.
https://doi.org/10.1006/rtph.1996.0006

[91] M. H. Ward, T. M. deKok, P. Levallois, J. Brender, G. Gulis, B. T. Nolan, & J. VanDerslice, Workgroup Report: Drinking-Water Nitrate and Health—Recent Findings and Research Needs. *Environ. Health Perspect.*, 113 (**2005**) 1607–1614.

https://doi.org/10.1289/ehp.8043

[92] S. Duan, T. Tong, S. Zheng, X. Zhang, & S. Li, Achieving Low-cost, Highly Selective Nitrate Removal with Standard Anion Exchange Resin by Tuning Recycled Brine Composition. *Water Res.*, 173 (**2020**) 115571.

https://doi.org/10.1016/j.watres.2020.115571

[93] S. Wiriyathamcharoen, S. Sarkar, P. Jiemvarangkul, T. T. Nguyen, W. Klysuban, S. Padungthon, Synthesis optimization of hybrid anion exchanger containing triethylamine functional groups and hydrated Fe(III) oxide nanoparticles for simultaneous nitrate and phosphate removal. *Chem. Eng. J.*, 381 (**2020**) 122671.

https://doi.org/10.1016/j.cej.2019.122671

[94] G. You, C. Wang, J. Hou, P. Wang, Y. Xu, L. Miao, J. Liu, Effects of Zero Valent Iron on Nitrate Removal in Anaerobic Bioreactor with Various Carbon-to-nitrate Ratios: Bio-electrochemical Properties, Energy Regulation Strategies and Biological Response Mechanisms. *Chem. Eng. J.*, 419 (**2021**) 129646.

https://doi.org/10.1016/j.cej.2021.129646

[95] J. Li, Y. Li, P. Chen, K. Sathishkumar, Y. Lu, S. Naraginti, Y. Wu, H. Wu, Biological Mediated Synthesis of Reduced Graphene Oxide (rGO) as a Potential Electron Shuttle for Facilitated Biological Denitrification: Insight into the Electron Transfer Process. *J. Environ. Chem. Eng.*, 10 (**2022**) 108225.

https://doi.org/10.1016/j.jece.2022.108225.

[96] K. Häyrynen, E. Pongrácz, V. Väisänen, N. Pap, M. Mänttäri, J. Langwaldt, R. L. Keiski, Concentration of Ammonium and Nitrate from Mine Water by Reverse Osmosis and Nanofiltration. *Desalination*, 240 (**2009**) 280–289.

https://doi.org/10.1016/j.desal.2008.02.027

[97] H. C. Duong, H. T. Cao, N. B. Hoang, L. D. Nghiem, Reverse Osmosis Treatment of Condensate from Ammonium Nitrate Production: Insights into Membrane Performance. *J. Environ. Chem. Eng.*, 9 (**2021**) 106457.

https://doi.org/10.1016/j.jece.2021.106457

[98] A. Lejarazu-Larrañaga, J. M. Ortiz, S. Molina, Y. Zhao,, E. García-Calvo, Nitrate-selective Anion Exchange Membranes Prepared Using Discarded Reverse Osmosis Membranes as Support. *Membranes*, 10 (**2020**) 1–18.

https://doi.org/10.3390/membranes10120377

[99] Y. Liu, J. Wang, Reduction of Nitrate by Zero Valent Iron (ZVI)-based Materials: A Review. *Sci. Total Environ.*, 671 (**2019**) 388–403.

https://doi.org/10.1016/j.scitotenv.2019.03.317

[100] X. Liu, M. Huang, S. Bao, W. Tang, T. Fang, Nitrate Removal from Low Carbon-to-nitrogen Ratio Wastewater by Combining Iron-based Chemical Reduction and Autotrophic Denitrification. *Bioresour. Technol.*, 301 (**2020**) 122731.

https://doi.org/10.1016/j.biortech.2019.122731

[101] N. Song, J. Xu, Y. Cao, F. Xia, J. Zhai, H. Ai, D. Shi, L. Gu, Q. He, Chemical Removal and Selectivity Reduction of Nitrate from Water by (Nano) Zero-valent Iron/Activated Carbon Micro-electrolysis. *Chemosphere*, 248 (2020) 125986.

https://doi.org/10.1016/j.chemosphere.2020.125986

[102] F. Guo, Y. Luo, W. Nie, Z. Xiong, X. Yang, J. Yan, T. Liu, M. Chen, Y. Chen, Biochar Boosts Nitrate Removal in Constructed Wetlands for Secondary Effluent Treatment: Linking Nitrate Removal to the Metabolic Pathway of Denitrification and Biochar Properties. *Bioresour. Technol.*, 379 (**2023**) 129000.

https://doi.org/10.1016/j.biortech.2023.129000

[103] T. L. Messer, D. N. Miller, H. Little, & K. Oathout, Nitrate-N Removal Rate Variabilities in Floating Treatment Wetland Mesocosms with Diverse Planting and Carbon Amendment Designs. *Ecol. Eng.*, 174 (**2022**) 106444.

https://doi.org/10.1016/j.ecoleng.2021.106444

[104] Y. Tsuchiya, Y. Amano, M. Machida, Nitrate Ion Adsorption Characteristics of Activated Carbon Fibers with and without Quaternary Nitrogen Effective for Anion Adsorption. *Chem Pharm Bull (Tokyo)*, 68 (**2020**) 1001–1007.

https://doi.org/10.1248/cpb.c20-00364

[105] T. Liu, H. Du, L. Zhang, Y. Liu, Selective Reduction of Nitrate to Nitrogen Gas with Hydrating Electrons from the Photo-corrosion of Natural Pyrite. *Sep. Purif. Technol.*, 318 (**2023**) 123947.

https://doi.org/10.1016/j.seppur.2023.123947

[106] N. Barrabés, J. Sá, Catalytic Nitrate Removal from Water, Past, Present and Future Perspectives. *Appl. Catal. B*, 104 (**2011**) 1–5.

https://doi.org/10.1016/j.apcatb.2011.03.011

[107] C. L. Constantinou, C. N. Costa, A. M. Efstathiou, Catalytic Removal of Nitrates from Waters. *Catal. Today*, 151 (2010) 190–194.

https://doi.org/10.1016/j.cattod.2010.02.019

[108] M. Al Rayaan, The Feasibility of Adoption of Catalytic Removal of Nitrate in Saudi Arabia's Groundwater: A Gate-to-gate Environmental Analysis. *Cleaner Eng. Technol.*, 10 (**2022**) 100542.

https://doi.org/10.1016/j.clet.2022.100542

[109] J. Ma, W. Wei, G. Qin, T. Xiao, W. Tang, S. Zhao, L. Jiang, S. Liu, Electrochemical Reduction of Nitrate in a Catalytic Carbon Membrane Nano-reactor. *Water Res.*, 208 (**2022**) 117862.

https://doi.org/10.1016/j.watres.2021.117862

[110] G. Tokazhanov, E. Ramazanova, S. Hamid, S. Bae, W. Lee, Advances in the Catalytic Reduction of Nitrate by Metallic Catalysts for High Efficiency and N_2 Selectivity: A Review. *Chem. Eng. J.*, 384 (**2020**) 1385–8947.

https://doi.org/10.1016/j.cej.2019.123252

[111] M. Amarine, B. Lekhlif, E. M. Mliji, J. Echaabi, Nitrate Removal from Groundwater in Casablanca Region (Morocco) by Electrocoagulation. *Groundw. Sustain. Dev.*, 11 (**2020**) 100452.

https://doi.org/10.1016/j.gsd.2020.100452

[112] H. Tounsi, T. Chaabane, K. Omine, V. Sivasankar, H. Sano, M. Hecini, A. Darchen, Electrocoagulation in the Dual Application on the Simultaneous Removal of Fluoride and Nitrate Anions Through Respective Adsorption/Reduction Processes and Modelling of Continuous Process. *J. Water Process. Eng.*, 46 (**2022**) 102584.

https://doi.org/10.1016/j.jwpe.2022.102584

[113] V. Supriya, B. Sowjanya, D. Kiran Kumar, V. R. Poiba, M. Vangalapati, Modelling and Optimization of Nitrates Adsorbed on Iron Plate Electrodes by Electrocoagulation Process Analyzed by Response Surface Methodology. *Mater. Today Proc*, (**2023**), *in press.*

https://doi.org/10.1016/j.matpr.2023.05.154

[114] E. Lacasa, P. Cañizares, C. Sáez, F. J. Fernández, M. A. Rodrigo, Removal of Nitrates from Groundwater by Electrocoagulation. *Chem. Eng. J.*, 171 (**2011**) 1012–1017.

https://doi.org/10.1016/j.cej.2011.04.053

[115] X. Zhang, Y. Wang, C. Liu, Y. Yu, S. Lu, B. Zhang, Recent Advances in Non-noble Metal Electrocatalysts for Nitrate Reduction. *Chem. Eng. J.*, 403 (**2021**) 126269.

https://doi.org/10.1016/j.cej.2020.126269

[116] A. Ceballos-Escalera, N. Pous, P. Chiluiza-Ramos, B. Korth, F. Harnisch, L. Bañeras, M. D. Balaguer, S. Puig, Electro-bioremediation of Nitrate and Arsenite Polluted Groundwater. *Water Res.*, 190 (**2021**) 116748.

https://doi.org/10.1016/j.watres.2020.116748

[117] N. Pous, M. D. Balaguer, J. Colprim, S. Puig, Opportunities for Groundwater Microbial Electro-remediation. *Microb. Biotechnol.*, 11 (**2018**) 119–135. https://doi.org/10.1111/1751-7915.12866

[118] N. Pous, S. Puig, M. Coma, M. D. Balaguer, J. Colprim, Bioremediation of Nitrate-Polluted Groundwater in a Microbial Fuel Cell. *J. Chem. Technol. Biotechnol.*, 88 (**2013**) 1690–1696.

https://doi.org/10.1002/jctb.4020

[119] M. Baghodrat, F. Mehri, S. Rowshanzamir, Electrochemical Performance and Enhanced Nitrate Removal of Homogeneous Polysulfone-based Anion Exchange Membrane Applied in Membrane Capacitive Deionization Cell. *Desalination*, 496 (**2020**) 114696. https://doi.org/10.1016/j.desal.2020.114696

[120] M. Zhang, M. Ma, Z. Miao, W. Chai, Y. Cao, Coal-based Activated Carbon Functionalized with Anionic and Cationic Surfactants for Asymmetric Capacitive Deionization of Nitrate. *Colloids Surf. A Physicochem. Eng. Asp.*, 663 (**2023**) 131054. https://doi.org/10.1016/j.colsurfa.2023.131054

[121] J. J. Lado, R. E. Pérez-Roa, J. J. Wouters, M. I. Tejedor-Tejedor, C. Federspill, J. M. Ortiz, M. A. Anderson, Removal of Nitrate by Asymmetric Capacitive Deionization. *Sep. Purif. Technol.*, 183 (**2017**) 145–152. https://doi.org/10.1016/j.seppur.2017.03.071

[122] D. Wan, J. Wang, Y. Shi, D. Qu, J. Zhang, Construction of Continuous-flow Electrodialysis Ion-exchange Membrane Bioreactor for Effective Removal of Nitrate and Perchlorate: Modelling and Impact Analysis of Environmental Variables. *Chem. Eng. J.*, 462 (**2023**) 142144. https://doi.org/10.1016/j.cej.2023.142144

[123] M. Aliaskari, A. I. Schäfer, Nitrate, Arsenic and Fluoride Removal by Electrodialysis from Brackish Groundwater. *Water Res.*, 190 (**2021**) 116683. https://doi.org/10.1016/j.watres.2020.116683

[124] A. Lejarazu-Larrañaga, J. M. Ortiz, S. Molina, S. Pawlowski, C. F. Galinha, V. Otero, E. García-Calvo, S. Velizarov, J. G. Crespo, Nitrate Removal by Donnan Dialysis and Anion-Exchange Membrane Bioreactor Using Upcycled End-of-life Reverse Osmosis Membranes. *Membranes*, 12 (**2022**) 101. https://doi.org/10.3390/membranes12020101

[125] A. Marican E. F. Durán-Lara, A Review on Pesticide Removal through Different Processes. *Environ. Sci. Pollut. Res.*, 25 (**2018**) 2051–2064. https://doi.org/10.1007/s11356-017-0796-2

[126] P. Kajitvichyanukul, V. H. Nguyen, T. Boonupara, L. A. Phan Thi, A. Watcharenwong, S. Sumitsawan, P. Udomkun, Challenges and Effectiveness of Nanotechnology-based Photocatalysis for Pesticides-contaminated Water: A Review. *Environ. Res.*, 212 (**2022**) 113336.

https://doi.org/10.1016/j.envres.2022.113336

[127] M. H. El-Saeid, M. O. Alotaibi, M. Alshabanat, M. M. Al-Anazy, K. R. Alharbi, A. S. Altowyan, Impact of Photolysis and TiO_2 on Pesticides Degradation in Wastewater. *Water*, 13 (**2021**) 655.

https://doi.org/10.3390/w13050655

[128] S. D. Ayare, P. R. Gogate, Sonochemical, Photocatalytic and Sonophotocatalytic Oxidation of Flonicamid Pesticide Solution Using Different Catalysts. *Chem. Eng. Process.: Process Intensif.*, 154 (**2020**) 108040.

https://doi.org/10.1016/j.cep.2020.108040

[129] N. S. Deshmukh, M. P. Deosarkar, A Review on Ultrasound and Photocatalysis-based Combined Treatment Processes for Pesticide Degradation. *Mater. Today: Proc.*, 57 (**2022**) 1575–1584.

https://doi.org/10.1016/j.matpr.2021.12.170

[130] M. Kask, M. Krichevskaya, J. Bolobajev, Sonolytic Degradation of Pesticide Metazachlor in Water: The Role of Dissolved Oxygen and Ferric Sludge in the Process Intensification. *J. Environ. Chem. Eng.*, 7 (**2019**) 103095.

https://doi.org/10.1016/j.jece.2019.103095

[131] S. Singh Kalra, B. Cranmer, G. Dooley, A. J. Hanson, S. Maraviov, S. K. Mohanty, J. Blotevogel, S. Mahendra, Sonolytic destruction of Per- and Polyfluoroalkyl Substances in Groundwater, Aqueous Film-Forming Foams, and Investigation Derived Waste. *Chem. Eng. J.*, 425 (**2021**) 131778.

https://doi.org/10.1016/j.cej.2021.131778

[132] C. M. Martínez-Escudero, I. Garrido, C. Ros, P. Flores, P. Hellín, F. Contreras, J. Fenoll, Remediation of Pesticides in Commercial Farm Soils by Solarization and Ozonation Techniques. *J. Environ. Manage.*, 329 (**2023**) 117062.

https://doi.org/10.1016/j.jenvman.2022.117062

[133] L. Hu Z. Xia, Application of Ozone Micro-nano-bubbles to Groundwater Remediation. *J. Hazard. Mater.*, 342 (**2018**) 446–453.

https://doi.org/10.1016/j.jhazmat.2017.08.030

[134] T. Garoma, M. D. Gurol, O. Osibodu, L. Thotakura, Treatment of Groundwater Contaminated with Gasoline Components by an Ozone/UV Process. *Chemosphere*, 73 (**2008**) 825–831.

https://doi.org/10.1016/j.chemosphere.2008.06.061

[135] A. S. Derbalah, N. Nakatani, H. Sakugawa, Photocatalytic Removal of Fenitrothion in Pure and Natural waters by Photo-Fenton reaction. *Chemosphere*, 57 (**2004**) 635–644.

https://doi.org/10.1016/j.chemosphere.2004.08.025

[136] A. Ismail, A. Derbalah, S. Shaheen, Monitoring and Remediation Technologies of Organochlorine Pesticides in Drainage Water. *Polish J. Chem. Technol.*, 17 (**2015**) 115–122.

https://doi.org/10.1515/pjct-2015-0017

[137] H. Ghanbarlou, B. Nasernejad, M. Nikbakht Fini, M. E. Simonsen, J. Muff, Synthesis of an Iron-graphene Based Particle Electrode for Pesticide Removal in Three-dimensional Heterogeneous Electro-Fenton Water Treatment System. *Chem. Eng. J.*, 395 (**2020**) 125025.

https://doi.org/10.1016/j.cej.2020.125025

[138] C. Zekkaoui, T. Berrama, D. Dumoulin, G. Billon, Y. Kadmi, Optimal Degradation of Organophosphorus Pesticide at Low Levels in Water Using Fenton and Photo-Fenton Processes and Identification of By-products by GC-MS/MS. *Chemosphere*, 279 (**2021**) 130544.

https://doi.org/10.1016/j.chemosphere.2021.130544

[139] J. A. Rodríguez-Liébana, A. López-Galindo, C. Jiménez de Cisneros, A. Gálvez, M. Rozalén, R. Sánchez-Espejo, E. Caballero, & A. Peña, Adsorption/Desorption of Fungicides in Natural Clays from Southeastern Spain. *Appl Clay Sci*, 132–133 (**2016**) 402–411.

https://doi.org/10.1016/j.clay.2016.07.006

[140] M. Zahoor, Removal of Pesticides from Water Using Granular Activated Carbon and Ultrafiltration Membrane—A Pilot Plant Study. *J. encapsulation adsorpt. sci.*, 3 (**2013**) 71–76.

https://doi.org/10.4236/jeas.2013.33009

[141] L. Domergue, N. Cimetière, S. Giraudet, P. Le Cloirec, Adsorption onto Granular Activated Carbons of a Mixture of Pesticides and their Metabolites at Trace Concentrations in Groundwater. *J. Environ. Chem. Eng.*, 10 (**2022**) 108218.

https://doi.org/10.1016/j.jece.2022.108218

[142] M. Dolatabadi, H. Naidu, S. Ahmadzadeh, Adsorption Characteristics in the Removal of Chlorpyrifos from Groundwater Using Magnetic Graphene Oxide and Carboxy Methyl Cellulose Composite. *Sep. Purif. Technol.*, 300 (**2022**) 121919.

https://doi.org/10.1016/j.seppur.2022.121919

[143] C. De Smedt, F. Ferrer, K. Leus, P. Spanoghe, Removal of Pesticides from Aqueous Solutions by Adsorption on Zeolites as Solid Adsorbents. *Adsorb Sci Technol*, 33 (**2015**) 457–485.

https://doi.org/10.1260/0263-6174.33.5.45

[144] A. Shoiful, Y. Ueda, R. Nugroho, K. Honda, Degradation of Organochlorine Pesticides (OCPs) in Water by Iron (Fe)-based Materials. *J. Water Process. Eng.*, 11 (**2016**) 110–117.

https://doi.org/10.1016/j.jwpe.2016.02.011

[145] C. J. Ottley, W. Davison, W. M. Edmunds, Chemical Catalysis of Nitrate Reduction by Iron (II). *Geochim Cosmochim Acta*, 61 (1997) 1819–1828. https://doi.org/10.1016/s0016-7037(97)00058-6

[146] N. Bensalah, R. Nicola, A. Abdel-Wahab, Nitrate Removal from Water Using UV-M/$S_2O_4^{2-}$ Advanced Reduction Process. *Int J Environ Sci Technol (Tehran)*, 11 (**2014**) 1733–1742.

https://doi.org/10.1007/s13762-013-0375-0/

[147] W. Zhao, X. Zhu, Y. Wang, Z. Ai, D. Zhao, Catalytic Reduction of Aqueous Nitrates by Metal Supported Catalysts on Al Particles. *Chem. Eng. J., 254* (**2014**) 410–417.

https://doi.org/10.1016/j.cej.2014.05.144

[148] B. Ramavandi, S. B. Mortazavi, G. Moussavi, A. Khoshgard, M. Jahangiri, Experimental Investigation of the Chemical Reduction of Nitrate Ion in Aqueous Solution by Mg/Cu Bimetallic Particles. *React. Kinet. Mech. Catal.*, 102 (**2011**) 313–329. https://doi.org/10.1007/s11144-010-0274-z/

[149] Y. H. Liou, C. J. Lin, I. C. Hung, S. Y. Chen, S. L. Lo, Selective Reduction of NO_3^- to N_2 with Bimetallic Particles of Zn Coupled with Palladium, Platinum, and Copper. *Chem. Eng. J.*, 181–182 (**2012**) 236–242. https://doi.org/10.1016/j.cej.2011.11.071

[150] W. Hu, L. Wang, K. Zhu, F. Wu, H. Qiao, Y. Li, Facile Copolymerization Synthesis of Vinylimidazole/Dibromodecane/Vinylpyridine Polymer with High Capacity for Selective Adsorption of Nitrate from Water. *J. Water Process. Eng.*, 49 (**2022**) 103052. https://doi.org/10.1016/j.jwpe.2022.103052

[151] C. V. Lazaratou, D. V. Vayenas, D. Papoulis, The Role of Clays, Clay Minerals and Clay-based Materials for Nitrate Removal from Water Systems: A Review. *Appl Clay Sci*, 185 (**2020**) 105377. https://doi.org/10.1016/j.clay.2019.105377

[152] N. B. Singh, G. Nagpal, S. Agrawal, Rachna, Water Purification by Using Adsorbents: A Review. *Environ. Technol. Innov.*, 11 (**2018**) 187–240. https://doi.org/10.1016/j.eti.2018.05.006

[153] C. Trellu, H. Olvera Vargas, E. Mousset, N. Oturan, M. A. Oturan, Electrochemical Technologies for the Treatment of Pesticides. *Curr Opin Electrochem*, 26 (**2021**) 100677. https://doi.org/10.1016/j.coelec.2020.100677

[154] S. Mirehbar, S. Fernández-Velayos, E. Mazario, N. Menéndez, P. Herrasti, F. J. Recio, I. Sirés, Evidence of Cathodic Peroxydisulfate Activation via Electrochemical Reduction at Fe(II) Sites of Magnetite-decorated Porous Carbon: Application to Dye Degradation in Water. *J. Electroanal. Chem.*, 902 (**2021**) 115807. https://doi.org/10.1016/j.jelechem.2021.115807

[155] M. Dortsiou, I. Katsounaros, C. Polatides, G. Kyriacou, Electrochemical Removal of Nitrate from the Spent Regenerant Solution of the Ion Exchange. *Desalination*, 248 (**2009**) 923–930.

https://doi.org/10.1016/j.desal.2008.10.012.

[156] X. Li, L. Wang, W. Sun, Z. Yan, Y. He, X. Shu, G. Liu, Study on Electrochemical Water Softening Mechanism of High-efficient Multi-layer Mesh Coupled Cathode. *Sep. Purif. Technol.*, 247 (**2020**) 117001.

https://doi.org/10.1016/j.seppur.2020.117001

[157] F. H. Adnan, E. Mousset, S. Pontvianne, M. N. Pons, Mineral Cathodic Electro-precipitation and its Kinetic Modelling in Thin-film Microfluidic Reactor During Advanced Electro-oxidation Process. *Electrochim. Acta*, 387 (**2021**) 138487.

https://doi.org/10.1016/j.electacta.2021.138487

[158] H. Jin, Y. Yu, L. Zhang, R. Yan, X. Chen, Polarity Reversal Electrochemical Process for Water Softening. *Sep. Purif. Technol.*, 210 (**2019**) 943–949.

https://doi.org/10.1016/j.seppur.2018.09.009

[159] H. Jin, Y. Yu, X. Chen, Membrane-based Electrochemical Precipitation for Water Softening. *J. Memb. Sci.*, 597 (**2020**) 117639.

https://doi.org/10.1016/j.memsci.2019.117639

[160] E. Helmy, M. Hussein, Study on the Removal of Water Hardness by Electrocoagulation Technique. *IJCBS*, 12 (**2017**) 1–17.

[161] T. N. Tuan, S. Chung, J. K. Lee, J. Lee, Improvement of Water Softening Efficiency in Capacitive Deionization by Ultra Purification Process of Reduced Graphene Oxide. *Curr Appl Phys*, 15 (**2015**) 1397–1401.

https://doi.org/10.1016/j.cap.2015.08.001

[162] C. Weidlich, K. M. Mangold, K. Jüttner, Conducting Polymers as Ion-exchangers for Water Purification. *Electrochim. Acta*, 47 (**2001**) 741–745.

https://doi.org/10.1016/s0013-4686(01)00754-x

[163] S. Garcia-Segura, M. Lanzarini-Lopes, K. Hristovski, P. Westerhoff, Electrocatalytic Reduction of Nitrate: Fundamentals to Full-scale Water Treatment Applications. *Appl. Catal. B*, 236 (**2018**) 546–568.

https://doi.org/10.1016/j.apcatb.2018.05.041

[164] D. E. Kim, D. Pak, Ti Plate with TiO_2 Nanotube Arrays as a Novel Cathode for Nitrate Reduction. *Chemosphere*, 228 (**2019**) 611–618.

https://doi.org/10.1016/j.chemosphere.2019.04.071

[165] L. Su, K. Li, H. Zhang, M. Fan, D. Ying, T. Sun, Y. Wang, J. Jia, Electrochemical Nitrate Reduction by Using a Novel Co_3O_4/Ti Cathode. *Water Res.*, 120 (**2017**) 1–11.

https://doi.org/10.1016/j.watres.2017.04.069

[166] X. Ma, M. Li, C. Feng, Z. He, Electrochemical Nitrate Removal with Simultaneous Magnesium Recovery from a Mimicked RO Brine Assisted by in situ Chloride Ions. *J. Hazard. Mater.*, 388 (**2020**) 122085.

https://doi.org/10.1016/j.jhazmat.2020.122085

[167] I. Katsounaros, G. Kyriacou, Influence of Nitrate Concentration on its Electrochemical Reduction on Tin Cathode: Identification of Reaction Intermediates. *Electrochim Acta*, 53 (**2008**) 5477–5484.

https://doi.org/10.1016/j.electacta.2008.03.018

[168] D. Reyter, D. Bélanger, L. Roué, Study of the Electroreduction of Nitrate on Copper in Alkaline Solution. *Electrochim. Acta*, 53 (**2008**) 5977–5984.

https://doi.org/10.1016/j.electacta.2008.03.048

[169] E. Pérez-Gallent, M. C. Figueiredo, I. Katsounaros, M. T. M. Koper, Electrocatalytic Reduction of Nitrate on Copper Single Crystals in Acidic and Alkaline Solutions. *Electrochim. Acta*, 227 (**2017**) 77–84.

https://doi.org/10.1016/j.electacta.2016.12.147

[170] R. Abdallah, F. Geneste, T. Labasque, H. Djelal, F. Fourcade, A. Amrane, S. Taha, D. Floner, Selective and Quantitative Nitrate Electroreduction to Ammonium Using a Porous Copper Electrode in an Electrochemical Flow Cell. *J. Electroanal. Chem.*, 727 (**2014**) 148–153.

https://doi.org/10.1016/j.jelechem.2014.06.016

[171] L. K. Wu, Y. J. Shi, C. Su, H. Z. Cao, G. Q. Zheng, Efficient Electrochemical Reduction of High Concentration Nitrate by a Stepwise Method. *Catal Letters*, 149 (**2019**) 1216–1223.

https://doi.org/10.1007/s10562-019-02715-9/figures/5

[172] W. Duan, G. Li, Z. Lei, T. Zhu, Y. Xue, C. Wei, C. Feng, Highly Active and Durable Carbon Electrocatalyst for Nitrate Reduction Reaction. *Water Res.*, 161 (**2019**) 126–135.

https://doi.org/10.1016/j.watres.2019.05.104

[173] Y. Zhang, Y. Zhao, Z. Chen, L. Wang, P. Wu, F. Wang, Electrochemical Reduction of Nitrate via Cu/Ni Composite Cathode Paired with Ir-Ru/Ti Anode: High Efficiency and N_2 selectivity. *Electrochim. Acta*, 291 (**2018**) 151–160.

https://doi.org/10.1016/j.electacta.2018.08.154

[174] K. Tada, K. Shimazu, Kinetic Studies of Reduction of Nitrate Ions at Sn-modified Pt Electrodes Using a Quartz Crystal Microbalance. *J. Electroanal. Chem.*, 577 (**2005**) 303–309.

https://doi.org/10.1016/j.jelechem.2004.11.039

[175] Y. Y. Birdja, J. Yang, M. T. M. Koper, Electrocatalytic Reduction of Nitrate on Tin-modified Palladium Electrodes. *Electrochim. Acta*, 140 (**2014**) 518–524.

https://doi.org/10.1016/j.electacta.2014.06.011

[176] Z. Zhang, Y. Xu, W. Shi, W. Wang, R. Zhang, X. Bao, B. Zhang, L. Li, F. Cui, Electrochemical-catalytic Reduction of Nitrate over Pd–Cu/γAl_2O_3 Catalyst in Cathode Chamber: Enhanced Removal Efficiency and N_2 Selectivity. *Chem. Eng. J.*, 290 (**2016**) 201–208.

https://doi.org/10.1016/j.cej.2016.01.063

[177] C. Sun, F. Li, H. An, Z. Li, A. M. Bond, J. Zhang, Facile Electrochemical co-Deposition of Metal (Cu, Pd, Pt, Rh) Nanoparticles on Reduced Graphene Oxide for Electrocatalytic Reduction of Nitrate/Nitrite. *Electrochim. Acta*, 269 (**2018**) 733–741.

https://doi.org/10.1016/j.electacta.2018.03.005

[178] W. Gao, L. Gao, D. Li, K. Huang, L. Cui, J. Meng, J. Liang, Removal of Nitrate from Water by the Electrocatalytic Denitrification on the Cu-Bi Electrode. *J. Electroanal. Chem.*, 817 (**2018**) 202–209.

https://doi.org/10.1016/j.jelechem.2018.04.006

[179] W. Gao, L. Gao, J. Meng, D. Li, Y. Guan, L. Cui, X. Shen, J. Liang, Preparation of a Novel Cu-Sn-Bi Cathode and Performance on Nitrate Electroreduction. *Water Sci. Technol.*, 79 (**2019**) 198–206.

https://doi.org/10.2166/wst.2019.049

[180] M. Li, C. Feng, Z. Zhang, N. Sugiura, Efficient Electrochemical Reduction of Nitrate to Nitrogen Using Ti/IrO_2–Pt Anode and Different Cathodes. *Electrochim. Acta*, 54 (**2009**) 4600–4606.

https://doi.org/10.1016/j.electacta.2009.03.064

[181] M. Ghazouani, H. Akrout, L. Bousselmi, Nitrate and Carbon Matter Removals from Real Effluents Using Si/BDD Electrode. *Environ. Sci. Pollut. Res.*, 24 (**2017**) 9895–9906.

https://doi.org/10.1007/s11356-016-7563-7/

[182] H. Cheng, K. Scott, P. A. Christensen, Application of a Solid Polymer Electrolyte Reactor to Remove Nitrate Ions from Wastewater. *J Appl Electrochem*, 35 (**2005**) 551–560.

https://doi.org/10.1007/s10800-005-1519-9/

[183] P. M. Tucker, M. J. Waite, B. E. Hayden, Electrocatalytic Reduction of Nitrate on Activated Rhodium Electrode Surfaces. *J Appl Electrochem*, 34 (**2004**) 781–796.

https://doi.org/10.1023/b:jach.0000035607.19248.b6/

[184] M. Fedurco, P. Kedzierzawski, J. Augustynski, Effect of Multivalent Cations upon Reduction of Nitrate Ions at the Ag Electrode. *J. Electrochem. Soc.*, 146 (**1999**) 2569–2572.

https://doi.org/10.1149/1.1391973/xml

[185] T. Ohmori, M. S. El-Deab, & M. Osawa, Electroreduction of Nitrate Ion to Nitrite and Ammonia on a Gold Electrode in Acidic and Basic Sodium and Cesium Nitrate Solutions. *J. Electroanal. Chem.*, 470 (**1999**) 46–52.

https://doi.org/10.1016/S0022-0728(99)00210-7

[186] M. C. P. M. Da Cunha, M. Weber, F. C. Nart, On the Adsorption and Reduction of NO_3^- Ions at Au and Pt Electrodes Studied by in situ FTIR spectroscopy. *J. Electroanal. Chem.*, 414 (**1996**) 163–170.

https://doi.org/10.1016/0022-0728(96)04697-9

[187] E. Lacasa, P. Cañizares, J. Llanos, M. A. Rodrigo, Effect of the Cathode Material on the Removal of Nitrates by Electrolysis in Non-chloride Media. *J. Hazard. Mater.*, 213–214 (**2012**) 478–484.

https://doi.org/10.1016/j.jhazmat.2012.02.034

[188] M. Dortsiou, I. Katsounaros, C. Polatides, G. Kyriacou, Influence of the Electrode and the pH on the Rate and the Product Distribution of the Electrochemical Removal of Nitrate. *Environ. Technol.*, 34 (**2013**) 373–381.

https://doi.org/10.1080/09593330.2012.696722

[189] M. Li, C. Feng, Z. Zhang, Z. Shen, N. Sugiura, Electrochemical Reduction of Nitrate Using Various Anodes and a Cu/Zn Cathode. *Electrochem commun*, 11 (**2009**) 1853–1856.

https://doi.org/10.1016/j.elecom.2009.08.001

[190] I. Katsounaros, G. Kyriacou, Influence of the Concentration and the Nature of the Supporting Electrolyte on the Electrochemical Reduction of Nitrate on Tin Cathode. *Electrochim. Acta*, 52 (**2007**) 6412–6420.

https://doi.org/10.1016/j.electacta.2007.04.050

[191] G. Pérez, R. Ibáñez, A. M. Urtiaga, I. Ortiz, Kinetic Study of the Simultaneous Electrochemical Removal of Aqueous Nitrogen Compounds Using BDD Electrodes. *Chem. Eng. J.*, 197 (**2012**) 475–482.

https://doi.org/10.1016/j.cej.2012.05.062

[192] J. Martínez, A. Ortiz, I. Ortiz, State-of-the-art and Perspectives of the Catalytic and Electrocatalytic Reduction of Aqueous Nitrates. *Appl. Catal. B*, 207 (**2017**) 42–59.

https://doi.org/10.1016/j.apcatb.2017.02.016

[193] E. Lacasa, J. Llanos, P. Cañizares, M. A. Rodrigo, Electrochemical Denitrificacion with Chlorides Using DSA and BDD Anodes. *Chem. Eng. J.*, 184 (**2012**) 66–71.

https://doi.org/10.1016/j.cej.2011.12.090

[194] C. H. M. Fernandes, B. F. Silva, J. M. Aquino, On the Performance of Distinct Electrochemical and Solar-based Advanced Oxidation Processes to Mineralize the Insecticide Imidacloprid. *Chemosphere*, 275 (**2021**) 130010.

https://doi.org/10.1016/j.chemosphere.2021.130010

[195] E. Lacasa, P. Cañizares, J. Llanos, M. A. Rodrigo, Removal of Nitrates by Electrolysis in Non-chloride Media: Effect of the Anode Material. *Sep. Purif. Technol.*, 80 (**2011**) 592–599.

https://doi.org/10.1016/j.seppur.2011.06.015

[196] J. Ding, W. Li, Q. L. Zhao, K. Wang, Z. Zheng, Y. Z. Gao, Electroreduction of Nitrate in Water: Role of Cathode and Cell Configuration. *Chem. Eng. J.*, 271 (**2015**) 252–259.

https://doi.org/10.1016/J.CEJ.2015.03.001

[197] O. M. Cornejo, M. F. Murrieta, L. F. Castañeda, J. L. Nava, Characterization of the Reaction Environment in Flow Reactors Fitted with BDD Electrodes for Use in Electrochemical Advanced Oxidation Processes: A Critical Review. *Electrochim. Acta*, 331 (**2020**) 135373.

https://doi.org/10.1016/j.electacta.2019.135373

[198] F. F. Rivera, T. Pérez, L. F. Castañeda, J. L. Nava, Mathematical Modeling and Simulation of Electrochemical Reactors: A Critical Review. *Chem. Eng. Sci.*, 239 (**2021**) 116622.

https://doi.org/10.1016/j.ces.2021.116622

[199] M. Paidar, K. Bouzek, H. Bergmann, Influence of Cell Construction on the Electrochemical Reduction of Nitrate. *Chem. Eng. J.*, 85 (**2002**) 99–109.

https://doi.org/10.1016/s1385-8947(01)00158-9

[200] D. Clematis, M. Panizza, Solid Polymer Electrolyte as an Alternative Approach for the Electrochemical Removal of Herbicide from Groundwater. *Electrochim. Acta*, 378 (2021) 138127.

https://doi.org/10.1016/j.electacta.2021.138127

[201] F. F. Rivera, I. González, J. L. Nava, Copper Removal from an Effluent Generated by a Plastics Chromium-plating Industry Using a Rotating Cylinder Electrode (RCE) Reactor. *Environ. Technol.*, 29 (**2008**) 817–825.

https://doi.org/10.1080/09593330801987327

[202] J. L. Arredondo, F. F. Rivera, J. L. Nava, Silver Recovery from an Effluent Generated by Plating Industry Using a Rotating Cylinder Electrode (RCE). *Electrochim Acta*, 147 (**2014**) 337–342.

https://doi.org/10.1016/j.electacta.2014.09.127

[203] J. E. Terrazas-Rodríguez, S. Gutiérrez-Granados, M. A. Alatorre-Ordaz, C. P. De León, F. C. Walsh, The Use of a Rotating Cylinder Electrode to Selective Recover Palladium from Acid Solutions Used to Manufacture Automotive Catalytic Converters. *J Appl Electrochem*, 41 (**2011**) 89–97.

https://doi.org/10.1007/s10800-010-0212-9

[204] D. Reyter, D. Bélanger, L. Roué, Optimization of the Cathode Material for Nitrate Removal by a Paired Electrolysis Process. *J. Hazard. Mater.*, 192 (**2011**) 507–513. https://doi.org/10.1016/j.jhazmat.2011.05.054

[205] L. Szpyrkowicz, S. Daniele, M. Radaelli, S. Specchia, Removal of NO_3^- from Water by Electrochemical Reduction in Different Reactor Configurations. *Appl. Catal. B*, 66 (**2006**) 40–50.

https://doi.org/10.1016/j.apcatb.2006.02.020

[206] H. K. Kim, J. Y. Jeong, H. N. Cho, & J. Y. Park, Kinetics of Nitrate Reduction with the Packed Bed Iron Bipolar Electrode. *Sep. Purif. Technol.*, 152 (**2015**) 140–147.

https://doi.org/10.1016/j.seppur.2015.08.010

[207] M. Paidar, K. Bouzek, L. Jelínek, Z. Matějka, A Combination of Ion Exchange and Electrochemical Reduction for Nitrate Removal from Drinking Water Part II: Electrochemical Treatment of a Spent Regenerant Solution. *Water Environ. Res.*, 76 (**2004**) 2691–2698.

https://doi.org/10.1002/j.1554-7531.2004.tb00231.x

[208] M. A. Hasnat, S. Ben Aoun, M. M. Rahman, A. M. Asiri, N. Mohamed, Lean Cu-immobilized Pt and Pd films/–H^+ Conducting Membrane Assemblies: Relative

Electrocatalytic Nitrate Reduction Activities. *Journal of Industrial and Engineering Chemistry*, 28 (2015) 131–137.

https://doi.org/10.1016/j.jiec.2015.02.008

[209] P. Gayen, J. Spataro, S. Avasarala, A. M. Ali, J. M. Cerrato, B. P. Chaplin, Electrocatalytic Reduction of Nitrate Using Magnéli Phase TiO_2 Reactive Electrochemical Membranes Doped with Pd-Based Catalysts. *Environ. Sci. Technol.*, 52 (**2018**) 9370–9379.

https://doi.org/10.1021/acs.est.8b03038

[210] F. H. Adnan, M. N. Pons, E. Mousset, Mass Transport Evolution in Microfluidic Thin Film Electrochemical Reactors: New Correlations from Millimetric to Submillimetric Interelectrode Distances. *Electrochem commun*, 130 (**2021**) 107097.

https://doi.org/10.1016/j.elecom.2021.107097

[211] E. P. Rivero, F. F. Rivera, M. R. Cruz-Díaz, E. Mayen, I. González, Numerical Simulation of Mass Transport in a Filter Press Type Electrochemical Reactor FM01-LC: Comparison of Predicted and Experimental Mass Transfer Coefficient. *Chemical Chem Eng Res Des*, 90 (**2012**) 1969–1978.

https://doi.org/10.1016/j.cherd.2012.04.010

[212] A. J. Bard, L. R. Faulkner, *Electrochemical Methods: Fundamentals and Applications*, 2nd ed (Wiley, **2001**)

[213] J. Luis Nava-M. De Oca, E. Sosa, C. Ponce De León, M. T. Oropeza, Effectiveness Factors in an Electrochemical Reactor with Rotating Cylinder Electrode for the Acid-cupric/Copper Cathode Interface Process. *Chem. Eng. Sci.*, 56 (**2001**) 2695–2702.

https://doi.org/10.1016/s0009-2509(00)00514-5

[214] J. L. Nava, E. Sosa, G. Carreño, C. Ponce-de-León, M. T. Oropeza, Modelling of the Concentration–time Relationship Based on Global Diffusion-charge Transfer Parameters in a Flow-by Reactor with a 3D Electrode. *Electrochim. Acta*, 51 (**2006**) 4210–4217.

https://doi.org/10.1016/j.electacta.2005.12.002

[215] F. F. Rivera, J. L. Nava, M. T. Oropeza, A. Recéndiz, G. Carreño, Mass Transport Studies at Rotating Cylinder Electrode: Influence of the Inter-electrode Gap. *Electrochim. Acta*, 55 (**2010**) 3275–3278.

https://doi.org/10.1016/j.electacta.2009.12.060

[216] D. R. Gabe, G. D. Wilcox, J. Gonzalez-Garcia, F. C. Walsh, The Rotating Cylinder Electrode: Its Continued Development and Application. *J Appl Electrochem*, 28 (**1998**) 759–780.

https://doi.org/10.1023/a:1003464415930/metrics

[217] F. C. Walsh, G. Kear, A. H. Nahlé, J. A. Wharton, L. F. Arenas, The Rotating Cylinder Electrode for Studies of Corrosion Engineering and Protection of Metals—An Illustrated Review. *Corros Sci*, 123 (**2017**) 1–20.

https://doi.org/10.1016/j.corsci.2017.03.024

[218] Standard Methods For the examination of water and wastewater. https://www.standardmethods.org/

[219] H. Uchiyama, Q. L. Zhao, M. A. Hassan, G. Andocs, N. Nojima, K. Takeda, K. Ishikawa, M. Hori, T. Kondo, EPR-Spin Trapping and Flow Cytometric Studies of Free Radicals Generated Using Cold Atmospheric Argon Plasma and X-Ray Irradiation in Aqueous Solutions and Intracellular Milieu. *PLoS One*, 10 (2015).

https://doi.org/10.1371/journal.pone.0136956

[220] F. F. Rivera, C. P. De León, J. L. Nava, F. C. Walsh, The Filter-press FM01-LC Laboratory Flow Reactor and its Applications. *Electrochim. Acta*, 163 (**2015**) 338–354.

https://doi.org/10.1016/j.electacta.2015.02.179

[221] F. F. Rivera, L. Castañeda, P. E. Hidalgo, G. Orozco, Study of Hydrodynamics at AsahiTM Prototype Electrochemical Flow Reactor, Using Computational Fluid Dynamics and Experimental Characterization Techniques. *Electrochim. Acta*, 245 (**2017**) 107–117.

https://doi.org/10.1016/j.electacta.2017.05.134

[222] M. A. Sandoval, R. Fuentes, F. C. Walsh, J. L. Nava, C. P. de León, Computational Fluid Dynamics Simulations of Single-phase Flow in a Filter-press Flow reactor having a stack of three cells. *Electrochim. Acta*, 216 (**2016**) 490–498.

https://doi.org/10.1016/j.electacta.2016.09.045

Publications and Meetings

Publications in scientific indexed journals

[1] **R. Oriol**, J.L. Nava, E. Brillas, O. Cornejo*, I. Sirés*, Modeling hydrodynamics, mass transport and current distribution for nitrate removal in a rotating cylinder electrode reactor. *Chemichal Engineering Journal* (Submitted, MS number CEJ-D-23-13591).

[2] **R. Oriol**, J.L. Nava*, E. Brillas, I. Sirés*, Characterization of mass transport regime in a rotating cylinder electrode reactor used for electrochemical denitrification. *Journal of Environmental and Chemical Engineering* 10 (**2022**) 108839. https://www.doi.org/10.1016/j.jece.2022.108839

[3] T. Andreu*, M. Mallafré, M. Molera, M. Sarret, **R. Oriol**, I. Sirés, Effect of thermal treatment of nickel-cobalt electrocatalyst for glycerol oxidation. *ChemElectroChem* 9 (**2022**) e202200100. https://www.doi.org/10.1002/celc.202200100

[4] Z. Ye, **R. Oriol**, C. Yang, I. Sirés*, X.-Y. Li, A novel NH_2-MIL-88B(Fe)-modified ceramic membrane for the integration of electro-Fenton and filtration processes: A case study on naproxen degradation. *Chemical Engineering Journal* 433 (**2022**) 133547. https://www.doi.org/10.1016/j.cej.2021.133547

[5] **R. Oriol**, E. Brillas, P.L. Cabot, J.L. Cortina, I. Sirés*, Paired electrochemical removal of nitrate and terbuthylazine pesticide from groundwater using mesh electrodes. *Electrochimica Acta* 383 (**2021**) 138354. https://www.doi.org/10.1016/j.electacta.2021.138354

[6] I.C. Da Costa Soares, **R. Oriol**, Z. Ye, C.A. Martínez-Huitle, P.L. Cabot, E. Brillas, I. Sirés*, Photoelectro-Fenton treatment of pesticide triclopyr at neutral pH using Fe(III)–EDDS under UVA light or sunlight. *Environmental Science and Pollution Research* 28(19) (**2021**) 23833–23848. https://www.doi.org/10.1007/s11356-020-11421-8

[7] **R. Oriol**, D. Clematis, E. Brillas, J.L. Cortina, M. Panizza, I. Sirés*, Groundwater treatment using a solid polymer electrolyte cell with mesh electrodes. *ChemElectroChem* 6 (**2019**) 1235-1243.

https://www.doi.org/10.1002/celc.201801906

[8] **R. Oriol**, M.P. Bernícola, E. Brillas, P.L. Cabot, I. Sirés*, Paired electro-oxidation of insecticide imidacloprid and electrodenitrification in simulated and real water matrices. *Electrochimica Acta* 317 (**2019**) 753-765. https://www.doi.org/10.1016/j.electacta.2019.05.002

[9] **R. Oriol**, I. Sirés*, E. Brillas, A.R. De Andrade*, A hybrid photoelectrocatalytic/photoelectro-Fenton treatment of Indigo Carmine in acidic aqueous solution using TiO_2 nanotube arrays as photoanode. *Journal of Electroanalytical Chemistry* 847 (**2019**) 113088. https://www.doi.org/10.1016/j.jelechem.2019.04.048

Oral presentations in meetings

[1] **R. Oriol**, J.L. Nava, E. Brillas, I. Sirés, Computational fluid dynamics simulations applied to nitrate electroreduction for groundwater treatment. *4th E3 Mediterranean Symposium: Electrochemistry for Environment and Energy,* September 15th–17th, **2022**, Orvieto (Italy).

[2] **R. Oriol**, J.L. Nava, M. Madrid, E. Brillas, I. Sirés, Caracterización electroquímica y del transporte de masa para la reducción de nitrato en un reactor con electrodo de cilindro rotatorio. *XLII Reunión del Grupo Especializado de Electroquímica de la Real Sociedad Española de Química,* July 6th–8th, **2022**, Santander (Spain).

[3] T. Andreu, M. Mallafré, M. Molera, M. Sarret, **R. Oriol**, I. Sirés, Efecto del tratamiento térmico en electrocatalizadores de níquel y cobalto para la oxidación electroquímica del glicerol. *XLII Reunión del Grupo Especializado de Electroquímica de la Real Sociedad Española de Química,* July 6th–8th, **2022**Santander (Spain).

[4] I.C. Da Costa Soares, **R. Oriol**, Z. Ye, C.A. Martínez-Huitle, P.L. Cabot, E. Brillas, I. Sirés, Solar photoelectro-Fenton treatment of pesticides in aqueous medium at near-neutral pH using ethylenediamine-*N,N'*-disuccinic acid (EDDS). *11th European Conference on Solar Chemistry and Photocatalysis: Environmental Applications (SPEA)*, June 6th–10th, **2022**, Turin (Italy).

[5] **R. Oriol**, J.L. Nava, E. Brillas, I. Sirés, Caracterización de la difusión-reacción en un reactor electroquímico con electrodo de cilindro rotatorio empleado para la

eliminación de nitrato. *XXV Congreso de la Sociedad Iberoamericana de Electroquímica (XXV SIBAE),* April 3rd–6th, **2022**, Mexico (virtual event).

[6] **R. Oriol**, E. Brillas, P.L. Cabot, F. Centellas, I. Sirés, Simultaneous electrochemical removal of nitrate and terbuthylazine pesticide from low-conductivity groundwater. *XLI Reunión del Grupo de Electroquímica de la Real Sociedad Española de Química y 1st French-Spanish Atelier/Workshop on Electrochemistry*, July 7th–9th, **2021**, Paris (France).

[7] **R. Oriol**, E. Brillas, P.L. Cabot, I. Sirés, Tratamiento electroquímico de agua subterránea. *V Workshop de la Red E3TECH / I Workshop Iberoamericano a Distancia 'Aplicaciones Medioambientales y Energéticas de la Tecnología Electroquímica' (V E3TECH)*, October 28th–31st, **2020** (virtual event).

[8] **R. Oriol**, I.C. Da Costa Soares, Z. Ye, C.A. Martínez-Huitle, P.L. Cabot, E. Brillas, I. Sirés, Degradation of triclopyr in water at pH 7.0 by photoelectro-Fenton using Fe(III)-EDDS complex and UVA light or sunlight. *XL Meeting of the Specialized Group of Electrochemistry of the Royal Spanish Society of Chemistry and XX Iberian Meeting of Electrochemistry,* July 9th–12th, **2019**, Huelva (Spain).

[9] **R. Oriol**, D. Clematis, E. Brillas, J.L. Cortina, M. Panizza, I. Sirés, Pesticide removal from groundwater using a solid polymer electrolyte cell with a mesh BDD anode. *25th Topical Meeting of the International Society of Electrochemistry,* May 10th–15th, **2019**, Toledo (Spain).

[10] **R. Oriol**, Removal of contaminants of emerging concern from groundwater with integration of electrochemical technologies. *Regional Student Meeting* at *XXXVIII Reunión del Grupo de Electroquímica de la Real Sociedad Española de Química & 3rd E3 Mediterranean Symposium*, July 2nd–5th, **2018**, Madrid (Spain).

Poster presentations in meetings

[1] **R. Oriol**, J.A. Padilla, E. Xuriguera, I. Sirés, Robocasted steel as novel cathode material for electrocatalytic nitrate removal: a proof of concept. *4th E3 Mediterranean Symposium: Electrochemistry for Environment and Energy,* September 15th–17th, **2022**, Orvieto (Italy).

[2] **R. Oriol**, M.P. Bernícola, E. Brillas, P.L. Cabot, I. Sirés, Tratamiento electroquímico dual para el aumento de la eficiencia de descontaminación de agua subterránea. *XXIV*

Congreso de la Sociedad Iberoamericana de Electroquímica, December 7th–10th, **2020**, Uruguay (virtual event).

[3] **R. Oriol**, I.C. Da Costa Soares, Z. Ye, C.A. Martínez-Huitle, P.L. Cabot, E. Brillas, I. Sirés, Tratamiento electroquímico del pesticida triclopyr con catálisis homogénea fotoasistida a pH 7. *V Workshop de la Red E3TECH / I Workshop Iberoamericano a Distancia 'Aplicaciones Medioambientales y Energéticas de la Tecnología Electroquímica' (V E3TECH)*, October 28th–31st, **2020** (virtual event).

[4] **R. Oriol**, E. Brillas, P.L. Cabot, F. Centellas, I. Sirés, Simultaneous electrochemical removal of nitrate and terbuthylazine pesticide from low-conductivity groundwater. *71st Annual Meeting of the International Society of Electrochemistry*, August 31st–September 4th, **2020**, Belgrade (Serbia).

[5] **R. Oriol**, M.P. Bernícola, E. Brillas, P.L. Cabot, I. Sirés, Simultaneous pesticide and nitrate removal from groundwater. *XXXVIII Reunión del Grupo de Electroquímica de la Real Sociedad Española de Química & 3rd E3 Mediterranean Symposium*, July 2nd–5th, **2018**, Madrid (Spain).